KfK 4944
EUR 14015 EN
Oktober 1991

Nuclear Fusion Project Annual Report of the Association KfK/EURATOM

October 1990 - September 1991

Projekt Kernfusion

Kernforschungszentrum Karlsruhe

KfK 4944
EUR 14015 EN
October 1991

Nuclear Fusion Project Annual Report of the Association KfK/EURATOM

October 1990 - September 1991

compiled by

G. Kast

Kernforschungszentrum Karlsruhe

Kernforschungszentrum Karlsruhe GmbH
Postfach 3640, 7500 Karlsruhe 1

ISSN 0303-4003

Preface

The Nuclear Research Centre Karlsruhe (KfK) was associated to the European Fusion Programme in 1983, at the time when the Next European Torus (NET) study group and the European Fusion Technology Programme were founded. The NET project had the objective to demonstrate a stable plasma burn and to demonstrate technologies relevant and needed for a fusion power reactor. With its background from nuclear technology projects, particle accelerator development, superconductivity research, and expertise in material science, KfK was able to add resources to the European effort. On a national basis the contribution of KfK complemented the work on plasma physics of IPP Garching and on plasma wall interaction of KFA Jülich, the two other German laboratories associated to the European Fusion Programme.

The expertise for the complex technology tasks is distributed over many departments of KfK which necessitates a project organization, the nuclear fusion project (PKF). A small management group coordinates the work inside KfK and establishes and maintains the links to outside partners and institutions. The general guidelines for the work are derived from the European Community Programme, the KfK part of the work is discussed and agreed with the European Commission, which in turn gets advice from the Fusion Technology Steering Committee. Within KfK, the fusion project draws on about 20 % of the scientific and technical potential of the organization in balance with several non fusion activities. While competing with these other programmes on the resources, the nuclear fusion project capitalizes on expertise being gained in neighbouring work fields such as nuclear safety for light water reactors, remote handling and materials development. A variety of special services support the project: Data processing, assistance in operation of larger experiments, central workshops, irradiation- and hot cell facilities.

The major part of the work reported refers to critical issues in the NET/ITER programme and to tasks addressing fusion power reactors. For NET/ITER, the development of tritium processing components and loops, superconducting magnets and remote operation within the plasma chamber are highlights of the KfK program. Special testing facilities have been built or are under preparation to test prototypical components and units for NET/ITER. In particular important are the test facility for superconducting magnets TOSKA-upgrade, the in-vessel-handling mock-up EDITH and the tritium laboratory TLK. Having been planned for NET, these installations may as well qualify for being essential tools for ITER in the forthcoming engineering design phase.

Breeding blanket development, investigations into radiation and high heat load resistant structural materials and safety studies are topics of the long term programme. Gyrotrons as power sources to heat the reactor plasma are a special item which originated from earlier particle accelerator work.

These various activities are described in the present annual report which compiles actual scientific results and serves to provide the interested reader with some information on the participating research staff and with references for more insight into the work reported.

J.E. Vetter

Contents **Seite**

Report on the Technology Programme for NET

Plasma Facing Components

Introduction:

In the period to which this report refers KfK has continued to contribute to the already established tasks and in addition increased its share in taking up work on the new tasks related to CFC materials (PPM 0) and CFC-metal joints (PSM 4.4). The rather modest commitment to structural materials investigations has essentially remained the same.

Without anticipating the reporting by the task-leaders it may be allowed to stress a few highlights.

The machine for multiaxial isothermal fatigue tests as sketched in the previous report is near completion. An improved cooling is being installed for the thermal fatigue testing device (PSM 3.9).

An analysis has been made on stress distributions in a bonded ceramic-metal specimens and geometric means to reduce the peak stresses are under consideration (PSM 4.4).

Three different high emissivity coatings on the basis of Al_2O_3-TiO_2 have been selected for fatigue and thermal shock tests, and the respective 316 L tube specimens will be tested in the same devices as used for PSM 3.9 (PSM 8.1 + 2).

A characterization program accounting for the complex anisotropic behaviour of CFC and the wide range of operating temperatures has been set up, pretests on available machinery have been started with monolithic graphite as long as the CFC specimens have not been supplied yet (PPM 0.3).

The investigations on SiC have concentrated on post-irradiation measurement of thermal conductivity and fracture strength. For these properties the neutron dose thresholds were found to be different (PPM 1.2).

The influence of irradiation on fracture strength of insulator materials has comprehensively been investigated, and an understanding of microstructural evolution was achieved. Similarly the mechanism for thermal conductivity deterioration could be clarified for the high temperature region (PPM 4.1).

Means for continuously measuring dielectric properties between 70 and 400 K have been established, and a detection limit for tan δ down to 3×10^{-6} could be attained. On the basis of the steep decrease with temperature engineering design work for cryogenically cooled windows has carried on (PPM 4.2).

The facility for thermomechanical tests of FW mock-ups is nearing completion. The NET specimen TS1 has been received and is being adapted. A wishable further instrumentation at the tile attachment seems not be possible (PDT 1.4).

In the modified plasma-spray facility the screening tests with divertor bulk materials have been completed. From these pure W and liquid phase sintered metals have to be ruled out as heat sink materials (PDT 2.1).

PSM 3 Pre- and Post-Irradiation Low Cycle Fatigue of the Reference 316L Steel and Welds

Subtask 9: Tubular Unaxial and Multiaxial Isothermal and Thermal Fatigue on 316L

The loading of the First Wall (FW) of a fusion reactor causes cyclic temperature gradients. This leads with the thermal expansion and the boundary conditions to cyclic stresses and to fatigue. To reliably design the FW it is necessary to estimate the lifetime under this loading. But it is not clear yet, if experimentally determined isothermal fatigue data can be used to predict the lifetime of the FW under cyclic thermal and multiaxial loading. Neumann [1] applied loads on tubes in a way which simulates FV conditions and compared the results with LCF-tests (uniaxial isothermal loads) on 316L specimens. He observed remarkably shorter times in the first case. In this program the influence of multiaxial and thermocyclic loading is investigated on 316 L (N) steel to obtain the results necessary for a reliable design.

In the last year tubes were delivered to KfK made from a specially ordered 316L (N) charge. The production and chemical composition were ordered according to instructions of the NET-Team. Metallurgical tests result in a satisfactory chemical composition and texture of the tubes [2]. From the rough material specimens were fabricated with polished surfaces for fatigue tests under isothermal and thermal loading. With these specimens first tests were performed [2] under thermal loading with the same experimental set up as described in [1] and under uniaxial and multiaxial isothermal loading with a specially developed set-up.

Parallel to the manufacture of the specimens the machines to test the material were modified. The set-up for thermal tests described in [1] was analysed again. It was noticed that a better cooling of the specimen is necessary to ensure that no boiling will occur, which may influence lifetime, even if higher temperature gradients will be used as before. Therefore a reconstruction was done. The modifications were manufactured for the most part. The build-up of the new machine is under work.

For isothermal tests under multiaxial loading similar to the loading of the FW no commercial machine is available. Therefore a tensile test device has been reconstructed. Tubes will be tested under tension/compression and additional internal/external pressure in this device. The rebuilding for internal pressure only is finished (Fig. 1). First tests on 316L (N) specimens were performed satisfactorily [2]. The fabrication of the components for additional external pressure is finished for the most part. For measuring the axial and circumferential strains in the experiments, pretests were performed. With inductive pick-ups the diameter of the tube will be measured. The axial strain will be measured with an extensometer.

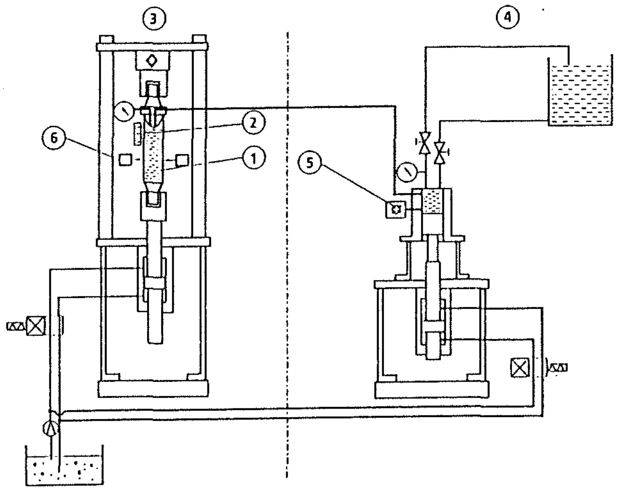

Fig. 1: Sketch of the experimental set-up to test tubes under internal pressure and axial tension/compression

1. specimen
2. extensometer for axial strain
3. tension test device
4. pressure actuator
5. pressure transducer
6. extensometer for circumferential strain

References:

[1] J. Neumann, unpublished report of KfK, 1990

[2] B. Schinke, B. Windelband, unpublished report of KfK, 1991

Staff:

W. Hartlieb
B. Schinke
B. Windelband

PSM 4 Pre- and Post-Irradiation Properties of Joinings

Subtask 5: Properties Braces and Protection Tiles to Mo Alloys T = Service Temp.; 1 dpa

Very high heat fluxes will load the surface of the divertor in a fusion reactor. To provide a good cooling, protection tiles made of CfC will be brazed directly on metallic cooling tubes.

After cooling down from brazing temperature to room temperature residual stresses can cause critical failure like it is shown in Figure 1 for a brazed Ck 45/Al_2O_3 joint.

The failure starts in ceramic at the edges of the free surface, near the interface. Further distribution occurs in the interior of the ceramic. A curved crack front can be observed. High local normal and shear stresses at the free edges are due to critical mixed mode loading conditions calculated by the finite elements method with linear elastic material behaviour (Figure 2 and Figure 3).

In this subtask methods will be investigated to reduce the local stress fields and to test the strength of the joint.

A main concept to reduce the stresses near the edges of the free surface, in particular to avoid critical tensile stresses in ceramic, is the change of geometry in the interface region. Some details in construction for TZM-CFC joints are in consideration. Until now some effects were studied for other joint systems (brazed NiFe42/Al_2O_3- and Ck45/Al_2O_3 joints respectively).

After delivery of CFC materials by the NET-Team in October 1991 the fabrication of joints will begin. The mechanical strength of the joints will be determined under different mechanical loading conditions (4-point-bending, tensile loading).

Staff:

R. Kußmaul

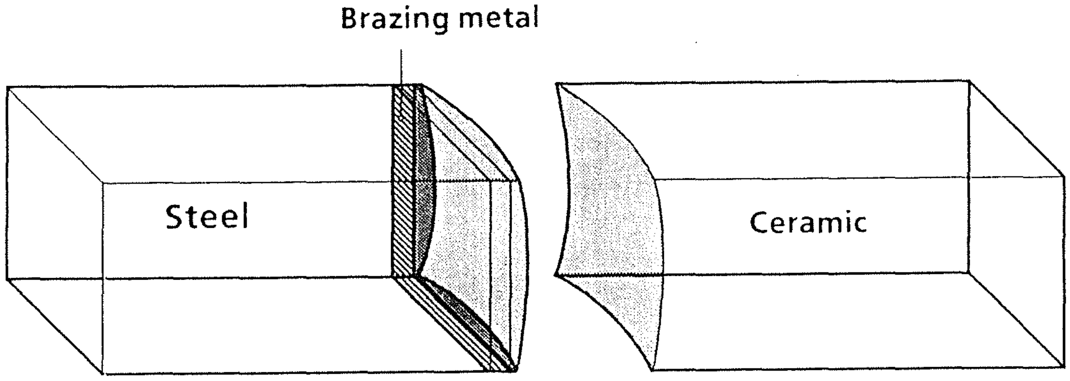

Ceramic:	Al_2O_3	45 x 10 x 11 mm^3
Brazing metal:	Ag Cu Ti 70.5 26.5 3	0.1 x 10 x 11 mm^3
Steel:	Ck 45	45 x 10 x 11 mm^3

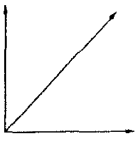

Fig.1: Failure induced by residual stresses in a Ck 45/Al_2O_3-joint.

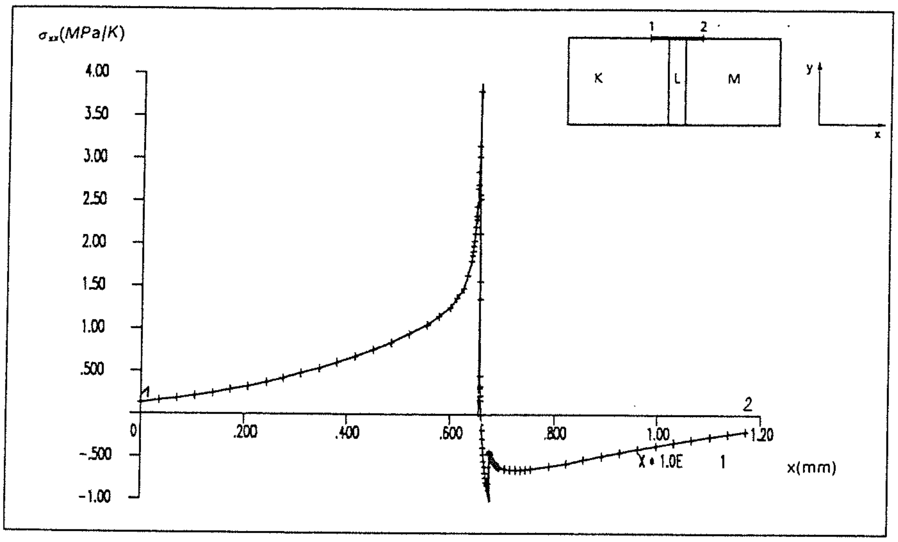

Fig. 2: Normal stresses σ_{xx} a long free surface near the interface

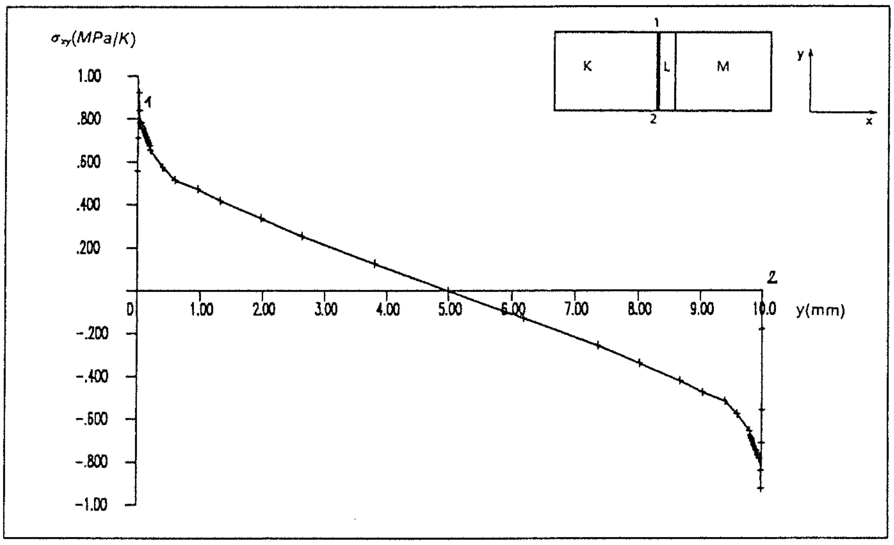

Fig. 3: Shear stresses τ_{xy} in the interface

PSM 8 Coatings and Surface Effects on 316 L

Subtask 1: Development of High Emissivity Coatings on 316L

The objective of this investigation is to develop and examine oxide coatings for the first wall of a fusion device with radiatively cooled protective tiles.

After numerous pretests and emissivity measurements (the degree of absorption is equal to the degree of emissivity) three coatings on the basis of Al_2O_3-TiO_2 were chosen for further comparative tests in the frame of the European fusion technology programme:

1. VPS (vacuum plasma spray) coating Al_2O_3 + 13 % TiO_2 without any intermediate layer;
2. VPS coating Al_2O_3 + 13 % TiO_2 with intermediate NiCrAl layer;
3. APS (air plasma spray) coating Al_2O_3 + 40 % TiO_2 with intermediate NiCrAl layer.

The comparative tests will include thermal fatigue (PSM 8.2), low cycle fatigue (to be done by ECN, Petten) and thermal shock tests (PSM 8.3). Blank specimens of 316 L suitable for these tests (tubes, LCF specimens and disks) were shipped to a subcontractor and the coatings were ordered.

Staff:
A. Skokan

Subtask 2: Low-Cycle Fatigue of High-Emissivity Coatings on 316 L (N)

To improve the emissivity of the metallic part of the First Wall (FW) a coating will be used. The loading of the FW causes cyclic temperature gradients, cyclic stresses and fatigue. Therefore the coating will be loaded cyclicly, too. The objective of this subtask is now to examine different coatings under cyclic thermal and thermally induced mechanical loading simular to FW-conditions. For these tests tubes made of steel 316 L (N) will be coated by different laboratories and tested with an experimental set up described in [1].

In the last year tubes were delivered to KfK made from a specially ordered 316 L (N) charge. The production and chemical composition were ordered according to specifications of the NET-Team. Metallurgical tests resulted in satisfactory chemical composition and texture of the tubes [2]. From the rough material specimens were fabricated with polished surfaces for fatigue tests under thermal loading. These specimens were sent to JRC Ispra, KfK (IMF I) and ECN Petten to produce different coatings.

The set-up for thermal tests is identical with the one described under PSM 3.9.

References:

[1] J. Neumann, unpublished report of KfK, 1990

[2] B. Schinke, B. Windelband, unpublished report of KfK, 1991

Staff:

W. Hartlieb
B. Schinke
B. Windelband

PPM 0 Development and Characterization of Graphites and CFCs Including Neutron Irradiation Effects

Subtask 3: Development and Characterization of High Conductivity CFC Materials

A test program is planned at KfK for characterization of CFC-materials under mechanical loads at room temperature and elevated temperatures. CFC-materials are candidate materials for the divertor of fusion reactors and for protection tiles of the first wall. The temperature gradient in these structures gives rise for thermal stresses, which may cause failure. The mechanical failure modes may be:

1.) spontaneous failure

2.) subcritical crack growth under static load

3.) or cyclic fatigue

In order to qualify candidate CFCs and to obtain materials data to design components it is necessary to investigate CFCs experimentally. Therefore the following experiments are planned in the temperature range of 25°C to 1400°C:

a.) Bending strength measurements in 3- or 4-point bending tests

b.) Determination of fracture toughness with Chevron-notched specimens and Double-Cantilever specimens.

c.) Bending tests under static load at different load levels.

d.) Interlaminar shear strength.

e.) Cyclic fatigue tests.

In 1991 different pretest were performed to develop appropriate methods for this type of tests.

At room temperature a commercial tensile test device is available to perform 3- or 4-point bending tests for strength measurements or for interlaminar shear strength tests. A tool was developed and fabricated to test different specimen sizes. Some first tests were performed with specimens made of ceramics. First bending strength measurements on CFCs were performed using specimens cut from circular samples which were available from the thermocyclic test program in PSA within the PDT 2-task.

For 4-point bending tests under static load special set ups with dead weights had been developed to test ceramics in IMF II, KfK. Now, some of these machines are available to test CFCs.

For cyclic tests a set up was modified to investigate CFC under reversed bending with R = −1 (Fig. 1). The specimen (1) is fixed at its ends in brass tubes (2) by an epoxy resin (3). Due to the low Young's modulus of the epoxy resin compared with the Young's modulus of the specimen, the load can be applied without any notch effect. The cyclic load is generated by the magnet system of two loudspeakers (4) and transferred to the specimen by a cantilever (5). The bending moment is measured by strain gauges (6) provided on the fixing bracket as well as directly on special specimens used for calibration. At the moment of failure, a silver strip (8) on the specimen is interrupted, the loudspeaker stops working and a time counter is stopped.First tests on carbon-materials were performed with monolytic graphite. The results were satisfactory.

To perform tests at high temperatures a tensile test device, which has been used for tension tests on metals before, is under modification First pretests were done with metallic specimens in a vacuum furnace at high temperatures. Based on the results a reconstruction of the furnace is under way in that tungsten will be used for electrical heating and heat shielding and to manufacture new loading tools in tungsten. With a new controller of the machine 3- and 4-point bending tests will be possible at the beginning of 1992. The temperature can be chosen between 25°C and 1600°C in vacuum. In summer 1992 it will be possible to measure force-extension diagrams, too.

Staff:

F. Ansorge
T. Fett
B. Schinke
H. Schneider

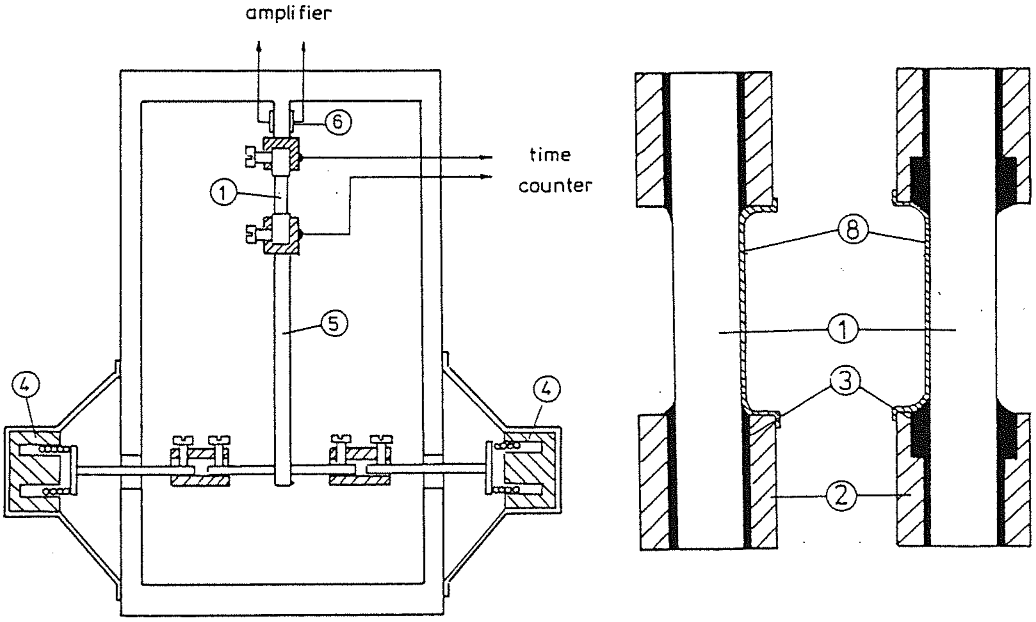

Fig. 1: Testing device for alternating bending tests

PPM 1 Development and Characterization, Neutron Irradiation Effects, Development of Coating Techniques for Doped C Composites

Subtask 2: Thermomechanical Properties of Sintered SiC and HIPped SiC

SiC qualities of industrial manufacturers are to be tested concerning the durability of tiles protecting the first wall against plasma instabilities and disruptions. KfK work has concentrated on determining the critical heat load under quasistationary conditions, including the consideration of property changes measured after neutron irradiation. The properties mainly concerned in this respect are thermal conductivity and fracture strength.

New results of the thermal conductivity of irradiated HIP-SiC could be obtained (Fig. 1). The irradiations were performed in Los Alamos at the LAMPF spallation neutron source (5x10^{20} f.n/cm^2; 0.5 dpa; 600 K), in Geesthacht (Germany) in a thermal fission reactor (4x10^{19} f.n/cm^2; 0.07 dpa; 353 K) whereas the α-particle irradiation was conducted at the KfK-cyclotron (1x10^{17} α/cm^2; 0.001 dpa; 700 K). The thermal conductivity after irradiation is reduced over a wide temperature range. At temperatures above 1600 K the thermal conductivity values approach those of the nonirradiated specimens. The temperature dependence changes from decreasing thermal conductivity in the nonirradiated case, which is typical for ceramics of high purity, to a slightly increasing thermal conductivity with increasing temperature in cases of the LAMPF and Geesthacht irradiations. The α-irradiated sample shows an intermediate behavior with a nearly constant thermal conductivity.

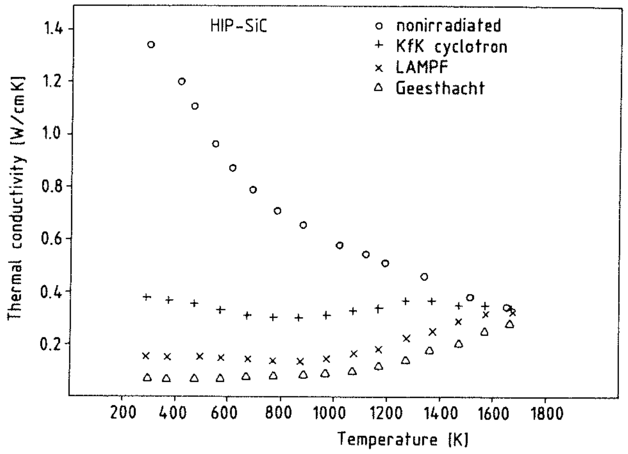

Fig. 1: Thermal conductivity of irradiated HIP-SiC.

The irradiation temperature is an important parameter which determines sensitively the extent of lattice damage which remains after the irradiation. Although the LAMPF specimen is irradiated with a dose which is more than 10 times higher than that received by the Geesthacht sample, the thermal conductivity is less reduced. This effect can be explained by the higher irradiation temperature (T_{IRR} = 600 K compared to 353 K). Since the defect mobility is higher at elevated temperatures (and therefore the probability of annealing increases), the number of remaining stable defects decreases with increasing temperatures. This fact is also reflected in the annealing behavior. Fig. 2 shows room temperature thermal conductivity data obtained after annealing the sample for one hour as a function of the annealing temperature.

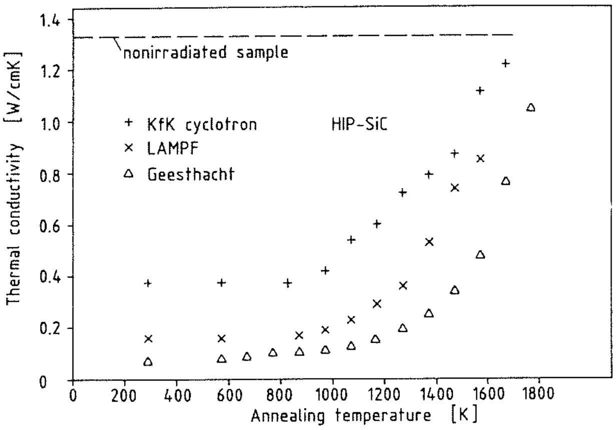

Fig. 2: Recovery of irradiated HIP- SiC.

The evaluation of various irradiation experiments conducted to investigate the strength change under neutron irradiation has been finished, and a survey of the results can be presented. An example of the strength decrease is given in Fig. 3. At neutron fluences ≥ 1x10^{26} n/m^2 a large reduction of the mean ultimate bending strength had occurred in general, combined with a large decrease of the Weibull modulus to values ≤ 5. An overall picture of the dependence of the strength change on the neutron fluence is given in Fig. 4 and 5. Some literature data were added for SSiC.

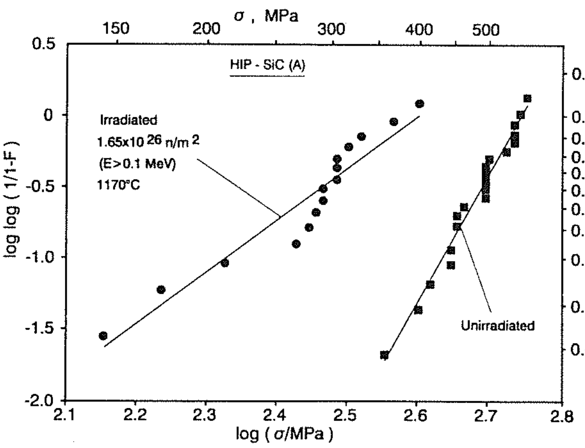

Fig. 3: Ultimate bending strength of HIP-SiC before and after irradiation.

A considerable decrease in fracture strength requires neutron fluences ≥ 3x10^{25} n/m^2 (E > 0.1 MeV), at temperatures up to 1150 °C for HIP- and CVD-SiC. At higher temperatures the decrease may already start at lower neutron fluences. A

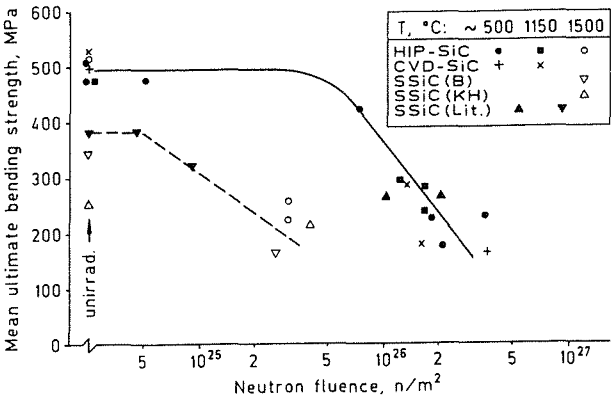

Fig. 4: Strength decrease of various SiC types under different irradiation conditions.

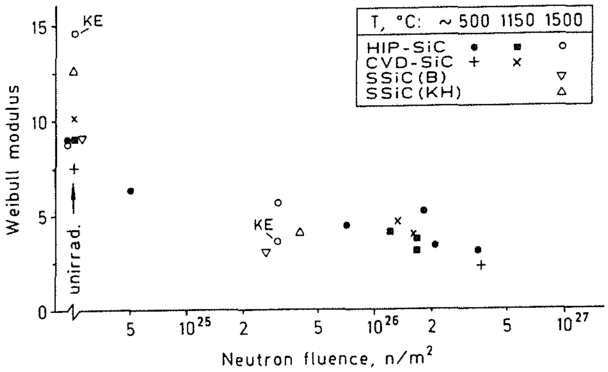

Fig. 5: Decrease of the Weibull modulus of SiC under irradiation.

transition at about 1200 °C would be intelligible, because thermal diffusion becomes fast at this temperature (~ 0.5 T_m in K). In any case the neutron dose threshold of considerable deterioration is much higher for the fracture strength than for the thermal conductivity, about 10x at the minimum. This has to be ascribed to the fact that the strength reduction is due to the agglomeration of irradiation defects, whereas the thermal conductivity is sensitive to point defects. The decrease of the mean ultimate bending strength could be explained by a reduction of the crack toughness. On the other hand, the general decrease of the Weibull modulus can better be attributed to the irradiation effect on crack initiating flaws in the ceramic material.

Concerning the irradiation behaviour of the various SiC types, the results presented in Fig. 4 and 5 show that no significant difference could be found. In particular, there is no indication of an exceptionally good behaviour of CVD-SiC, which consisted of > 95 % cubic β-SiC, compared to the other SiC types consisting of virtually pure hexagonal α-SiC.

It had been exemplified that unirradiated SiC material could fulfill the requirements set by the thermal load on wall protection tiles under normal operation and also under plasma disruption conditions. But no considerable margin is left for the deterioration of relevant properties under irradiation.

In this respect, the decrease of the thermal conductivity seems less restrictive with regard to the recovery at high operation temperature. The crucial change is the general reduction of the fracture strength by a factor of about 2x (to 4x at very low failure probability) which cannot be avoided by modifications either of the operation conditions, particularly of the temperature, or of the material type.

References:

M. Rohde, Reduction of the thermal conductivity of SiC by radiation damage, J. Nucl. Mater. 182 (1991) 87

W. Dienst, Assessment of silicon carbide as a potential wall protection material for fusion reactors, 2nd Int. Symp. on Fusion Nuclear Technology, June 2-7, 1991, Karlsruhe; to appear in Fusion Engrg. Des.

Staff:

W. Dienst
P. Fitzi
G. Gausmann
M. Rohde
H. Zimmermann

PPM 4 Material Characterization and Irradiation Effects in Ceramic Insulators

Subtask 1 : Pre and Post Irrad. Properties of Ceramic Insul. from 20 to 800°C
and
Subtask 2: Pre Irradiation Properties of Ceramics at Cryogenic Temperatures

Ceramic insulator materials (like Al_2O_3, $MgAl_2O_4$, AlN) are to be selected with regard to their resistance to thermal crack formation by dielectric loss in RF-windows. These windows shall be applied to separate wave guides for ECR heating from the plasma vacuum. KfK work has concentrated on the extension of the data base for dielectric properties, especially at 145 GHz, including further improvement in the measuring accuracy and, particularly, measurements at cryogenic temperatures. The irradiation-induced deterioration of all relevant properties, also of thermal conductivity and mechanical strength, is investigated in several neutron irradiation experiments.

Concerning the decrease of the fracture strength under irradiation, different types of Al_2O_3 and a HIP quality of AlN were examined after irradiation to fast neutron fluences of $5x10^{24}$ n/m^2 to $3x10^{26}$ n/m^2 at temperatures of 400 to 550 °C. The mean ultimate bending strength (UBS) appeared still undiminished at about $5x10^{24}$ n/m^2. At high neutron fluences $\geq$ $1x10^{26}$ n/m^2 the reduction of the mean UBS was rather similar for all sample materials, to 50 - 60 % of the initial values, surprisingly also for single crystal Al_2O_3, while some literature data promised unchanged strength for irradiated sapphire.

In order to compare and analyse the strength reduction of the different materials in various irradiation experiments, it appeared especially helpful to plot the mean UBS versus the volume increase, which is to represent the development of the irradiation defect structure. Fig. 1 shows quite similar slopes of the strength decrease, at least of all the Al_2O_3 types including CEA results for an additional polycrystalline Al_2O_3 grade irradiated in the common OSIRIS experiment. Thus the initial ranking with regard to mean UBS is widely maintained.

The rather uniform picture developing from the Al_2O_3 results gives the impression, that the strength decrease is mainly due to intracrystalline irradiation defects which do not considerably interact with the microstructure flaws conditioned by the production process and determining the crack initiation. Consequently, one has to presume that the irradiation defects are effective in decreasing the crack toughness.

The picture given for high neutron fluences in Fig. 1 could be interpreted as a saturation of the strength reduction. However, the continuing decrease of the Weibull modulus, which signifies broadening of the UBS distribution, will produce a different picture for much lower failure probability, which is of major technical importance. Fig. 2 shows a relevant modification of Fig. 1. The extrapolation to a failure probability of 1 % results in a continuous UBS decrease over the whole range of irradiation damage investigated. A similar picture is already obtained, if simply the minimum UBS values measured are plotted.

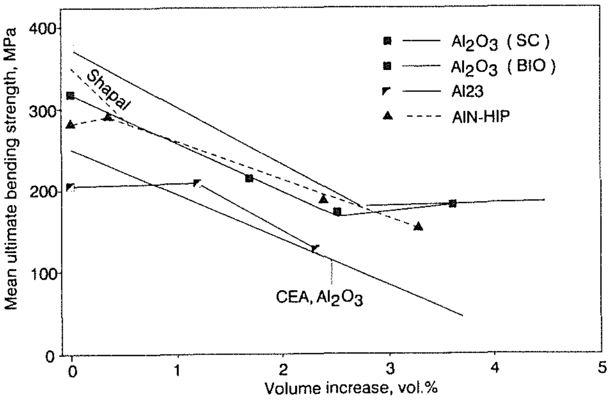

Fig. 1: Decrease of the bending strength versus volume increase under neutron irradiation.

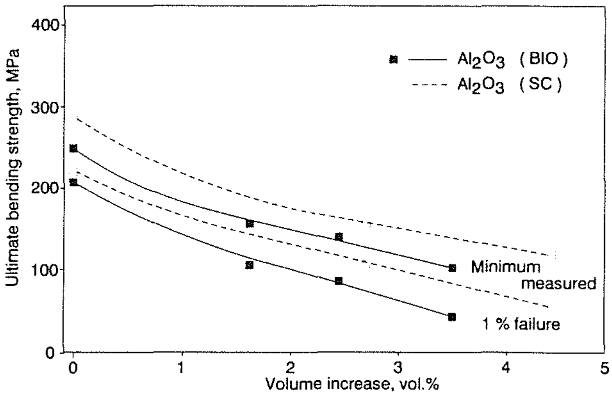

Fig. 2: Minimum and 1 % failure strength versus volume increase.

Some uncertainty remains concerning the definite position of the neutron fluence threshold for considerable strength reduction. Therefore an additional HFR irradiation is going on to a maximum fluence of $2x10^{25}$ n/m^2 at about 100 °C.

In order to evaluate the behavior of the thermal conductivity in Al_2O_3 at high damage doses, data of normalized thermal conductivity (λ_i is the intrinsic thermal conductivity of nonirradiated Al_2O_3 at $T = 300$ K) were plotted against the damage dose given in dpa (Fig. 3). Although the data scatter widely at high doses, a saturation level is reached which is marked as a dashed line. The differences in the thermal conductivity at lower damage doses are mainly due to different irradiation temperature. Irradiation at low temperatures results in higher concentration of isolated point defects and therefore in a stronger reduction of the thermal conductivity, whereas high irradiation temperatures are producing defect aggregates rather than point defects due to diffusion processes. These aggregates are not so effective in reducing thermal conductivity. The results of calculations on the basis of a microscopic model (Fig. 4) are in fair agreement with the experimental data. The data are enclosed by the two limiting cases of low and high irradiation temperatures, respectively.

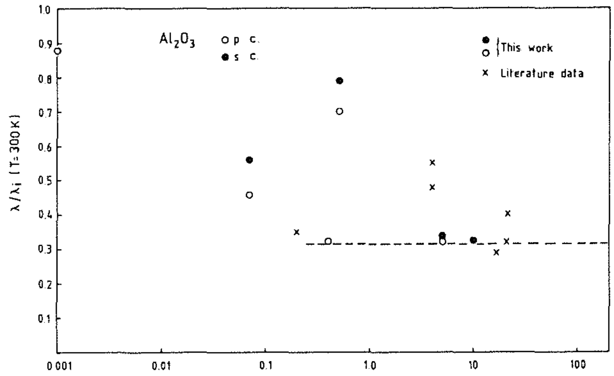

Fig. 3: Relative reduction of thermal conductivity versus damage dose.

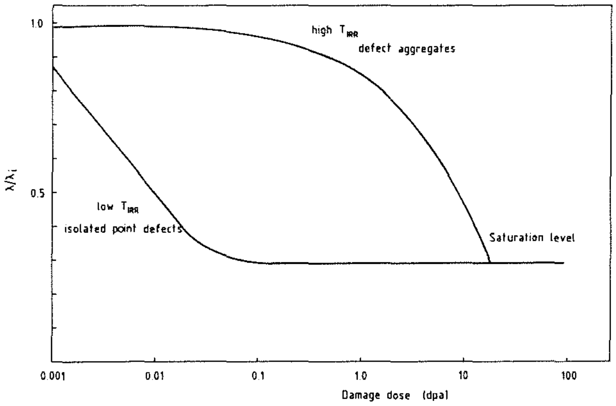

Fig. 4: Calculated thermal conductivity reduction versus damage dose.

The laser flash apparatus for measuring thermal diffusivity of irradiated samples has now been transferred into the KfK hot cells. Measurements on highly radioactive samples can start still in 1991.

The low temperature measurements of thermophysical properties started with the determination of the specific heat of AlN, $MgAl_2O_4$ and Al_2O_3 (Fig. 5).

But the main point in the investigation of low temperature properties was a critical review of the thermal conductivity literature data. As shown in Fig. 6 on the example of Al_2O_3, the absolute value of the maximum thermal conductivity as well as the temperature at which it appears is strongly dependent on impurities. Beyond the maximum the thermal conductivity depends on grain size in polycrystalline and on sample thickness in monocrystalline Al_2O_3.

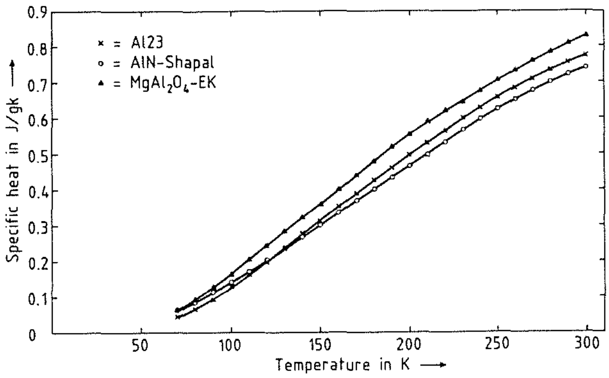

Fig. 5: Specific heat of ceramic insulators.

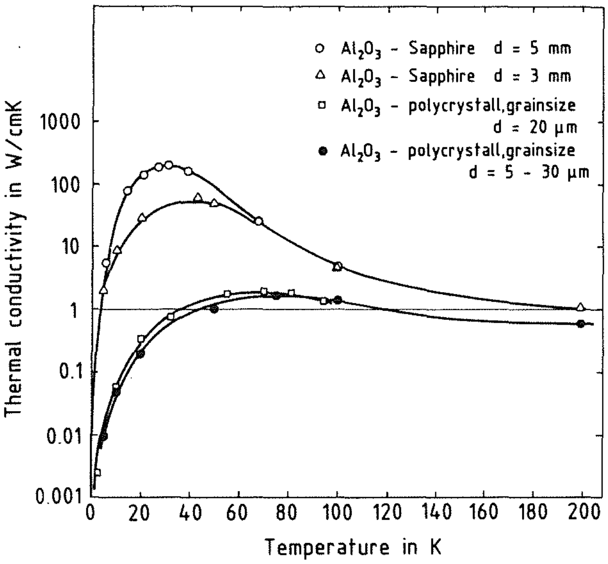

Fig. 6: Thermal conductivity of Al_2O_3 in the low temperature region.

The engineering design work for cryogenically-cooled windows for Electron Cyclotron Resonance Heating systems has identified the dielectric loss as the key parameter which will determine the operation temperature. Therefore experimental work on dielectric prooperties was focussed on getting smaller uncertainty levels in the measurement system at 145 GHz that covers the temperature range between 70 K and 400 K. As a major milestone, a measurement routine was established which allows the resonator system to warm up without supplementary heating under simultaneous registration of its mm-wave parameters. As a consequence, dielectric data are obtained quasi-continuously in temperature and systematic errors arising from thermal gradients are efficiently suppressed. At low temperature, the dielectric loss tangent tan δ appears to be quantifiable down to $3x10^{-6}$.

The observed temperature functions of dielectric properties at 145 GHz are being substantiated by intercomparison work with C.I.E.M.A.T./Madrid, where a dielectric measurement system for 15 GHz is available. A variety of mono- and polycrystalline alumina grades is under investigation. Both systems have yielded so far equivalent temperature curves of the dielectric data. In particular, a major decrease of tan δ with decreasing temperature has again been put to evidence for sapphire. A variety of differing loss curves is being found in polycrystalline alumina grades, for which purity appears to be an important factor. As for permittivity, the temperature dependence of all alumina grades could be described by an additional T^2 term (Fig. 7). The non-linear T-dependence entails that cryogenically-cooled windows will be less subjected to inhomogeneities in the electrically effective thickness (arising from temperature profiles) than conventionally-cooled windows.

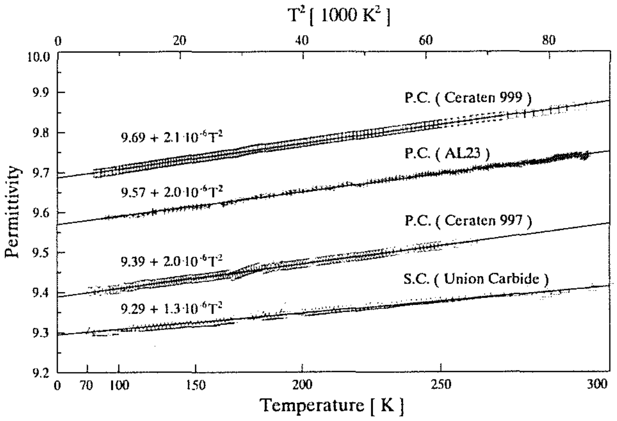

Fig. 7: The mm-wave permittivity of mono- and polycrystalline (s.c./p.c.) alumina grades plotted as a function of temperature.

Special attention was devoted to mono-crystalline silicon with small levels of extrinsic charge carriers. Due to its homopolar structure, dielectric loss is caused by free charge carriers, in contrast to Al_2O_3 where the contribution of the ionic lattice dominates, which explains that the dielectric loss behaviour of Si becomes increasingly attractive with increasing frequency. At 145 GHz, the grade with the lowest carrier concentration available proves to be superior in loss to sapphire for 300 K. Its temperature dependence, however, was found to be much more complex. The increasing mobility of the extrinsic charge carriers determines loss below room temperature, and above 330 K intrinsic conductivity becomes dominant. This means, that the excellent loss properties at room temperature can only be maintained in a very limited temperature interval.

References:

M. Rohde and B. Schulz, The effect of the exposure to different irradiation sources on the thermal conductivity of Al_2O_3, J. Nucl. Mater. 173 (1990) 289

R. Heidinger, Dielectric loss of alumina between 95 and 330 K at ECRH frequences, J. Nucl. Mater. 173 (1990) 243

R. Heidinger, The mm-wave dielectric properties of Al_2O_3 after irradiation to moderate neutron fluence, 6th Europhysical Topical Conference: Lattice Defects in Ionic Materials, Groningen, Sept. 3-7, 1990; to appear in J. of Radiation Effects and Defects in Solids

R. Heidinger, Design parameters of ceramic insulator materials for fusion reactors, J. Nucl. Mater. 179-181 (1991) 64

R. Heidinger, A. Hofmann, H.-U. Nickel and P. Norajitra, The impact of neutron irradiation to the performance of cryogenically cooled windows for electron cyclotron resonance heating, 2nd Int. Symp. on Fusion Nuclear Technology, June 2-7, 1991, Karlsruhe; to appear in Fusion Engrg. Des.

W. Dienst, Reduction of the mechanical strength of Al_2O_3, AlN and SiC under neutron irradiation; to be presented at the 5th Int. Conf. on Fusion Reactor Materials, Nov. 17-22, 1991, Clearwater, Florida

Staff:

M. Blumhofer
St. Burghartz
W. Dienst
P. Fitzi
G. Gausmann
R. Heidinger
G. Link
M. Rohde
B. Schulz
H. Zimmermann

PDT 1 Thermomechanical Tests of First Wall Mock-ups

Subtask 4: Thermomechanical Tests on Specimens Protected by Mechanically Attached C-Based Tiles

A test program FIWATKA is planned at KfK for testing first wall (FW) sections in order to:

1. observe the integral behaviour of different FW concepts including protection tiles.
2. provide an experimental basis to improve confidence in the prediction of thermal fatigue life by:
    a) validation of computational methods for
        - thermo-mechanical analysis
        - crack initiation by cyclic plastic deformations
        - fatigue crack propagation in complicated geometries.
    b) life time determination including
        - observation during life
        - study of failure modes for prototype FW sections under representative thermomechanical conditions.

The test specimens will be tested under mechanical boundary conditions and thermal loads as close as possible to those of a fusion device except for internal heat sources in the specimens and for disruption forces.

The specimen will be positioned in a vacuum chamber; it will be actively cooled with water and will be heated by thermal radiation in a cyclic manner.

A resistance heater made of a graphite plate at temperatures up to 2200°C in vacuum will serve as a heat source. It will radiate heat for a few minutes onto the surfaces of two specimens placed on both sides of the heater plate in a distance of two or three centimeters. The heater power will be turned down periodically for one or two minutes with the result that the temperature profile and the corresponding stress and strain profiles in the specimen change also periodically and cause thermal fatigue.

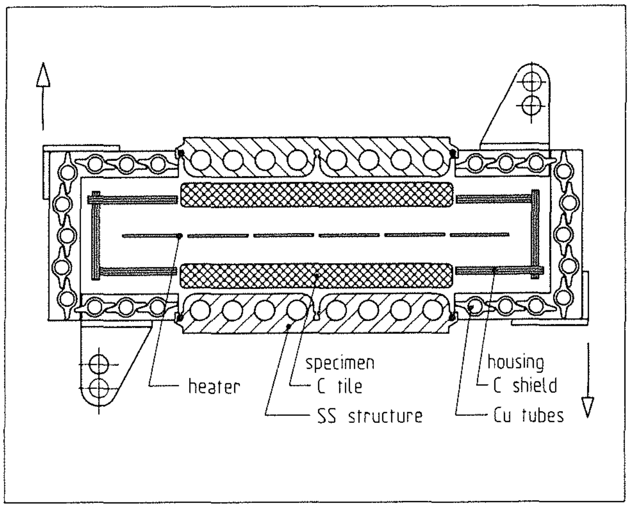

Fig. 1: Horizontal cross section through tile protected specimens and heater housing

Two specimens are integrated as the two main walls into a water cooled housing surrounding the heater as shown in the horizontal cross section of Fig. 1. The remainder of the housing is constructed from copper tubes with longitudinal fins shielding the vacuum vessel from direct thermal radiation; all of the housing inner surface may be covered with protection tiles for better uniformity of the heating conditions if the specimen is also tile-protected. A housing to fit the NET specimen TS 1 has been fabricated and is to be mounted in the vessel.

The vacuum vessel is connected to two cooling water circuits, an electrical power supply, a vacuum pump stand and a flooding gas system as shown in the simplified flow chart of Fig. 2; all these systems are installed and were checked including their control and safety instrumentation; part of these tests was running a complete heater without housing for short periods of time.

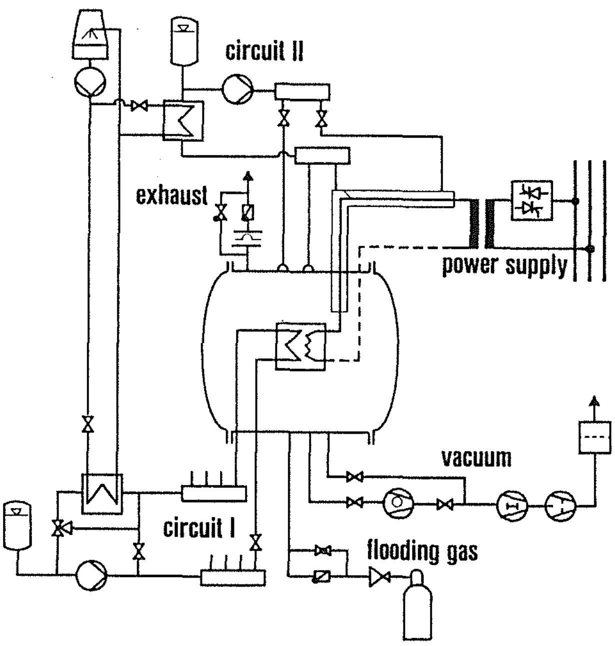

Fig. 2: FIWATKA flow chart (simplified)

The first full power tests will be conducted with two dummy specimens; they will also form the background in front of which the uniformity of the heat flux to the specimen will be measured with a movable heat flux sensor scanning the specimen surface. Both the dummy specimens and the sensor traversing unit are under construction now.

The NET specimen TS1 was received recently; modification of the coolant headers to fit the needs of the test facility were started.

TS1 is instrumented with 40 thermocouples (TCs) to measure the temperature distribution in the steel part. In order to measure the heat transfer from the tile to the wall there is need to manufacture further instrumentation near the attachment of the tile. Therefore it was checked with pretests whether further instrumentation of TS1 is possible. Different constructions were investigated. In all cases 0.5 mm diameter TCs were brazed into grooves or holes. It was necessary to develop special techniques to braze the TCs into grooves using hard solder or into blind holes using soft solder without introducing voids near the tip of the TCs: Brazing needs a uniform temperature of the specimen and the TCs must be pressed into the hole. This goal could not be achieved by local heating of specimens. Therefore, it seems that there is no way to add further instrumentation to TS1 without destroying the existing instrumentation.

As an alternative a so-called mini-test-section is under discussion; it would be well instrumented with TCs in the vicinity of the attachment rail.

References:

Hofmann, G.; Eggert, W.; FIWATKA - A first wall thermal fatigue test facility; Proc. of the Second Intern. Symposium on Fusion Nuclear Technology, Karlsruhe (to be published in Fusion Eng. and Design)

Staff:

E. Diegele
E. Eggert
G. Hofmann
H. Kreuzinger
B. Schinke
G. Schweinfurther

PDT 2 Tests of Divertor Samples and Mock-ups

Subtask 1: Pretests of Bonded Divertor Samples

The testing program on the thermomechanical behavior of candidate divertor and high heat flux components materials involves:

1. Screening tests with bulk materials up to 10^3 cycles
   a. on 31 carbon based materials
   b. on 14 copper and refractory alloys

2. Extended tests with selected materials up to 10^4 cycles
   a. on carbon fiber composites (Aerolor 05)
   b. on copper and copper alloys
   c. on molybdenum and tungsten alloys

3. Tests with bonded samples

In these tests disc-shaped samples 5 cm in diameter and 0.8 cm thick are exposed to heat pulses of typically $Q_O = 15$ MW/m^2 absorbed heat flux and $t_H = 2.3$ s pulse duration. A modified plasma spray facility (PSA) producing an Ar-10%He flame is used as heat source and pulse control device.

Tests with bulk materials (1 and 2) have been completed and have partially been documented, or evaluation and post test examination are in progress. The tests with bonded samples (3) are waiting for sample delivery. In the following the results obtained so far will be summarized.

Screening tests with carbon based materials

Results of tests up to 1000 cycles with a variety of fine grained graphites, carbon fiber composites, pyrolytic graphite, and ceramics (as described in part in the last annual report), were presented in [1].

Screening tests with copper and refractory alloys

The tests included candidate structural materials considered for the divertor, i.e., 4 molybdenum alloys, 3 tungsten alloys, 4 liquid phase sintered metals (LPSM), and 3 copper alloys. Between 2 and 4 samples of each material were cycled up to 1000 cycles, and the phenomena observed by optical microscopy range from "no visible damage" via different types of surface defects up to spontaneous "fracture" or "plastic deformation". Table 1 indicates the number of samples revealing the phenomenon out of the number of samples tested. For example, 2 of 3 tungsten (W) samples showed no visible change, and 1 of 3 tungsten samples fractured. The conclusions drawn for further testing are:

Material	Number of Cycles	Phenomena Observed at Number of Samples per Samples Tested						
		No visible change	Surf. roughening	Leaching	Surf. deterioration	Network surf. cracks	Fracture	Plastic deformation
TZM	1000	4/4						
Mo-5Re	1000			2/2				2/2
Mo-41Re	1000		2/2					2/2
$Mo-ZrO_2$	1000		2/2					2/2
W	≃1000	2/3					1/3	
W-5Re	1000	2/2						
W-26Re	1000		2/2					
Mo33	154		2/2	2/2	2/2	2/2		2/2
D17K	246		2/2	2/2	2/2	2/2		2/2
D18K	600		2/2	2/2	2/2			2/2
E2M	1000		2/2					2/2
OFHC	1000	2/2						
CuCrZr	1000	2/2						
Al-25	1000	2/2						
Conditions: $Q_0 \simeq 15 MW/m^2$, $t_H = 2.3$s, $T_{surf} \simeq 1100-1200$°C. (For Cu and Cu alloys $t_H = 1.5$s, $T_{surf} \simeq 530$°C)								

Table 1: Screening Tests with Copper and Refractory Alloys

- No damage is indicated by TZM and W-5Re, and by the three copper alloys. Those have been selected for extended cycling.

- Pure tungsten has proved to be too brittle (as was expected) and is no viable option as heat sink material.

- The LPSMs, which promised to combine the favourable physical properties of the base metals (Mo or W) with the good machinability of sintered materials, are prone to serious surface damages and plastic deformation. They were eliminated from further tests.

- The alloys with high Re content (Mo-41Re, W-26Re) may meanwhile be prohibitive because of their poor thermal conductivity and tremendous price. Yet, Mo-41Re was included in the extended cycle program for comparison.

Extended tests with carbon fiber composites

A total of six samples fabricated from four versions of Aerolor 05 with the high thermal conductivity being oriented parallel to heat flux (A05||) were exposed to 10^4 cycles. Main concerns were the mechanical integrity, erosion resistance, and degradation of properties (e.g., bending strength). The material grades were:

A05|| (assembled from standard plates)
A05|| mono (fabricated from monolithic blocks)
A05|| +SiC (as A05|| but SiC-impregnated)
A05|| + SiC mono (as A05|| mono but SiC-impregnated)

A detailed report is given in [2], a brief summary and conclusions are reproduced below:

A05|| has proved to be a very forgiving material in terms of mechanical integrity. No deterioration, no distortions, and no signs of fatigue were observed under the testing conditions applied, which were close to typical operating conditions expected for the NET divertor. Therefore, the mechanical integrity of this type of protection material is not considered as a major issue in divertor design under the expected operating conditions.

The SiC-impregnated material, A05||+SiC, is inferior to A05|| in all respects. The thermal stresses and the temperature levels are much higher (under the same loading conditions) and the strength is lower, and seems to be further diminished during cycling. Consequently, the three A05||+SiC samples showed a radial crack after a few thousand cycles.

The extremely low erosion rate of A05||+SiC obsered during the screening tests could not be preserved at higher cycle numbers (Figure 1). Therefore, the only supposed advantage of the A05||+SiC over the nonimpregnated material does not hold. (Note that in this case the erosion rate of A05||+SiC is even higher than that of A05||, which is attributed to higher surface temperatures.)

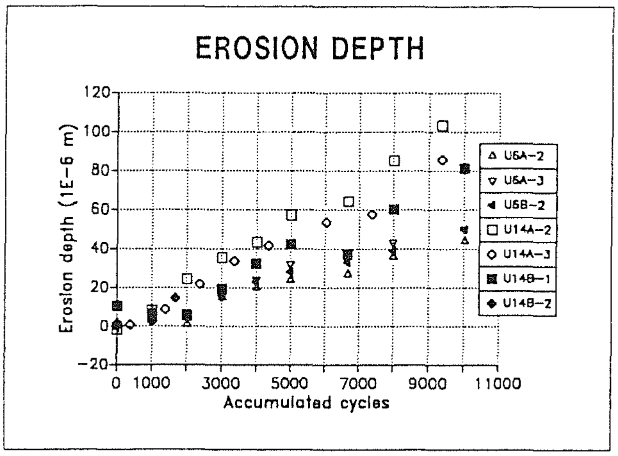

Fig. 1: Erosion Depth Measured at Intermediate Inspections. (Samples U6A = A05||, U6B = A05|| mono, U14A, = A05|| +SiC, U14B = A05|| + SiC mono)

No significant difference is seen between the assembled samples and the specially fabricated monolithic samples of both A05|| and A05||+SiC. In fact, the supposedly existing interfaces between the assembled pieces could not be identified, even not by the aid of a light microscope. Consequently, both versions (at least in the quality of the samples tested) are considered equivalent in terms of the thermomechanical behavior.

Extended tests with copper and copper alloys

Six samples fabricated from 3 different copper base materials (OFHC, Cu-.65Cr-.08Zr, Glidcop Al-25) were exposed to 10^4 cycles with stepwise increasing heat pulse lengths (t_H = 1.5 - 2.3s) resulting in maximum surface temperature of $T_{surf} \simeq$ 530 - 650 °C and calculated stress levels (elastic model) on the order of 140 MPa, which is far beyond yield strength.

While the OFHC-copper started to show surface cracks after a few thousands of cycles with increasing intensity accompanied by plastic deformation up to $\simeq$ 120 - 150 μm (convex shape at the rear side), no surface cracks and very minor deflections were observed at the dispersion hardened copper alloys after 8000 cycles. Further metallographic post test analysis is foreseen.

Extended tests with molybdenum and tungsten alloys

Six samples fabricated from TZM, Mo-41Re, and W-5Re were exposed to 10^4 cycles with t_H = 2.3 s and maximum surface temperatures of $T_{surf} \simeq$ 1200 - 1300 °C resulting in calculated stress amplitudes (elastic model) on the order of 400 MPa, which is in excess of yield strength but below ultimate strength.

Only Mo-41Re seems to develop surface cracks, whereas at the other materials no deterioration was observed by optical microscopy after 5000 cycles. Post test analysis is still in progress.

Contribution to divertor design

In order to assess stress and temperature levels generated in PSA tests, finite element analyses on divertor structures were performed. Besides the usual two dimensional modelling a 3d model was applied to a section of the so-called monoblock divertor as under development for NET on the basis of a TZM tube brazed into a block of carbon fiber composites (CFC).

The thermo-elastic analysis shows that the CFC reaches a peak temperature of 1250 °C and the TZM tube a peak temperature of 778 °C at 15 MW/m^2. Peak stresses are obtained in the brazing layer, equivalent stresses (v. Mises) ranging up to 560 MPa in the TZM and 90 MPa in the CFC [3]. This is larger than the expected tensile strength of candidate CFCs. However the results must be taken with caution because of the insufficient data base for strongly anisotropic materials like CFC.

In view of ever growing heat flux demands in divertor design a study was performed on the potential and feasibility of a liquid metal film (LMF) divertor concept. The preliminary findings and critical issues in terms of turbulent flow, heat transport, material choice, film evaporation, and design considerations were presented at an expert meeting [4]. The supportive recommendations of that meeting led to the proposal for a small-scale test stand to investigate principles of gallium technology. Meanwhile work in this field has been terminated, since the current EC program does not include R&D on advanced divertor concepts.

References:

[1] K: Kleefeldt, G. Class, K. Schramm et al.: Thermomechanical Cycle Tests on Candidiate Divertor Materials in a Plasma Spray Facility, 16th Symposium on Fusion Technology, London 3-7, September 1990, p. 433-437.

[2] K. Kleefeldt, K. Schramm, C. Strobl: unpublished report of KfK.

[3] C. Strobl: unpublished report of KfK.

[4] G. Class: Liquid metal divertor target, Presentation at the ITER Expert Meeting on Advanced Divertor Concepts, Garching, Oct. 17-19, 1990.

Staff:

G. Class
K. Kleefeldt
K. Schramm
C. Strobl

Superconducting Magnets

Introduction:

The confinement of plasmas in NET/ITER relies on a superconducting magnet system consisting of 16 D-shaped toroidal field coils, a central solenoid to drive the plasma current and a set of poloidal field coils for plasma stabilization. KfK is together with the NET team and other associated European laboratories involved in the development of these magnet systems. It develops technical conductors up to industrial production feasibility. Components of these conductors, subsize conductor assemblies and test coils are examined for their performances. Materials to be used in coil construction are qualified for their application under cycling load. Cryogenic loops and components are developed to establish stable forced flow conditions to cool the magnets. An important task consists of upgrading the existing large magnet test facility TOSKA to test prototype coils made out of different industrially manufactured conductors.

The safety of superconducting magnets is analyzed by code development and by experimental studies of effects, potentially initiating a sequence of events leading to an accident.

MCON Manufacturing of Short Length of Full-Size 40 kA Conductor

Subtask 3: 40 kA-Nb_3Sn Wind and React Conductor - I_c Characterization

The aim of the sub-task is the I_c characterization of Nb_3Sn strands and subcables under the effects of field and external strain in the high field test facility FBI.

In a joint workshop at CEA Cadarache in April 10-11, 1991, the distribution of the work was discussed. It was agreed that the strand measurement will be performed by CEA Grenoble and KfK will measure the subsize cables. The samples will be fabricated as soon as the strand material will be delivered.

The sample current capacity of the 10 kA power supply of the high field test facility FBI was not sufficient to measure the maximum critical current of the last stage NET subsize cables of the ABB and LMI conductors (see NET contracts). The assessment of different possibilities led to the result that the increase of magnetic field up to 15 T is an acceptable solution without extended and time consuming changes in the facility. Offers for such a 15 T split coil system were discussed with different companies and an order was placed.

Staff:

W. Specking

MTOR Design, Manufacturing and Test of an Outer Coil for TORE SUPRA

Subtask 2: Testing of Cooling Pipe Insulating Breaks

The task MTOR is a joint effort of KfK and CEA.

The aim of the task is the development, manufacturing and testing of NbTi conductors and specific components for the outer poloidal field coils of Tore Supra and NET. All development steps are relevant for NET:

- Development and testing of a subscale conductor in an overall verification test in the Polo model coil at KfK.
- Manufacturing and testing of a PF coil in Tore Supra using previous developments and design principles.
- Manufacturing and testing of full size (40 kA) conductor for the outer PF coils of NET and test in a pancake (Task MCOI).

The first step is being performed at KfK. The superconducting Polo model coil is under construction. The typical specifications for the operation of a Polo coil were taken from Tore Supra. The basic design principles of conductor, coil components and testing method are relevant for the Tore Supra and NET/ITER PF coils, respectively.

End of August two of four double pancakes were wound and leak tested by GEC-Alsthom, Belfort. The TOSKA facility is ready prepared for the Polo model coil test. The current leads will be tested end of this year. It is expected that the Polo model coil will be delivered to KfK middle of 1992.

1. Conductor

The basic investigations for the assurement of the conductor concept were continued. The pressure profiles measured in the stability experiment were compared with numerical calculations obtained from a simple model (Fig. 1) and were in good agreement (collaboration with the Moscow Power Eng. Institute, USSR).

For short disturbances (< 10 ms) over a long conductor length the stability limit was determined by the one dimensional heat diffusion equation. Such disturbances are fast field changes. Specially for an exponential field decrease a simple stability criteria can be derived.

Two fabrication processes for jacketing fusion conductors were successfully developed for a long conductor length. The jacketing by laser beam welded stainless steel sections and the jacketing by butt welding of extruded jacket pieces in which finally the conductor is pulled in and compacted are still reference procedures for jacketing forced flow cooled superconducting cables for the magnet of NET/ITER. The gained experience for the laser beam welded jacketing will be reported within a NET contract. In both fabricaiton methods it was not possible to keep an insulation system between subcables-subcables and subcables-jacket healthy through all fabrication steps. The experiments showed that the losses were for the intended application within the limits obtained also by resistive barriers.

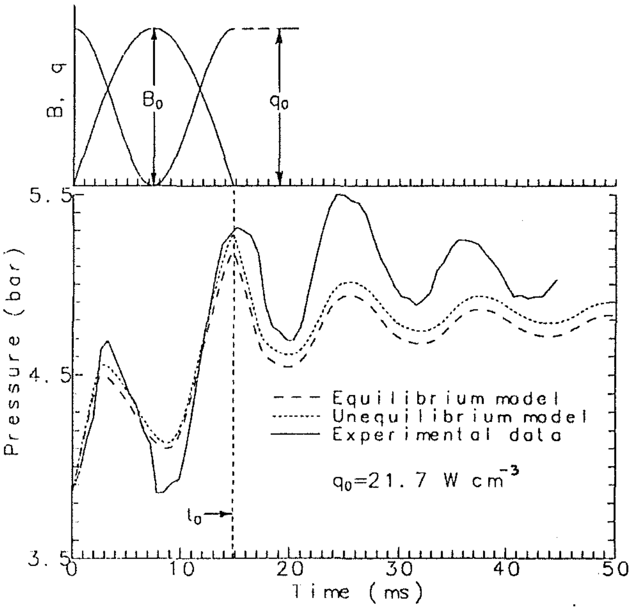

Fig. 1: Pressure increase in the Polo conductor caused by losses generated by a field pulse. The measured results are compared with two calulation models.

2. The Tore Supra Coil

The status of the work for the Tore Supra EHS coil was exchanged in a joint workshop in Cadarache April 10-11, 1991.

The main part of the work was the evaluation and interpretation of the test results of the two current leads for the Tore Supra EHS coil developed by CEA Grenoble and tested at KfK Karlsruhe. The experimental results were analyzed with the computer code "CURLEAD". This leads to improvements of "CURLEAD" and gives useful experience for further high current lead tests. The carefully evaluated results were presented in a report. The main results are summarized in the following:

The 10 kA variable cross section current leads have given the proof of being well designed for the Tore Supra application. The consumption at zero current is very low, the consumption in the pulsed mode is moderate, and the big thermal capacity at the warm end protects them from overheating for a long time period.

The determination of the friction factor by means of the so called "cross-flow-model" led to acceptable results with respect to the pressure drop behaviour at room temperature whereas at operation temperature levels the agreement is worse (Fig. 2).

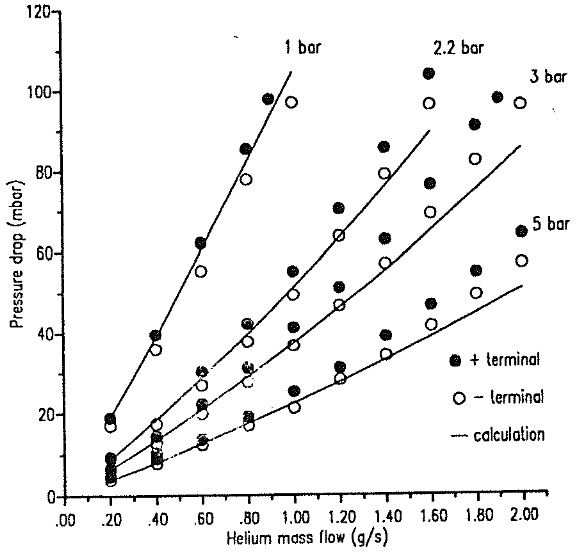

Fig. 2: Comparison of the measured and calculated pressure drop for the Tore Supra current lead

Staff:

H. Bayer
I. Donner
P. Duelli
S. Förster
P. Gruber
W.Heep
R. Heller
H. Irmisch
U. Jeske
R. Kaufmann
P. Klingenstein
W. Lehmann
G. Nöther
A. Nyilas
U. Padligur
W. Ratajczak
C. Rieger
K. Rietzschel
L. Schappals
G. Schenk
C. Schmidt
K. Schweikert
E. Specht
H.-J. Spiegel
J. Seibert
F. Süpfle
F. Süß
M. Süßer
A.Ulbricht
D.Weigert
F. Wüchner
G. Würz
H.P. Zinecker
V. Zwecker

MTOS Upgrade of the TOSKA Facility for Model Coil Testing

Subtask 1: Preparation of TOSKA for the Test of the NET Model Coil

The aim of the task is the upgrading of the TOSKA facility for testing NET/ITER model coils. An intermediate step is the testing of the LCT-coil at 1.8 K up to 10 T field level in task MBAC. Useful basis component development and testing method which can be transferred later on to NET/ITER model coils and test procedures is running in MTOR.

The main activities were the elaboration of the technical requirements of the TOSKA facility together with the NET team, the completion of the refrigerator building, the start of the installation of the 2 kW refrigerator and the installation of the 50 kA power supply.

1. Technical Specification for the TOSKA Upgrade Facility

A technical specification for the TOSKA facility is being elaborated together with the NET team. The aim is to consider and create all technical requirements necessary to perform a successful test program of the stack of NET/ITER model coils in TOSKA (Fig. 1). For the installation of the stack of model coils in the TOSKA vacuum vessel a procedure was elaborated. The coil stack has to be assembled outside the vacuum vessel to have the necessary space to handle heavy parts of the structure. For lifting the coil stack in the vacuum vessel the use of a truck crane or the use of the existing 50 t crane upgraded to 60 t combined with a new 60 t crane on the same rails were investigated. The upgrading of the existing 50 t crane combined with a new 60 t crane will have the higher flexibility and will be cheaper for more than two lifting procedures than the use of the truck crane with its implication (removal of part of the roof of the building).

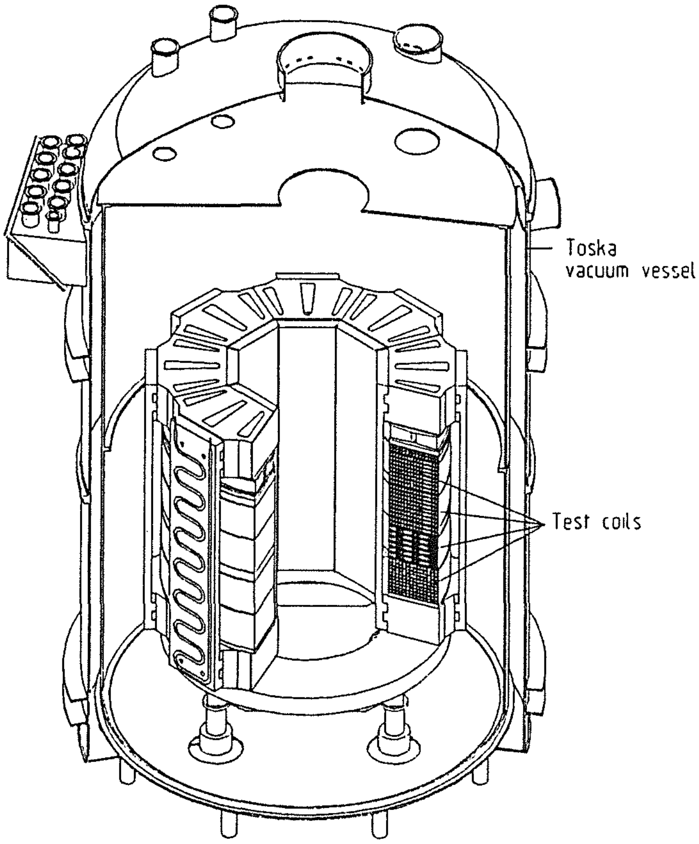

Fig. 1: Test of NET-model coils in the TOSKA facility

The cryogenic components of the system were carefully analyzed with respect to the heat loads and it was checked that the refrigerator capacity is sufficient. Necessary developments were identified, e.g. regarding the current leads. The developed current lead for 23 kV, 30 kA in MTOR has to be upgraded to 60 kA. For the operation of an extended superconducting bus bar system up to now no experience exists especially for the high quality of joints and insulation technique. Most attention was paid to an adequate simulation of the transient loading of the conductor coils which has to sustain plasma ramp up, plasma position control, divertor sweeping and plasma disruption. According to the knowledge of Task MTOR the field transients can be generated by fast discharging of sections of the model coil solenoid while other sections are shortened (Fig. 2 and 3). A sophisticated switching circuit was designed by the NET team with respect to already available power supplies to fulfill the requirements of the transient tests of the program. The circuit has to be analyzed and adapted that it can be realized with reliable electrical components.

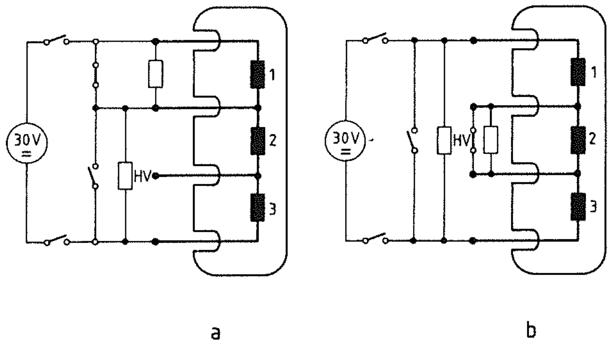

Fig. 2: Possibilities for fast discharge of NET solenoid sections. The tested model coil is short circuited (persistant mode operation) while the others are fast discharged.

a) Short circuited outer coil

b) Short circuited center coil

The instrumentation of the model coil and facility uses available measuring techniques except the instrumentation at high voltage level which is being developed and tested for the Polo model coil (Task MTOR). An extended documentation about the NET/ITER model coil is needed to assure safe operation and interpretation of test results.

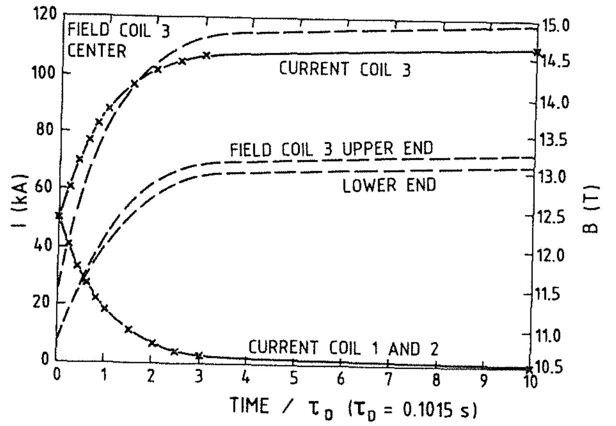

Fig. 3: Current and field versus time for circuit b.).

2. The 50 kA Power Supply

The installation of the 50 kA power supply was started in June 91 with the delivery of the transformers, thyristor rectifiers, high current switches and water cooled aluminium bus bars. The installation of the high current circuit will be finished end of August 1991.

3. The New 2kW Refrigerator

The new He plant has a 4.4 K equivalent cooling capacity of 2 kW. It is designed as a flexible multi-purpose refrigerator and liquefier, able to operate the TOSKA facility and other test set ups. Operation is possible in a wide range of cooling modes down to a temperature of 3.3 K.

3.1 Performance data

The simplified flow sheet, Fig. 4, shows the process and the design performance data. In the basic design mode the refrigerator will be operated at 3.3 K for cooling the coils. The current leads will be supplied with 4.4 K refrigeration as well as with liquefied He. It is possible to increase the cooling capacity by precooling with liquid He from the 10 000 liter storage tank and with LN_2. For the cool down of large magnet systems a cooling capacity of 20 kW is available with LN_2 precooling. Down to 80 K the plant will supply a mass flow up to 100 g/s at pressure levels up to 13 bar.

The flexible He plant can also be used as a pure refrigerator with a capacity of 1500 W at 4.4 K or as a sheer liquefier with a delivery rate of 22 g/s LHe in case of LN_2 precooling.

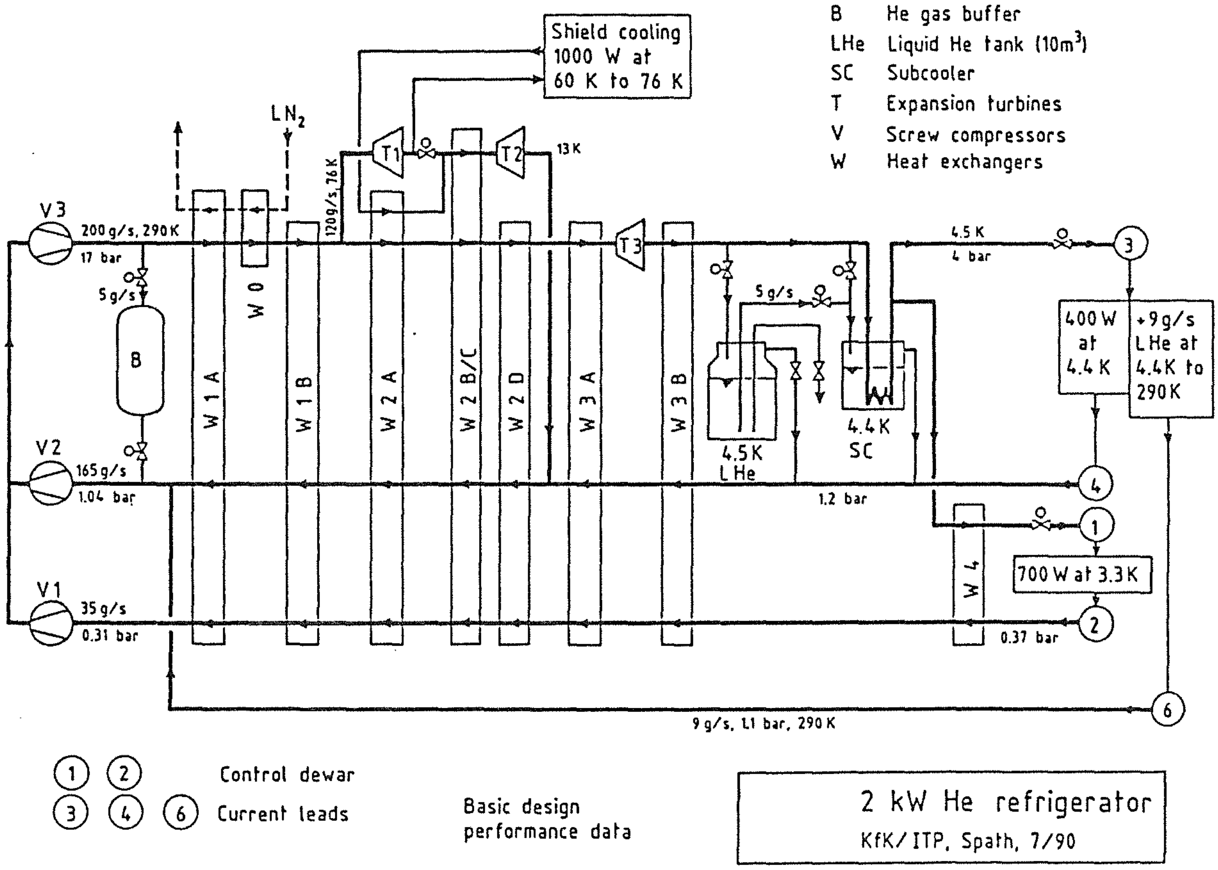

Fig. 4: Fow diagram of the 2 kW He refrigerator

3.2 Process and Main Components

For the cooling process a Claude cycle with three Sulzer dynamic gas bearing turbines (T1 to T3, the third as a JT expander) will be used. The He compressors (V1 to V3) are Aerzener oil injected screws with slide valves. A Siemens modular industrial process control system will handle the whole refrigerator automatically at different operation modes.

3.3 Status and Schedule of the Task

The general contractor Linde TVT, Munich, in cooperation with Sulzer Brothers, Switzerland, were working together with some qualified subsuppliers on the design and manufacturing of the complete He plant. Now all main components are on site and the installation is in progress (Fig. 5). The construction of the new building with a size of 25 m x 17 m x 10 m is finished. The new refrigerator will be ready for operation in the middle of 1992.

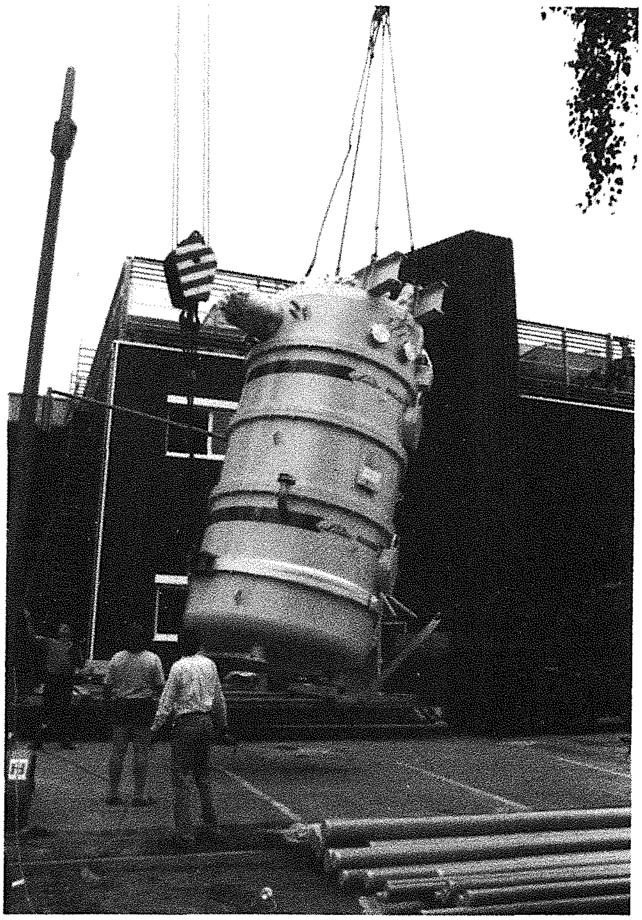

Fig. 5: The cold box, the heart of the refrigerator, being lowered into the plant hall through an opening in the roof.

Staff:

H. Barthel
A. Baumgärtner
A. Grünhagen
W. Heep
R. Heller
R. Heil
W. Herz
K. Jentzsch
H. Kapulla
B. Kneifel
W. Lehmann
W. Maurer
K. Rietzschel
L. Schappals
L. Siewerdt
A. Speier
F. Spath (for 3.)
M. Süßer
E. Ternig
A. Ulbricht
D. Weigert
F. Wüchner
G. Zahn

MBAC Development of Conductor Cooling Technique at 1.8 K

Subtask 1: He II Forced Flow Cooling: EU LCT Test at 1.8 K + DEV. Circul. Pumps

The 1.8 K cooling technique is indispensible, if technically applicable superconducting materials shall obtain their highest field levels. Therefore the task was started with a program part for the development of components included in such a cooling circuit and is continued with the operation of a large forced flow cooled fusion magnet, the Euratom LCT coil. The last experiment is an intermediate step in the sequence for upgrading the TOSKA facility for NET/ITER model coil test (Task MTOS).

1. The 1.8 K Test of Euratom LCT Coil

The installation of the 1.8 K control cryostat, transfer lines, valve box (Fig. 1) and the required upgrading of the control system was completed. All components have been tested and the system was operated at 1.8 K with a good performance. A piston pump and the heat exchanger were mounted into the 1.8 K control cryostat and a centrifugal pump was pretested at 4.2 K and will be also installed into the 1.8 K cryostat. The 1.8 K transfer line from the 1.8 K control cryostat to the vacuum vessel was designed and ordered. A call for tender was sent out for the cold He transfer lines between TOSKA and the new refrigerator.

The connection piece between the current leads (developed in task MTOR) and the Euratom LCT-coil was also designed.

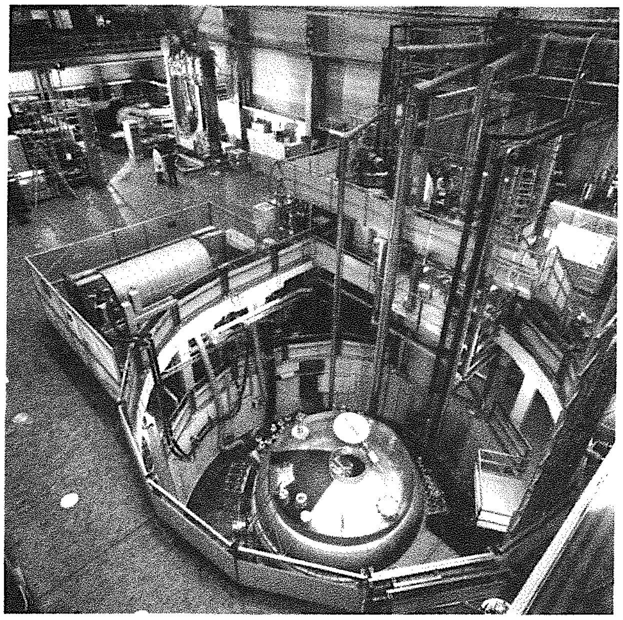

Fig. 1: The TOSKA vacuum vessel with its cryogenic supply system (3.8 K and 1.8 K control cryostat for the forced flow loops, pumps and heat exchangers). The Euratom LCT coil in the background.

The reinforcement structure was ordered from an industry company and is now in fabrication. Running FEM calculation shall clarify the effectiveness of prestressing the reinforcement structure cooling loops.

2. Thermomechanical pumps (TMP)

The development of basic technology for operating large superconducting devices with forced flow of superfluid helium has been continued. The thermomechanical pump (TMP) which has been designed to be suited for operating the EU-LCT coil at 1.8 K is being fabricated in the KfK workshop. Some components, mainly the heat exchangers, are shown in Fig. 2. The pump has been designed with the capabilities of extracting a thermal load of about 70 W from the LCT cooling loop, and of achieving a peak flow rate of about 50 g/s in loops with small flow impedances and a peak pressure difference of about 0.4 bar at small flow rate.

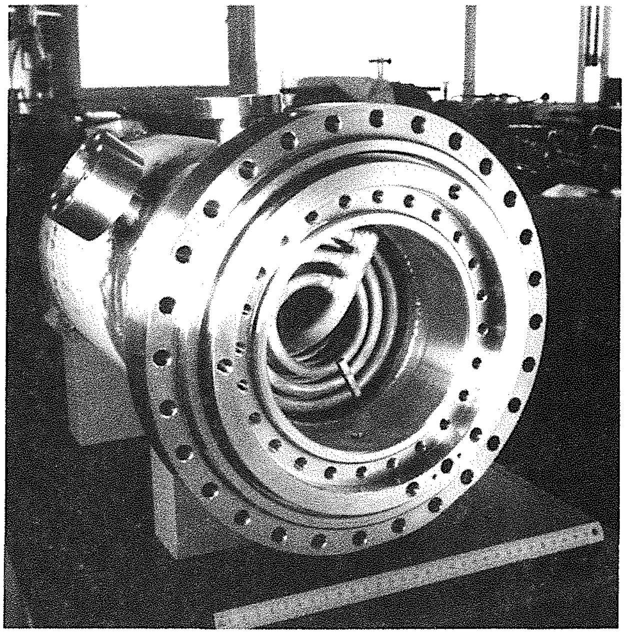

Fig. 2: Heat exchangers of the LCT-TMP (during fabrication).

Some of the pump components, i.e. the heat exchangers and the porous plugs are being tested prior to their completion. This concerns a) the most adequate treatment of the heat exchanger surfaces and b) the choice of the porous plug material.

As to the heat exchangers, it was found that sandblasting of the surfaces is very effective. In comparison with normally machined surfaces the size of such heat exchangers can be reduced by about 30 percent.

The porous plugs as used in previous experiments (pressed Al_2O_2 powder and stacks of cellulose nitrate membranes) prove to have not enough mechanical stability for technically applied devices. Therefore, additional tests are being done with sintered ceramic and metallic materials. First experiments with commercially available porous ceramic yield good results. Other probes will be tested to find the optimum also for future applications.

Staff:

H. Barthel
H. Bayer
F. Becker
G. Friesinger
A. Grünhagen
R. Heller
A. Hofmann (for 2.)
W. Herz
M. Irmisch
K. Jentzsch
H. Kapulla
B. Kneifel
W. Lehmann
W. Maurer
C. Rieger
K. Rietzschel
L. Schappals
L. Siewerdt
F. Spath
J. Spiegel
F. Süß
M. Süßer
A. Ulbricht
D. Uhlich
T. Völkel
B. Vogeley
G. Zahn (for 1.)

MFAU 1 Safety Relevant Models for NET Magnets

Subtask 1: Code Development for Simulation of Thermal Failure Propagation in Coils

To facilitate the transfer of the MAGS code system to other computers and to reduce its computing time existing ASSEMBLER routines have been reformulated in FORTRAN and the kernel of the system has been adapted to FORTRAN77 standards. This allows in a future step to apply available tools for vectorisation of the code and capabilities of vector processor computers.

The Helium hydrodynamics of the computer code SARUMAN [1], developed at NET has been introduced into the MAGS system to replace the module COOL. This new module named SARUMAN solves mass-, momentum- and energy balance for Helium coolant and has special functions for pressure drop and heat transfer applicable to cable in conduit conductors. It interacts with the module HEAT by calculating the amount of heat exchanged between the coolant and the structure. Problems with the stability of the code could be resolved.

Several analyses with the so completed code system showed up difficulties with specification of boundary conditions for the module SARUMAN. SARUMAN expects coolant pressure and coolant temperature at inlet and outlet of each pancake. They had to be specified by the user. These must be calculated in the case that in a pancake quench has occurred leading to flow reversal and to a hot gas jet into the inlet plenum of the coil. Therefore the module LINKUP has been prepared capable to simulate the piping to and from the coil and the plena at the inlet and outlet as well. LINKUP solves mass-, momentum- and energy balance but somewhat simplified compared to SARUMAN and prepares the boundary conditions for SARUMAN. The user has only to specify the boundary conditions for the coil. Additionally a check valve function was introduced to allow the prescription of a maximum pressure in the system.

To allow a simpler preparation of EFFI input the code TOKEF, available at KfK has been added to MAGS as a module.

The analysis of the quench propagation needs averaged material properties to represent the complicated conductor cross sections as well as to reduce the number of meshes. A detailed report has been prepared [2] compiling the knowledge in this field. The study shows that the presently available concepts and methods to determine averaged thermal properties are subject to several methodical shortcomings. These as well as the insufficient knowledge about the properties of the conductor cable induce uncertainties in the numerical results. Experiments on typical superconductors are necessary.

References:

[1] L. Bottura: Code development for 3D Quench Analysis NET CONTRACT NET 88/153 March 1990

[2] T. Malmberg: Internal Report.

Staff:

R. Meyder
T. Malmberg
Y. Hoang

Evaluation of Experimental Investigations

Behaviour and I-V-Characteristics of free burning arcs and arcs burning under spatial restricted conditions have been investigated. The conditions which an arc would find in a magnet system like NET were the main subject of simulation. The experimental investigations of arcs supplied by the magnet stored energy have been evaluated further. Questions like the burning voltage, influence of magnetic field on arc's behaviour and multi-arcing have been clarified. The experimental results are reproducible and explainable. Evaluation of the collected data renders feasible to transfer the results to other magnet systems like NET or ITER and to make a prediction of their behaviour in case of disturbances like shorts and arcs.

In case of a short-circuit over one complete coil, of the NET two-circuit TF system a maximum current enhancement of 260% occurs, if both circuits are discharged. If only the disturbed circuit is discharged, the coil current is slightly reduced. The short-circuit has no effect on the current distribution if only the undisturbed second circuit is discharged.

The transfer of arcing voltages to NET delivers values between 100 V and 250 V for the earlier 16 kA version of NET and values between 150 V and 400 V for the 40 kA version for a 20 mm arc. These data may be applied to calculations of current distributions in case of failures.

The amount of energy, which can be converted in case of an arc in the current path and simultaneous system discharge, depends on the arc voltage and on the discharge rate of the system. If both coil curcuits are discharged simultaneously into a 2 Ω resistor the arc's energy varies between 80 and 210 MJ with the arcing voltage in the aforementioned range. The energy is reduced by a factor of 3 if only the circuit with arc is discharged. In this case the arc's energy varies between 25 MJ and 70 MJ.

In addition, examples of conceivable arc behaviour and effects of an arc on the NET TF coil system have been investigated. Both incidents which occurred in existing magnet systems and those failures regarded as especially critical were studied. One failure occurring rather frequently is a short-circuit in a coil being converted to an arc due to overheating during discharge. Recently, such an effect was reported by Tore Supra [1]. Electrical breakdown during a fast discharge is a further origin of arcs in magnets or between magnets and ground as occurred in a coil test of the T-15 Tokamak [2]. In general, also breakage or overheating of a current lead or of a current connection between coils can lead to generation of arcs and cannot be absolutely excluded.

The work done up to now is dedicated to the investigation of occurrence and behaviour of shorts and especially arcs in a superconducting magnet system. The resulting experience, the collected data and the appied codes allow the prediction of the behaviour of future magnet systems under a number of important fault situations and is therefore successfully finished. Future work will have to stress more the possible ways of arc generation in very detailed magnet system designs.

References:

[1] Bessette, D., Ciazynski, D., Duchateau, J.L., Riban, P., Turck, B., Story of Damaged BT 17 Coil of the Superconducting Magnet of TORE SUPRA, 16. SOFT, London, 1990

[2] Cheverev, N.S., et al., T-15 Results: Testing of Systems and Parts, Proceedings of 15-SOFT, Utrecht, 1988, pp. 356-360

Staff:

P. Duelli
K.P. Jüngst
H. Kronhardt
G. Obermaier
E. Süss

MTC 1 Industrial Manufacturing of React-and-Wind Nb_3Sn Conductors and of TF Model Coils

(concluded in December 1990)

Studying both the fabrication procedure and the physical properties of react-and-wind (r&w) conductors a reduced size NET conductor at the scale of 1:1.75 with $I_c < 10$ kA at 12 T has been industrially manufactured by Vacuumschmelze and Dour Metal. The test results were summarized in a report transmitted to the NET team. The conductor fulfills all specifications for the NET-TF-coils except of keeping its superconducting state in case of a plasma disruption.

The coupling losses cannot be reduced because of its soldered core which is indispensible for this conductor type. The fact that other conductor types, e.g. "Cable in Conduit" (CIC) and Polo type (Task MOC) have the development potential to withstand a plasma disruption remaining in the superconducting state there is presently no neccessity to proceed now with the industrial production of few km of react-and-wind conductor. The development work for KfK-NET-TF conductor was concluded, the actual measurements and the comparison with a wind-and-react CIC conductor are presented in the following.

The jacketed KfK-NET-TF subsize conductor was investigated in the high field test facility FBI, i.e. the effect of static and cyclic axial strain, ε_a, on the critical current, I_c, under loaded and unloaded conditions at B = 12 T, illustrated in Fig. 1. $I_{co} = 3.93$ kA represents I_c at $\varepsilon_a = 0$, $I_{cm} = 5.25$ kA the maximum of Ic at $\varepsilon_a = \varepsilon_m$ and the ratio $I_{co}/I_{cm} = 0.75$ a measure of degradation of I_c caused by the prestrain $\varepsilon_m = 0.36\%$. This prestrain acting onto the Nb_3Sn filaments caused by the surrounded components (bronze,copper, steel) due to the higher thermal contraction from reaction (assembling) to test temperature. During the testing procedure I_c was first measured by steps under static loading up to point 1. Then the load was removed and I_c tested again, leading to point 1' with an enhanced value of $I_c = 4.48$ kA and $\varepsilon_a = 0.1\%$, the residual plastic strain of the sample. Then the load was supplied again up to point 2,etc, and the numbers 1 to 6 measured under load corresponds to numbers 1' to 6' obtained under unloaded conditions.

Irreversible behavior of I_c vs ε_a occurs between points 2 and 3 ($\varepsilon_a \approx 0.6\%$). But in contrary to such measurements recently performed on CIC conductors, both values of I_c and ε_a are slightly increased in the unloaded state with respect to those obtained under load. Thus, the irreversibility has lead to a positive change of the I_c vs ε_a characteristic. Therefore with respect to an advanced conductor in a magnet the "practical irreversible strain" should be higher than the highest ε_a value measured (point 6), i.e. "ε_{irr}" $\geq 1.04\%$.

Since fusion conductors will be exposed to cyclical loading the effect of strain cycling on the critical current has to be investigated. Therefore the subsize conductor with jacket (Fig. 1) was first statically strained up to $\varepsilon_a = 0.37\%$ and then cycled 10^3 times with 0.1 Hz between 0.10 and 0.37% strain, thus corresponding to the stress values of 0 and 345 MPa. Then I_c was measured again at 0.10 and 0.37% strain but did not show any degradation under these conditions. Finally the strain was enhanced in order to follow the I_c vs ε_a curve statically in both loaded and unloaded states.

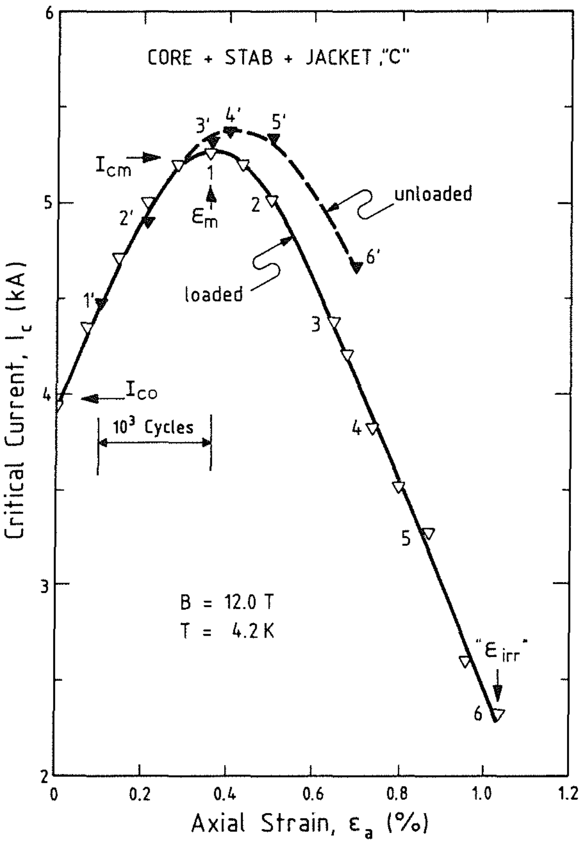

Fig. 1: Critical current as a function of axial strain under both loaded and unloaded conditions at B = 12 T for the KfK-NET-TF jacketed subsize conductor. Between 0.1 and 0.37% strain 10^3 cycles were applied to the sample at T = 4.2 K.

Summary of the main results:

(1) The delicate process of jacketing of the already reacted Nb_3Sn cable for a several meter conductor length has no negative effect on I_c, confirmed by these investigations in comparison with earlier measurements at the same unjacketed conductor.

(2) Cycling strains up to 10^3 cycles at T = 4.2 K and $\varepsilon_a \leq 0.4\%$ has no influence on the critical current.

(3) The degradation of I_c due to prestrain being "moderate" in comparison with CIC conductors fabricated by the react-and-wind technique.

The latter point illustrates more clearly Fig. 2 where the normalized critical current, I_c/I_{cm}, is plotted as a function of the intrinsic axial strain, $\varepsilon_o = \varepsilon_a - \varepsilon_m$, for both the ITP and a CIC conductor with 29 braided strands deliverd by ABB. At Ic/Icm = 1 the Nb_3Sn filaments supposed to be in an axial

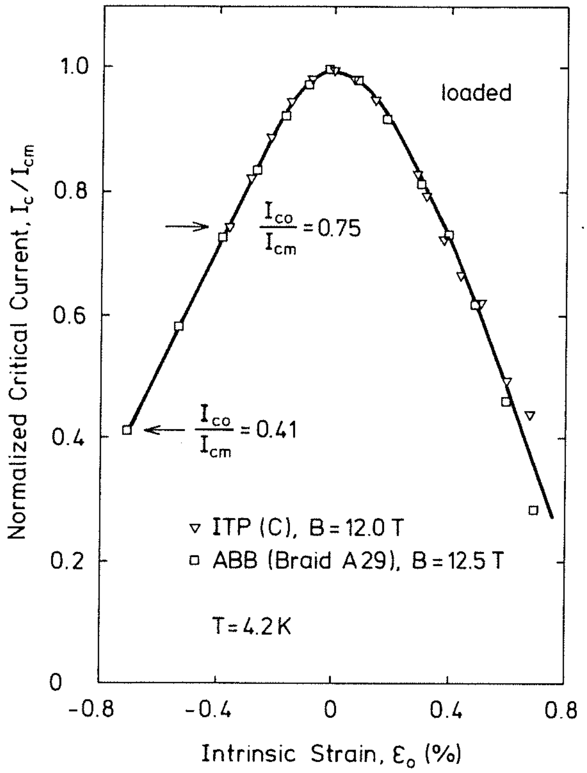

Fig. 2: Comparison between KfK-NET-TF r & w and ABB w & r conductor by plotting the normalized critical current in dependence of the intrinsic axial strain, $\varepsilon_o = \varepsilon_a - \varepsilon_m$.

strain free state, at $\varepsilon_o < 0$ under compression and at $\varepsilon_o > 0$ under tension. Both curves follow one line. However, the main difference being the end of each curve at the left hand side of the maximum where I_{co}/I_{cm} amounts to 0.75 for the ITP and 0.41 for the ABB sample (I_{co}/I_{cm} ranges from 0.41 to 0.60 for all CIC conductors measured). In this case the degradation of I_c without applied strain is about twice as high for the CIC than for the ITP conductor.

In spite of the various geometry and composition of both samples the main reason for the different I_c decrease seems to be the different manufacturing process. At the wind-and react route of CIC the complete sample including the SS conduit was heat treated up to 650°C, while at the react-and-wind process of the KfK-NET-TF conductor the conduit was drawn onto the cable at room temperature after the reaction heat treatment of the cable. This produces in case of the CIC sample an additional prestress of the conduit during cooling from 650 to 20° C resulting in an enhanced reduction of I_c.

Staff:

H. Kiesel
M. Klemm
W. Specking
A. Ulbricht

Vacuum and Fuel Cycle

Introduction:

KfK contributes essentially to NET-Fuel Cycle development by its acticities in the areas of plasma vacuum pumping and plasma exhaust gas purification. The Tritium Laboratory (TLK) will provide the means to verify the concepts developed for a fusion-relevant tritium-atmosphere. For the testing of large prototypical vacuum components preparations are under way to provide the necessary infrastructure.

In the following a few highlights have been extracted from the reports on the tasks and study contracts given below.

Graphite dust, a major concern in long-term vacuum components performance of a fusion device, will not pose a problem in the burn-mode, but possibly in the dwell-mode. Particle entrainment in case of sudden pressure vise is currently being investigated (TPV 1.1).

Measurements of pumping speed on specimens which have survived frequent regeneration cycles have shown that NET-specifications can easily be attained both by charcoal and zeolite sorbents. The emphasis is now more on thin, low tritium inventory cryosorption layers (TPV 2.1).

The performance of a large cryopanel has been tested in a simulated cryopump configuration with NET-typical gas mixtures. No poisoning could be observed, even in a two-stage operation mode when the sorption panel is loaded not only by He but also by the surplus of hydrogen and those impurities that cannot condense on the LN-cooled baffle (TPV 2.2).

A test program has been inserted on the suitability of He cryotrapping in Argon frost. Satisfactory He-pumping could be verified with the restriction that a two-stage operation mode where hydrogen condensation would have to occur in conjunction with He-trapping on the same panel is not possible (TPV 2.4).

TPV 1 Development of Solid Particle Separators for Plasma Exhaust

Solid particles generated during plasma/wall interaction can be transported into the plasma exhaust pumping system where they can influence the operation of the vacuum components (valves, pumps). The objectives of the task are to investigate the transport of solid particles during normal operation and during accidents and to develop solid particle separators for installation in front of the plasma exhaust pumping system.

The experiments are performed in a facility (SPARTA) designed on the basis of the similarity principles to conform to the NET I fusion reactor.

The results from the previous studies made under steady-state conditions, as in the burn- and dwell-modes, have been transferred to the suction line of a NET I assembly. After the capability of particle transportation has been confirmed, particle separation in the dwell mode seems to be necessary.

Further investigations under non-steady-state conditions, e.g. pressure rise in the fusion reactor, are envisaged to clarify the necessity of particle separation. For this, the resuspended amount of dust and the transport path of that dust must be determined.

The test section consists of a pipe (D = 0.1 m and L = 1 m). The bottom of the pipe in that test section is covered with a probe onto which carrier platelets made of glass (7.6x2.6 cm^2) are placed. The dust is dosed onto the carrier platelets in the vacuum.

For evaluation, the test facility is exposed to careful venting and the probe is removed. The carrier platelets are evaluated individually under the microscope and the transport path is determined by reference to the following criteria:

L_{min}: no more agglomeration recognizable in the deposit

L_{max}: segregation towards finer fraction.

The transport path L is the mean value of both variables.

With a view to investigate the dependence on size of particle transport the dusts 1 and 2 are used with the distribution of particle sizes as determined in the Coulter-Counter analysis (see Fig. 1).

The pressure and throughput parameters are varied in the investigations of the dependence of particle transport on laminar flow, Reynolds number, molecular flow, and Knudsen number.

Whereas particle transport is independent of the pressure (in the range from 5.2 x 10^{-2} to 5.2 x 10^{-3} mbar) in this investigation, the transport path has a linear course with rising throughput of dusts 1 and 2. The course of the transport path is steeper for dust 1 (see Fig. 2) [1].

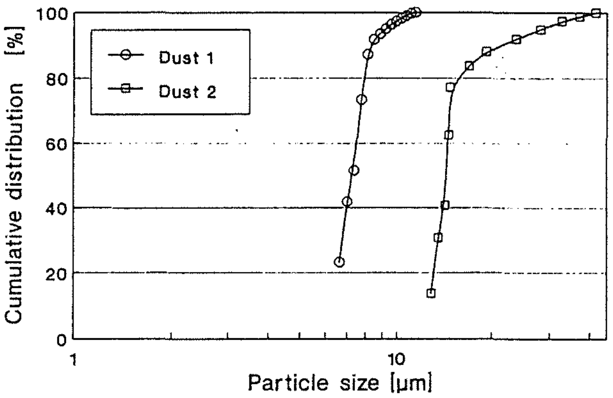

Fig. 1: Particle size distributions for dusts 1 and 2 as determined in the Coulter-Counter analysis

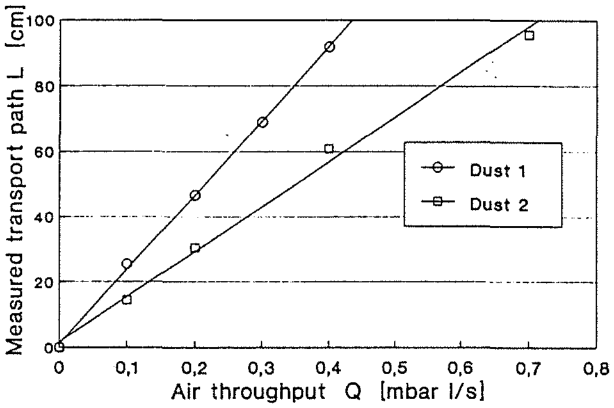

Fig. 2: Transport path versus throughput of dusts 1 and 2

Neglecting the initial velocity of the particles, the trajectories can be calculated from the equation of motion of the particles in a plane flow field:

$$L = \frac{v}{w_g} \cdot D \qquad (1)$$

The trajectories are straight lines whose slopes at constant flow rate v depend exclusively on the settling rate w_g.

The settling rate is calculated from the balance of forces acting in the steady-state settling motion; a law of resistance applicable to spherical particles in the rarefied gas is introduced for this calculation.

This yields the relative transport path L/D for the particles with a shape factor k:

$$\frac{L}{D} = \frac{Q}{A} \; \frac{1}{\rho_p g} \; \frac{K}{d_{SV}} \; \frac{1}{N_o N_{gas}} \qquad (2)$$

where

$\dot{Q}$: gas flow

A : pipe cross-sectional area

ρ_p : particle density

g : acceleration due to gravity

k : shape factor

d_{sv} : Sauter diameter

N_o : constant

N_{gas} : velocity of gas molecules

Comparison of the calculated with the measured transport paths yields a maximum deviation of 13% for dust 1.

Transferring the measured results to NET I and taking into account the material data of the deuterium/tritium mixture in formula (2) with the shape factor for dust 1 determined in the experiment gives:

$$\left(\frac{L}{D}\right)_{burn} = 0{,}55$$

$$\left(\frac{L}{D}\right)_{dwell} = 22$$

It can be seen that for this graphite dust no transport over longer distances into the vacuum pump system must be anticipated in the burn mode, whereas in the dwell mode the dusts are entrained over longer distances [1].

It is of greater interest to know the conditions for the capability of particle transport upon pressure rise in the fusion reactor after inflow of air or rupture of a coolant line. This will be the task of future investigations.

The NET I operating conditions upon pressure rise are simulated at the SPARTA model facility (equal Reynolds numbers). Two types of accidents will be simulated:

- Air inflow into the vacuum system:
  In case of air inflow, a pressure rise of 1 mbar/s (in the model 15 mbar/s) is expected.
- Rupture of a coolant water line:
  Upon rupture of a coolant water line steam enters the torus which causes the pressure to rise by 30 mbar/s (in the model 450 mbar/s). As humidity is undesirable in the vacuum model facility, this pressure rise is simulated by the air flow.

An orifice will be provided at the model facility for metering in the necessary air flow. The diameter of the bore of an orifice required for a specified pressure rise is first calculated and then definitely specified on the basis of the experiments. For this, the pressure rise was first recorded and the value subsequently determined from the pressure curve which increases linearly with the time (see Fig. 3). For the 15 or 450 mbar/s pressure rise to be simulated in NET I the orifice diameter has been determined to be 4.5 or 26.4 mm.

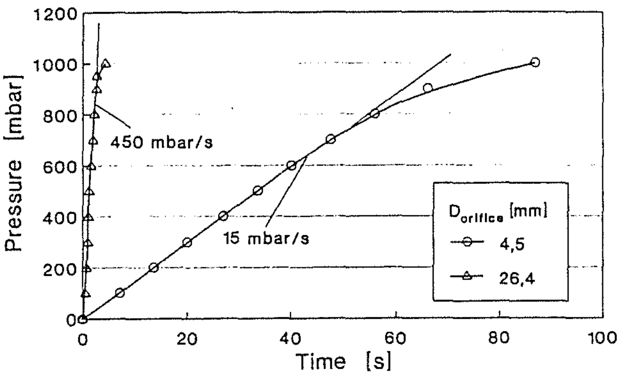

Fig. 3: Pressure curve upon pressure rise in the model equipment

The test parameters are the amount of dust metered in and prepared, respectively, for application covering the surface area or piled up as well as different particle size distributions of the dusts applied. The dependence of the amount of dust raised on the amount of dust deposited and on the different distributions of particle sizes must be determined by parameter variation.

The results of the first tests involving 450 mbar/s pressure rise are evident from fig. 4 and table 1.

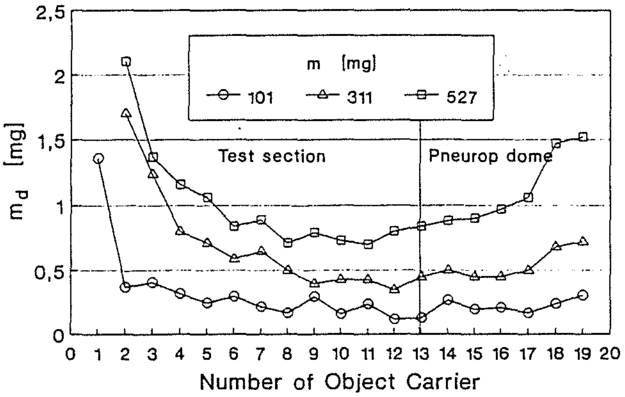

Fig. 4: Amount of dust deposited m_d on the carrier platelets for different kinds of dust application

The test section consists of 13 carrier platelets made of glass arranged one behind the other in direction of flow. Another six carrier platelets are likewise installed on the probe in a Pneurop dome connected in series with the test section.

Table 1 shows the amount of dust m_a applied to the first carrier platelet before sudden pressure rise. All other platelets were dust-free. During sudden pressure rise of 450 mbar/s the dust was partially suspended from the first platelet and deposited on other platelets and in the test section. The amount of dust on all platelets was weighed and entered in Table 1. The amount of resuspended dust m_r from the first platelet as well as the resuspension ratio m_r/m_a have been determined. The resuspension ratio decreases with rising amount of dust.

The amount of dust deposited on the carrier platelets decreases within the test section (1 - 13) and increases in the Pneurop dome (14 - 19); this tendency continues with rising amount of dust m (see fig. 4).

It is proposed to investigate in further experiments not only the influence exerted by the various pressure rises, but also the influence of the kind of dust application (piled up and covering the surface, resp.) and of the particle size distribution on the capability of transportation.

The present NET II fusion reactor differs from NET I both in terms of geometry and in the design of the exhaust line:

		NET I	NET II
Pipe diameter	:	1.5 m	2 m
Pipe length	:	6 m	15 m
Design	:	horizontal	horizontal and inclined

According to [2, 3, 4] three accident conditions have been defined for the NET II fusion reactor which are characterized by a pressure rise of 250 mbar/s upon inflow of air and by a pressure rise of 40 and 15 mbar/s, resp., upon inflow of steam.

References:

[1] Lieberknecht, M.: unpublished report of KfK, November 1990

[2] Jahn, H. : Final Report on Reactions of Graphite with Air, in-Vessel Combustion for the NET/ITER Machine GRS-A-1713, August 1990

[3] Jahn, H.: Final Report on Reaction of Graphite with Water/Steam Modelling of Combustible Gas Production, Distribtion and Consequence Analysis, GRS-A-1582, June 1989

[4] Drimille, E.: NET Final Report, Milestone 4 : Safety Assessment Report Based on Final Results on Loca Inside the Vacuum Vessel for the Reference Cases, TA/DI/SEPS/91/198, 07/03/91

Staff:

W. Höhn
M. Lieberknecht
I. Özdemir
D. Perinic
R. Rinderspacher

Platelet 1 [mg]				**Platelets 2-13 [mg]**		**Platelets 4-19 [mg]**	
before m_b	after m_a	resuspended m_r	resuspension ratio m_r/m_b	before	after	before	after
101.38	1.36	100.02	98.66	0	4.35	0	1.40
311.08	34.36	276.72	92.67	0	42.61	0	3.30
527.10	128.15	398.95	79.18	0	140.14	0	6.36

Table 1: Applied amount of dust m, deposited amount of dust m_d, and resuspension ratio m_r/m

TPV 2 Optimization of Cryogenic Vacuum Pumping of Helium

This task is aimed at developing and optimizing cryogenic vacuum pumping of plasma exhaust containing helium. To develop cryosorption panels, a variety of eligible material combinations for helium cryosorption will be tested on a reduced scale. The best suited technical solutions will be optimized on a technical scale under simulated NET operating conditions. As a result of these investigations design data and requirements will be obtained-with respect to the operation of the compound cryopumps to be used in the plasma exhaust pumping system of a fusion machine.

Subtask 1: Sorbant Pre-Selection

1. Cryopanel coating technology

A spraying technique has been developed for coating large-area cryosorption panels with sorbent material; patents have been applied for. By means of pneumatic nozzles inorganic cement and sorbent material are sprayed onto the panel surface.

2. Small-scale tests

Up to now more than 60 specimens have undergone cryosorption screening tests with helium gas at ~ 4.2 K and specific helium flows typical of NET/ITER.

In Fig. 1 the values of the pumping speed are plotted for 54 specimens. The results, classified by material groups and the methods of fixation used for some selected specimens, have been entered in Table 1.

Values of the relative pumping speed between 0.006 and 6.9 l/s have been measured. On the average, better results are obtained with the activated-charcoal coated specimens than with molecular-sieve coated specimens. Although the molecular-sieve coated specimens do not produce the same good results as the activated-charcoal coated specimens do, they are still within the limits of the required pumping speeds. On the other hand, specimens covered with a thin metallic layer applied by the plasma spray technique have not attained sufficient pumping speed.

In an intercomparison of the techniques of fixation, e.g. for activated charcoal particles, it has been found that the weight ratios of bonding masses to sorbent masses exert an influence on the measured results. For instance, for specimens having a low fraction of bonding material and, consequently, a larger free sorbent surface the results obtained have been more favourable.

Contrary to the large scattering of results for the cemented specimens, brazing on the average, produces constant results.

A surface layer of a specimen with the activated charcoal embedded in the bonding paste was removed mechanically, i.e. the sorbent was laid bare. This has considerably improved the results.

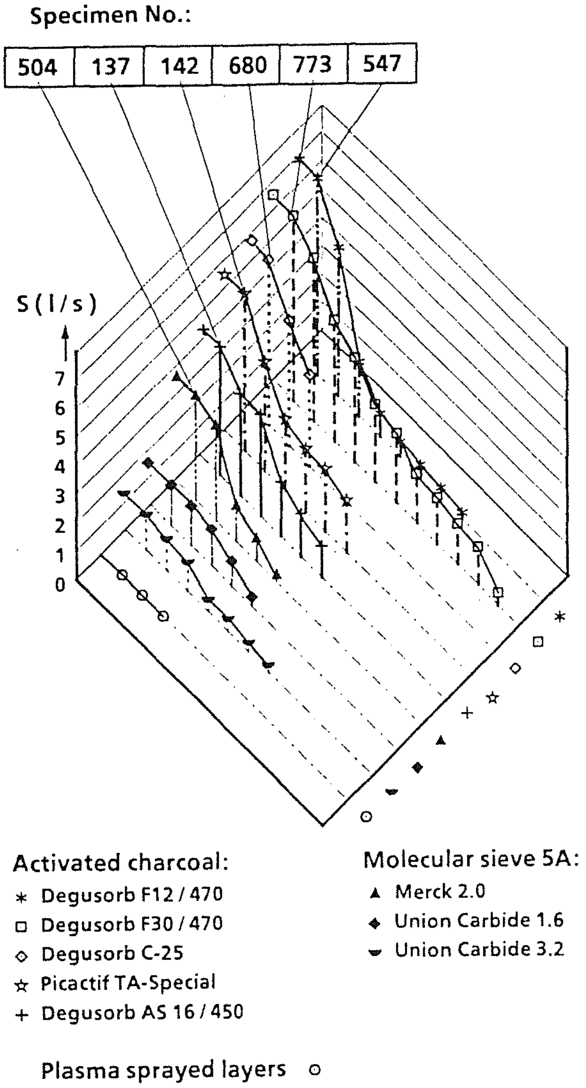

Fig. 1: Values of pumping speed for 54 specimens

Different makes of molecular sieves with identical pore sizes have produced clearly different results of pumping speeds.

On the basis of the results obtained, it can be stated that, independent of the sorbent applied, inorganic cements can be used. The copper added to the cements to increase the thermal conductivity does not show a significant influence on the measured results.

Subtask 2: Sorband Pumping Speed

After the test series 1 and 2 described in the preceding annual report the investigations were continued at the TITAN test facility (Fig. 2), with the cryosorption panel no. 3 (sorbent: activated charcoal Degusorb AS16/450, bonding: reactive braze Degussa 7200, substrate: copper E-Cu57 DIN 1787, Fig. 3).

Specimen No.	Sorbent	Bonding	Substrate	Pumping speed (90 min) [l/s]
504	Molecular sieve 5A Merck, pearls 2 mm	Cement Thermoguß	Copper	3.63
745	Molecular sieve 5A Merck, pearls 2 mm	Cement Aremco Coat	Copper	3.27
684	Molecular sieve 5A Union Carbide; pellets 1.6 mm	Cement Fortafix + copper	Copper	1.41
514	Molecular sieve 5A Union Carbide; pellets 1.6 mm	Cement Thermoguß + copper	Copper	1.39
746	Molecular sieve 5A Union Carbide; pellets 3.2 m;	Cement Aremco Coat	Copper	1.24
757	Molecular sieve 5A Union Carbide; pellets 3.2 mm	Cement Thermoguß	Alu--minium	1.09
547 *)	Activated charcoal Degusorb F12/470; pellets 1.2 mm	Cement Fortafix	Copper	6.9
147	Activated charcoal Degusorb F12/470; pellets 1.2 mm	Reactive braze Degussa CH 1AP	Copper	5.2
773	Activated charcoal Degusorb F30/470; pellets 3.0 mm	Cement Thermoguß + copper	Alu--minium	6.48
118	Activated charcoal Degusorb F30/470; pellets 3.0 mm	Reactive braze Degussa AgTi/CN1	Copper	4.23
457	Activated charcoal Degusorb F30/470; pellets 3.0 mm	Plasma sprayed copper	Copper	1.89
680	Activated charcoal Degusorb C-25; particles <2 mm	Cement Fortafix + copper	Copper	5.8
151	Activated charcoal Degusorb C-25; particles <2 mm	Reactive braze Degussa CH 1AP	Copper	4.46
142	Activated charcoal Picactif Ta Special; particles 6x3.5 mm	Reactive braze Degussa CH 1AP	Copper	5.5
568	Activated charcoal Picactif Ta Special; particles 6x3.5 mm	Cement Thermoguß	Copper	2.52
137	Activated charcoal Degusorb AS16/450; pellets 1.6 mm	Reactive braze Vakuumschmelze C2962	Copper	4.28
715	Activated charcoal Degusorb AS16/450; pellets 1.6 mm	Cement Thermoguß	Steel	3.54
446	Plasma sprayed copper	——	Copper	0.0059

Specimen diameter Ø 50 mm
Helium metering (4 ÷ 6) x 10^{-4} mbarl s^{-1}
Specimen temperature < 4.3 K
Initial pressure 10^{-4} ÷ 10^{-5} mbar

*) surface layer removed by machining

Table 1: Results of HELENE pumping speed screening tests for selected specimens

The gas pressure was measured by a Bayard-Alpert hot cathode vacuum gauge and corrected by comparison with a Baratron capacitance diaphragm gauge.

The limit of saturation of the cryopump was investigated in test no. 3 with the gas mixture typical of NET/ITER, consisting of 0.113 Ar, 0.112 CO_2, 0.225 CO, 0.194 N_2, 0.236 O_2, 1.44 CH_4, 5.02 He (in vol. percent) and residual H_2. This gas mixture was also used in the subsequent tests nos. 3, 5, 7, 8 and 9.

Metering of test no. 3 started with the extremely high gas throughput of 16.9 mbarl/s, which was then reduced to 3.38

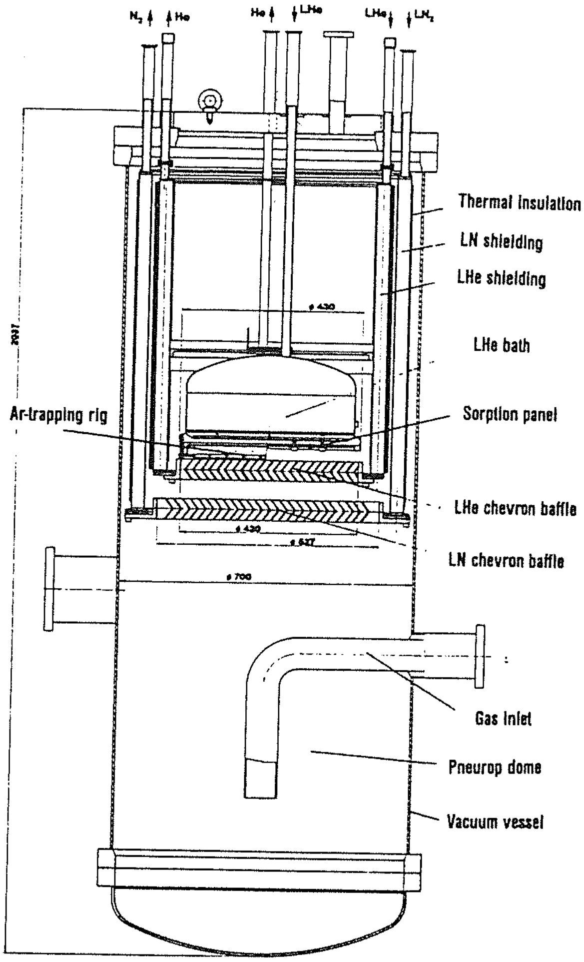

Fig. 2: TITAN test facility

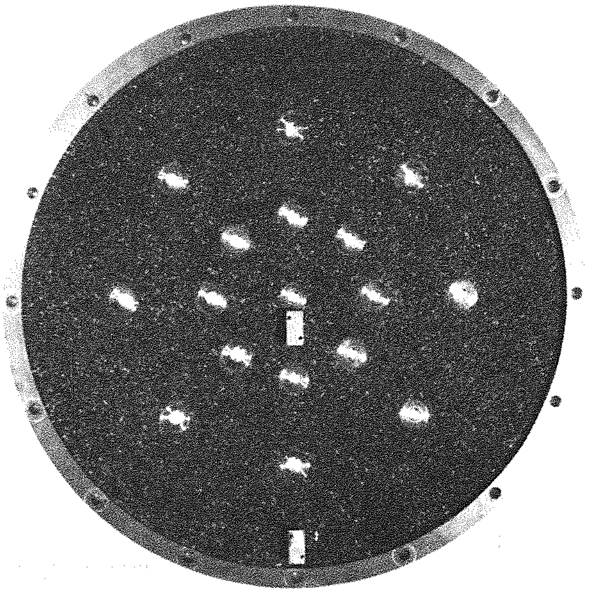

Fig. 3: Panel no. 3 for TITAN cryosorption tests

mbarl/s towards the end of the test. The pumping pressure was maintained between $1.4x10^{-3}$ and $4.4x10^{-3}$ mbar. The initial operation temperatures of the cryopanel amounted to 5.2 K (centre) and 5.1 K (edge). During the test, the temperatures of the panel and the baffles changed in spite of the constancy of the cooling conditions. The central panel temperature decreased from 5.2 K to 4.7 K while the edge temperature was reduced from 5.1 K to 4.8 K during the test. At the same time, the baffle temperature increased from 5.8 K (centre) and 5.2 K (edge) to 7.2 K (centre) and 6.2 K (edge), respectively. A total amount of gas of 219 311 mbarl was metered in without the limit of saturation of the pump being reached. A total amount of helium of 11 573 mbarl was pumped.

After regeneration of the panel and the second baffle at 90 K, pure helium was metered in during the test no. 4. The throughput attained was 1.38 mbarl/s. The objective of that test was to check whether poisoning effects could be measured before reactivation of the active surface. A total amount of helium of 35802 mbarl was pumped which is about 30 % more than in test no. 1. This corresponds to a specific amount of 162 mbarl helium pumped per gramme of charcoal or to 30.19 $mbarl/cm^2$, which is an extremely high value for this type of sorption panel. A value of 0.054 $mbarl/cm^2$ is required in NET/ITER. In this test, this value is exceeded by the factor of 559. This again indicates that there are no negative poisoning effects after 84 pumping/regeneration cycles and a saturation cycle with impurities.

Prior to test no. 5, the cryosorption panel was reactivated at 150 °C. The whole cryopump including the vacuum vessel was heated to this temperature level and degassed. Subsequently, the limit of saturation of the pump was investigated under operating conditions similar to those in test no. 3. At the very low starting pressure of $9.3x10^{-8}$ mbar, metering of the gas mixture started with a throughput of 16.9 mbarl/s. After metering of 245 146 mbarl of gas, the limit of saturation was attained. The pumping pressure increased to $1.2x10^{-2}$ mbar without causing any "runaway" of the cryopump. This safe high-pressure operation of the TITAN cryopump results from the multi-layered thermal insulation of the cryogenic reservoirs inside the pump. It is obvious from an intercomparison of tests nos. 3 and 5 that there are no significant differences in the pumping behaviour before and after reactivation of the sorption panel. The operation is not adversely affected by the impurities.

After regeneration at 90 K, test no. 6 was performed with a view to investigate pure helium pumping under operating conditions similar to those in test no. 4. In test no. 6, the pumping speed and the pumped amount of gas were slightly lower than in test no. 4, however, essential differences have not been found.

In test no. 7, copumping of helium and hydrogen including impurities was investigated at the same active surface. The internal baffle was not cooled actively. The relatively high gas throughput of 6.25 mbarl/s, which is similar to that in test no. 2, caused a relatively high pumping pressure of $1.0x10^{-2}$ mbar at the beginning of the test. A total amount of gas of 11504 mbarl was pumped.

Copumping with smaller throughputs, ranging from 0.17 to 0.68 mbarl/s, was investigated in test no. 8. The pressure level of 4.5×10^{-5} to 1.6x10-4 could be maintained. It was shown that copumping of the gas mixtures containing impurities is feasible in a two-stage cryopump. The hydrogen is being pumped together with the helium at the sorption panel.

The operating conditions of test no. 9 were identical to those of test no. 8. A 3-stage configuration was used with the second baffle being cooled by liquid helium. Consequently, lower pumping pressures resulting in a higher pumping speed were measured.

The results of the cryopumping tests with the cryopanel no. 3, compiled in Table 2, show that at a temperature level of about 5 K and NET/ITER typical specific throughputs the following helium pumping speed values (relative to the active panel surface) can be achieved: 4.41 l/s cm^2 for a three-stage pump configuration and 2.05 l/s cm^2 for a two-stage pump configuration. Copumping of helium, hydrogen and impurities was proved to be feasible at the same active surface. "Poisoning" of the sorbent by impurities has not been observed. An extremely high helium cryocapacity of 30.19 mbarl/cm^2 was achieved.

Solid sorbent cryopumping, unlike cryotrapping, shows that copumping is possible which can improve the pumping efficiency by a factor of 4.

Subtask 3: Sorband Endurance Tests

In early 1991 work started on the technical concept and on the specification of the LOTTE (Long Term Testing of Cryopanels) test facility.

It is envisaged to procure a cryopump for testing of panels (200 - 300 mm) of any geometry under NET/ITER specific conditions. It is intended to pump the plasma exhaust at three stages of this cryopump. The impurities in the gas condense on a baffle cooled to 80 - 100 K. At the second stage, a baffle cooled to < 6 K, both the remaining impurities and the hydrogen isotopes and their compounds are fixed by condensation. The remaining helium is adsorbed at the third stage, a surface coated with sorption material and cooled to $T < 5.0$ K. Two- stage operation should be possible, too.

After each pumping cycle of 80 minutes duration regeneration of 40 minutes duration is scheduled. During this partial regeneration the condensation and sorption surfaces are heated to 80 - 100 K. After the gases released have been removed by mechanical vacuum pumps, the respective cryosurfaces can be cooled again to the operating temperature, conditioning them for another pumping cycle of 80 minutes duration. It is intended to perform these process sequences automatically with the help of a process control system.

The suitability of the panels in permanent operation will be studied at the same facility under NET/ITER similar conditions, i.e. at similar operating temperatures and with similar pumping durations, similar gas loading and gas composition. Potential deteriorations of the pump characteristics ("poisoning") by the impurities present in the plasma exhaust will be studied at panels with different coatings within 84 pump cycles (one week permanent operation in NET/ITER). Moreover, the problem will be studied in the test of the loadability during permanent operation (1000 pumping cycles) of the coating applied by a technique developed at KfK.

Subtask 4: Argon Spray Tests

After tests with the cryosorption panel no. 3 the TITAN test facility was modified for tests of helium cryotrapping using argon frost. A nozzle system for argon was installed between the LHe baffle and the vessel bottom of the LHe bath. The nozzle system is made as a closed ring pipe (414 mm external diameter) with distributing grid (Fig. 4). The grid system of 40 mm mesh size is provided with 76 bores (dia. = 0.1 mm). The

Test No.	1	2	3	4	5	6	7	8	9
Kind of gas	He	mixture[3]	mixture	He	mixture	He	mixture	mixture	mixture
Throughput (mbar l s^{-1})	0.0844 - 8.44	6.246	16.88 - 3.376	1.384	16.88	1.384	6.25 - 0.34	0.169 - 0.675	0.169 - 0.675
Start pressure (mbar)	2.2×10^{-5}	$8.3 - 8.7 \times 10^{-4}$	1.4×10^{-3}	3.4×10^{-4}	1.3×10^{-3}	3.4×10^{-4}	1.0×10^{-2}	4.5×10^{-5}	2.5×10^{-5}
End pressure (mbar)	2.7×10^{-2}	$1.0 - 1.2 \times 10^{-3}$	4.4×10^{-3}	1.0×10^{-2}	1.2×10^{-2}	2.9×10^{-2}	3.0×10^{-1}	1.6×10^{-4}	7.4×19^{-5}
Pumping speed (ls^{-1})	3837 - 313	7526 - 5206	12060 - 770	4072 - 138	1300 - 282	4072 - 48	625 - 1	3752 - 4221	6753 - 9126
Sp. He pumping speed [1] (l$s^{-1}cm^{-2}$)	3.24 - 0.26	6.35 - 4.39	10.2 - 5.5	3.43 - 0.12	10.96 - 0.24	3.43 - 0.04	$0.53 - 10^{-3}$	3.16 - 3.56	5.69 - 7.69
Sp. pumping speed [2] (l$s^{-1}cm^{-2}$)	1.76 - 0.14	3.45 - 2.39	0.65 - 0.35	1.87 - 0.06	5.96 - 0.13	1.87 - 0.02	$0.29 - 10^{-3}$	1.72 - 1.94	3.1 - 4.18
Pumped gas quantity (mbar l)	22027	29984	219311	35802	245146	24505	11504	6078	4812
Pressure before pumping (mbar)	1.4×10^{-8}	$1.1 - 1.5 \times 10^{-6}$	6.0×10^{-7}	1.4×10^{-6}	9.3×10^{-8}	1.1×10^{-6}	1.5×10^{-6}	8.3×10^{-7}	7.7×10^{-6}
Pressure after pumping (mbar)	4.7×10^{-3}	$3.0 - 5.5 \times 10^{-5}$	2.9×10^{-3}	8.0×10^{-3}	9.5×10^{-2}	1.4×10^{-2}	2.4×10^{-2}	7.7×10^{-6}	1.4×10^{-5}

[1] relative to the active panel surface 1186 cm^2
[2] relative to the LN baffle surface 2181 cm^2
[3] Vol. percent 0.113 Ar, 0.112 CO_2, 0.225 CO, 0.194 N_2, 0.236 O_2, 1.44 CH_4, 5.02 He, remainder H_2

Table 2: Results of cryopumping tests with panel no. 3

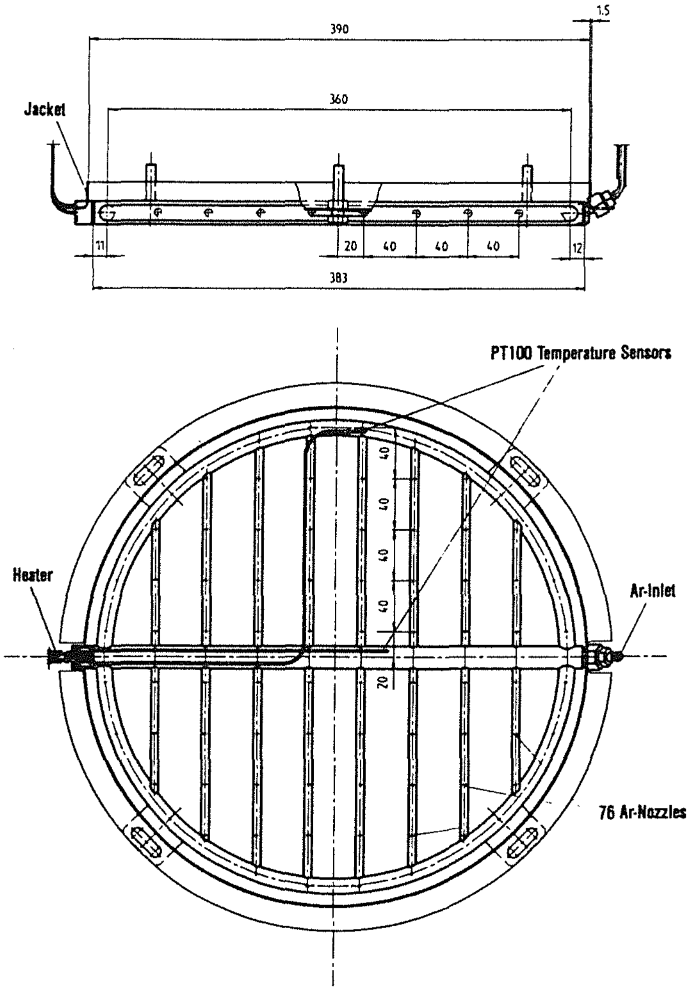

Fig. 4: Nozzle grid for He-cryotrapping by Ar

nozzle apertures are 27 mm distant from the vessel bottom of the LHe bath. The total argon frost surface is assumed to be 1195 cm^2 which is determined by a circular limiter.

Before the test series starts, the facility is baked at 120 °C and evacuated to ~ 10^{-8} mbar. The LN shield is filled with LN at least one day before the experiment starts. To cool down the LHe vessels to < 90 K, the recipient is flooded with GHe up to 10 mbar. Then the recipient is evacuated to < 10^{-7} mbar and the LHe vessels are filled up to the specified levels. To allow the pumps to be operated, the gas is metered in stepwise at predefined intervals. The dosage of trapping gas is started before the pumping gas. Between each dosing step pumping gas metering is interrupted until the equilibrium pressure has established. Figure 5 shows a typical pressure curve for test no. 19. The LHe vessels are not replenished in the metering process. Following the last dosing step, the LHe cold surfaces are heated to 90 K. The gas enters the closed recipient as vapour. Then the recipient is evacuated via the TMP set. The LN shield remains filled during regeneration.

The maximum and minimum values obtained in the experiments performed have been compiled in Table 3. The values of the pumping speeds entered in Table 3 are the quotients of the flow rates of the metered gas and the pressures in the PNEUROP-dome.

These are the results obtained for the individual programme items:

- Influcence of the He/Ar ratio

In test no. 19 the He-pumping speed was measured as a function of the He/Ar ratio. The He/Ar ratio was varied from 1/10 to 1/50. The helium flow remained constant at 0.043 mbarl/s. The helium pumping speed increased up to an He/Ar ratio of 1/30. At the He/Ar ratio of 1/50 no further improvement of the pumping speed was recognized.

- Influence of helium flow rate

Tests nos. 23 and 26 served to investigate the influence of the helium flow rate at constant He/Ar ratio (1/30). The helium flow was varied between 0.03 and 1.3 mbarl/s. At higher flow rates pressure instabilities occur which persist also when the helium flow is varied or stopped. Additional experimental studies are necessary to identify the relevant parameters.

- Influcence of the cryosurface temperature

In test no. 22 the LHe bath temperature was decreased from 4.3 to 3.6; 3.0 and 2.8 K through pumping down. The corresponding temperatures in the centre of the cryopumping surface were 4.7; 4.2; 3.7 and 3.5 K. The argon flow was kept constant at 0.51 mbarl/s. The helium dosing rate was adjusted such that the pressure in the recipient established at values between 5.0x10^{-6} and 5.5x10^{-6} mbar. No influence has become evident of the surface temperatures, and helium pumping speed.

- Influence of impurities in trapping gas

The tests nos. 30, 31 and 42 were performed with 10%, 25% and 5% impurities in the argon trapping gas. The impurities were composed as follows: 4% CO; 4% O_2; 16% D_2 and 66 % CH_4 (Vol. fractions). The He-pumping speed is reduced slightly when the argon trapping gas contains 5% impurities. At 25% impurity content, the pressure rises within a few minutes and the pump can no longer be operated.

- Influence of internal three- and two-stage configurations

In tests nos. 29 and 37 the pump was operated in the two-stage mode which means that the LHe shield vessel was not filled. Its temperature was about 110 K. In test no. 29, 0.043 mbarl/s helium was pumped and in test no. 37, 0.337 / 0.395 mbarl/s of a NET/ITER relevant gas mixture (s. tab. 3). Pure helium can be pumped in the two-stage mode at a pressure level about two times higher than in the three-stage mode. With the NET/ITER relevant gas mixture, pressures higher by one decade compared to three-stage operation were achieved. The pumping speed drops quickly within a few minutes. The results in hand show that the NET/ITER typical gas mixtures cannot be pumped by the argon trapping technique in two-stage copumping operation.

- Argon backstreaming

Ar backstreaming through the LHe and LN baffles into the recipient was determined in tests nos. 28 (three-stages), 29 and 37 (two-stages). In test no. 28 the recipient pressure could be maintained at about 10^{-9} mbar during metering of pure argon. In test no. 29, a maximum of 1.1×10^{-5} mbar and in test 37, a maximum of 4.1×10^{-7} mbar were measured in the recipient during pure argon metering. With a non-cooled intermediate baffle provided, the injector configuration tested causes strong argon backstreaming, which increases the ultimate base pressure and makes pumping impossible.

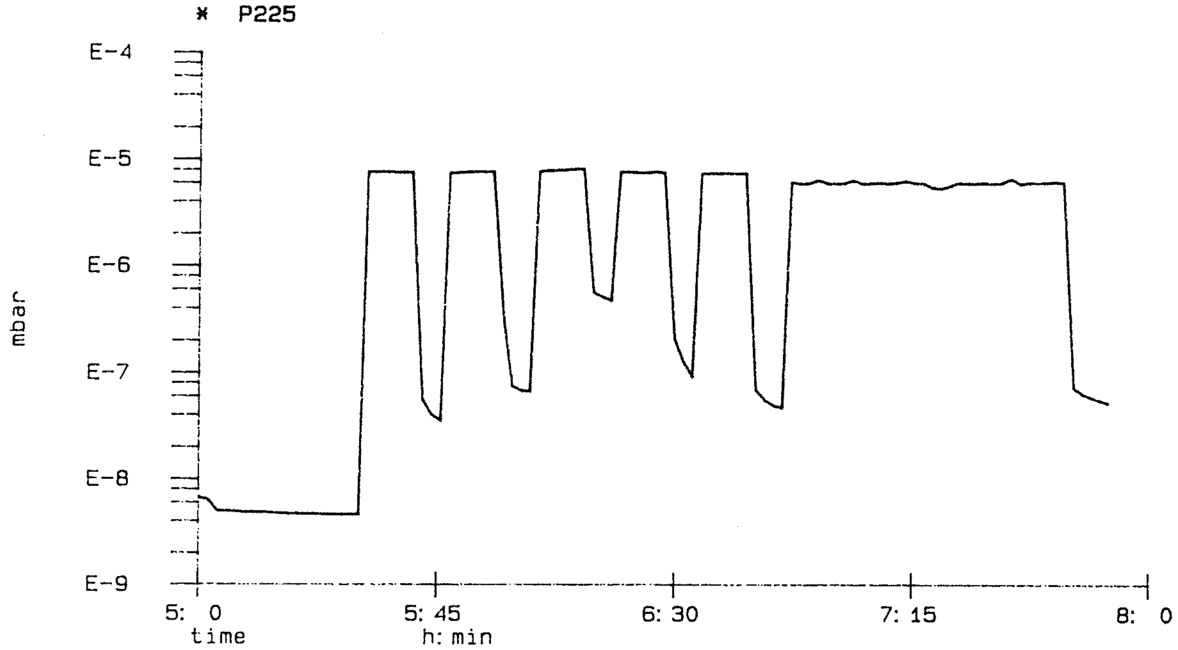

Fig. 5: Test No. 19 Pressure in PNEUROP dome

Test No.	19	22	23	26	27	28	29	30	31	37	42
Kind of trapping gas	Ar	Ar	Ar	Ar	Ar	Ar	Ar	M4[4]	M5[5]	Ar	M6[6]
Kind of pumping gas	He	He	He	He	M3[3]	—	He	He	He	M3[3]	He
Min. flow of pumped gas [mbar l/s]	0.0429	0.0304	0.0255	0.0429	0.1688	—	0.0429	0.0429	0.0429	0.3377	0.0429
Max. flow of pumped gas [mbar l/s]	0.0429	0.0338	0.1992	0.0429	0.3377	—	0.0429	0.0429	0.0429	0.3377	0.0429
Min. flow of trapping gas [mbar l/s]	0.429	0.5065	0.7598	1.3	0.2026	1.3	0.4221	1.3	1.3	0.3951	1.3
Max. flow of trapping gas (mbar l/s)	2.144	0.5065	5.9936	1.3	0.3883	8.4417	2.1442	1.3	1.3	0.3951	1.3
Min. pumping pressure [mbar]	7.7×10^{-6}	5.0×10^{-6}	5.5×10^{-6}	1.1×10^{-5}	1.7×10^{-5}	2.2×10^{-9}	1.4×10^{-5}	1.3×10^{-5}	1.0×10^{-3}	1.3×10^{-4}	1.2×10^{-5}
Max. pumping pressure [mbar]	8.8×10^{-6}	5.5×10^{-6}	1.5×10^{-4}	1.3×10^{-5}	4.0×10^{-5}	1.6×10^{-7}	1.9×10^{-5}	8.0×10^{-5}	1.0×10^{-2}	3.6×10^{-2}	1.5×10^{-4}
Max. pumping speed [l/s]	5569	6139	4635	3899	9931	—	3063	3300	43	2597	3574
Min. pumping speed [l/s]	4873	6078	1328	3299	8442	—	2257	536	4.3	9	286
Max. sp. pumping speed[1] [l/scm^2]	3.58	2.81	2.13	1.79	4.55	—	1.40	1.51	0.02	1.19	1.64
Min. sp. pumping speed[1] [l/scm^2]	2.55	2.79	0.61	1.51	3.87	—	1.03	0.25	0.002	0.004	0.13
Max. sp. He-pumping speed[2] [l/scm^2]	6.52	5.13	3.88	3.26	—	—	—	2.76	0.04	—	2.99
Min. sp. He-pumping speed[2] [l/scm^2]	4.66	5.09	1.11	2.76	—	—	—	0.45	0.004	—	0.24
Quantity of trapping gas [mbar l]	4026	5865	35102	13962	4060	15975	3607	9672	5460	1067	20436
Quantity of pumped gas [mbar l]	131	380	589	618	2867	—	129	309	52	891	631
Pressure before pumping (mbar)	8.3×10^{-9}	3.0×10^{-9}	8.3×10^{-9}	2.8×10^{-9}	4.2×10^{-9}	5.5×10^{-8}	1.4×10^{-7}	1.3×10^{-8}	1.0×10^{-7}	2.4×10^{-9}	9.4×10^{-9}
Pressure after pumping (mbar)	8.3×10^{-7}	1.3×10^{-7}	1.1×10^{-7}	5.5×10^{-7}	1.3×10^{-7}	4.3×10^{-10}	5.5×10^{-8}	1.7×10^{-5}	1.0×10^{-2}	3.6×10^{-2}	1.5×10^{-5}

[1] related to the LN-baffle surface, 2182 cm^2

[2] related to the cryofrost surface, 1195 cm^2

[3] mass percent: 0.1 O_2, 0.1 CO_2, 0.1 Ar, 0.2 N_2, 0.2 CO, 0.83 H_2, 1.4 CH_4, 3.95 He, remainder D_2

[4] Vol. percent: 0.4 CO, 0.4 O_2, 2.6 D_2, 6.6 CH_4, remainder Ar

[5] Vol. percent: 1.0 CO, 1.0 O_2, 6.5 D_2, 16.5 CH_4, remainder Ar

[6] Vol. percent: 0.2 CO, 0.2 O_2, 1.3 D_2, 3.3 CH_4, remainder Ar

Tab. 3: Results of Ar-trapping tests

The results of the tests of helium cryotrapping by argon frost show that for nominal gas throughputs which are specific of the NET/ITER burn time, helium pumping is feasible in a three-stage pump configuration.

But there are essential disadvantages of this method compared to solid sorbent pumping which must be taken into account before a pumping concept for NET/ITER reactor operation will be chosen. These are pressure instabilities at higher specific helium throughputs, sensitivity to impurities in the trapping gas, backstreaming of argon in two-stage operation, accumulation of argon inside the pump, and the need of heating the argon spray system to 100 K inside a LHe cooled cavity.

Subtask 5: Backing Pumps

After completion, followed by modification of the flowsheet and the installation plan, the overview and detailed drawings were made for the FORTE forepump test facility. All valves and pipe components still required have been ordered. The order was placed for manufacture of the parts and assembly of the facility. The support frame was planned, manufactured and erected.

The NORMETEX pumps were inspected. Contamination of the process gas chamber was found in all pumps. Surface contaminations (UF_6) up to $A\alpha = 4.5$ Bq/cm^2 and $A\beta = 22.0$ Bq/cm^2 were detected by direct measurement.

Little damage was detected at the volute inserts of the 600 m3/h pump. It was possible to repair the defect and to make a trial run. The end pressure measured in that run towards the atmosphere was 2.5×10^{-2} mbar.

The electric connection of the control cabinets for the pumps was checked and wiring of the main switching cabinet has started. The mimic diagram has been ordered.

All further activities in connection with general assembly work have been coordinated. Accordingly, the facility could be completed in late 1991 and, after a trial run and acceptance, start operation approximately in March 1992.

Staff:

A. Edinger
M. Haas
J. Hanauer
W. Höhn
T. Höhn
S. Horn
H. Illbruck
B. Kammerer
D. Kausch
U. Kirchhof
H. Lukitsch
A. Mack
D. Perinic
W. Reeb
D. Stern
J. Weinhold
D. Zimmerlin

TEP 1 Cryosorption on Molecular Sieves or Alternative Cryosorbents

Subtask 2: Molecular Sieves KfK

The amount of tritiated water adsorbed in zeolites employed for the removal of gases from process streams in the fusion fuel cycle determines the tritium inventory of adsorber beds, and strongly influences the adsorption capacity of zeolites for impurities.

Using a thermogravimetric technique the max. water adsorption capacity at room temperature of the zeolites 3A (cation K, effective pore diameter 0.3 nm), 4 A (cation Na, effective pore diameter 0.4 nm), 5A (cation Ca, effective pore diameter 0.5 nm), zeolon 200 H (synthetic mordenite, $SiO_2/Al_2O_3 = 10$, cation H, effective pore diameter 0.8-0.9 nm, about 20 % binder), and zeolon 900 H (synthetic mordenite, $SiO_2/Al_2O_3 = 10$, cation Na, effective pore diameter 0.7 nm) was found to be 23.8, 21.6, 25.5±0.3, 10.9±0.6, and 14 wt. $\%/g_{\mathrm{activated\ zeolite}}$, respectively. With the same technique at a heating rate of 10 K/min the weight loss rate of various zeolites (220 - 240 mg) initially loaded up to saturation was compared. The results shown in Fig. 1 indicate that the adsorbed water is released more readily from mordenites than from type A zeolites.

The equilibrium water adsorption isotherms at 25, 100, 200 and 300 °C of commercial type 3A, 4A, and 5A zeolites are relatively similar (see Fig. 2). While at room temperature the equilibrium adsorption of type A zeolites increase in the order 5A, 3A, 4A, at 200 °C the order is 3A, 5A, 4A. As a consequence, type 4A shows the highest adsorption capacity at room temperature, but is at the same time the most difficult to regenerate (detrimental with respect to the tritium inventory). Optimal dehydration conditions for type 5A zeolite were found to be a stepwise heating up to 450 °C for an extended period of time (of the order of several days) under a vacuum of 10^{-4} mbar. The dehydration of mordenites was found to require a somewhat lower temperature, i.e. 350-400 °C.

In view of the above, type 5A zeolite was selected for first measurements on the adsorption isotherms of hydrogen, deuterium, and helium in the temperature range 0 to -200 °C. The experiments were carried out in a closed loop comprising an integrated cryostat, which has been described in detail in previous reports. The zeolite sample in the cryostat was activated in situ by heating up to 450 °C under continuous evacuation for a period of several days. Typical results on the adsorption of hydrogen and deuterium on zeolite 5A at temperatures within the range -75 to -200 °C are presented in Fig. 3. The scattering observed in the low pressure region of the isotherms is attributed to an inadequate pressure sensor, which will be replaced in future work. In agreement with data from the literature it was found that deuterium is adsorbed to a greater extent than hydrogen. Table 1 gives deuterium/hydrogen adsorption ratios at various temperatures and equal equilibrium pressures in the range 160-1600 mbar as obtained from the data in Fig. 3.

Experiments for the determination of separation factors using binary hydrogen isotope mixtures are presently under way.

The adsorption of helium on type 5A zeolite at -200 °C was found to be very small (see Table 2). For example, from a 1: $1 = H_2$: He mixture at a total pressure of 1 bar only a few % of He will adsorbed on zeolite 5A at -200 °C. In future work these experiments will be extended to lower temperatures and higher pressures.

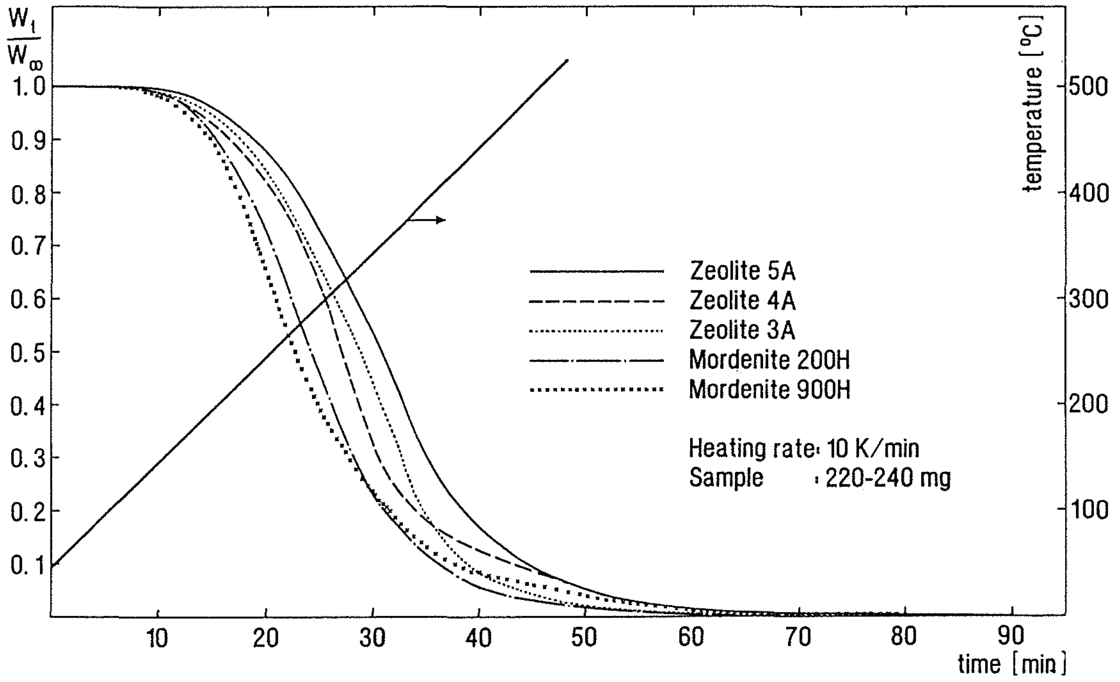

Fig. 1: Thermogravimetric comparison of type A zeolites and mordenites

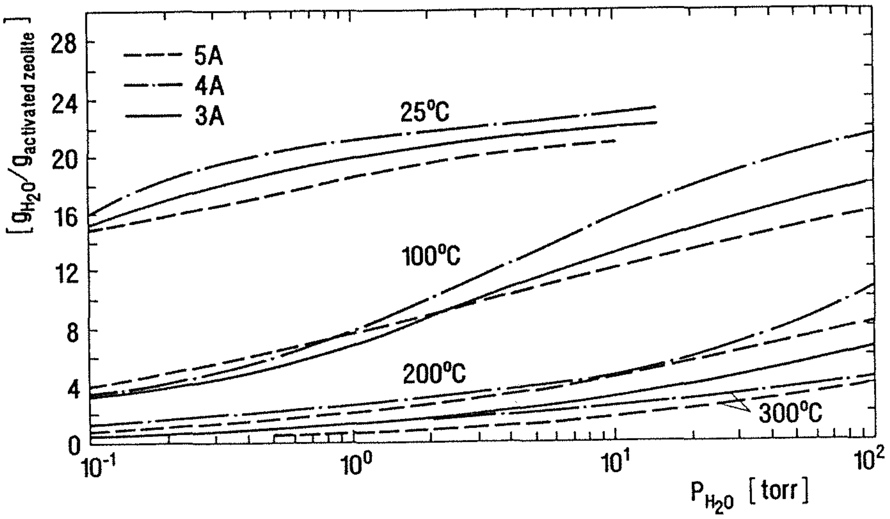

Fig. 2: Equilibrium water adsorption isotherms of commercial type A zeolites

Table 1: Deuterium/hydrogen adsorption ratio on type 5A zeolite as obtained from single component isotherms at equal equilibrium pressures at pressures in the range 160-1600 mbar.

Temperature [°C]	$^aD2/^aH2$
- 200	1.13 ± 0.02
- 175	1.20 ± 0.03
- 150	1.30 ± 0.07
- 125	1.36 ± 0.12
- 100	1.47 ± 0.05
- 75	1.68 ± 0.07

Table 2: Adsorption of helium on zeolite 5A at -200 °C

p [mbar]	926.4	740.9	555.8	370.8	185.4
adsorption [cm³ STP/g]*	3.9	3.3	3.2	2.2	1.2

* g of activated zeolite

Staff:

U. Göttlicher
H.E. Noppel
R.-D. Penzhorn

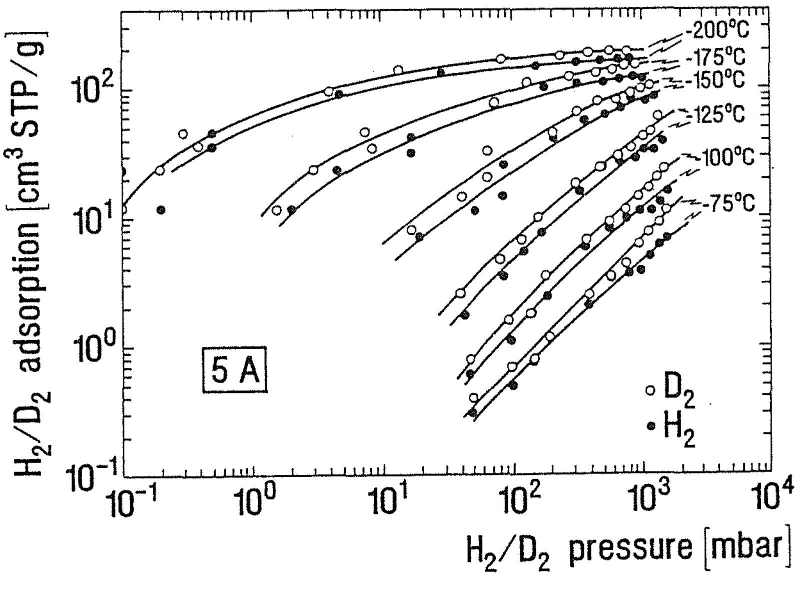

Fig. 3: Adsorption isotherms of hydrogen and deuterium on zeolite 5A

TEP 2 Plasma Exhaust Processing Alternative Options

Subtask 1: Permeator Studies

Main objective of the PETRA facility is a long-term endurance test of a commercial palladium/silver permeator placed in a outer containment to achieve tritium compatibility. In addition, the PETRA facility will a) contribute to the development of in-line infrared process analytics of gases such as methane, carbon dioxide, and carbon monoxide in a tritium environment, b) yield information on the performance of auxiliary equipment over extended periods of time and c) increase knowledge on the use of ZrCo for tritium handling.

The installation of the PETRA facility in the Tritium Laboratory Karlsruhe (TLK) is approaching completion. Two 1.5 m long glove boxes with an integrated tritium removal system have been placed in the TLK and are now ready for leak tests. All major components and most of the small components have been delivered. Component assembly in a rag that fits into one of the two glove boxes is under way. A detailed report describing the experiment and a preliminary safety report have been written.

The fully tritium compatible 0.12 m^2 permeator (see Fig. 1) has been integrated into a loop comprising as major components a 1500 l buffer vessel and a 150/60 as well as a 15/18 m^3/h Normetex pump combination in series. The large pump combination is used to maintain a vacuum of 3 - 10 mbar at the pure hydrogen isotope side of the permeator. The small pump combination is employed to compress the gas from the large buffer vessel (kept at pressures below 220 mbar for safety reasons) into the crude gas inlet side of the permeator. The pressure in the buffer vessel fluctuates between 150 and 220 mbar depending upon the process conditions. The pressure on the crude gas inlet side of the permeator was kept constant at approximately 1000 mbar at all times, the gas flow rates were varied with two throttle valves (one placed between the buffer vessel and the 18/15 m^3/h pump combination and the other placed behind the bleed gas exit).

The permeator has now been in continuous operation at 400 °C for several consecutive weeks without any problems. Experiments have been carried out with pure hydrogen, pure deuterium, and mixtures of these two hydrogen isotopes (see Table 1.

Argon was selected as impurity instead of helium to avoid mass spectrometric conflicts with deuterium. Some typical results have been compiled in Table 2. At constant inlet gas pressure of approx. 1000 mbar a continuous increase in inlet gas flow rate causes a corresponding increase in bleed flow rate and permeate gas flow rate. Under the employed conditions the max. permeation capacity of the permeator was found to be approx. 5 [l/min]. While at low inlet flow rates almost all hydrogen isotopes permeate (ca. 99 % Ar in bleed) at increasing inlet gas flow rates hydrogen begins increasingly to breakthrough (> 4 [l/min]). The H/D ratio in the bleed begins at first to decrease because of the isotope effect (hydrogen permeates better than deuterium). The effect does not become apparent in the H/D ratios of the permeate gas (H/D approx. 2) because essentially all hydrogen isotopes permeate. As the inlet flow rate is increased up to ca. 8 l/min the H/D ratio of the bleed begins to approach again the starting H/D ratio (H/D = 2). The isotope effect now becomes apparent in the permeate and is less pronounced in the bleed (much of the gas passes through the permeator without permeating). The experimental results obtained on the performance of the permeator were compared with results calculated from a two isotope model

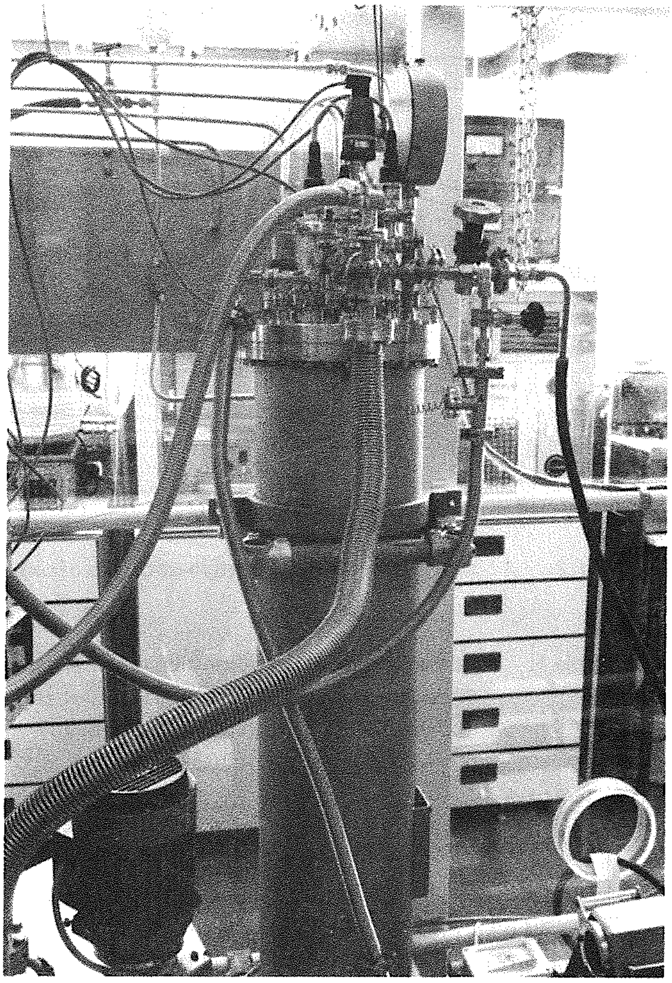

Fig. 1: Pd/Ag permeator of the PETRA experiment

Table 1: Gaseous mixtures investigated with the 0.118 m^2 permeator

hydrogen %	deuterium %	argon %
69.75	23.25	7
62	31	7
46.5	46.5	7

Table 2: Permeation of a hydrogen isotope/argon gas mixture (62 % H_2, 31 % D_2 and 7 % Ar) through a 0.118 m^2 permeator at 400 °C.

Flow rate [l/min]			pressure [mbar]		% Ar in bleed		H/D in bleed		H/D in permeate	
inlet	permeate	bleed	inlet	bleed	meas.	calc.	meas.	cal.	meas.	calc.
1.712	1.567	0.150	994	971	99.4	99.4	1.72	2.00	1.92	2.00
2.765	2.535	0.242	1001	954	99.2	99.4	1.67	2.00	2.01	2.00
3.543	3.234	0.311	1004	940	98.4	99.4	1.66	2.00	1.97	2.00
3.762	3.436	0.329	997	925	99.0	99.3	1.68	2.00	2.04	2.00
4.057	3.704	0.361	1002	922	97.8	99.3	0.80	2.00	2.03	2.00
4.264	3.891	0.366	998	913	98.6	99.3	0.93	1.96	2.01	2.00
4.577	4.159	0.434	999	897	89.9	94.3	0.63	0.55	2.01	2.01
4.853	4.403	0.429	997	890	90.3	76.8	0.62	0.49	1.99	2.07
5.041	4.557	0.469	1002	886	86.1	64.9	0.54	0.56	1.97	2.12
5.367	4.777	0.568	1002	860	74.0	47.7	0.65	0.71	1.97	2.22
5.662	4.950	0.711	1001	820	59.9	37.3	0.75	0.84	2.03	2.30
5.957	5.093	0.877	999	774	49.1	30.4	0.72	0.96	2.00	2.37
6.352	5.247	1.121	1005	714	39.6	24.8	0.86	1.07	2.12	2.46
6.690	5.362	1.354	1002	632	33.4	21.0	0.95	1.18	2.16	2.53
7.129	5.467	1.688	1003	521	30.1	17.7	1.02	1.29	2.13	2.60
7.524	5.592	1.932	999	398	30.4	15.5	0.96	1.38	2.13	2.66
7.812	5.678	2.134	1001	300	24.0	14.2	1.12	1.44	2.28	2.70

developed at the IRCh (see calculated % Ar in bleed, H/D in bleed and H/D in permeate in Table 2). Considering the necessary assumptions made on the pressures in the permeator it is considerd that the agreement between theory and experiment is satisfactory and that the model is adequate for the design of future permeators.

Specimens of palladium/silver have been homogeneously implanted with helium at 300 °C employing an implantation rate of 0.013 appm/s at implantation times of less than 64 hours to reach implantation concentrations of 200, 500, 1000, and 3000 appm. The attained implantations simulate the effect of helium produced from the β-decay of tritium during steady operation of a permeator used for fuel clean up over a period of approx. one year. Tensile tests of irradiated and unirradiated control samples were carried out at 300 °C under vacuum as well as under 0.1 MPa of hydrogen. The results indicate that with increasing helium content the yield strength and the tensile strength increase while elongation to fracture significantly decreases (in vacuum for specimens containing 3000 appm the reduction in total elongation amounts to 83 % and a change in tensile strength of 27 %. A hydrogen atmosphere was found to reduce both strength and ductility by approx. one third of the vacuum values.). SEM observations indicate that with increasing helium content a change from a ductile transcrystalline fracture to a brittle intercrystalline occurs.

A new facility has been constructed to evaluate the performance of the ZrCo getter beds supplied by Culham Laboratories under conditions that simulate those of the PETRA experiment. The ZrCo beds will be used not only for tritium storage, but also to bring the experiment into the safe condition in case of abnormal occurences. Test parameters will be a) the reaction rate of ZrCo with hydrogen as a function of the bed cooling, the influence of impurities, the heat evolution during gettering, and b) the rate of release rate from the ZrCo hydride as a function of heating rate.

Staff:

U. Berndt
M. Glugla
W. Jung
E. Kirste
A. Möslang
R.-D. Penzhorn

Subtask 2: Catalytic Cracking Process

A process concept based on extensive laboratory work including experiments with relevant concentrations of tritium and investigations on a technical scale of all the major components has been proposed for the processing of all primary vacuum exhaust gases of NET/ITER. In a first step the unburned hydrogen isotopes are recovered by selective permeation. Tritiated and non-tritiated impurities in the bleed gas from the permeator are then processed in a loop that combines catalytic reaction steps (hydrocarbon cracking and water gas shift reaction) with selective hydrogen permeation. The processing of pump down gases is accomplished in two consecutive catalytic water gas shift/hydrogen isotope removal permeation steps.

Several integral laboratory tests with tritium at TSTA, Los Alamos, USA, served to demonstrate the basic feasibility of the catalytic plasma exhaust process. A new integral technical facility (Catalytic Purification Experiment, CAPRICE) to be installed in the Tritium Laboratory Karlsruhe, having 1/8th NET/ITER scale is now being planned. On the basis of a detailed Job Enquiry Specification prepared at KfK, a call for tender led to six bids from different companies from four European countries and Canada. A contract aimed at proving the plasma exhaust clean-up process with tritium was awarded to National Nuclear Corporation, Great Britain for the design, manufacture, assembly, and commissioning of the CAPRICE facility. The work, which was started in March 1991 is expected to be completed by the end of 1991.

During the first seven months of the project a very detailed design concept document illustrated in the block flow diagram shown in Fig. 2 was prepared. The document describes extended design criteria of the primary and secondary system, which are also included in the System Functional Specifications. A careful analysis of the design comprises issues such as standby loop circulation, standby look filling, bottled gas feed, simulant mixing, choice of hydrogen isotope mixtures for the experiment, performance during pump down, optimization of buffer vessel volumes and reduction of tritium inventory, control simplification and instrument location, complete mathematical modelling of all process steps. A performance study of all basic units such as permeators, catalytic reactors, pumps, and the vaporizer has been completed and some components i.e. catalytic reactors, vaporizer, and cold trap have been substantially redesigned from the point of view of performance, safety, tritium economy, and operability. With respect to control and instrumentation the design and number of tritium monitors has been reviewed, the control scheme for the permeator was subjected to close analysis, and all design issues affecting safety and operation (explosion limit monitoring, contamination control, etc.) were carefully established. A safety assessment including emergency shut down and safe shut down is now completed. The design scope of the safety studies so far undertaken was single faults or failures leading to tritium release. The detailed layout of the CAPRICE facility in the Tritium Laboratory including four 1.5 m long glove boxes, a separate glove box for the large dry scroll pump, the safety cabinets for gas bottles, the electrical process control cabinets, the detritiation systems, the ion chamber troleys, the operation console, the PLC cubicle, the instrument cubicle, the solenoid valve cubicle, and the liquid nitrogen supply has been planned.

To assist the NNC engineering work algorithms have been developed to model a two hydrogen isotope permeation through palladium/silver membranes and to model process streams within the facility. A new and unique permeator design that takes into account the singularities of plasma exhaust fuel processing has emerged from intensive discussions within the IRCH and with industry. The review of the permeator design has led to potential improvements in its vacuum performance and to an optimization in the permeation tube number. Complementary basic research activities with the aim of identifying the most adequate cracking catalyst, to demonstrate the technical vaporizer design concept from NNC, to verify the two component permeation mode, to demonstrate the selected pump combinations have either been completed or all well under way. A tritium compatible gas chromatograph has been selected and adapted to the requirements of the CAPRICE facility. All questions concerning the installation of the facility in the Tritium Laboratory, in particular the supply and return of tritium to the infrastructure, the supply of service gases, the cooling water supply have been addressed.

The general design will be frozen within a few weeks to allow placement of hardware purchase orders. Many components critical with respect to delivery time have already been ordered. Up to now the project is within the anticipated time schedule. The costs have remained within the established limits.

Staff:

M. Glugla
R.-D. Penzhorn

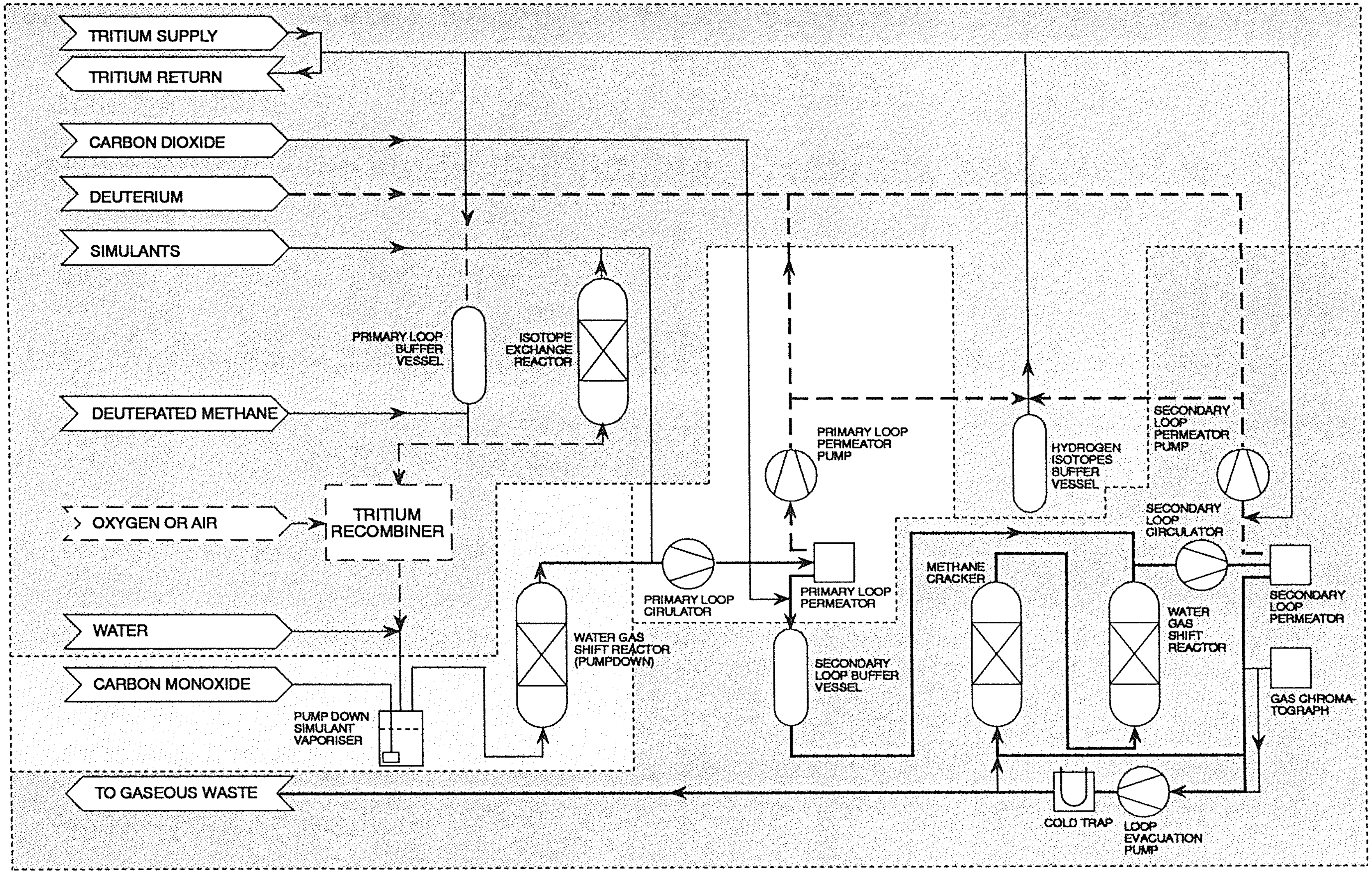

Fig 2: Outline flow diagram of CAPRICE

TCP 3 Atmospheric Processing

Subtask 3: Inert Atmosphere Processing

Large inert gas streams containing small amounts of tritium such as the torus maintenance cover gas, glove box atmospheres, inert waste gases etc. need to be detritiated to activity levels acceptable for recirculation. One method to reach this goal utilizes catalytic oxidation to oxidize tritium and tritium containing compounds to tritiated water. This water is removed from the gas stream by large dryers and then drained periodically to be processed in the Waste Water Detritiation System. Alternative methods consist in direct absorption of hydrogen isotopes and impurities using modified zeolites or metal getters.

In all these cases it would be advantageous to separate molecular tritium in a single process step for interim storage on a getter bed from where it would be available for the fuel cycle without further processing. Such a step would also enhance the decomposition of tritiated compounds since there is always a strong tendency for an equilibrium to be built up between the compounds and the molecular form of the hydrogen isotopes.

A Pd/Ag diffuser operated at temperatures of 400 - 500°C is a well known tool for the separation of hydrogen isotopes from other gaseous components. The experience with diffusers is limited, however, to tritium/hydrogen partial pressures in the range > 1 mbar, while the concentrations to be discussed here are of the order of 10^{-3} to 10^{-7} mbar (1 Ci tritium/m^3 corresponds to a partial pressure of $0.385 \cdot 10^{-3}$ mbar).

We have started, therefore, to investigate the performance of a small commercial diffuser (Leybold PA-150 with 270 cm^2 membrane surface area) as a function of hydrogen inlet pressure and of gas flow rate. The carrier gas pressure was 1.2 bar in all cases, the range of flow rates was 1 l/min... 16 l/min, and the inlet concentrations were varied between 0.5 % (= 6.0 mbar) and 0.07 ppm.

1. Performance of the diffuser at inlet concentrations in the range of 10^3 ppm H_2

The test gas mixtures containing He and H_2 were prepared in one of the two gas collection tanks (V = 16/106 l) of the PEGASUS facility and circulated through the closed test loop for about 1 hour to obtain saturated surfaces and a homogeneous gas mixture. After quantitative determination of the H_2 concentration (by gas chromatography) the gas was transmitted through the diffuser which was evacuated at its back side to 10^{-5} mbar.

Fig. 1 shows results of three tests (P-2...P-4) for gas flow rates of 1, 2, and 4 l/min and inlet concentrations of some 10^3 ppm H_2.

The result of the continuous H_2 removal is a steady decrease of the inlet concentrations c_{in} as well as of the non-permeated hydrogen (Bleed), which is described by

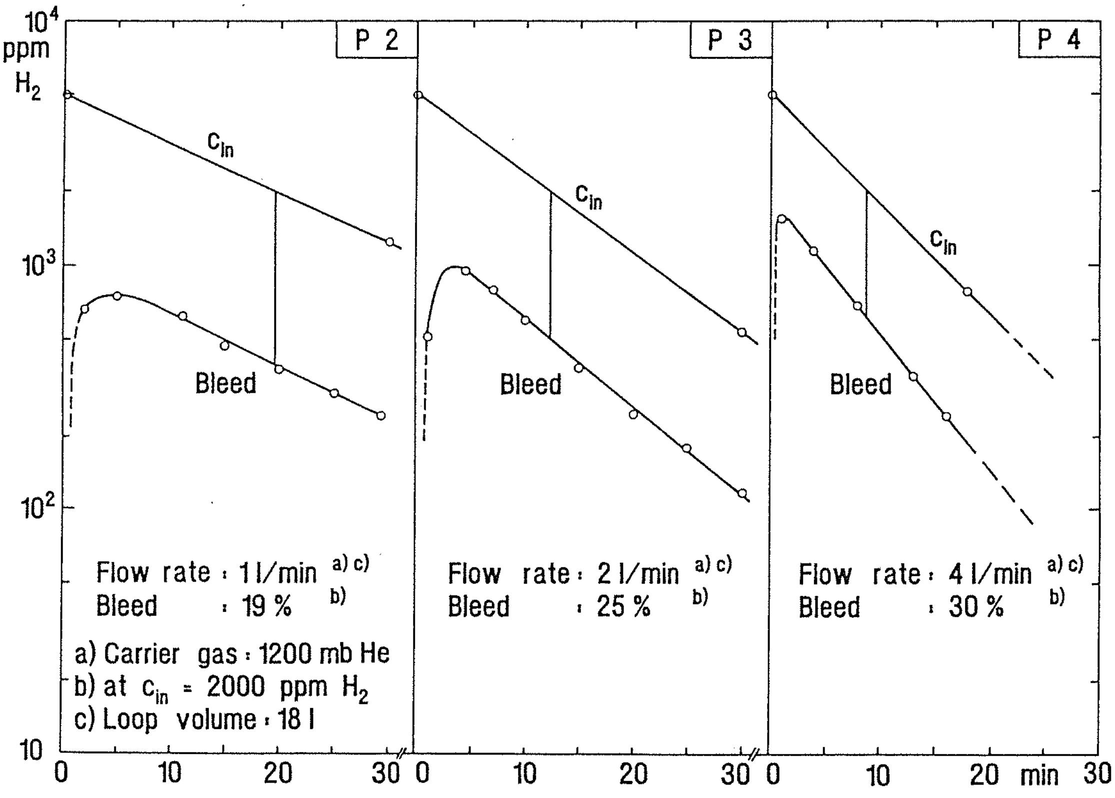

Fig. 1: Operational characteristics of the diffuser at H_2 inlet concentrations of some 10^3 ppm

$$c_{in} = c_o \cdot e^{-f \cdot a \cdot t} \quad with\ a = \frac{d}{p \cdot V} \tag{1}$$

$$c_{out} = c_{in} \cdot (1 - f) \quad (\equiv Bleed) \tag{2}$$

where

c_o = initial H_2 concentration (t=0)
f = removal coefficient ($0 \leq f \leq 1$)
d = gas flow rate [mbar·l/min]
p = test gas pressure [mbar]
V = test gas volume [l]

The following results can be derived from Fig. 1:

a) In the initial phase of the tests the Pd/Ag membrane is filled up with hydrogen until an equilibrium concentration is reached. During this phase the H_2 removal is more effective than in the remaining time of the test. This effect is obviously more pronounced at low gas flow rates, as the fill up of the membrane occurs more slowly than at higher flow rates.

b) The bleed fraction increases at increasing gas flow rate. This can be explained by the decreasing dwell time of a given gas volume in the diffuser which leads to a reduced collision frequency between the H_2 molecules and the Pd/Ag membrane.

c) The removal factor f was not constant during the experiments, because according to (2) the measured bleed curves should have been parallel to the c_{in} curves for f = const. It is concluded that in the first 10 - 15 min of the tests the permeating hydrogen was not sufficiently pumped off by the turbo molecular pump at the back side of the diffuser (the employed Alcatel Drytel 25 pump had a pumping speed of only 180 l H_2/min).

2. Influence of back pressure

For test P-9 the back pressure has been plotted as a function of time in Fig. 2 in addition to the curves for the inlet pressure and the bleed pressure. In the initial phase of the test, the diffuser membrane was loaded with H_2 while the back pressure increased from 10^{-5} mbar to $5 \cdot 10^{-2}$ mbar. The maximum of the back pressure depends on the amount of hydrogen supplied to the diffuser per unit of time, on H_2 con centration at the back side, and on the capacity,determined by mass and temperature of the membrane alloy.

After the maximum was reached, the back pressure decreased faster than the H_2 inlet pres-sure and the bleed pressure. This is an indication that the Balzers TSU-050 pump provided a more adequate pumping speed than the above mentioned Alcatel pump.

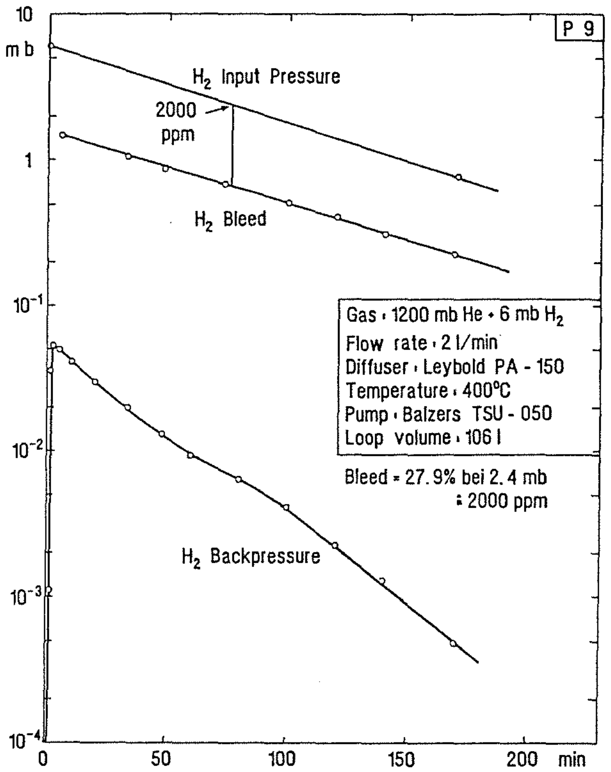

Fig. 2: H_2 back pressure and bleed as a function of H_2 input pressure

3. Influence of gas flow rate and H_2 inlet concentration

Fig. 3 describes the performance of the diffuser at gas flow rates of 5 - 16 Nl/min and at H_2 inlet concentrations which are one order of magnitude lower than in the tests described above. Again it can be seen that the bleed fractions increase at increasing gas flow rates. During the course of the individual tests, however, the bleed fractions were found to decrease. This would mean an in- creasing separation efficiency of the present diffuser/turbo pump combination at lower inlet concentrations.

To investigate these findings at still lower H_2 concentrations, the Carlo Erba gas chromatograph with helium ionization detector was replaced by a GC of Trace Analytics with a 100 times lower H_2 detection limit (10 ppb). (The detector principle of this GC is based on chemical reduction of HgO and subsequent measurement of Hg vapor by the use of a UV photometer.)

Fig. 4a/b shows results of tests P-19/P-20 with inlet concentrations in the range 10 - 0.07 ppm at a gas flow rate of 2 Nl/min. In comparison to test P-3 (Fig. 1) there was a slower increase of the bleed in the initial test phase. At c_{in} = 1 ppm the bleed was either the same (23.0 %) or even less (14 %) than in test P-3 at c_{in} = 10^3 ppm. It can be concluded, therefore, that at $c_{in} \leq 1$ ppm the permeation efficiency was at least as good as at c_{in} = 10^3 ppm under the prevailing test conditions.

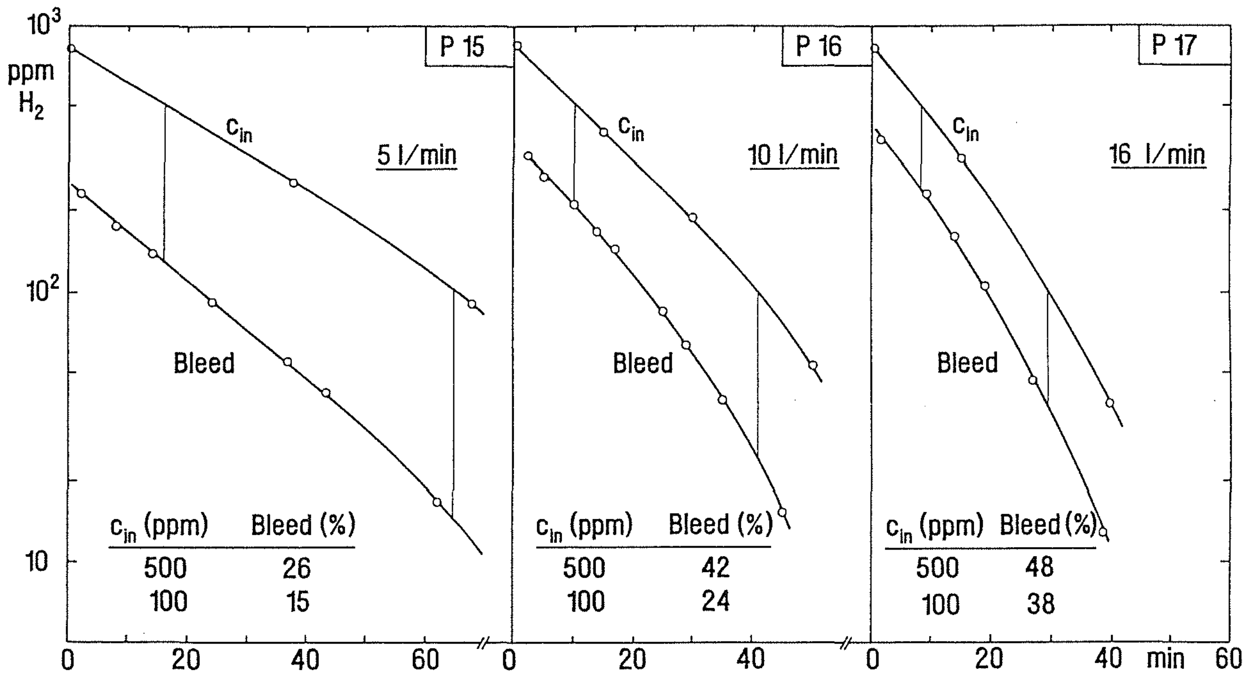

Fig. 3: Dependence of H_2 bleed fraction on gas flow rate and H_2 inlet concentration; volume of the closed loop: 106 l

It is not yet understood, however, why the bleed fractions tended to increase towards the end of both tests P-19 and P-20. We expect to find an explanation by repeating these tests and using a pump with increased H_2 pumping speed.

4. Summary and Conclusions

A series of scoping tests have been carried out at the PEGASUS facility to investigate the behavior of a small Pd/Ag diffuser (with 270 cm^2 surface area) with respect to permeation rate as a function of H_2 inlet concentration (0.5% - 0.07 ppm) and of gas flow rate (up to 1 m^3/h). The main results and conclusions are summarized as follows:

1. At low input concentrations a load up phase of the diffuser is observed, during which the bleed fractions are very low ($\leq$10%). Later on, an equilibrium is established between the inlet concentration and the bleed fraction, which is determined by the H_2 mass flow at the diffuser inlet and the pumping efficiency at the back side.

2. The fraction of non-permeating hydrogen (bleed) increases with increasing gas flow rate. This effect can be reduced by using a diffuser with a larger membrane surface aerea.

3. The requirement for the pumping speed at the diffuser back side is not very high: for gas streams with a flow rate of 1 m^3/h and 1 Ci tritium/m^3 the volume to be pumped off is less than 10^{-5} Nl/min. A pump with a pumping speed of about 10 m^3/h at 10^{-6} mbar is sufficient in this case. (In most of the scoping tests the pumping speed has been only 180 l/min.)

4. The results lead to the conclusion that Pd/Ag diffusers have promising properties for tritium removal from gas streams with concentrations even as low as 10^{-3} - 10^{-4} Ci/m^3. The tests performed so far cover a range of inlet concentrations of nearly five orders of magnitude. As a H_2 concentration of 0.07 ppm corresponds to 0.17 Ci tritium/m^3, three additional orders of magnitude have to be investigated. This has to be done with tritium for two reasons: (a) the detection limit for H_2 achievable with a gas chromatograph is about 10 ppb, i.e. the envisaged range of inlet concentrations cannot be covered with H_2 tests; (b) a decision on the applicability of the diffuser

References:

[1] H. Fujita et al.: J. Nucl. Sci. Technol. 17 (1980) 436

[2] H. Yoshida et al.: Nuclear Technology/Fusion 3, (1983) 471

[3] J. Chabot et al.: Fusion Technology 14 (1988) 614

[4] F.J.Ackermann et al.: J. of Chem. and Eng. Data 17,1 (1972) 51

Staff:

H. Albrecht
U. Kuhnes

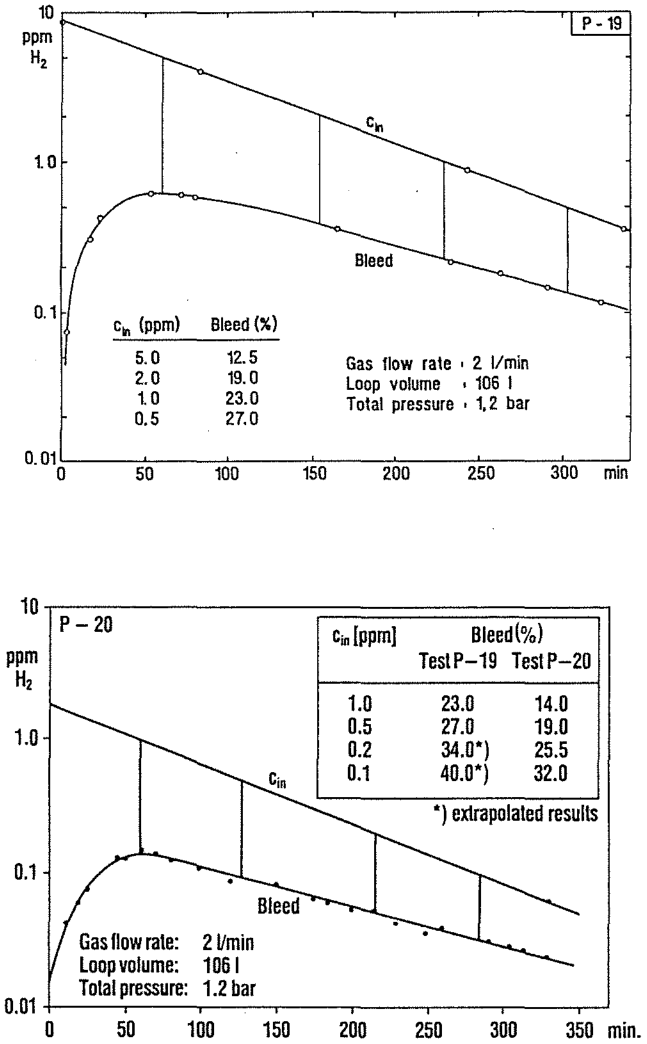

Fig. 4 a/b: Bleed of the diffuser at H_2 inlet concentrations in the range of 0.07 - 10 ppm

NSN 1 Neutronics Data Base for Shielding

The objective of this task is the improvement of the nuclear data base and integral checks of data and calculational methods for shielding.

Subtask 1: Elaboration of EFF Data Base

At present the main task of KfK Karlsruhe is establishment of an improved evaluation of the neutron resonances of iron adequate for fusion applications, in particular shielding and activation calculations. Highly relevant new resonance data from neutron transmission and capture measurements for the important nuclides ^{56}Fe, ^{58}Ni and ^{60}Ni were reported from Oak Ridge National Laboratory and CBNM Geel in early 1991. This necessited a reevaluation and extension towards higher energies of the resonance parameter files in EFF-1.

Accurate shielding and activation calculations are not possible without due account of resonance self-shielding. In the unresolved resonance region (for ^{56}Fe between roughly 0.9 and 2.5MeV) one must rely on level statistics, which means on average resonance parameters for the partial waves with $1 = 1, 2, 3$. Because of discrepancies between observed and statistically generated total cross sections the average resonance parameters for ^{56}Fe and ^{54}Fe in EFF-1 had to be revised. The revision, based on statistical analysis of resolved resonance parameters, is completed. A thick-sample transmission measurement with high resolution, being prepared at CBNM Geel, will show how well the new level-statistical parameters allow to reproduce the effects of the unresolved cross section resonances.

A first version of the covariance files for the resolved resonances needed for an assessment of the accuracy of shielding and activation calculations was established for the main iron isotopes, ^{56}Fe and ^{54}Fe. At present they are being reassessed in view of the new Oak Ridge and Geel data, with the emphasis on the roughly 300 resolved resonances of ^{56}Fe, each with three parameters: energy, neutron and radiation width. Various schemes are under study to reduce the sheer volume of the covariance data, and thus to enhance their practical usefulness.

Subtask 2: Derivation of working library

Working libraries for the Monte Carlo transport code MCNP have been produced at ENEA Frascati and PSI Würenlingen from the European Fusion File EFF-1 for use in the EC. In cooperation with ENEA Frascati KfK suggested and performed specific benchmark calculations to intercompare the two MCNP libraries. Perfect agreement has been obtained for all benchmark problems except one concerning the neutron transport in an iron assembly. This disagreement could be traced back to an error on the underlying EFF-1 data file of ^{56}Fe.

Subtask 3: Data base validation

Benchmark calculations for the qualification of cross-section data have been performed for beryllium. This choice has been made in view of its great importance and the fact that recently double-differential beryllium cross-sections (DDX-data) from the ENDF/B-VI data file became available which, for the first time, are given as tabulated functions, i.e. pointwise in energy and angle, in the laboratory system. This data representation is appropriate for use in the rigorous S_N-transport procedure, developed at KfK (see subtask 1.4), as it allows to treat neutron transport problems wihtout making any use of the Legendre fit approximation. Thus it is possible to judge the quality of the S_N/P_ℓ-approximation being usually applied for both blanket design and shielding calculations.

Actually it has been found that the conventional S_N/P_ℓ-approximation is inadequate for describing the 14 MeV neutron transport in beryllium when using the tabulated ENDF/B-VI beryllium DDX-data [1]. As an example **Fig. 1** shows the neutron leakage spectra for a beryllium spherical shell of 30 cm thickness fed with a central 14 MeV neutron source. The spectra calculated by the approximative SN/Pℓ-procedure (ONETRAN-code) converge as the Legendre order is increased (note that the P_3-calculation already agrees with the P_5-calculation). The converged spectrum, however, differs from the spectrum calculated by the rigorous S_N-calculation (ANTRA1-code). If, on the other hand, beryllium DDX-data are used, whose angular dependence is described by a truncated Legendre series expansion on the data file (as it is the case for EFF-1 for instance), perfect agreement between approximative S_N/P_ℓ-calculations and the rigorous S_N-calculation is achieved.

Thus the inadequacy of S_N/P_ℓ-calculations when using tabulated beryllium DDX-data reflects the deficiencies of the numerical Legendre fit to these data, introduced by the data processing procedure with the NJOY-code. There is a clear need for using tabulated DDX-data on the data file and, furthermore, for using them in an appropriate way in the transport calculation.

Subtask 4: Data related code development

The development of one- and two-dimensional S_N-transport codes with rigorous treatment of the anisotropic neutron scattering is finished and documented [2]. Both transport codes, ANTRA1 and ANTRA2, are extensively used in benchmark analyses of 14 MeV neutron transport problems.

The NJOY89 processing code has been further developed to allow the generation of angular segmented transfer matrices from tabulated DDX-data in ENDF/B-VI format for use in rigorous S_N-calculations. The original NJOY89-code performs a numerical Legendre fit to tabulated angular distributions on the data file. Thus the main advantage of the tabulated data representation is lost in the processing procedure. We introduced a calculational procedure into NJOY, in which the tabulated DDX-data are integrated over specified angular bins (according to the angular segments of the subsequent

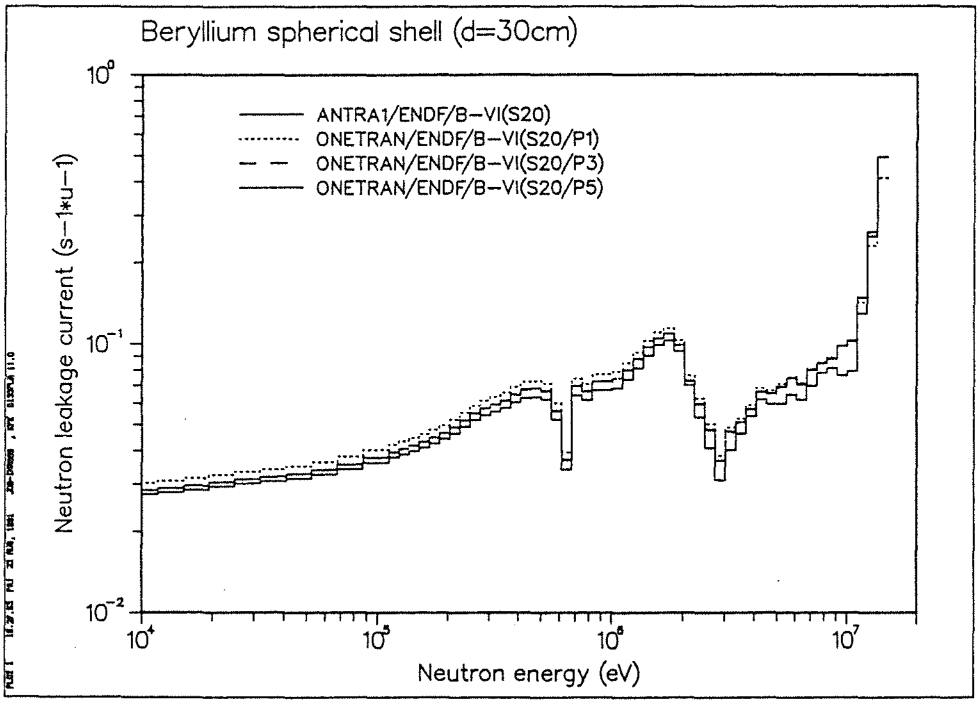

Fig. 1: Neutron leakage spectra of a 30 cm thick beryllium spherical shell: comparison between rigorous (ANTRA1) and approximative S_N/P_ℓ (ONETRAN) calculations with ENDF/B-VI DDX-data (Note: ONETRAN P_3- and P_5-calculations coincide)

S_N-calculations) and by-passed the Legendre fit procedure originally given there. Angular segmented transfer matrices, therefore, can be produced without relying on any approximation, if the DDX-data are given as tabulated functions on the data file. The newly developed NJOY-version has been tested and used in the beryllium benchmark calculations (subtask 1.3).

References:

[1] U. Fischer, A. Schwenk-Ferrero, E. Wiegner: Analyses of 14 MeV neutron transport in beryllium, Proc. 2. Int. Symp. Fusion Nuclear Technology, Karlsruhe, Germany, June 2 - 7, 1991.

[2] A. Schwenk-Ferrero: Verfahren zur numerischen Lösung der Neutronentransportgleichung mit strenger Behandlung der anisotropen Streuung, KfK-4788 (September 1990).

Staff:

F. Fröhner
U. Fischer
A. Schwenk-Ferrero
E. Wiegner

Remote Handling / Maintenance

Introduction:

Due to the activation of most components of the NET /ITER basic machine, all operations of inspection, maintenance, connection and disconnection, assembly and disassembly will have to be carried out remotely from the very start of the physics phase. Hands-on or semi-remote maintenance will be possible only in limited areas and for some peripheral components.

The maintenance of the in-vessel components has been identified as a key problem. The preferred solution for NET and ITER is the removal of divertor plates and protective tiles through equatorial ports by an articulated boom or an in-vessel vehicle and of blankets by a blanket handling device from top openings. The equipment for in-vessel maintenance will have to operate under extreme conditions of radiation and temperature. The large variety of operations to be carried out requires versatile and replaceable tools attached to different work units with large lifting capabilities. The high availability targeted by NET will require that in-vessel operations have to be carried out with relatively high speed.

Most of the KfK work concentrates on the development of an In-vessel Handling Unit (IVHU) with an articulated boom transporter and different work units (task RHT 1.1). This system is primarily needed for the maintenance or replacement of in-vessel components during short term interventions.

The Experimental Device for In-Torus Handling EDITH is the prototype of this system (task RHT 1.2). It is required to demonstrate that the maintenance of plasma facing components can be carried out with the anticipated reliability and time. It is also needed to optimize the IVHU components and subassemblies and to test different control algorithms.

EDITH will be constructed in full scale, supplemented by full scale mock-ups for divertor plate and protective tiles handling (RHS 3.2). The hardening of sensitive IVHU components for NET/ITER typical temperature and radiation levels are being performed in close cooperation with SCK/CEN Mol (task RHS 2.5 - 6).

The work performed to standardize and qualify basic machine components and to develop remote techniques to assemble and dissassemble these items is described in task RHS 1. The basic machine components to be qualified are:

- Electrical connectors	(RHS 1.1)
- Pipe connectors	(RHS 1.2)
- Fluid connectors	(RHS 1.3)
- Welded connectors	(RHS 1.4)
- Cryogenic connectors	(HHS 1.6)

The demonstration of the different connection techniques will be performed in a full size mock-up of the NET/ITER connector box (BERT, task RHS 1.5).

RHS 1 Qualification of Standard Components

In the framework of this task, the connecting elements and tools for remote maintenance within the NET/ITER radiation shield are investigated, tested, qualified and standardized.

The data sheets resulting from these activities will constitute the main part of the Remote Handling Manual (R.H.M).

The following standard components are to be qualified:

- Electrical connectors
- Pipe connectors
- Fluid connectors
- Welded connectors
- Cryogenic connectors

The tests and follow-on qualification are performed in the test rigs and full-size mockups which were set up for these tasks.

Subtask 1: Electrical Connectors

Under this subtask a range of electrical connectors for standard nuclear use as well as for special application were investigated, tested and qualified.

The results may be summarized as follows:

- As described in the final report [1], the requirements were fulfilled best by the connectors manufactured by LEMOSA.
- For general nuclear use the push-pull-type connector manufactured by LEMOSA should be chosen as the standard connector.
- Because of the better handleability and visibility during insertion the elbow version should be preferred whenever possible. The straight-on version should be regarded as a back-up.

The handling deficiencies which were found during testing lead to a number of modifications for all the versions tested. These modifications were extensively discussed and coordinated with the selected manufacturer LEMOSA to provide a basis for integrating the modified designs into series production.

The remote handling trials on the electrical connectors for special application were completed by tests on three different types of high-pin-density connectors (Fig. 1). The test results, a video displaying the remote handling trials, pictures taken during testing and proposals for the R.H.M. data sheets were compiled in the form of a final report [2].

Subtask 2: Flange Pipe Connectors

The objective of this subtask is to rationalize a range of flange connectors which are suitable for remote handling. These connectors will be used to connect pipes which may contain water, liquid metal, cooling gas or vacuum. Following the selection of the JET type as the standard flange, emphasis was placed on the redesign, modification, testing and qualification of the NET/ITER standard UHV flange on the basis of the JET UHV flange design.

The R.H. trials on flanges with additional modifications to improve the handleability were completed. An interim test report was submitted to NET and JET for internal discussion [3].

The leak test on the JET-type UHV flange was also completed. The test report [4] describing the test procedure, the test results and the test facility was handed over to NET to be reviewed. Fig. 2 shows the test jumper with the JET-type UHV flange in the test facility.

Several proposals for the development of a tritium-compatible flange with double seals and leak detection function were worked out and discussed with different NET/JET groups. General drawings of standard pipe flanges were made for selected diameters in accordance with NET. The data sheet proposals for the standard range of UHV flanges were submitted to NET.

The tests of the soft iron material (trade name ARMCO) as a gasket material for liquid-metal pipe connections were completed. In view of the good corrosion resistance and R.H. capability revealed during testing, ARMCO can be recommended as a sealing material for Pb-17Li supply lines. The test results of the preliminary trials were compiled in a final report [5].

Subtask 3: Fluid Connectors

This subtask intends to select, rationalize and qualify a range of small-bore fluid connectors suitable for remote handling. In general nuclear use these connectors will be applied to couple flexible hoses which may contain water or compressed air.

The preselection of the different types of connectors to be investigated for standard nuclear use was followed by qualification tests and the implementation of modifications necessary to improve the connectors' R.H. capability (Fig. 3).

The modified-connector test results were discussed with the potential suppliers to be able to assess possibilities of a future integration of these modifications into R.H. fluid connector manufacturing. These trials were completed. The results were compiled in the final report [6].

Subtask 4: Welded Connection of Pipes (BERT)

The main objective of this subtask is to develop remote techniques, e.g. tools, to provide welded pipe connections and to verify the assembly and disassembly of T-shaped lip seals and flanged pipe jumpers. These techniques were demonstrated in the BERT experimental facility. BERT (Blanket Remote Handling Test Facility) is a full-size mockup

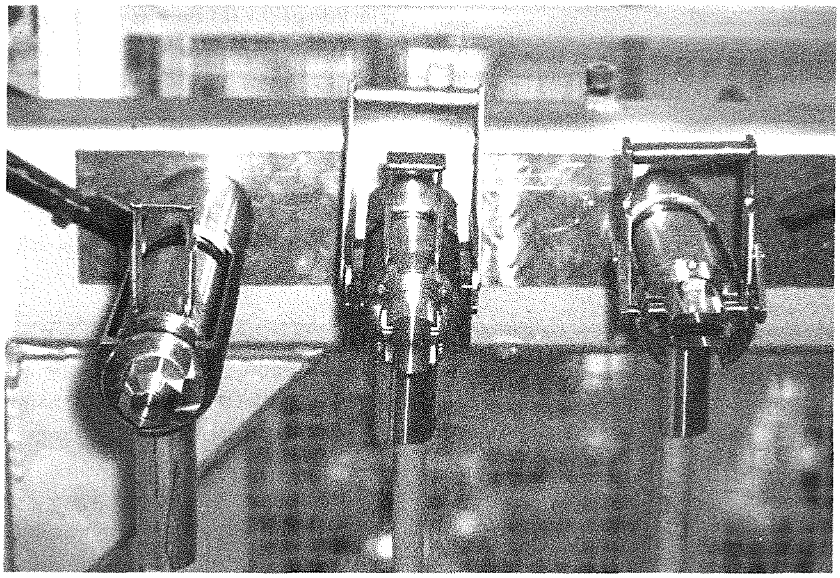

Fig. 1

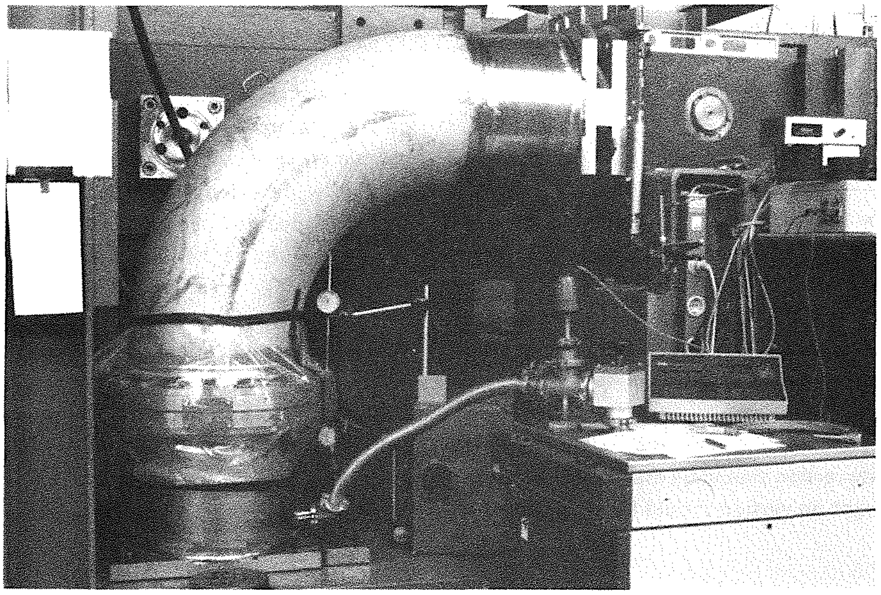

Fig. 2

of the upper parts of the NET I blanket connections and the blanket supply lines to be connected. Work in BERT focused on the remote exchange of the different types of flanged pipe jumpers.

The so far available results of the trials are summarized in an interim test report [7]. Fig 4 shows the present state of BERT.

The pipe cutting and welding tools were tested and qualified in the FEROS test facility (Fig. 5).

After the FEROS test facility had been commissioned for remote pipe welding/cutting tools, basic tests using the already existing cutting/welding tools were performed. R.H. trials in FEROS focused on the P.O.P. test using

- Swarf-free cutting tools for 200 mm OD
- TIG welding tools for 200 mm OD
- Pipe-end preparations for 200 mm OD

So far, pipe cutting and welding has been identified as a NET-related joining technique for class I and II maintenance tasks. Originally, it was planned to continue P.O.P. trials also with welding/cutting tools in BERT as it exists. KfK made a proposal for the installation of additional supply lines for P.O.P. tests of welding/cutting tools.

A modified BERT option is under discussion which is able to give a more realistic representation of the current NET/ITER layout.

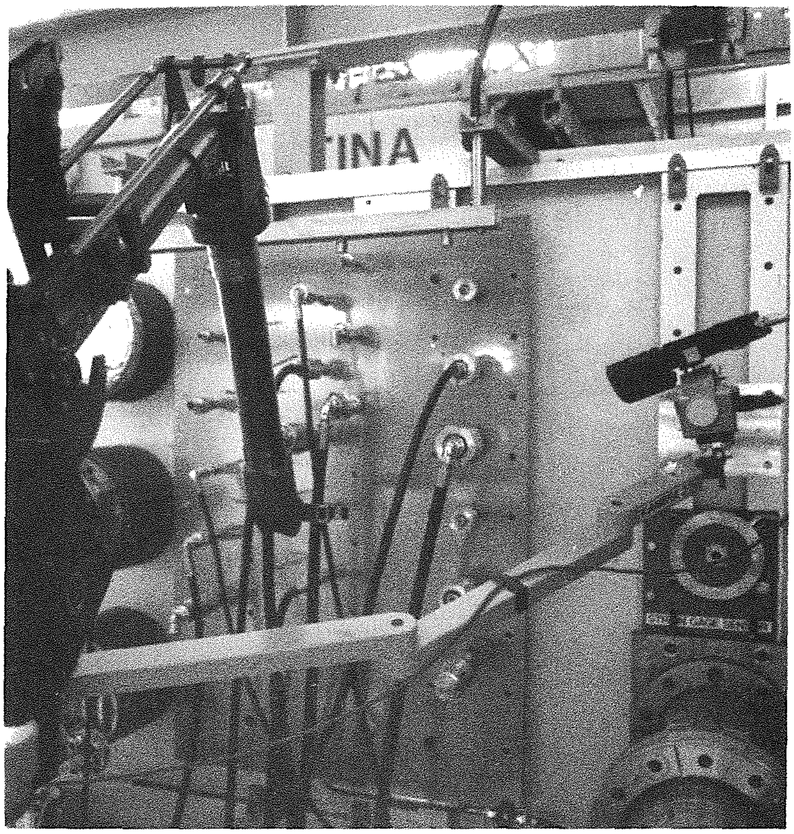

Fig. 3

NET has requested that priority be given to subtask 1.6 "cryogenic connectors". When the decision was made to use the welding/cutting technique for the disassembly and reassembly of the cryogenic connectors, the larger part of activities under this subtask was shifted to subtask 1.6.

Subtask 5: Welded Vacuum Lip Seals of Blanket Segments

The objective of this subtask is to develop remote handling equipment and procedures for maintaining welded vacuum lip seals, and remote lip weld inspection techniques. Originally, it was planned to demonstrate the method of welding and cutting lip-welded vacuum seals to the blanket upper flange under NET-relevant conditions in the BERT test facility.

Since NET gave priority to the general investigation of techniques for the cutting and rejoining of horizontal access ports (e.g. test blanket) and vacuum ducts, KfK decided to make the development of UU lip-welded seals and the corresponding lip welding and cutting systems the point of main effort of the activities in the period under review.

For this purpose, several design drafts were developed and working sequences were investigated which were discussed with NET in several meetings.

The final KfK tooling concept was submitted to NET together with the design of the P.O.P. test rig. The NET comments were taken into account. An agreement was achieved on the new proposal. The tooling concept was outlined in a draft report which was handed over to NET for comments. [8].

The FELIS test facility was set up for the performance of NET-related P.O.P. tests using the already existing modules of the universal lip welding/cutting tooling systems.

First trials using the lip welding trolley and the cutting head were performed on a NET-related UU lip configuration.

A proposal was made for a lip welding/clamping device which, to achieve the required welding quality, is able to transmit sufficiently high forces to press the lips together to a remaining 1 - 2 mm gap.

Progress was also made in the rationalization of the different lip seal configurations.

Subtask 6: Cryogenic Connectors

The objective of this subtask is to design a superconducting-magnet cryogenic connector prototype suitable for remote maintenance, to design and develop remote proof-of-principle techniques for assembly, disassembly and postmaintenance inspection, and to demonstrate that connection and disconnection can be carried out using P.O.P. equipment and existing tools in a mockup of the environment envisaged for NET.

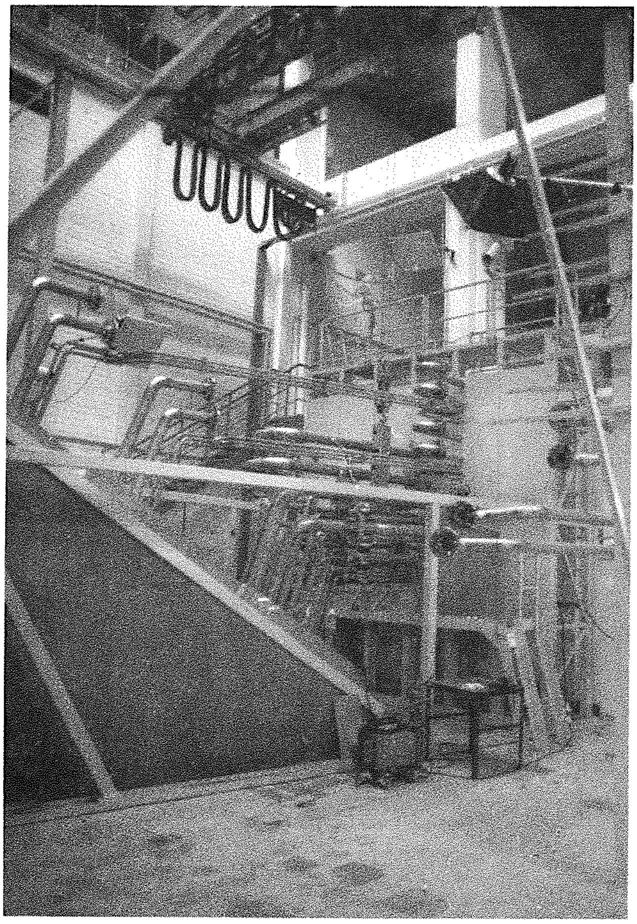

Fig. 4

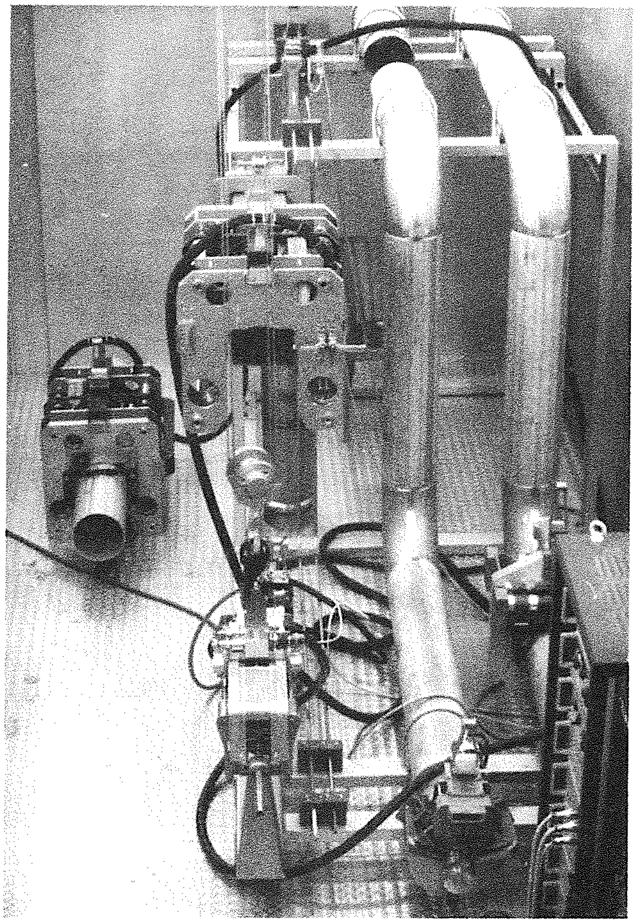

Fig. 5

Several alternative solutions for cryogenic pipe connectors were investigated. In agreement with NET, it was decided to focus work on the design of three different versions of cryoline connectors. The layout of the connectors, the working steps for assembly and disassembly and the tools were investigated. The results were compiled in several unpublished reports.

The design of the cryogenic connectors was completed. The general layout of the remote handling procedure for cutting and rewelding was agreed with NET. The proposals made and the results gained so far were compiled in an interim report [9].

KfK and NET have agreed on a test program to verify the design proposed. In the framework of the current technology program, only P.O.P. trials are planned to investigate the feasibility of the cutting/welding procedure. The P.O.P. trials will demonstrate the critical cutting and rewelding operations involved in the remote assembly/disassembly procedure.

The trials with already existing pipe cutting/rewelding tools were started. Fig. 6 shows the final stage of the test facility as planned for the P.O.P. trials.

Work on the design of the prototype connectors was continued. The general arrangement drawings for the flexible and rigid cryogenic connectors were completed. Both full-size connectors are planned to be manufactured using suitable materials. The connectors will be assembled without welding so that they may be assembled and reassembled to prove the maintenance feasibility. Detail drawings were completed in agreement with NET. A proposal for the continuation of the Technology Program from 1992 to 1994 was prepared and handed over to NET.

<u>References:</u>

[1] Selig, M.,Unpublished report of KfK, July 1990.

[2] Selig, M., et al., Unpublished report of KfK, Dec. 1990.

[3] Gutzeit, H., et al., Unpublished report of KfK, Nov. 1990.

[4] Ullrich, U., Unpublished report of KfK, April 1991.

[5] Kirchenbauer, U., Selig, M., Unpublished report of KfK, Febr. 1991.

[6] Selig, M., et al., Unpublished report of KfK, Sept. 1991.

[7] Gutzeit, H., et al., Unpublished report of KfK, Jan. 1991.

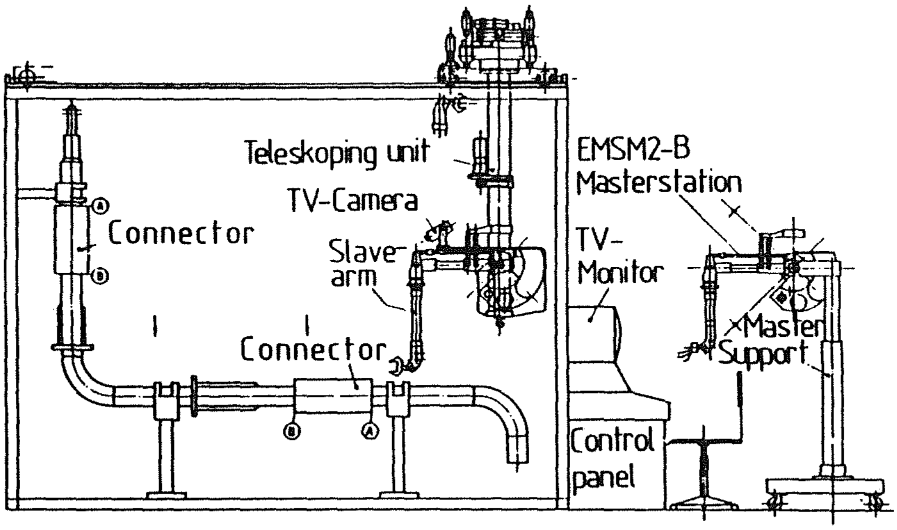

Fig. 6

[8] Gumb, L., et al., Unpublished report, April 1991.

[9] Gumb, L., et al., Unpublished report of KfK, Febr. 1991.

Staff:

R. Gaa
L. Gumb
U. Kirchenbauer
H. Krause
R. Müller
W. Reeb
A. Schäf
M. Selig
D. Stern
M. Trettin
R. Ullrich

RHS 2 Material Tests for Remote Maintenance Equipment

Components of the NET In-Vessel Handling Unit (IVHU) have to be qualified with respect to reliability, accuracy, radiation and temperature resistance. These will be done in collaboration with the supplier and according to the results of material tests. The material tests include pre-tests, irradiation tests and post-irradiation tests.

Components to be tested by KfK in collaboration with CEN/SCK MOL are motors, resolvers, inclinometers, ultrasonic proximity sensors and lubricants [1].

Subtask 5: Pre- and Post-Irradiation Tests of Position Sensors for Articulated Boom Transporter (ABT)

Various components and base materials have been irradiated in the gamma irradiation facility of the BR2 reactor at Mol, which are indispensable to the design and construction of remote handling sensors [2]. A point of main effort was the irradiation of two online instrumented resolvers being operated in a realistic gamma and temperature environment with a gamma dose up to 1E7 Gy-Si and T = 150 °C, respectively. The functionality of the resolvers was surveyed by a pneumatic drive system which was equipped with a pressure and temperature instrumentation, and the angular motion to pre-set mechanical resolver stops was measured by an individual resolver electronics. The availability of qualified resolvers has been nearly reached by exchanging the connector cable insulation and the choice of a suitable lubricant. But both resolvers showed partial blockages after 192 hours of gamma exposure and after having accumulated 2E6 Gy-Si due to halogenous degasing effects from a specific thin coil holder insulation foil. This foil is now subject to be replaced by an ULTEM plastic base material which must become modified and mechanically formed to a thin coil support by the furnisher SIEMENS.

Most of the plastics being exposed to up 1E7 Gy-Si must become excluded from an applicability as a consequence of embrittlements and fragmentary surfaces and structures. In this context, the quality decay of nearly all electrical cables with plastic insulations was obvious. ULTRAPEK from BASF and RADOX from SUHNER did operate satisfactorily only under static and non-bending conditions. The results of six gamma irradiation campaigns during the time of review underline the necessity of more irradiation tests with specific plastics to overcome serious problems in the field of sensor development and instrumentation.

The out-of-pile tests with two inclinometers type SCHAEVITZ LSRP-90- HT failed after four months of operation and the adapted electronics showed a time dependent offset and an incorrect analog signal output. As a consequence, the preparation work and the construction of a modified irradiation basket was interrupted at the end of 1990. The complete inclinometer system was sent back for repair and modification to the furnisher SCHAEVITZ / USA in December 1990 and has not yet arrived for further tests.

Subtask 6: Pre- and Post-Irradiation Tests of Drive Components for Articulated Boom Transporter (ABT)

This subtask includes mainly the testing of motors. In preliminary irradiation tests motor base materials have been already tested at CEN/SCK MOL [2]. The results of these tests were taken into account for the modification of standard motors. The modified motors were supplied by Maccon and Moog.

For the pre-irradiation tests a motor testbed with heating chamber was built at which the technical data of the motors were measured at both ambient and NET typical operating temperatures 3. The results of these tests are summarized in [3]. Figure 1 shows a typical power/torque curve in dependance of the motor speed and the temperature increase of the test motor. The test results will serve for comparison reasons to identify changes due to irradiation and temperature.

The irradiation tests in a test rig at the BR2 at CEN/SCK MOL are ongoing. The test rig was manufactured at KfK. It allows to operate the motors during testing at no-load conditions [4].

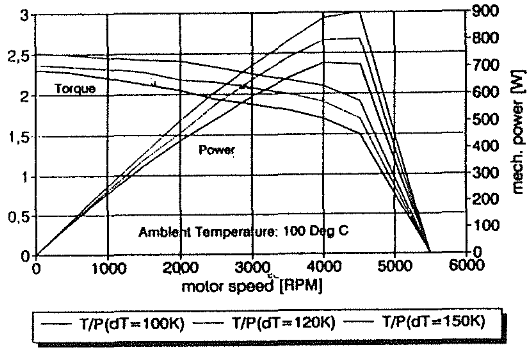

Fig. 1: Power/torque graph of a test motor

References:

[1] Rohrbacher, H.A. Suppan, A.: Unpublished report, March 1991.

[2] Rohrbacher, H.A. et al.: Unpublished report, April 1991.

[3] Suppan, A.: Intermediate Report, not published, in preparation.

[4] Kast, G.: Nuclear Fusion Project - Annual Report of the Association KfK/Euratom - October 1989 - September 1990, KfK 4774, EUR 131551 EN, September 1990.

Staff:

I. Aberle
B. Bartholomay
R. Döbele
D. Klein
K.H. Lang
W. Link
G. Müller
H.A. Rohrbacher
P. Schultheiss
A. Suppan

RHS 3 Mock-up of In-Vessel Components and Test Facilities

Subtask 2: Protective Tiles and Divertor Plate Handling Devices

Objective of the task is to design and manufacture a proof of principle remote handling equipment for a rapid tile replacement and the replacement of upper and lower divertor plates. The scope of the work includes designing tools and end-effectors for these tasks which are either attachable as work units to the NET articulated boom system or may be handled by means of a work unit. The tools and the end-effectors will be tested in a full scale mock-up with EDITH as basic equipment.

Protective tile handling device

The investigations for the replacement of protective tiles (Figure 1) are based on [1]. In a first stage the replacement task was split into different steps to identify the required equipment. An optimization of the replacement time and the reliability led to a concept with special tools for the different operations. In particular the following main tools are part of these concept:

tile detachment device (TDD),
tile positioning device (TPD),
studs removal device (SRD) and
studs positioning device (SPD).

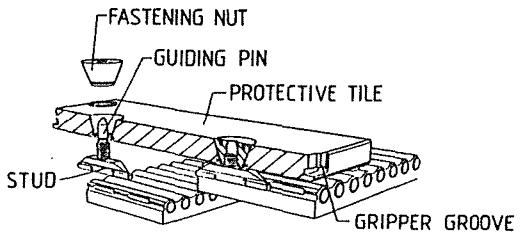

Fig. 1: NET design of a first wall section with radiatively cooled tile

A possible further tool may be used for the removal of the guiding pins. All the devices are capable to be remotely operated by an electrical master-slave servomanipulator which is attached at the articulated boom transporter

By means of the tile detachment device a tile to be removed will be grabbed using the gripper and the both tile fastening nuts will be trepanned simultaneously. Both drilling units are driven by a common electrical drive unit, the gripper is actuated by a lifting magnet. Trepanning dust will be exhausted. Gripper, trepanning unit and exhaust system are integrated into the TDD.

The tile positioning device (Figure 2) is composed of the gripper system and the screwing unit. The gripper system is based on a toggle lever system which is actuated by a lifting magnet. In a currentless status the gripper is closed, in combination with the toggle levers the uncontrolled unlocking is prevented. Both screw drivers are pressed against the tile fastening nuts automatically by springs. The screw drivers are operated by means of a common electrical drive unit. The torque of the screw drivers is limited by slipping clutches. A call for tender for a detailed design and fabrication of an operational model was launched.

For the studs removal device and the studs positioning device the concept investigations are ongoing.

Divertor plate handling device (DHD)

The investigations of KfK to design a DHD are based on [2]. The design is in a preliminary stage. Results of the investigation will be available end of 1991.

References:

[1] Reeve, T.J.: NET2-Definition of Requirements for the Design of Prototype Tile Handling Equipment, Doc.Nr.N2/P/023132/1/A, Issue Draft November 1989.

[2] Reeve, T.J.: Definition of Requirements for the Design of Prototype Divertor Handling Equipment, Doc.Nr.N2/P/023132/2/A, Issue Draft January 1990.

Staff:

J. Hübener
B. Haferkamp
W. E. Hörl
W. Link
A. Ludwig
A. Suppan

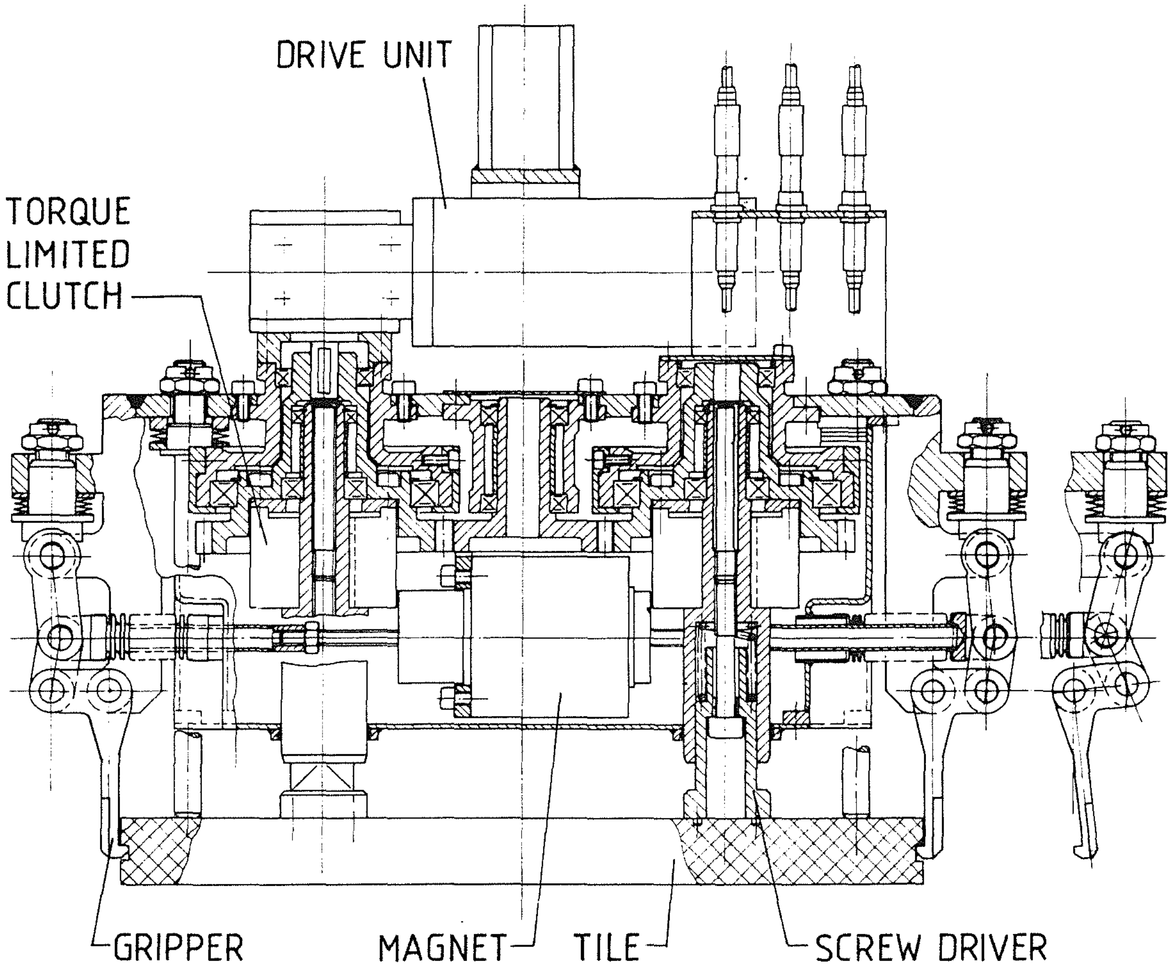

Fig. 2: Tile positioning device

RHT 1 Articulated Boom Transporter

The main objective of this task is the development of an In-Vessel Handling Unit (IVHU) for inspection, repair and replacement of NET in-vessel components. Main component of this equipment is a transport system on the basis of an articulated boom with attachable multi-purpose and special work units. KfK is developing this system.

The results of these investigations are summarized in [1], the technical specification for NET/ITER in-vessel transporters [2], the document "Divertor Maintenance Using IVHU" [3] and the document "Definition of Requirements for the Design of Prototype Divertor Handling" [4]. The articulated boom system (ABS) was selected as one of two transporter options mainly to be used for short term interventions [5]. In opposite to the boom, the vehicles system to be developed by other Assosiatons is devoted for long term interventions.

A prototype of the articulated boom in combination with a mock-up for the NET torus is needed to demonstrate the feasibility of the replacement of plasma facing components as well as the reliability of maintenance procedures and equipment in a mock-up. The prototype of the boom is the experimental device of in-torus handling (EDITH).Both, EDITH and mock-up are under construction and development, respectively.

Subtask 1: Preliminary Engineering Design of ABT

The work for the preliminary design of the articulated boom transporter (ABT) was continued and is now completed except the end-effector positioning unit and the work unit interface.

Mechanics

The mechanics, especially the overall structure of the ABT is unchanged from the description published in the semi-annual report 1989 [6]. In principle, the ABT link system has four yaw joints, one rotation joint and one pitch joint to compensate vertical deviations of the boom. The yaw joints are driven by coaxial drive units on the basis of Cyclo drives. For the rotation joint two Cyclo drives with a common spur wheel gear are foreseen and the pitch joint will be operated by a linear actuator based on two spur wheel gears which operate a planetary roller spindle.

At the front link of the ABT the end-effector positioning unit (EEPU) will be attached. It forms the connection between the ABT and the different work units (WU) and works similar to a telescopic mast to reach the upper and lower torus regions. The three extensions (slides) are guided by roller pads and operated by planetary roller spindles. Integrated is the work unit interface (WUIF) which serves for the remotely handlable connection of power supply, data transmission and as far as necessary cooling supply of the WUs.

Control System

The general goal of the RH control system investigation was to define a framework for the RH control system development, validation, test, safe task execution, easy maintainability, and easy integration of new and/or enhanced modules from different sources. The identification of functional modules of the control system and of useful interfaces was of main interest in the general investigation phase. The specific goal in the investigation was to specify the requirements for the IVHU area control system and to design its functions and architecture (Figure 1). The RH control system is a subsystem of the NET control system. The RH control system itself is partitioned into RH-areas, representing a set of RH equipment grouped around a major device (e.g. in-vessel handling unit, blanket handling unit). Each RH-area has its own RH-area control system organised as a hierarchy of computers and controllers dedicated to one RH-area. To run a RH area control system in the operational phase a Remote Handling Workstation (RHWS) is needed.

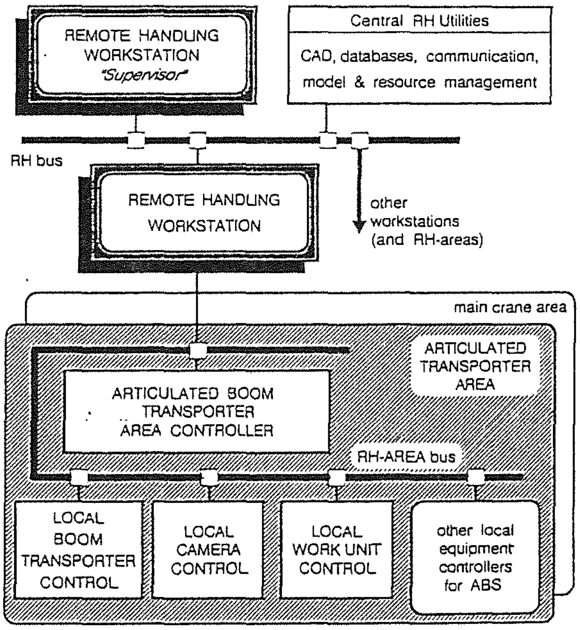

Fig. 1: RH control system architecture

Remote Handling Workstation

To support the tele-operator as flexible and complete as possible on a high level a general purpose remote handling workstation concept was developed [7] [8] [9]. The RHWS provides the man-machine interface and operational support functions classified into procedure oriented support, working space oriented support, and device oriented support. This operational support is based on task knowledge represented by procedure models, spatial models, and functional models. These models and the related simulation systems are used for planning, execution, monitoring, training, and recovery. The workstation represents an intelligent, interactive, multimedia handbook guiding the operator through planned procedures and in abnormal situations.

The basic subsystem of the RHWS will be a spatial simulation system like KISMET [10] [11], originally developed for the JET-TARM control system and already successfully transferred to various non-fusion applications. The development of a KISMET module for real-time static deflection simulation for the NET/ITER IVHU model is going on. Further enhancements of KISMET are: addition of new local modelling features using boolean operations, new rendering options (stereo, real-time shadows, photo-realistic images based on ray-tracing), adaption of the inverse kinematic model to general boom structures, overlay of graphics and video camera images using a commercially available frame grabber. In the NET context KISMET is actually being used for design studies in the area of divertor exchange, viewing system layout (camera arm design, camera positioning), and for presenting results of the AMBOSS system dynamically (see later).

To support the model generation for KISMET in the JET environment using the CATIA CAD system a set of software tools were implemented and brought into production [12].

Computer based real-time simulations require suitable models of the scenario to be simulated. The generation of such models is the main purpose of the software package ROBOT, which is running in the BRAVO-CAD environment. With its present version 2.1, ROBOT has become rather stable, and its further development is only due to minor changes.

ROBOT version 2.1 has been used to generate a hierarchical model structure of the ITER in-vessel handling scenario, where especially the replacement of divertor plates by the Articulated Boom Transporter has been addressed. Both, the environment (tokamak reactor) and the various handling devices (ABT, Divertor Handling Device, Transfer Unit) have been modelled with various levels of detailling in such a way that for each partial model it is possible to switch between these levels during a simulation. This model structure of the ITER scenario has been transferred to the real-time simulation system KISMET [13] [14].

A further hierarchical model structure has been produced using ROBOT which is dedicated to the mock-up scenario of the EDITH test facility. Again, the model contains various degrees of details which may be switched between. Figure 2 shows the model thoroughly with a high degree of details in a simulation scene where an upper divertor plate of the mock-up is to be removed.

IVHU-area control system

The IVHU-area control system is the integration of the control systems of the devices of the IVHU area. The IVHU control system is the basic subsystem of the IVHU-area control system. Other subsystems of the IVHU-area control system are for example the WU control systems and the camera control system. The main functions of the IVHU-area control system are: equipment control (non-motion), motion control, single command execution (manual mode), program execution (automatic mode), on-line teach/repeat, backtracking of pathes, operator support functions for manually controlled motions (e.g. jiggs). A central feature is the controllability via the NRWS, demanding for a full access to all functions of the RH-area control system.

IVHU Dynamic Simulation

For a complete dynamic simulation of the articulated boom transporter the AMBOSS (ADAMS-Modelled Boom Simulation System) software environment and ABT model have been set up. Main topics of the dynamic simulation are the evaluation of IVHU performance, selection and optimisation of the actuator design and of the control algorithms.

In contrast to existing remote handling systems or common robotic tasks, the NET in-vessel transporter is characterized by high payload, large dimensions and narrow environment. These conditions require a precise overall simulation that comprises full three-dimensional non-linear multibody dynamics, the structural deflection of the boom and a precise model of the actuators and the control system including non-linearities as backlash and friction.

The multibody dynamics of the transporter system are modelled with the commercial analysis package ADAMS. Elastic links and the dynamic actuator model shown in Figure 3 are introduced by applied forces, spring elements and differential equations. Nonlinear effects such as backlash and friction which have an influence on control stability and accuracy are taken into account.

The performance of the remote handling transporter is examined for a critical collision situation at the entrance to the vessel and a criticaldisturbance situation during load transfer. Passing the port of the vessel is the first situation investigated. A point-to-point path has been generated for the motion - unfolding outside the vessel - inserting the boom - moving to the point 90 degree away from the port. Therefore, several positions were fixed and the path between them was scaled to move with maximum velocity and acceleration. The whole path is run about five times faster than assumed in the layout.

Figure 4 shows the nominal path of the end-flange and the results for a suboptimal tuned PPI-cascaded control scheme and a PD-position controller at the motor shaft. For the PPI controller the performance is not satisfactory because the gain at the first joint Z1 had to be reduced to achieve stability when the boom is stretched.

The other critical in-vessel operation examined with the AMBOSS model is an accident situation at the upper divertor plate. A sudden load transfer of 1000 kg is assumed in the 90 degree position.

The boom, initially in a static balance suddenly changes to the loaded state and builds up to the new transient position with an additional deflection of about 20 mm. The path of the

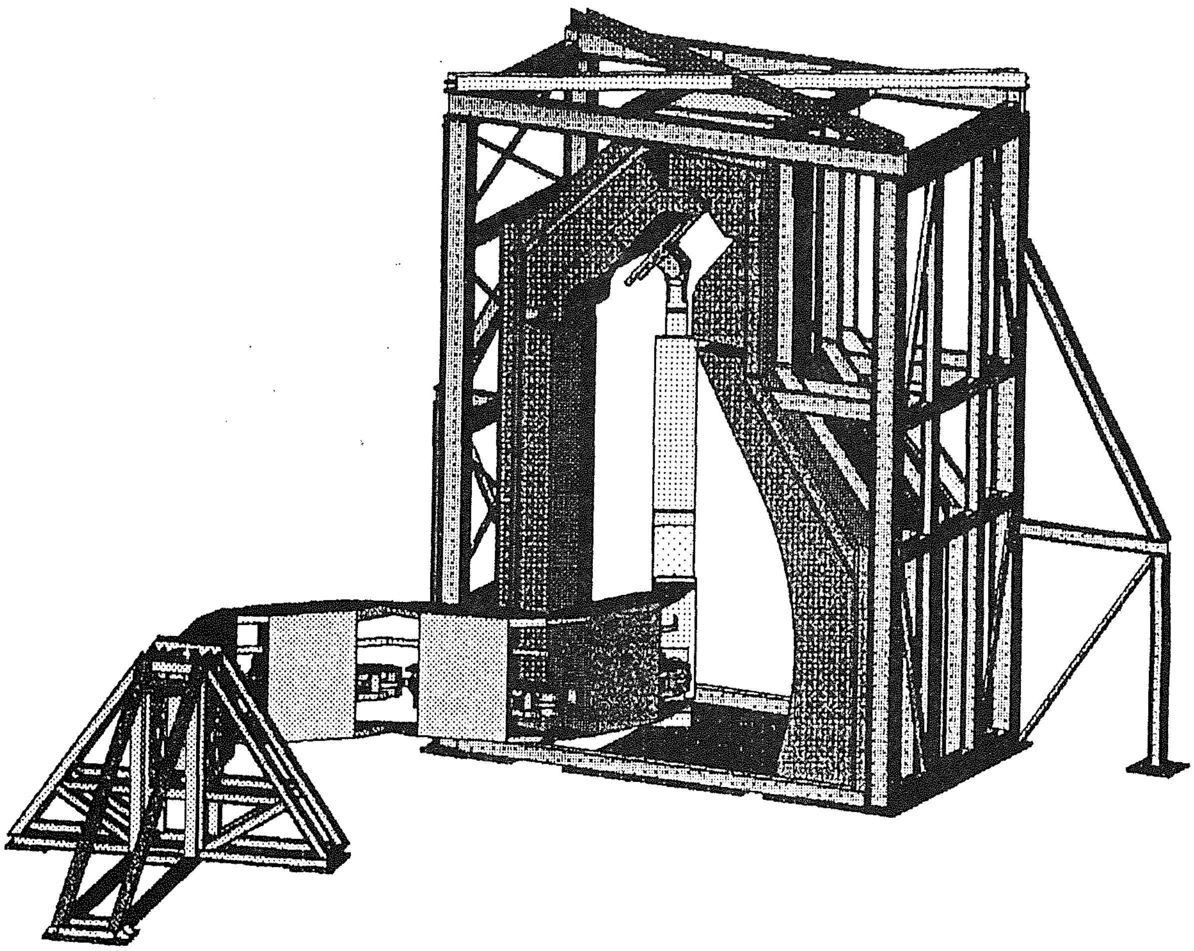

Fig. 2: Simulation of divertor plate removal: The picture shows EDITH and the planned tokamak mock-up

end-flange oscillation after load transfer is drawn in the three-dimensional plot in Figure 5.

Two facts are remarkable to be pointed out in the conclusion:

1. The maximum load on the actuators arises when a vertical load is applied on the tip of the bowed boom. This result proves that a full three-dimensional analysis is indispensable.
2. The motion of the boom can run more quickly as estimated in the layout. In simulation the unfold-insert operation does not take longer than three minutes. This reserve can be used to save maintenance time or to improve accuracy.

First preliminary measurements of the gear stiffness and the dominant eigenfrequency of the boom correspond with the simulation results. The next steps will be more reliable verification experiments with the full scale prototype device EDITH and the implementation of advanced control schemes.

Subtask 2: Design, Manufacture, Test of a Full Scale Prototype (EDITH)

Mechanics

The construction of EDITH, the full scale prototype of the ABT was started at the Remote Handling Laboratory at KfK (Figure 6). It is composed of the support structure, four links and the work unit dummy for tests to take over heavy loads, as there will be the divertor plates of the NET device. The work unit dummy will be substituted later on by the prototypes of the End-Effector Positioning Unit (EEPU) with the WUIF. The first one is designed and specified for manufacturing, while the WUIF requires pre-tests. Figure 7 shows a simplified WUIF for these tests.

The fabrication of other components and sub-assemblies is ongoing. A typical component is the coaxial drive unit for the link joints which is under development in cooperation with JET and the industry. A prototype of the drive unit is already

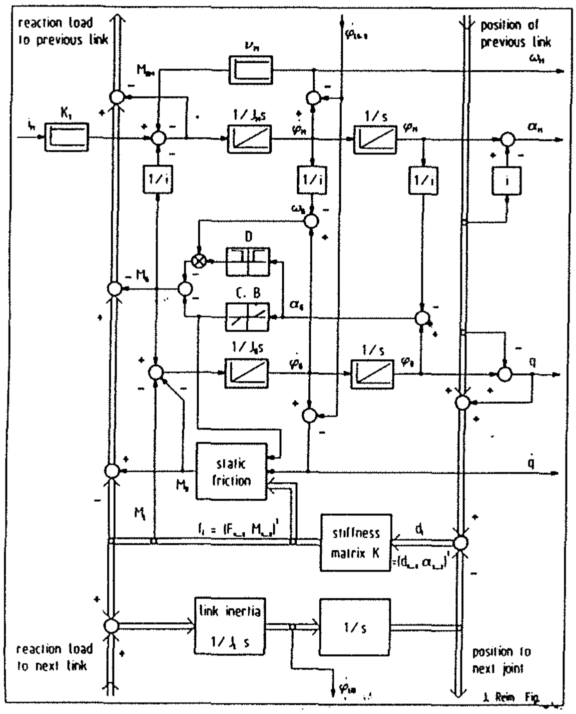

Fig. 3: Dynamic actuator model with backlash and static friction: symbol definiton:

iM	motor current,
KT	torque constant,
vM	motor damping,
JM	inertia of motor shaft,
M	tprque,
i	transmission ratio,
D	damping oif gear deformation
E	gear stiffness,
B	backlash,
Jg	inertia of gear output and half link,
K	stiffness matrix
di	deformation vector,
fi	load vector (in link),
JL	inertia of half link and fixed parts of the next drive unit,
ø	absolute position,
α	relative position

fabricated and pre-tested under ambient conditions at the industrial contractor ANSALDO (see Figure 8).

The tests have shown the potentiality to increase the stiffness of the drive units with respect to achieve an optimal control capability of the link joints. Therefore, changes and improvements will be performed at the other drive units to be manufactured until the end of 1991 for application at EDITH.

EDITH Control System

According to the general RH control system investigations the development of the EDITH remote workstation as a prototype of the proposed RHWS is going on based on the KISMET system. To attach KISMET to the EDITH control system the needed interface was implemented. For the experiments in the EDITH environment and planning activities the following geometric/kinematic models are available on KISMET: the EDITH arm, the mock-up of the torus, the dual arm master-slave manipulator system, the camera system, and models of the preliminary positioning unit and divertor handling unit. The EDITH arm model was successfully used for commissioning of the EDITH control system, whereby the control system running in the simulation mode drove the KISMET model instead of the real boom.

Motion control system for EDITH

The motion control system (MCS) of EDITH, which is part of a hierarchical control system was delivered in June 1991.

After delivery first tests with a so-called test-axis were started. The test-axis is up to a certain level a mock-up of an axis of EDITH. E.g. like in EDITH two motors are combined to drive the axis. A model of the axis was derived and a corresponding position control design was carried out [15].

The objectives of the work with this axis are the following:

- testing of MCS-functionality concerning single-axis commands
- testing of MCS-characteristics concerning process-signals
- testing of MCS position control performance

It is also intendend to use the axis as a test bed for research related to electric backlash removal.

After implementing the online link between the EDITH-MCS and KISMET the MCS-functionality w.r.t. movements in cartesian plane were investigated. E.g. motion sequences were defined using the MCS-Handbox and then the sequences were played back using KISMET to visualize the movements. Therefore it is easy possible to value the performance of the pathplanning-modul in the MCS.

Position control

The performance of the position control is depending among others from gear elasticity and damping. To examine the effects of these properties a linear model of he first axis of EDITH was derived [16]. The model consists of

- motors
- gears with elasticity and damping
- link

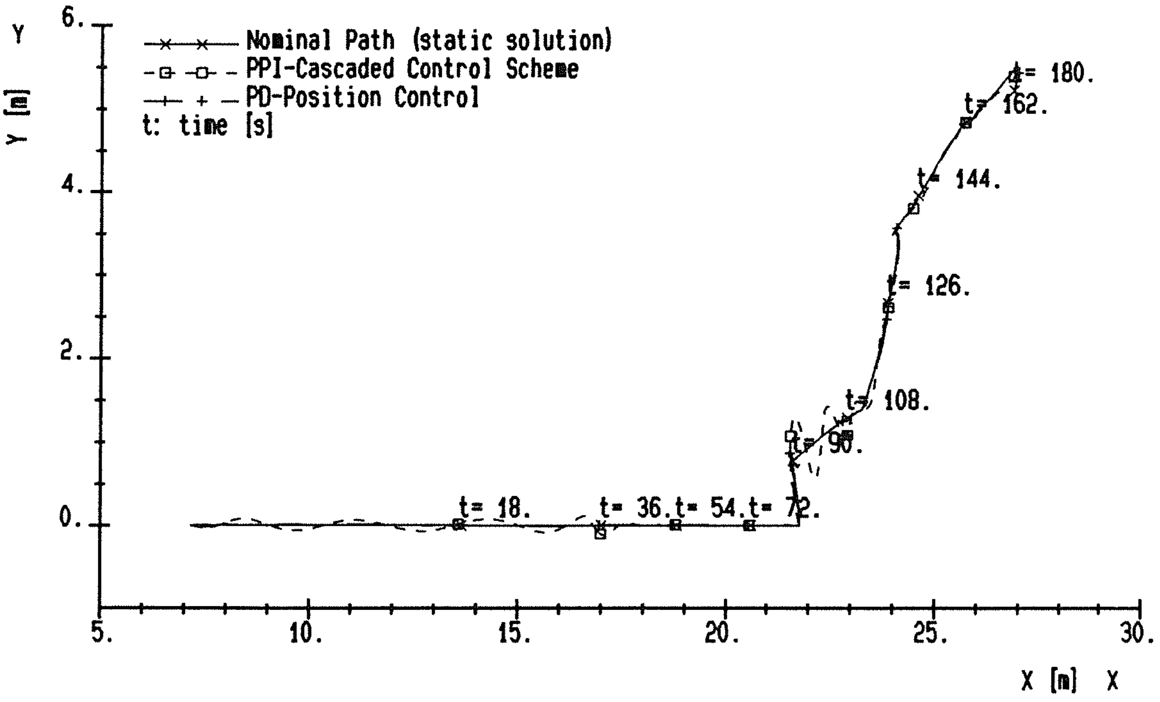

Fig. 4: Path of the end-flange in the horizontal plane

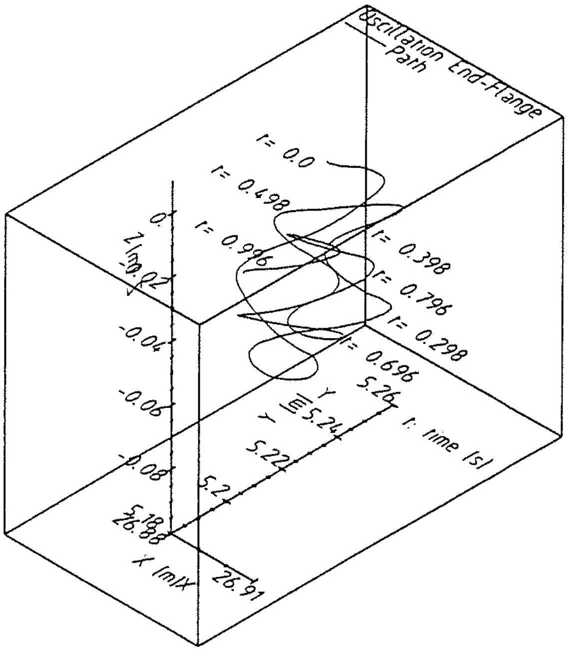

Fig. 5: Path of the end-flange after load transfer

Based on this model four different position controllers were examined:

- PD-controller using joint angles and joint velocities
- PD-controller using motor angles and motor velocities
- PD-controller using motor angles, motor velocities and joint velocities
- State-space-controller using joint angels and motor angles, as well as joint velocities and motor velocities

Simulation results using the program-system ManDy [17] show the characteristics of the different control schemes. It could be clarified that also in the presence of increasing gear elasticity and decreasing gear damping a good dynamic performance may be achieved by using a state space controller (Figure 9).

Drive Unit Control

The drive unit control is the lowest level of the control system. It will get the required control signals from the position control. Also the back-up control system will work at this level. Excepted the back-up system the drive unit control system was delivered and externally tested within the frame of the coaxial drive unit tests and the motor tests.

Safety and Reliability Analysis

Beginning with a "Functional Analysis" (FA) a safety and reliability analysis was carried out. The FA is a breakdown of the design in its functions and subfunctions. It is followed by a "Failure Modes, Effects and Criticality Analysis" (FMECA). In th FMECA the possible failures of all functions, the related consequences as well as the criticality and the provisions foreseen to mitigate either the likelihood of occurence or the criticality associated to the failure are listed. At the "Fault Tree" (FT) possible causes are summarized which may lead to a malfunction of subsystems or components and thus also to a failure of functions. Finally the "Fault Trees" (FT) are the basis for the determination of consequences and criticalities.

Summarizing the investigations it was shown in the intermediate report of the safety and reliability analysis [18] that the criticality levels I (demage or contamination of the NET machine) and II (failure to recover the articulated boom system) were eliminated by appropriate measures or that the

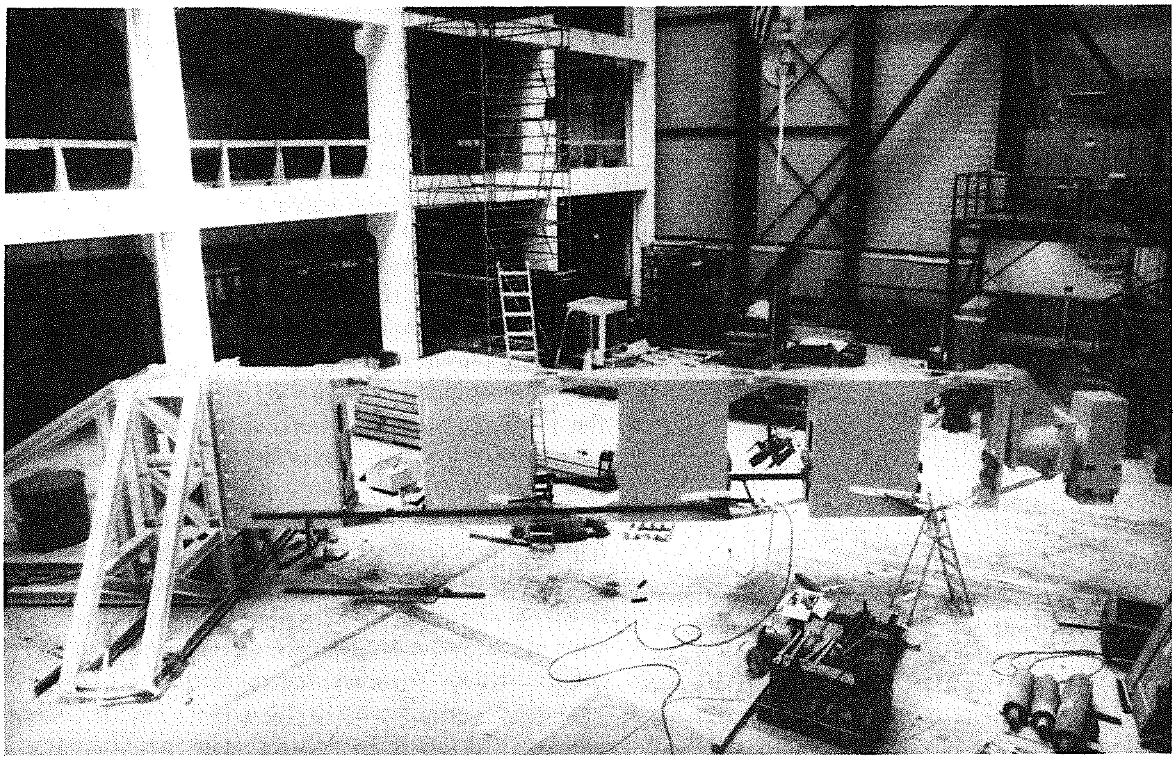

Fig. 6: Testbed EDITH under construction

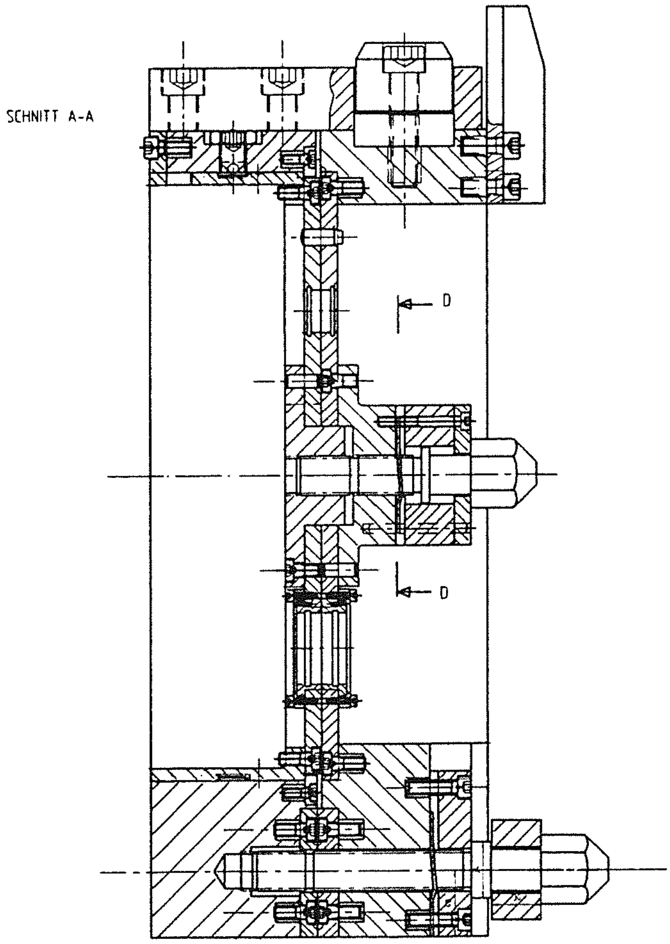

Fig. 7: Work unit interface (WUIF)

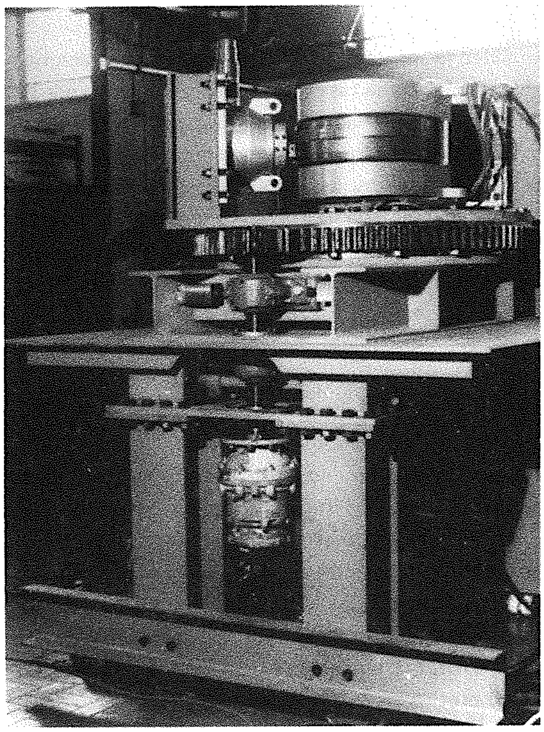

Fig. 8: Test-fixture with coaxial drive unit

probability of occurence is sufficiently low. In continuation of the analysis the influence of failures on the control level will have to be investigated.

Mock-up

As mentioned, EDITH will be complemented by a full scale mock-up as it is shown in Figure 2. The mock-up is based on

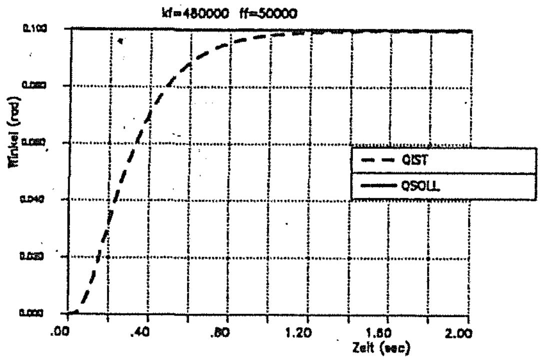

Fig. 9: Step response elastic model with state space controller

the NET torus geometry, represents one sector of the vacuum vessel with dummies of its internals and allows in combination with EDITH the demonstration of in-vessel maintenance operations. The design of the mock-up base structure permits the simulation of the upper as well as of the lower divertor region after changing the mock-up internals and the EDITH support structure [5].

Overall Geometry Measurement

Precise knowledge of the geometry of fusion machines considerably simplifies the task of its remote maintenance by reducing necessary sensor activities during the maintenance process to a minimum. For the surveying of out-of-vessel components, the geometry measurement system (GMS) has been developed at KfK. It bases on the surveying method of triangulation with two (ore more) theodolites. A prototype system with one theodolite is available to show that requirements can be met. For a detailed description, refer to [19], [20].

Remote control of GMS could only be achieved by applying the latest generation of theodolites. They are equipped with computer-controllable stepping motors for horizontal and vertical movement and for focusing of the telescope. An integrated CCD-Array supplies digital images alternatively from the telescope or from the wide-angle optics. Transferring these image data to a computer and a TV-screen via an image processing board allows for manipulation and viewing of the object image by a remote operator thus enabled to do precise aiming to target points. Measurement of sensor data (horizontal and vertical angles) is triggered by the remote operator, performed digitally by the theodolite and completed by the transfer to the control unit. The most important condition for the validity of these measurements is that the theodolites provide a precise horizontal reference level. Therefore modern theodolites are equipped with internal compensators. Due to the fact that the working range of such a compensator is very small (in general few 1/100s of a degree), manual actions for the theodolite's installation would be necessary. The development of an automatic levelling platform carrying the theodolite (Automatic Levelling Facility, ALF) at KfK completes GMS's full remote control.

The notion of a functional connection of GMS to CAD-systems had a great impact on system design. Geometric CAD-model data, which in most cases supply a very good approximation of the object to be measured, are utilized such that the theodolite's telescope is automatically positioned to the actual target point. So operator actions can be reduced and the surveying process speeds up considerably. Direct operator support is provided by the option to superimpose a wire-frame model of the object on the video image captured by the theodolite's camera. Along with the graphics model, additional information about the target points is available. This feature is specially helpful in the starting phase, when the theodolites are still disoriented, or in occasions, where a high density of similar target points might lead to confusion. The link-up of GMS with CAD is also utilized in the opposite direction: the actual 3D point coordinates, computed on the basis of the GMS measurements, can be transferred back to the CAD-system. Physically, the connection to CAD-systems has been designed flexible by choosing the neutral CAD-data interface IGES (Initial Graphics Exchange Specification) as an intermediate data format. Within the GMS-Project, pre- and postprocessors to the BRAVO 3 - System (Applicon) have been developed.

GMS has been employed as the surveying system for the bearing tests of the EDITH-boom (see Figure 10). The goal of the first test campaign was to determine the deflection and the permanent deformations of EDITH caused by different loads up to six tons. The conical ends of metal bars served as target points. The metal bars itself were mounted in the centres of the segment joints so that they physically realized the boom's axes. Due to this construction it is possible to determine absolute values of the axes' direction in a fixed coordinate frame and torsions of the boom in future tests. The coordinates of each target point have been estimated with a standard deviation better than 0.15 mm. Therefore, solid angles can be computed with an accuracy of around 0.005 degree. Further experiences of the first EDITH-surveying campaign showed that there is a strong need for better software support of the survey planning phase and of the processing of final object point coordinates.

References:

[1] Suppan, A., et al.: The NET Articulated Boom: Preliminary Investigations and Justification for a Full Scale Prototype, KfK 4809, Dec. 1990.

[2] Maisonnier, D.: NET/ITER In-Vessel Transporters - Technical Specification for their Conceptual and Preliminary Design, Doc.Nr. N2/P/3240/1/B, issue A, 24.10.1989.

[3] Reeve, T.J.: Divertor Maintenance Using IVHU - In-Vessel Operation, Doc.Nr. N2/P/0230/2/A, 11.05.1989.

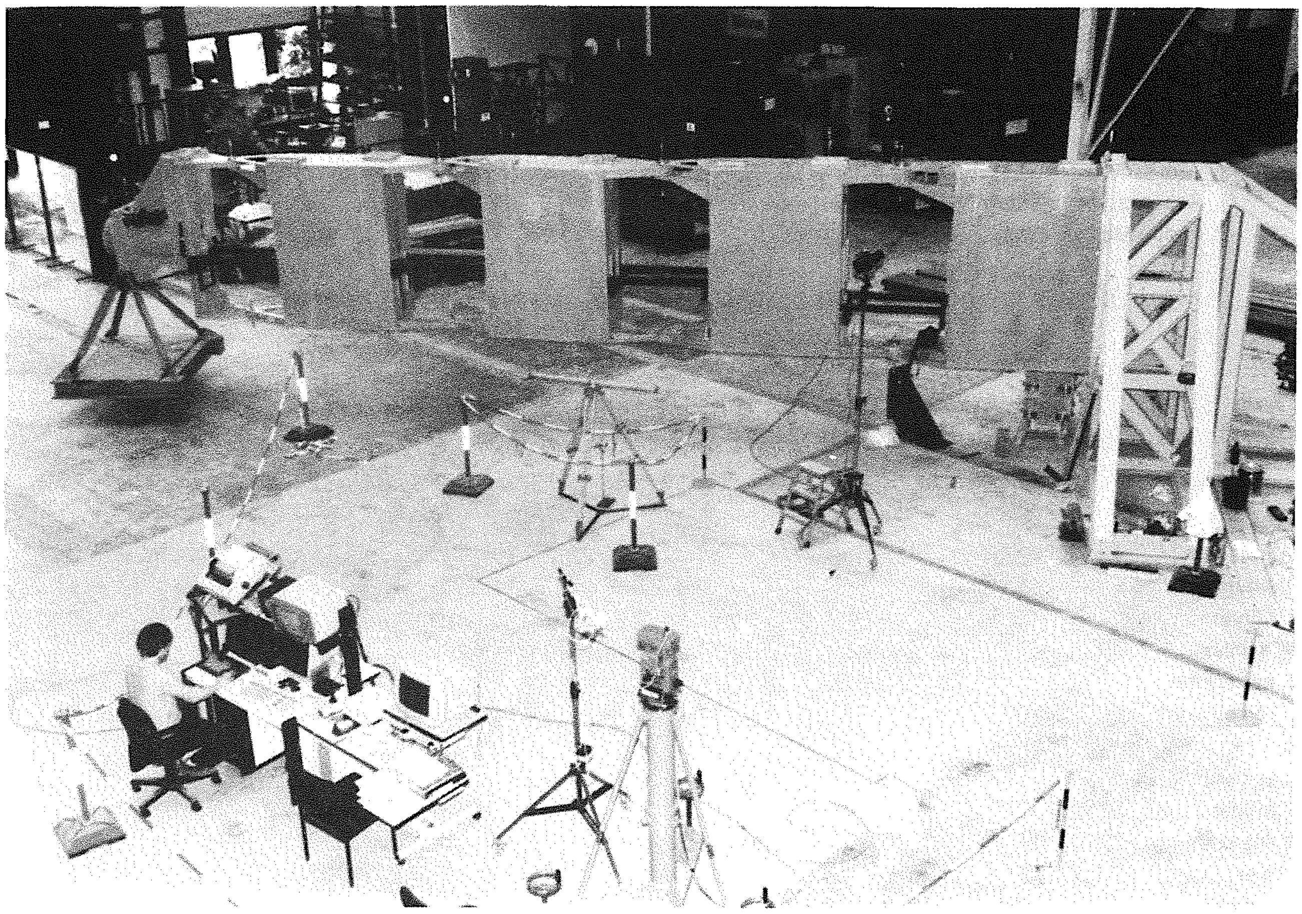

Fig. 10: Surveying of the EDITH-boom with GMS

[4] Reeve, T.J.: Definition of Requirements for the Design of Prototype Divertor Handling Equipment, Doc.Nr. N2/P/023132/2/A, issue Draft Jan. 1990.

[5] Kast, G.: Nuclear Fusion Project - Annual Report of the Association KfK/Euratom - October 1989 - September 1990, KfK 4774, EUR 131551 EN, September 1990.

[6] Kast, G.: Nuclear Fusion Project - Semi-annual Report of the Association KfK/Euratom - April 1989 - September 1989, KfK 4677, EUR 11397 EN, November 1989.

[7] Leinemann, K.: NET Remote Workstation. KfK-Bericht 4785, Oktober 1990.

[8] Leinemann, K.: Advanced Tele-Operator Support for Fusion Plant Maintenance. Proc. '91 International Symposium on Advanced Robot Technology ('91 ISART), Tokio, March 5-7, 1991, p.465-472.

[9] Leinemann, K.: Tele-Operator Support for Fusion Plant Maintenance: The EDITH Remote Workstation.ISFNT2, Second International Symposium on Fusion Nuclear Technology, June 2 - 2, 1991, Karlsruhe, Germany

[10] Kühnapfel, U.: Unpublished report, Dec. 1990.

[11] Kühnapfel, U., Leinemann, K.: Verfahren zur Manipulation in unzugänglichen Arbeitsräumen. DBP 3925275, 6.6.1991

[12] Pleschounig, W.: Unpublished report, May 1991.

[13] Kühnapfel, U., Ludwig, A.: Graphics and CAD Support for NET/ITER Boom Control. Proc. 16th SOFT, North-Holland (1991), p.1347-1352.

[14] Leister, P., Kühnapfel, U., Ludwig, A.: Computer Aided Simulation of a Remote Steam Jet Exchange in a Dissolver Cell. Proc. 4th ANS Topical Meeting on Robot and Remote Systems, Albuquerque, 1991, p.353-364

[15] Süss, U.: Unpublished report of KfK December 1990.

[16] Süss, U.: Unpublished report of KfK April 1991.

[17] Süss, U.: Unpublished report of KfK December 1988.

[18] Suppan, A.: Unpublished report, May 1991.

[19] Köhler, B.: GMS - a high-precision Geometry Measurement System for large fusion reactor components. IAEA,Technical Committe Meeting on Robotics and Remote Maintenance Concepts for Fusion Machines, Karlsruhe, 22.-24.2. 1988

[20] Heeg R., Köhler B.: Unpublished report, Nov. 1990.

Staff:

A. Frank
S. Geiger
R. Heeg
E. Holler
J. Hübener
H. Knüppel
B. Köhler
W. Köhler
U. Kühnapfel
K. Leinemann
W. Link
A. Ludwig
G. Müller
W. Pleschounig
J-Reim
M. Salaske
E.G. Schlechtendahl
U. Süss
A. Suppan

Safety and Environment

Introduction:

Within the revised European Fusion Technology Programme 1989-91 the safety analyses for NET/ITER which are being performed in parallel to the design efforts address mainly two different areas:

Plant Related Studies

- Radioactivity inventories and source terms (SEP 1)
- Environmental impact of tritium and activation products (SEP 2)
- Waste management and decommissioning (SEP 3)

and

Safety Assessment Studies

- Safety assessment for normal operation and maintenance (SEA 2)
- Analysis of reference accident sequences (SEA 3)
- Probabilistic safety studies (SEA 4)
- Assistance in the preparation of safety reports (SEA 5)

All component related studies (former SEC 1 - SEC 5) were closed, not achieved milestones integrated into task SEP 1 and task SEA 3, respectively.

KfK contributes to S+E tasks SEP 2, SEA 3, and SEA 5.

The KfK development of safety relevant models and codes for superconducting magnets are described in the magnet task MFAU 1 (former MSA 1).

SEP 2 Environmental Impact of Tritium and Activation Products

Subtask 2: Doses to the Public Due to Normal Operation and Accidental Releases

The computer model UFOTRI which dynamically describes the relevant transport processes of tritium in the environment, was established in a basic version. It was transferred to the Idaho National Engineering Laboratory (INEL). A user guide of the model is now available [1]. UFOTRI is being further developed, and the actual modelling will be presented at the Fourth Topical Meeting on Tritium Technology in Fission, Fusion, and Isotopic Applications in Albuquerque, 29.09. - 4.10.1991 [2].

Some submodels of UFOTRI were improved during this working period. In an experimental version, the model allows for calculating nearly all transfer rates internally, especially the deposition rates from the atmosphere to soil and plants as well as the re-emission rates from soil and plants to the atmosphere according to the changing hourly environmental conditions. The improved soil-water model has still to be validated against experimental data since the knowledge about soil resistance parametrization is sparse. This will be done in 1991/92 by a comparison calculation using experimental data measured by an environmental station of the Meteorological Institute of KfK near Karlsruhe. Two additional nutriment plant species (cereals and potatoes) were introduced in UFOTRI. Potatoes and cereals are an essential part of the human diet in Europe (50 - 70% of all consumed vegetables). The transfer rates of the improved ingestion model have still to be tested and defined by experiments performed by KfK.

UFOTRI participated in different benchmark exercises for calculating the off-site radiological consequences of an accidental release of tritium in both chemical forms (HT or HTO). Following the proposal of the NET benchmark from 1989/90, deterministic calculations for three different weather sequences with changing weather conditions were selected for the new benchmark [3]. The three weather sequences (extracted from hourly recorded meteorological data) were selected by expert judgement as representative to describe realistic worst case scenarios. Additionally, probabilistic calculations for the whole vegetation period were performed for accidental HTO releases. The meteorological data basis was the same as for the three deterministic cases. The resulting probability distribution of doses shows higher values (a factor of about 1.4) than calculated for the worst deterministic case, however with very low probability ($< 10^{-5}$). The results of the calculations will also be presented at the Fourth Topical Meeting on Tritium Technology in Fission, Fusion, and Isotopic Applications in Albuquerque, 29.09. - 4.10.1991 [4].

Calculations were performed for a benchmark with normal operation releases. Because a model for calculating doses from effluents during normal operation is still under development, the calculations were carried out using the model of the 'AVV Berechnungsgrundlage 1990' [5]. The evaluation of the results is under the way.

The new model (NORMTRI) for calculating doses from effluents under normal operation is based on the statistical atmospheric dispersion model ISOLA V [6]. It is capable to treat releases of tritium in both forms HT and HTO. HTO re-emission of deposited tritium is considered. Tritium concentrations in the foodstuffs are assumed to be the same as the specific concentrations of tritium in air humidity. A detailed modelling of special effects, such as consumption habits, food processing, feeding of animals in summer/winter, consideration of organically bound tritium, should allow to perform parameter studies and to assess the doses from the ingestion pathways in a more realistic manner.

The program system COSYMA [7] for probabilistic accident consequence assessments has been completed by data sets of dose conversion factors and normalized activity concentrations in foodstuffs for those activation products not included in the nuclide list. Preliminary calculations with 1 hour unit releases of activation products have been performed to generate a ranked list of nuclides contributing most to the effective doses. With similar calculations for effluents during normal operation of one year, the nuclide specific annual effective doses have been assessed.

References:

[1] Raskob, W.; Hasemann, I.: User Guide for UFOTRI: A Program for Assessing the Off-Site Consequences from Accidental Tritium Releases ,Report KfK-4853, Kernforschungszentrum Karlsruhe (1991)

[2] Raskob, W.: Modelling of the Tritium Behaviour in the Environment, in: Proceedings of the '4th Topical Meeting on Tritium Technology in Fission, Fusion, and Isotopic Applications', Albuquerque, 29.9.91 - 4.10.91, (to be published) 1992

[3] Gulden, W.: Dose Calculations for NET Accidental Releases, S+E Subtask SEP2.2, NI/R/0262/2/A, 29 May 1991

[4] Gulden, W.; Raskob, W.: Accidental Tritium Doses Based on Realistic Modelling, in: Proceedings of the '4th Topical Meeting on Tritium Technology in Fission, Fusion, and Isotopic Applications', Albuquerque, 29.9.91 - 4.10.91, (to be published) 1992

[5] Der Bundesminister für Umwelt, Naturschutz und Reaktorsicherheit, Allgemeine Verwaltungsvorschrift zu § 45 StrlSchV: Ermittlung der Strahlenexposition durch die Ableitung radioaktiver Stoffe aus kerntechnischen Anlagen oder Einrichtungen. Bundesanzeiger vom 21.02.1990, Bonn, (1990)

[6] Hübschmann, W. und Raskob, W.: ISOLA V - A FORTRAN 77-Code for the Calculation of the Long-Term Concentration Distribution in the Environment of

Nuclear Installations, Report KfK-4606, Kernforschungszentrum Karlsruhe (1990)

[7] COSYMA: A New Program Package for Accident Consequence Assessments, A Joint Report by KfK and NRPB, Commission of the European Communities, Report EUR-13028 (1991)

Staff:

J. Ehrhardt
I. Hasemann
W. Raskob

SEA 3 Analysis of Reference Accident Sequences

Subtask 2: Analysis of Reference Accident Sequence (RAS) Related to Magnets

Within subtask 3.2 KfK concentrates on RAS-1a (Uncontrolled growing normal conducting zone) and RAS-1b (Low ohm shorts and arcs on a magnet) while ENEA investigates RAS-1c (Loss of isolation vacuum) and RAS-1d (Loss of cooling for the coils). Subtask SEA 3.2 now includes also the remaining activities of former Subtasks SEC 3.1 and 3.2.

a) Analysis of a Growing Normal Conducting Zone with the Codes System MAGS

The system has been applied to analyse an accident where one TF coil is assumed to have a low ohm short and the TF system is dumped via the dump resistors for NET. It turned out that quench occurs at a current of 67kA, about 150% of the operating current. The quench propagation velocity along the conductor is in the order of 50m/s to 80m/s for the initiating pancake. The initiation of a quench in the neighbouring pancake depends on the magnetic field and takes more time than expected. The quench propagation via the Helium manifold could not be demonstrated because the module LINKUP was not available at that time.

The idea that an uncontrolled quench could lead to a break through of the coil for this scenario however seems to be less likely, because for a break a rupture plane in the coil is necessary requiring a much faster quench propagation normal to the conductor than along the conductor. The analysis shows the opposite here.

Another analysis investigating an uncontrolled growing normal conducting zone is under way.

b) Analyses of the Mechanical Behaviour of the PF Coils and of the Central Vault of the TF Coils under Accident Conditions

In these analyses faults of superconducting magnets are investigated which may lead to undesired displacements or loss of integrity of the coil system. Such a failure of magnet components could probably propagate in damaging e.g. surrounding electrical cables or coolent piping initiating further damage.

The events considered are short circuits or erroneous current switching for both toroidal field coils (TF-coils) and poloidal field coils (PF-coils). In continuating the work described in [1] the evaluation concerning the TF-coil faults has been finished [2, 3]. It turned out that a short at the terminal of a TF-coil after a fast discharge is leading to ciritical loads concerning the central vault formed by the wedge shaped inner legs of the TF-coils. According to the two circuit design for the TF-coils of NET two cases have been investigated: discharge of the circuit with the faulty coil (case b1) and discharge of both circuits (case b3). In both cases the asymmetrical load distribution due to the faulty coil produces bending moments and a shear loading at the coil interfaces. Under normal load the symmetrical centering forces of the coils wedge the inner legs together allowing for shear force loading due to friction across the insulated coil-coil interfaces. But under the loading after a discharge according to the above defined cases, due to the bending moment, shear forces and changed hoop forces gaps will open up at the coil interfaces and the mechanical integrity of the vault in the midplane of the machine cannot be maintained.

To give an overall stability of the coil assembly in the present design all coils are joined by insulated shear keys at the flanges at each end of the vault. The question arises, if this additional locking is able to

- introduce overall stability or even to
- maintain local vault stability and, if not, to
- prevent intolerable damage due to excessive displacements of the central vault.

Although in [4] it is concluded that "the shear keys can exert an important restraint on the displacements" and that "the solenoid is well able to support the extra pressure" of moving inner coil legs and that therefore "no damage occurs outside of the magnet system" further investigations seem to be necessary. Especially the type of vault failure will be of interest. If it should be of buckling type, e.g. the impact on the neighbouring structure may not be tolerable.

In order to study such effects theoretically more detailed FEM calculations are under way [5]. But it should be mentioned, that the calculation of the essential nonlinear effects of these problems, the friction, large displacements, the determination of load bearing capacity of rows of screws, are not state of the art and the results may be not very reliable.

To give a possiblility to assess the theoretical results it would be important to perform experimental investigations concerning the TF coil casing integrity under fault conditions including large displacements. A detailed proposal has been given in a "Requirement Definition Document" [6]. Thereby the general testing objectives are the following:

- Will the inner vault, composed of the inner legs of the TF coils, become unstable under fault load conditions? (Due to our investigations [2] this has to be expected.)
- Will the shear keys at the lower and upper ends of the vault allow for overall stability? (Due to our rough estimations [2] this may be doubtful.)
- Is it tolerable that under fault conditions the inner vault is becoming unstable; what is the extent of the plastic deformations and displacements and the resulting loading for the neighbouring structures?

Because of the complicated 3D-geometry, the large displacements of the structure, and the key influence of friction effects only an experiment performed with a coil model can reliably answer these questions. Similar experiments but for a different TF coil assembly (12 TF coils instead of 16) are under way elsewhere [7]. It is proposed to perform NET/ITER related experiments as soon as the NET/ITER design has reached a final or at least a more progressed version. The testing device then may also be used to assess improved design options.

The type of failure behaviour of the central vault has been investigated theoretically, too. In principle, the central vault is a cylinder which, under normal load conditions, is under outer pressure, axial tension and a torque around its axis. This is a typical buckling loading. A study revealed an unstable post buckling behaviour under such loadings. Therefore, even a local loss of mechanical integrity of the central vault may not be tolerable because of sudden large displacements.

So far, in the reference design the TF-coils are connected in two electrical series circuits. If this should be changed in a one circuit design as proposed in [8] case b1 is avoided and only case b3 has to be considered. As this loading is far from buckling loading (after discharge of both circuits only the faulty coil remains loaded), the consequences of a local vault failure may probably be less dangerous.

After the studies concerning the TF-coils similar work has begun for the PF-coils. Due to the amount of different PF coil circuits and the current program during a cycle, the number of possible high mechanical load candidate cases is considerably high compared to the TF coil system. Shorts may occur in each PF coil pair circuit and the time of fault initiation will also play a part concerning the resulting loads. Beyond this at any time faults in the current program may occur due to very different causes. In our investigations first shorts of a single or a pair of PF coils and from the category of erroneous control cases with constant power loading have been considered.

Concerning the mechanical loads the cases of most concern are low ohmic shorts which are initiated before fast transient phases in the current program occur, as the induced currents are proportional to the rate of change of the currents. Therefore the short initiation times have been chosen to be at the start of the cycle ($t = 0$) and at the end of plasma burning (EoB).

Fig. 1 shows as an example of the current transients for a single coil shorted (Fig. 1a) and a pair of coils shorted (Fig. 1b) for the two failure initiation times, respectively. The calculations are done without consideration of possibly reached quench conditions. A first result is that the cases with single coil short give the steeper current ramps and the higher final currents in the shorted coil and its nearest neighbours.

Before the calculation of the loads the transient currents under their corresponding magnetic fields have been checked against the critical quench data of the superconducting strands. It turned out that for the cases with a short in a solenoid coil quench was met with currents between 67 and 103 kA. For these currents the loading of the coils have been determined. One result was that e.g. with a short in the PF1 coils their vertical loads can yield up to 10 - 50 times the normal load. The mechanical consequences of these loadings will be investigated furtheron.

A similar work has been initiated for erroneous control of the power supply. On the search for high mechanical loading the most severe case should occur, if a circuit erroneously rests at full power supply for some period. Then the correspondent coils and its neighbours are ramped to high currents. The calculations performed so far led to current ramps of up to about 5 kA/s. These ramps lead to a subsequent quench in 10 - 20 s, a time which is short compared to the cycle time of 500 s. The loadings will be similar to the cases with a short in a pair of PF-coils.

References:

[1] Nuclear Fusion Project Annual Report of the Association KfK/Euratom, October 1989 - September 1990, KfK 4774 (Sept. 1990).

[2] S. Raff, E. Wehner,
Unpublished Report of KfK (July 1990).

[3] W. Kramer et.al,
Unpublished Report of KfK (August 1991).

[4] J. Raeder et. al,
ITER Safety, ITER Documentation series, No. 36, International Atomic Agency, Vienna, 1991.

[5] C.T.J. Jong,
Stress Analyses of ITER Field Coils under Fault Conditions, 16th Symposium on Fusion Technology (SOFT), London, UK, Sept. 1990.

[6] S. Raff, R. Krieg,
Internal note April 1991.

[7] M. Sugimoto et. al,
Mechanical Test of Superconducting Magnet System for Fusion Experimental Reactor, SOFT, Sept. 3-7, 1990, London.

[8] ITER Magnets, ITER Documentation Series, No. 26, IAEA/ITER/DS/26, IAEA, Vienna (1991).

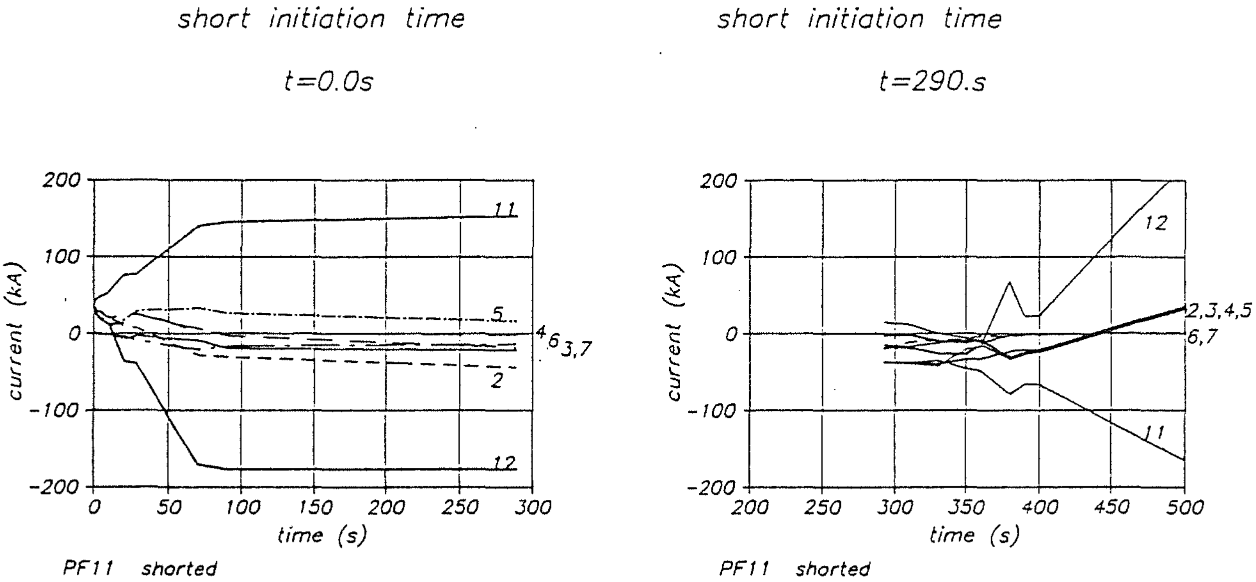

short initiation time

t=0.0s

short initiation time

t=290.s

a) single-coil short

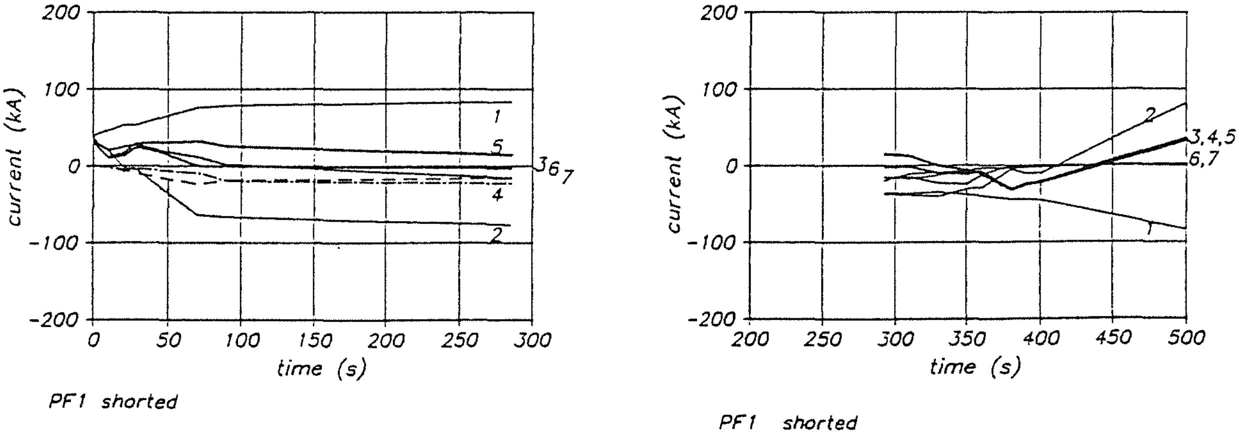

b) pair-of-coil short

Fig. 1: Currents due to a single-coil-short and a pair-of-coil-short assumed at the cycle times t = 0 and t = 290 s

Staff:

G. Bönisch
B. Dolensky
G. Hailfinger
Y.S. Hoang
R. Krieg
R. Meyder
S. Raff
E. Wehner

SEA 5 Assistance in Preparation of the Safety Reports

Subtask 2: Safety Assessment of the NET Magnet Systems

As a contribution to the preliminary safety report for NET a status report on the preliminary safety assessment of the NET magnet systems has been elaborated as of November 1990 [1].

This report includes the characterization of the magnet system, the definition of reference accident sequences grouped into direct failures and induced failures, the assessment of direct failures, a description of induced failures, a review of a first probabilistic safety assessment performed by ENEA, and finally some recommendations for the design.

The characterization of the magnet systems comprises a description of the functions of the magnets, the design boundary conditions and the design data base for the toroidal field coils, the poloidal field coils, the power supply, and the instrumentation and control. The main part of the report deals with the discussion of possible accidental events in superconducting magnets, the definition of reference accident sequences and the assessment of direct failures. The following direct failures are identified and discussed: uncontrolled growing normal conducting zone in a superconducting coil, low Ohm shorts and arcs on a magnet, loss of insulation vacuum, and loss of cooling for the coils. Concerning the uncontrolled growing normal conducting zone a parametric study showed that there is a need to calculate quench propagation phenomena in all three dimensions for the case of failure of the discharge system. From experimental investigations it is concluded that the faults of most concern are shorts, arcing internal to a coil, arcing across the leads, and an arc in the series current connection between coils or their power supply. For the investigation of short and arc events two types of faults were selected, that is a short or arc outside of a coil, and an arc in the series current connection between two coils or between one coil and the power supply. Investigations of the reference accident sequences "Loss of insulation vacuum" and "Loss of cooling" are performed at ENEA.

Concerning the induced failures the following items are identified: Fire, loss of off-site power, earthquake, drop of a heavy load, local external input to a coil, and magnetic field induced missiles. Analyses of these events should await further development of the design and decisions on siting, respectively. However, some preliminary information about these failures are outlined in the following.

Fire

A fire may occur within the cryostat, outside of the cryostat or in the vacuum vessel. In the first case a failure of the cryostat, burnable materials like cable insulation esp. from instrumentation and an igniting temperature, e.g. an arc, are required. The amount of stored energy and the number of conditions show that this event has a low risk. In the second case current and coolant lines as well as dump resistors may loose their function for the magnet system. More detailed design is required to see how such events can proceed. The third case follows from a severe accident in the vacuum vessel, e.g. a graphite fire where local heat loads could occur at the magnets.

The main safety demand for the design of the magnet systems is a safe shut-down and maintaining the magnet systems (and the plant) in a safe condition. Furthermore, it should be ensured, that the likelihood of any release of large energy, radioactive or toxic release remains within prescribed limits during and after any fault condition.

Loss of off-site power

Loss of off-site power is an event which may result mainly as a secondary effect from man-induced hazards like human intervention, or from natural-induced hazards like seismic events or lightning stroke. Initiating events should be considered to occur not only outside but also inside the plant. In case of a loss of off-site power the main safety demands on the plasma and the magnets are first a safe shut-down of the plasma burning process, and second a safe discharge of the PF magnets.

It should be investigated if the stored energy could be used as an energy source to maintain necessary functions of the plant.

Earthquake

To minimize the earthquake loads on the coils the support structures of the magnet system have to be designed against earthquakes. The general aim of protection of the magnet systems against earthquakes is to provide means to safely shutdown the magnets and to maintain them in a safe condition.

For the magnet systems the following items are of special concern:

- The discharge system
- the design of the legs of the TF coils to avoid interactions between the magnets and the vacuum vessel in small gaps

- the design of current leads and coolant lines

The seismicity is strongly dependent on the geographical locations. For example in Europe the earthquake map shows high and medium seismicity in the south and low seismicity in the north. A strong site dependence also exists for the response spectrum of the ground. The procedure of the structural analysis against earthquakes has been incorporated in various national codes and practices.

Drop of a heavy load

A typical heavy load that could drop on the magnet system is a blanket segment while it is exchanged. This can happen only during maintenance when the plant is shut down. The component that will be affected most by such an event is the cryostat. Other sensitive components are the coolant and current lines below the magnets. For a more detailed design it has to be checked which load could cause such an event. However, no release of radioactivity has to be anticipated.

Design measures as redundant cables on cranes or interlocks for the handling units should be used to adequately reduce the failure probability.

Local external heat input to a coil

This accident has its focus on the upper connection box, where the supply lines for the blanket segments run nearby the TF coils. If it is assumed that a loss of coolant accident in the blanket cooling system occurs in this box it will be heated up to coolant temperature. The question is whether the structure can withstand the hydrostatic load of the coolant or whether it fails. In the case of a failure the magnet insulation vacuum is lost. In both cases additional heat loads are exerted on the coils. The heatup ramp for the coils has to be determined and compared with ramps due to other events with similar consequences, like loss of insulation vacuum.

Magnetic field induced missiles

An event which can initiate an accident is a missile of loose parts, such as tools, accelerated by the magnetic field. In the worst case it might be assumed that a missile breaches the cryostat, the loss of vacuum leading to a magnet quench with the consequence of a plasma disruption.

To avoid such a type of missile the presence of loose parts, i.e. tools or components, in the cryostat has to be excluded by engineering and administrative measures during the design, construction and maintenance.

A missile generation as discussed in the literature due to a double rupture of the complete winding of a magnet, is considered to be highly hypothetical.

Compared to the status of the safety assessment described in [1] further analyses have been performed meanwhile in the following areas:

- Uncontrolled growing normal conducting zone

- Low Ohm shorts and arcs

- Loss of insulation vacuum (performed by ENEA)

The results of these investigations are illustrated in [2]. For more details see the contributions under SEA 3.2 and MFAU 1.

References:

[1] W. Kramer, R. Meyder, K.P. Jüngst, H. Kronhardt, unpublished report of KfK, Nov. 1990

[2] W. Kramer et al., unpublished report of KfK, August 1991

Staff:

K.P. Jüngst
W. Kramer
H. Kronhardt
R. Meyder
S. Raff

Long Term Program for Materials Development

Introduction:

KfK's activities in structural materials development have been continued with an emphasis on characterization of the martensitic steel MANET, investigations into the behaviour after irradiation both by thermal reactor neutrons and p+He beams and contributions to the low-activative materials (LAM) programme.

Some highlights from the reports given below are:

Characterization work on the first heat of MANET has essentially been completed. The strength exceeds requirements in all annealing conditions. The ductile-brittle transition temperature in the standard impact test is 27 °C. The second heat of MANET is being distributed to the European Associations (MANET 1)

In isothermal fatigue the influence both of temperature and strain rate on the number of cycles to failure (N_f) is small for MANET. In thermal fatigue N_f-values are smaller when compared to those under LCF conditions at the maximum temperature of thermal cycling (MANET 3.2).

A first set of measurements has been performed on irradiated (5dpa, different irradiation temperatures) subsize V-notch impact specimens. There is a considerable influence both of original heat treatment and irradiation temperature on the ductile-brittle transition curve. The shift in DBTT is comparable to literature data on other ferritic steels (MANET 3.4).

In the LCF experiments before and after dual-beam irradiation a pronounced influence of hold-times was observed. The additional effect of irradiation was rather small (MANET 5).

Data libraries on materials activation were completed accounting for all kinematically possible sequential reactions. Experimental benchmark testing of critical activation cross sections has started (LAM 2.1).

The characterization of the experimental heat of reduced activation alloy CETA has been completed. Mechanical properties from tensile testing are satisfactory whereas fracture toughness, in particular DBTT, is more favourable than for unmodified MANET (LAM 3).

LAM 2.1 Low Activation Fusion Materials Development

Calculations and Measurements of Neutron-Induced Activation in Fusion Reactor Materials

The previous work on improvements of nuclear data libraries and processing codes has been continued. An important shortcoming of hitherto performed activation calculations was the neglection of so-called "sequential (x,n) reactions" (SxRs) which have been shown to produce significant contributions to the total induced radioactivity. Thus appropriate estimates of induced radioactivities, related surface γ-dose rates, decay heats and biological hazards must include all kinematically allowed direct (n,x) reactions, sequential (x,n) reactions and their corresponding reaction chains. For this goal, additional computer code developments and the production of large new data libaries were necessary.

In the reporting period we finalized the production of three new data libraries for the complete treatment of all kinematically possible SxRs on all stable and radioactive nuclides with $T_{1/2} \geq 1$ day in the whole mass range $1 \leq A \leq 209$. The three types of required nuclear and atomic data refered to: (1) Neutron-induced charged particle emission cross sections as a function of both, incident neutron energy and energy of the emitted charged particles. (2) Charged-particle induced neutron emission cross sections. (3) Differential ranges in condensed matter for all light ions produced in first-step neutron-induced reactions. In producing the new libraries, excitation functions for (n,x) reactions were derived from the evaluated European Activation File (EAF-1). For the related normalized charged-particle spectra a new library , KFKSPEC, fully based on calculations with modern nuclear-reaction models was created. This contains now 62.300 spectra with ~1.500.000 data points. The same approach was adopted to produce a starter library, KFKXN, for cross sections of (p,n), (d,n), (α,n), (t,n), (^{3}He,n), (d,2n) and (t,2n) reactions which now contains 4.360 reactions with ~105.000 data points. A complete set of differential charged-particle ranges was generated by using the Ziegler formalism. The corresponding data library, KFKSTOP, includes data for charged particles x=p,d,t, ^{3}He and α stopped in all elements from H to U, which contains now 11.040 data points.

Although existing processing codes, especially the European Reference Code FISPACT, are highly developed, none of them was, a priori, designed for the treatment of SxRs. Therefore, we developed a new algorithm for use with FISPACT, which allows to treat SxRs in addition to (n,x) reactions without changing the inherent code structure. This was possible by introducing so-called "pseudo" cross sections which describe two-step SxRs by one number. "Pseudo" cross sections can then be used together with the "effective" (n,x) cross sections as a unified input to the global inventory code, where all pathways are traced including long chains of (n,x) reactions and SxRs for all possible permutations. Additional activation calculations with the new libraries have been carried out to perform more systematic studies of the effect of SxRs on integral element activations. Including in a first series of calculations only sequential (p,n), (d,n) and (α,n) reactions on all important nuclides of the elements from B to Mo, we found that SxRs are important for ~30% of these elements. In these cases SxRs dominate all or some of the integral radiological quantities in major portions of the cooling time from 10^{-3} to 10^6 years. A new extreme example obtained from our new studies is given in Fig. 1. This figure shows the integral surface γ-dose rate of fluorine versus time after irradiation. The difference of dose rates of the two curves calculated with and without SxRs is a measure of the contribution from the sequential $^{19}F(\alpha,n)^{22}Na$ reaction*). It can be seen that this SxR alters the dose rate by up to 11 orders of magnitude in a large fraction of the time range from10^{-3} to 10^2 years. Additional, comparative calculations for the remaining elements and the other types of SxRs are in progress.

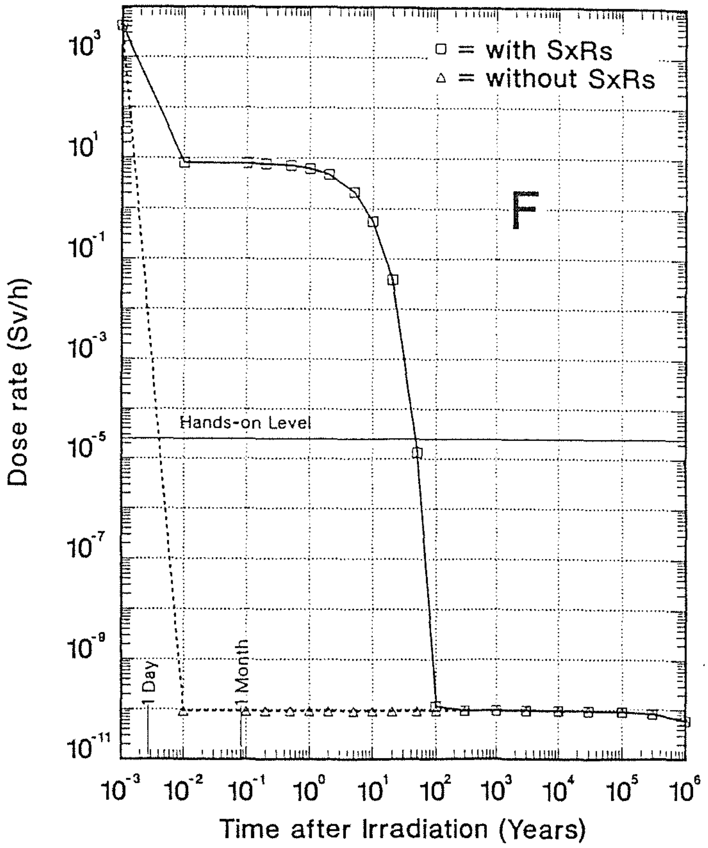

Fig. 1: Calculated dose rate versus cooling time for F. The results refer to neutron irradiation in the first wall of a DEMO fusion reactor. A first-wall 14-MeV neutron load of 12.5 MW yr m-2 was assumed

In addition to code and library developments, experimental benchmark data testing of critical activation cross sections has been started. For this purpose, a new test stand has been installed at the Karlsruhe Isochronous Cyclotron (KIZ). This facility involves a 50-MeV, 15-50 μA continuous deuteron beam bombarding a thick beryllium target. The facility provides a total neutron intensity of up to 4x10^{14} n/s, and a "white" neutron spectrum with an average energy of ~15 MeV. The induced radioactivity is currently measured with a calibrated Ge(Li) detector device, and specific product radionuclides are identified by characteristic γ-lines, γ-ray

---

*)Fluorine is a major constituent of FLIBE which has occasionally been considered as a liquid breeding material

multiplicities and half-lives. First measurements have been performed for a few dominating (n,x) reactions on V and for the important sequential two-step process $^{19}F(n,\alpha)+{}^{19}F(n,y\alpha) \rightarrow {}^{19}F(\alpha,n)^{22}Na$. The final evaluation of the experimental results is underway.

In connection with fusion materials development programs, the IMF has also participated in current international discussions on suitable candidate neutron sources for end-of-life fusion materials testing. Recently , the KfK proposal for a high-intensity 14-MeV cutoff neutron source based on the $^1H(t,n)^3He$ reaction has been selected as one of four candidates for a worldwide Intense Fusion Materials Irradiation Facility (IFMIF) to be further developed by an IEA IFMIF Working Group. In this context, additional work for the calculation of differential flux and spectrum distributions has been performed. Other studies on some additional technical details of the t-H source are in progress.

References:

[1] S. Cierjacks; Low-activation fusion materials development and related nuclear data needs; Invited Paper, IAEA Advisory Group Meeting on the Status and Requirements of Nuclear Data for Radiation Damage and Related Safety Aspects, Vienna, September 19-22, 1989, IAEA-TECDOC-72, p.53, 1990.

[2] S. Cierjacks; Nuclear data needs for low-activation fusion materials development; Fusion Engrg. Des. 13, 229-238 (1990).

[3] S. Cierjacks, K. Ehrlich; Nuclear data for fusion materials research; Invited Paper, Int. Conf. on Nuclear Data for Science and Technology, Jülich, FRG, May 13-17, 1991, Proceedings to be published.

[4] S. Cierjacks, Y. Hino; Status report on KfK work related to the European activation libraries and contemporary activation calculations; in "Low Activation Materials", Proc. of a European Workshop on Low Activation Materials, Sect. II, Contr. 2; Ispra, Italy, October 1-3, 1990, Commission of the European Communities, EUR/XII/457, January 1991.

[5] S. Cierjacks, P. Obložinský, B. Rzehorz; Production of new nuclear data libraries for the treatment of sequential (x,n) reactions in activation calculations, Section 3, Contribution c); in Proc. of an IEA Workshop on Low Activation Materials, Culham, UK, April 7-12, 1991.

[6] S. Cierjacks, P. Obložinský, B. Rzehorz; Nuclear Data Libraries for the Treatment of Sequential (x,n) Reactions in Fusion Materials Activation Calculations; Kernforschungszentrum Karlsruhe Report, KfK-4867, July 1991.

[7] S. Ravndal, P. Obložinský, S.Kelzenberg, S. Cierjacks; User Manual for the KfK Code PCROSS; Kernforschungszentrum Karlsruhe Report, KfK-4873, August 1991.

[8] S. Cierjacks; High-energy neutron production by the $^1H(t,n)^3He$ source reaction; Proc. Int. Fusion Materials Irradiation Facility (IFMIF) Workshop for the International Energy Agency, San Diego, February 14-17, 1989; Ed. R. Verbeek, Commission of the European Communities, Directorate XII, Brussels, Belgium, p.329, 1990.

[9] S. Cierjacks, Y. Hino, M. Drosg; Proposal for a high-intensity 14-MeV cutoff neutron source based on the $^1H(t,n)^3He$ source reaction; Nucl. Sci. Eng. 106, 183-191 (1990).

[10] S. Cierjacks, Y. Hino; Differential flux and spectrum calculations for a novel high-intensity 14-MeV cutoff neutron source based on the $^1H(t,n)^3He$ source reaction; Acta Physica Hungarica 69 (3-4) 283-306 (1991).

[11] S. Cierjacks, Y. Hino; Additional studies related to the proposal for a novel high-intensity 14-MeV cutoff neutron source based on the $^1H(t,n)^3He$ source reaction; Proc. Internat. Panel on 14-MeV Intense Neutron Sources Based on Accelerators for Fusion Materials Study; Eds. A. Miyahara, F.W. Wiffen; Tokyo, Japan, January 14-16, 1991, Nagoya National Institute for Fusion Science Report, NIFS-WS-2, p.147, 1991.

[12] S. Cierjacks, K. Ehrlich, E.T. Cheng, H. Conrads, H. Ullmaier; High-intensity fast neutron sources and neutron fields for fusion technology and fusion materials research; Nucl. Sci. Eng. 106, 99-113 (1990).

[13] S. Cierjacks, Guest Editor; Special Issues of NS&E devoted to high-intensity fast neutron sources and calibrated neutron fields for fusion technology and fusion materials research; October and November 1990 Issues, Nucl. Sci. Eng. 106, Nos. 2 and 3 (1990).

[14] F.H. Cönsgen, G.P. Lawrence, S. Cierjacks; Neutron Sources for Fusion Materials Testing; Invited Paper, Int. Conf. on Nuclear Data for Science and Technology, Jülich, FRG, May 13-17, 1991, Proceedings to be published.

Staff:

S. Cierjacks
P. Obložinský
K. Ehrlich

LAM 3 Development of Low Activation Martensitic Steels

First wall and blanket structures become activated by neutron irradiation, giving rise to problems in maintenance and repair, waste disposal or recycling. To minimize the risks of the activation the high activating alloying elements Nb, Mo and Ni have been omitted in the developmental alloy CETA. In order to maintain the mechanical properties of the steel these elements have been replaced by the low activating elements Ta, W and Ce. The mechanical properties have been investigated in tensile-, creep- and impact tests. Because of its loss at low temperatures the impact toughness is one of the most important mechanical properties of martensitic steels. The impact properties have been investigated in instrumented notch impact bending tests.

Fig. 1 shows the total impact energy in dependency of the test temperature and the thermal treatment. The full martensitic steel without any annealing has a low upper shelf energy and a high DBTT and therefore it is too brittle. After annealing at 600, 700 or 750°C the upper shelf energy increases and the DBTT decreases, the steel becomes tough. There is no considerable difference between 700°C and 750°C treatment.The steel with 600°C-treatment has the same DBTT as the steel MANET I (with 750°C-treatment) The DBTT of the steel CETA with 700 or 750°C-treatment is much lower. The upper shelf energy is sufficient. The J-Integral had been calculated from the energy E_l (P_{max}) up to the maximum load (instead of the unknown crack initiation):

$$\text{J-Int.} = E_l\,(P_{max}) \cdot 2 \,/\, B\,(W-a)$$

where B (W-a) is the fracture area.

The J-Integral depends on the test temperature and the annealing treatment as shown in Fig. 2. The amount of ≈ 1 MJ/m² is sufficient. The bending of the specimens up to the instable brittle fracture and the relative drop of the force during the brittle fracture show that at temperatures above ≈ 20°C there is no brittleness detectable for the steel annealed at 700 or 750°C.

Moreover an important mechanical property is the tensile strength, especially the yield strength at elevated temperatures. Fig. 3 shows the temperature dependency of all mechanical properties evaluable in the tensile test. The ultimate tensile strength and the yield strength of CETA are a little bit lower than of an unmodified martensitic chromium steel type 1.4914, but the total elongation, the uniform elongation and the reduction of area at fracture of CETA are in the same range or higher. The strength is sufficient in each annealing condition, but the total elongation of the 600°-treatment is a little bit too low at 250°C.

References:

[1] K. Anderko et al.; Journ. Nucl. Mater. 179-181 (1991) 492-495.

[2] M. Schirra et al.; European Workshop on Low Activation Materials, Ispra (1990), Brussels XII/457.

Staff:

W. Meyer
L.O. Schäfer
M. Schirra

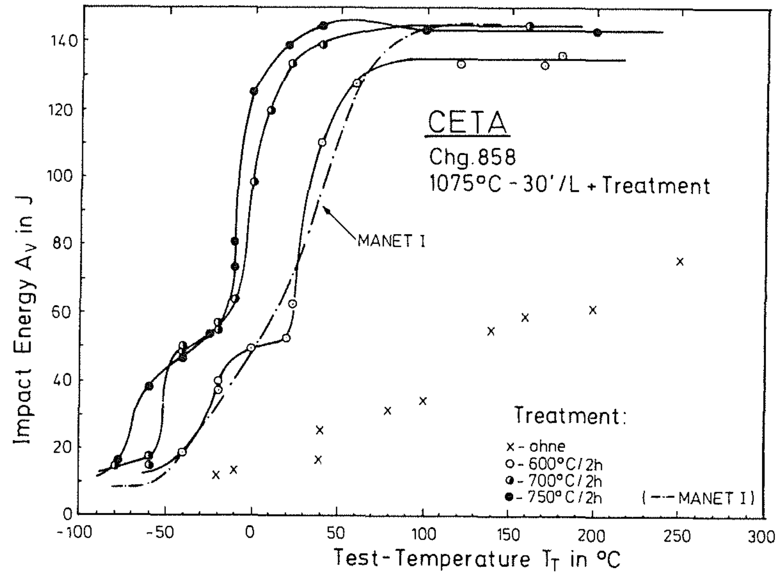

Fig. 1: Total impact energy of the steel CETA in dependency of the test temperature

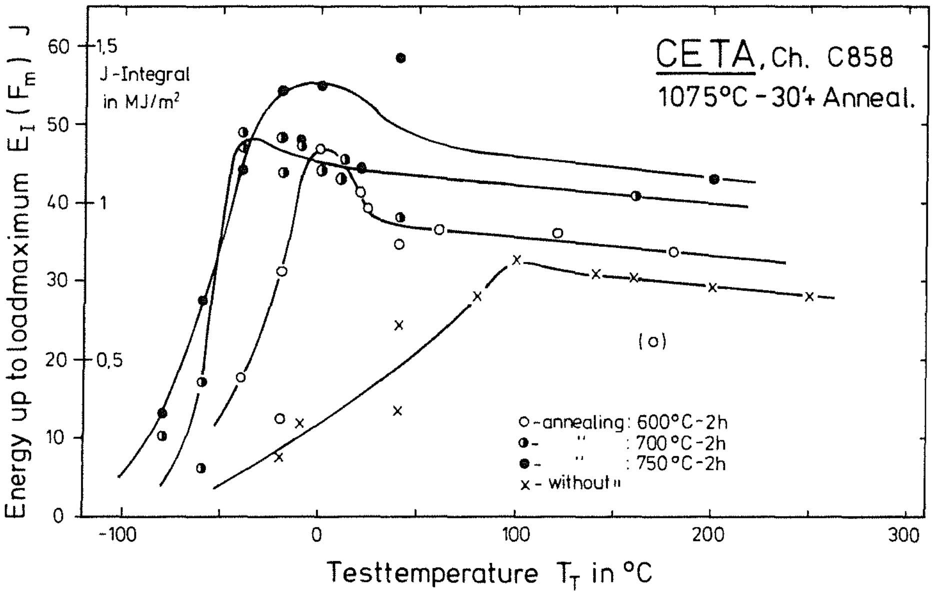

Fig. 2: Energy EI (Fm) and J-Integral of the steel CETA in dependency of the test temperature

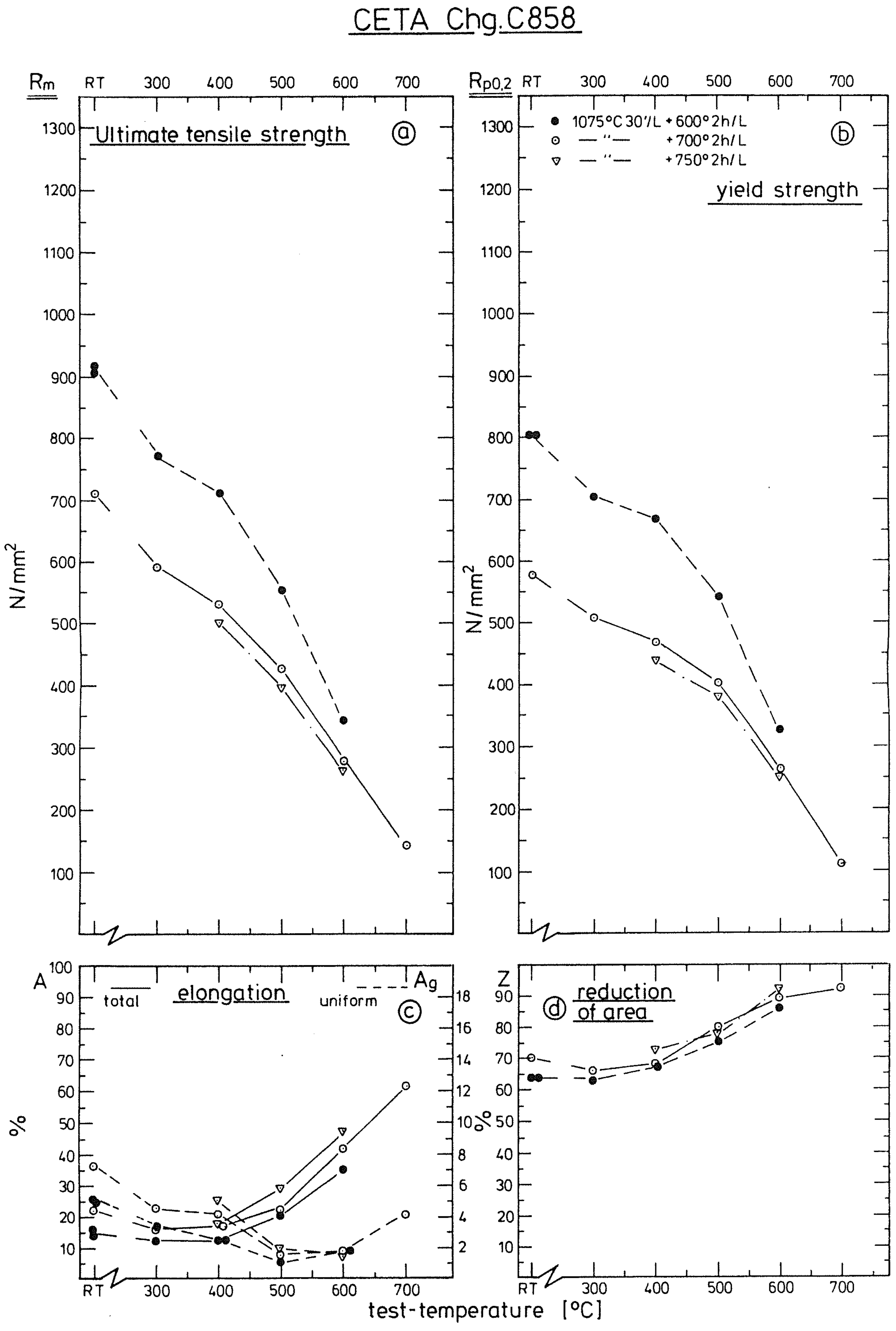

Fig. 3: Tensile properties of the steel CETA in dependency of the test temperature

LAM 5 Development of Low Activation Non-Ferrous Alloys

The metals Chromium and Vanadium reveal the lowest neutron-induced activity if a cooling time of a few years after irradiation is allowed for. [1] Vanadium and its alloys were investigated some years ago concerning the irradiation behaviour and the mechanical properties but not the impact properties.

The impact toughness is a very important property for alloys used as structural material in fusion reactors. Since the toughness of kubic body centered metals is strongly dependent on the temperature, notch impact bending tests with Vanadium and three Vanadium alloys in dependency of the test-temperature have been carried out. The results are shown in Fig.1.

Vanadium exhibits the same upper shelf energy as a martensitic steel, f.i. MANET-I, but the DBTT is about 40 K higher. The Vanadium alloys are more brittle than pure Vanadium, dependent on the amount of other alloying elements, as can be seen in the upper shelf energy. Because of the favourable other mechanical properties [2] the alloy V-3 Ti-1 Si is the best compromise.

References:

[1] S.Cierjacks, Fusion Engineering and Design 13 (1990) 229-238

[2] M. Schirra, KfK-Report 2440 (Jan. 1989)

Staff:

B. Dafferner
L.O. Schäfer

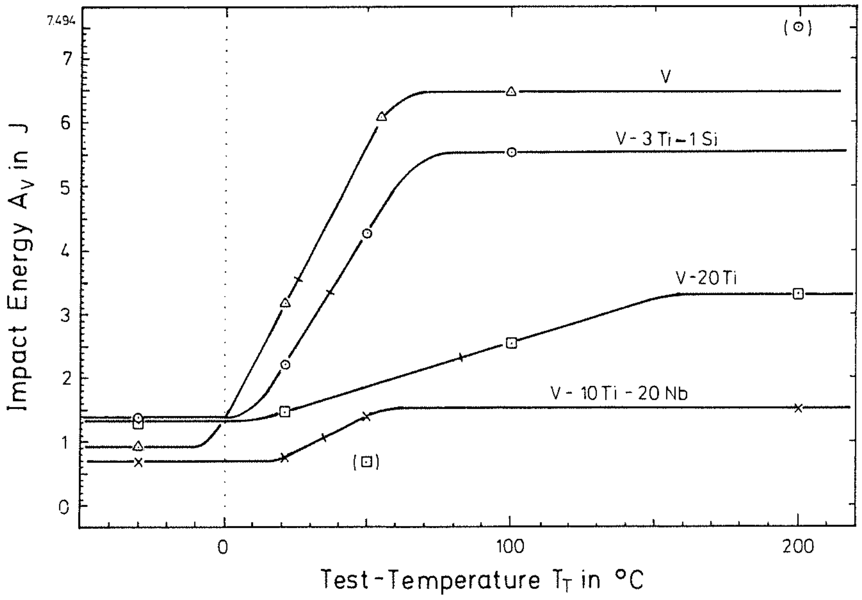

Fig.1: Total impact energy of different Vanadium alloys and pure Vanadium in dependency of the test temperature

MANET 1 Characterization and Optimization of MANET I and II Steels

Because of its loss at low temperatures the impact toughness is one of the most important mechanical properties of the steel MANET-I concerning its qualification as a material for first wall and blanket structures. Impact toughness is being evaluated by instrumented notch impact bending tests. Some characteristics of these tests are shown in fig. 1 in dependence of the test temperature. Part a) of the figure shows the total impact energy A_V. The upper shelf energy is quite sufficient, but the DBTT is relatively too high (+27°C). The J-Integral had been calculated from the energy up to the maximum load E_I (P_{max}) instead of the unknown crack-initation:

$$\text{J-Int.} = 2 \cdot E_I\,(P_{max})/B \cdot (W\text{-}a)$$

where B (W-a) is the fracture cross-section of the specimens. The values of the J-Int. are probably a little bit too high in the upper shelf region, but the amount of 1 MJ/m² and the DBTT ≈ -20°C should be sufficient.

Part b of the Fig. 1 shows the maximum load P_{max} and the fracture toughness K_{Id} calculated from P_{max} instead of the unknown load at the crack initiation:

$$K_{Id} = (P_{max} \cdot S/B \cdot W^{3/2}) \cdot f\,(a/W)$$

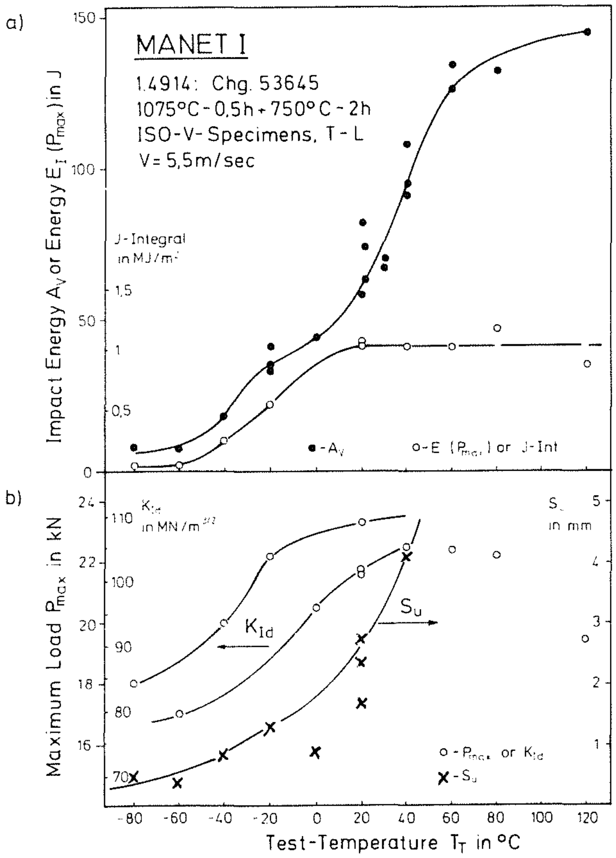

Fig. 1: Some characteristics of impact properties of MANET-I in dependency of test temperature.

where S, B, W, and a are the span, thickness, width and notch depth, respectively. The K_{Id} - values are a little bit too high, but they should be sufficient.

The bending S_u of the specimens up to the instable brittle fracture shows, that at temperatures above 40°C there is no brittleness detectable using impact tests. This finding agrees with the begin of the upper shelf of the total impact energy above 40°C.

The same specimens (B x W x L = 10 x 10 x 55 mm) with a notch depth a = 2 mm, but additional LCF-crack reveal results as given in Fig. 2. All characteristics of precracked specimens are worse compared to the notched-only specimens. Probably the results of the notched-only specimens are not conservative. The K_{Id}-values are not well established. Correct data are evaluated in the KfK-Primärbericht 03.02.02. P 75 B.

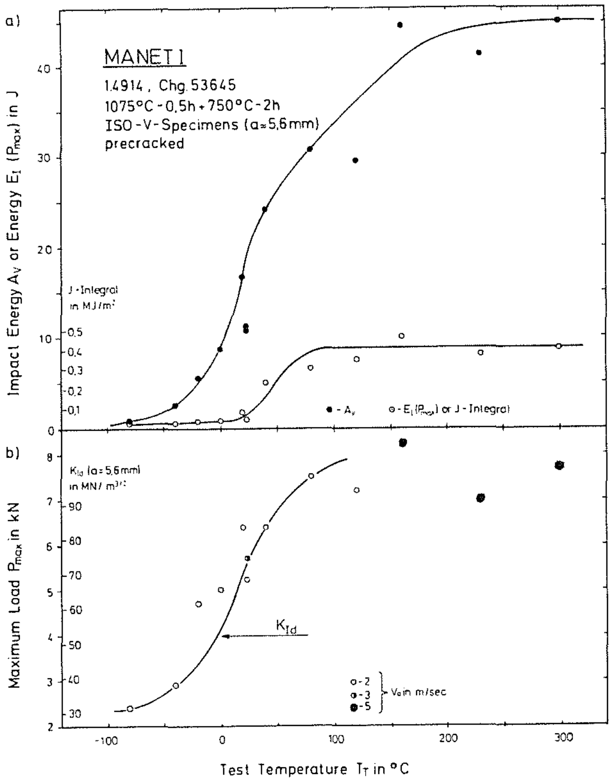

Fig. 2: Impact properties of precracked specimens of MANET-I in dependency of test temperature

The fracture-appearance transition temperature of notched-only specimens is FATT = 26°C. This value agrees very well with the DBTT = 27°C.

An important mechanical property is also the yield strength $R_{p0,2}$ at elevated temperatures. Fig. 3 shows the temperature dependency of all mechanical properties evaluable in a tensile test. The ultimate tensile strength R_m, the yield strength $R_{p0,2}$, the uniform elongation A_g, the total elongation A and the reduction of area Z agree with data of other martensitic chromium steels of type 1.4914. The strength at all temperatures exceeds the demand in all annealing conditions.

References:

[1] Schirra et al., KfK 4561 (1989)

Staff:

W. Meyer
L.O. Schäfer
M. Schirra

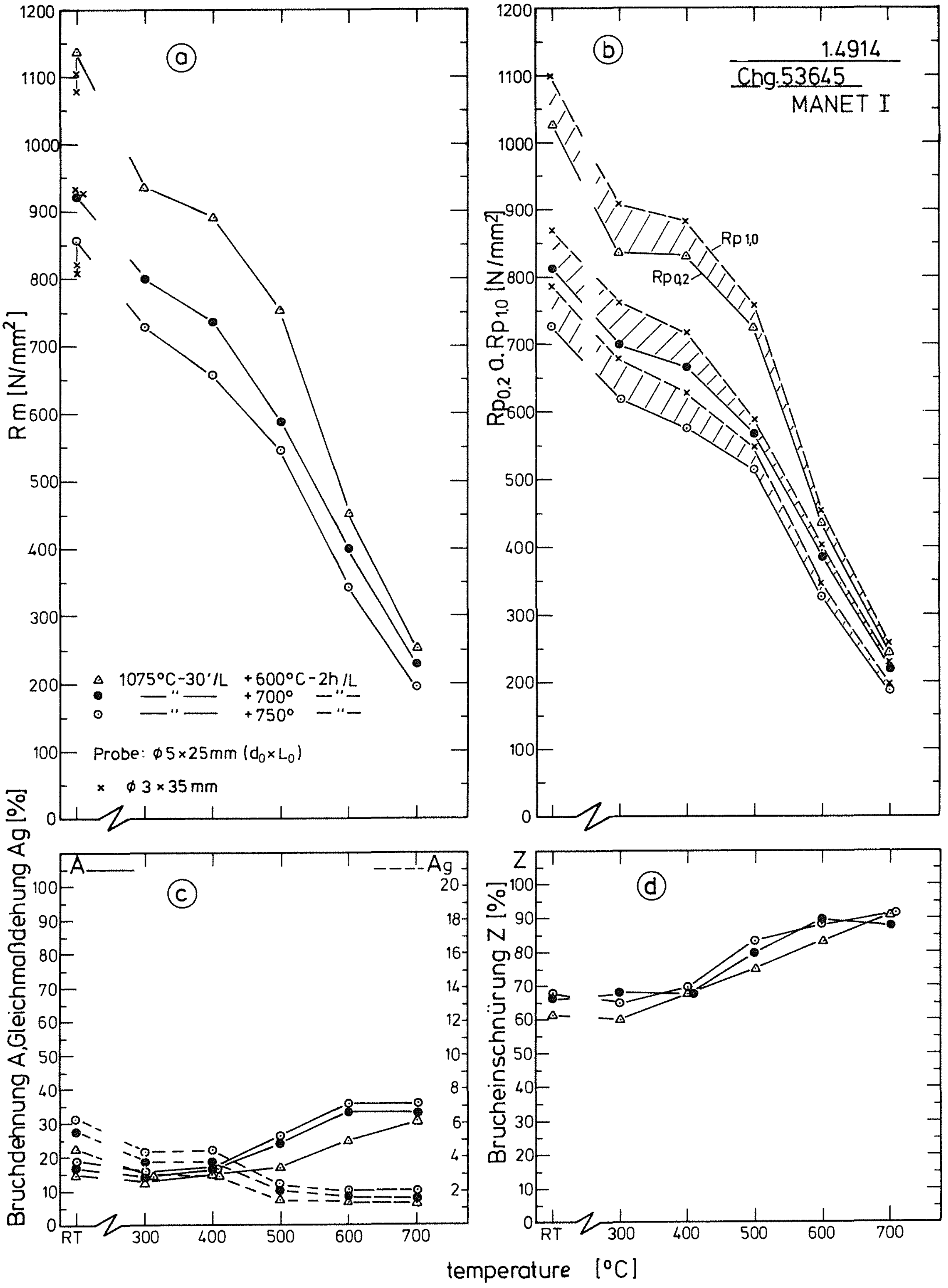

Fig. 3: Tensile properties of MANET-I in dependency of test temperature

MANET 3.2 Pre- and Post-Irradiation Fatigue Properties

Thermal cycling of large components is a serious problem for the designer. The structure considered in the present case is the first wall of a fusion reactor. Its surface, in the actual design concept, will be subjected to radiation heating from the plasma facing side which may lead to severe thermal stresses. Due to the discontinuous operational mode, thermal cycling will generate oscillating temperature gradients. These, depending on the loading conditions, will cause elastic or elasto-plastic reversed deformation, giving rise to thermal fatigue which at present is considered as the most detrimental lifetime phenomenon for the structure considered. The investigations of MANET 3.2 are devoted to this problem.

The studies to be reported within MANET 3.2 are:

- The influence of temperature upon isothermal low-cycle fatigue behaviour of MANET 1 in a temperature range between 250 °C and 650 °C on S-GRIM specimens.
- The influence of strain rate upon isothermal low-cycle fatigue behaviour of MANET 1 at 450 °C on S-Grim specimens.
- The influence of temperature and strain rate upon isothermal low-cycle fatigue behaviour of MANET 1 at 250°C and 550 °C and a strain rate range between $3 \cdot 10^{-3}$/s and $3 \cdot 10^{-5}$/s on H-Grim specimens.
- Thermal fatigue on H-Grim specimens from MANET 1 with a ΔT between 350 and 500 K and comparison with isothermal fatigue data.
- Microstructural examinations of thermally cycled MANET 1 specimens.

1. Isothermal Fatigue of MANET 1

The LCF-Tests on MANET 1 at RT and 650°C with a strain rate of $3 \cdot 10^{-3}$/s had been completed and published in the last annual report [1]. In the meantime the cyclic experiments on S-Grim and H-Grim specimens with $\dot{\varepsilon} = 3 \cdot 10^{-4}$ and $3 \cdot 10^{-5}$/s and strain ranges from 0.3 to 1.5% in the temperature range from RT to 650 °C were also completed.

The Fig. 1 shows the results on S-Grim specimens for a strain rate of $3 \cdot 10^{-4}$/s. Therefrom it is obvious that for larger strain ranges the number of cycles to fracture N_f are not very different for all temperatures. Concerning smaller amplitudes the difference in N_f-values is more pronounced (for instance a factor of 3 between RT and 650 °C at $\Delta\varepsilon_t = 0.6$ %). Experimental values of $\dot{\varepsilon} = 3 \cdot 10^{-3}$/s are nearly identical with data obtained at lower strain rates. Therefore the number of cycles to fracture vs. strain range as function of strain rate for only one temperature (450 °C) is given in Fig. 2. It can be seen that -in contrast to austenitic materials- there is only a slight reduction of N_f-value with decreasing strain rate. This is an indication that for MANET 1 the fatigue damage is the dominant failure mechanism.

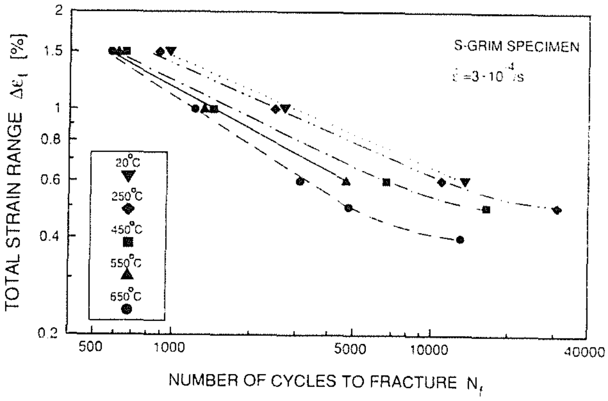

Fig. 1: Number of cycles to fracture vs. strain range as function of temperature for S-Grim specimens of MANET 1

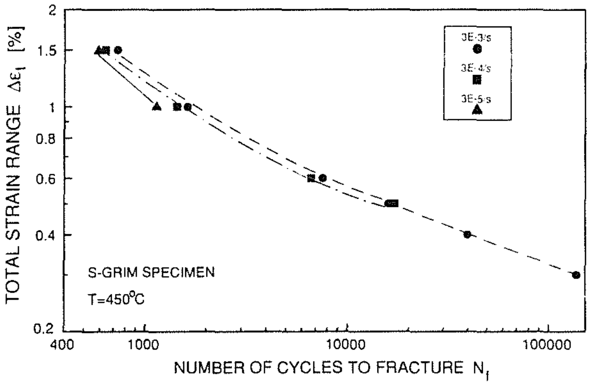

Fig. 2: Number of cycles to fracture vs. strain range as function of strain rate for MANET 1 (S-Grim specimens).

The modest influence of strain rate upon number of cycles to fracture causes very long test times especially at lower strain ranges. This is the reason why at $3 \cdot 10^{-5}$/s only a few results are available. This behaviour described above can be observed at all test temperatures. A detailed report is in preparation which will contain all the results for temperatures in the range of RT up to 650 °C.

In Fig. 3 the results of continuous cycling tests at three different strain rates on H-GRIM specimens can be seen. In order to get a better view the experiments of only two temperatures (250 and 550°C) are given. The report mentioned above will cover the results for the other temperatures. The Figure shows that for 250°C there is nearly no influence of strain rate upon N_f. At the higher temperature (550°C) the number of cycles to fracture decreases for lower $\dot{\varepsilon}$ in particular for $\Delta\varepsilon_t \leq 0.6$

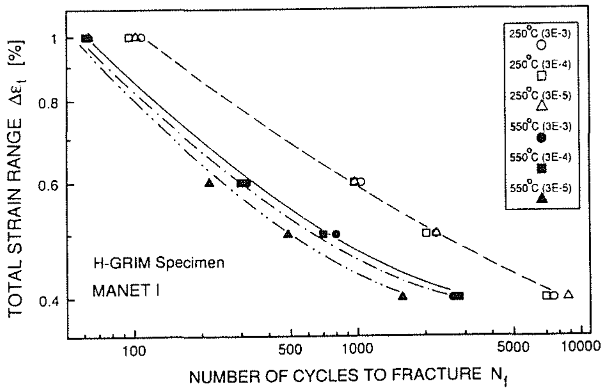

Abb. 3: Number of cycles to fracture vs. strain range as function of strain rate and temperature of H-Grim specimens of MANET-1

2. Thermal fatigue

2.1 Thermal fatigue of MANET 1

The thermal fatigue experiments on H-GRIM specimens with a Δt between 350 and 500 K -but without hold times- are completed. The test conditions had been:

Triangle temperatures cycles with constant heating and cooling rates T= =5.8 K/s in a range of a fixed minimum temperature (200 °C) and a variable maximum temperature (500°C to 700°C). Therefore frequencies range from 0.35 cpm to 0.5 cpm. Due to the fact, that the thermal fatigue testing device is not enabled to control the total mechanical strain range $\Delta\varepsilon_{t,m}$, both the stress range $\Delta\sigma$ and $\Delta\varepsilon_{t,m}$ change with the number of cycles, hence only the measured values during the stabilized hysteresis loop are shown for comparison.

As an example of typical hysteresis loop sequences of MANET 1 those of an experiment conducted between 200 °C and 650 °C are plotted in Fig. 4. After the first quatercycle in tension is reached by cooling down the sample to 200 °C, it responds during heating to 650 °C with a remarkable creep contribution.

The mean strain of the following cycles (ε_m = -0.2%) remains negative until fracture. Otherwise the deformation becomes nearly elastic up to cycle 450. Afterwards plastic deformation increases continously until fracture occurs.

Due to smaller thermal elongation of the ferritic-martensitic MANET 1-steel compared to austenitic AISI 316Ltotal mechanical strain amplitudes between 0.26% and 0.5% are evaluated under the above mentioned thermal conditions. From this data set the total mechanical strain range $\Delta\varepsilon_{t,m}$ is plotted versus N_f in Fig. 5 and compared with isothermal data sets from literature:

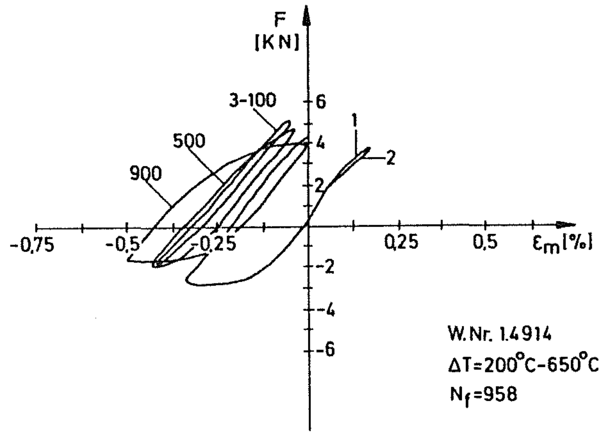

Fig. 4: Typical thermal cycling hysterisis loops for MANET 1 with ΔT = 200-650°C as load F versus mechanical strain ε_m dependency

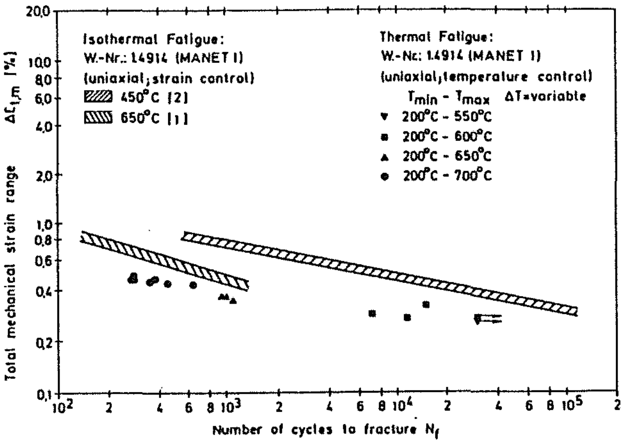

Fig. 5: Comparison of thermal fatigue data to isothermal strain controlled fatigue data of MANET 1 in a $\Delta\varepsilon_{t,m}$ versus N_f-diagram.

1) Strain controlled low cycle fatigue data at 650 °C from (1) and

2) Strain controlled low cycle fatigue data at 450 °C from (2)

The N_f-values at mean temperature of the thermal fatigue data set which range from 375°C to 450°C is found to be over one order of magnitude lower than N_f of isothermal fatigue data. The findings in the comparison at the higher temperature of 650°C were: The number of cycles to failure of thermally cycled samples with T_{max} equal to 650 and 700 °C have been found to be shorter than those of the isothermal data set [3].

Generally from this comparison follows, that thermal fatigue lives at temperatures equal to the mean temperatures of thermal cycling (375 to 450°C) and even shorter than at the maximum temperatures of thermal cycling (e.G. 650°C).

2.2 Microstructural observations

The main crack on all failed samples was situated approximately at the middle of the gauge length. In a posttest examination this crack was analysed by using a scanning electron microscope. Fig. 6 shows a typical fracture surface of MANET 1. It is characterized by striations, but seems to have a cleavage appearance. In general it can be observed that the average direction of the striation markings is perpendicular to the radius of the specimen. Transmission electron microscopy on deformed sections of thermally cycled samples have shown dislocation arrangements that consist of misorientated cell structures. The interior of these cells was generally free of dislocations. This is a typical feature in high temperature deformation (4).

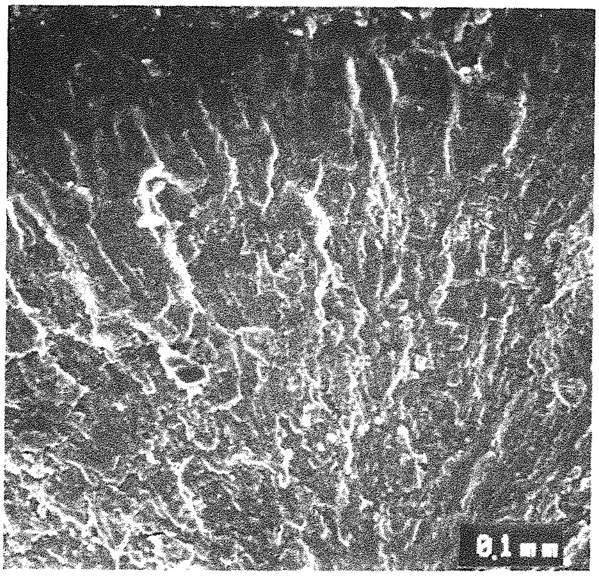

Fig. 6: Fracture surface of a thermally cycled H-Grim specimen of MANET 1 (top: outer surface)

Due to the thermal treatment, the undeformed ferritic-martensitic MANET 1-structure is built up by a lath structure of 0.5 µm width and several micrometer length within the prior austenitic grains. After the thermal fatigue deformation a rearrangement into near equiaxed cells was observed (Fig. 7). The traces of former lath structure are still detectable by linear pattern of $M_{23}C_6$-precipitates.

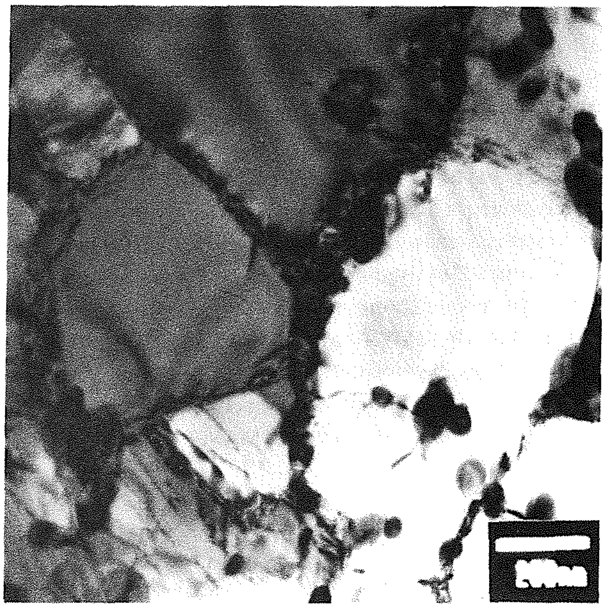

Fig. 7: Cell microstructure of thermally cycled MANET 1

References:

[1] W. Scheibe and R. Schmitt, MAT 1.9: Pre- and Post-Irradiation Fatigue Properties of 1.4914 Martensitic Steel in: Nuclear Fusion Project Semi-annual Report of the Association KfK/EURATOM, KfK 4774 (September 1990)

[2] W. Scheibe and R. Schmitt, MAT 1.9: Pre- and Post-Irradiation Fatigue Properties of 1.4914 Matensitic Steel in: Nuclear Fusion Project Semi-annual Report of the Association KfK/EURATOM, KfK 4677 (November 1989)

[3] C. Petersen, D. Rodrian and H. Schneider: Thermal Fatigue on Steels for the NET-Blanket, Proceedings of 16th MPA-Seminar, Stuttgart, FRG, Oct. 4.-5.1990, to be published in Nuclear Engineering and Design.

[4] C. Petersen and I. Alvarez-Armas: Thermal Fatigue on Steels, Proceedings of 8th Int. Symposium on Creep-Resistand Metallic Materials, Zlin, Czechoslovakia, 17.-19.09.1991

Staff:

W. Baumgärtner
M. Bocek
C. Petersen
D. Rodrian
W. Scheibe
R. Schmitt
H. Schneider
W. Schweiger
(I. Alvarez-Armas)
(A.F. Armas)

MANET 3.4 Pre- and Post-Irradiation Fracture Toughness

The instrumented impact V-notch test developed for a more quantitative study of fracture toughness behaviour of bcc materials has been used to investigate the influence of initial microstructure and the irradiation-induced defect microstructures on the impact properties of MANET-I steel within the SIENA irradiation program. An instrumented and remotely operated V-notch impact testing device using DIN 50115, subsize KLST V-notch impact specimens has been established in the Hot Cells of KfK in order to achieve the maximum of information on impact and dynamic fracture toughness behaviour of irradiated MANET-I steel.

The main investigation aims and aspects are directed to studying the effect of neutron dose and irradiation temperature on the characteristic fracture-mechanical quantities such as the J-integral and the stress intensity factor, KId, as well as the standard engineering quantities such as the ductile-to-brittle temperature (DBTT) and the upper-shelf energy (USE). The results attained so far for unirradiated and irradiated (SIENA) MANET-I steel KLST V-notch subsize specimens are summarized in Figures 1 and 2. The effect of neutron irradiation at 300°C to 5 dpa on the standard impact properties of MANET-I is illustrated in Fig. 1. The following trends emerge from the evolution of the experimental results:

1. The transition temperature being as low as -25°C for the unirradiated material in the reference heat treatment condition has shifted to 245°C when irradiated at 300°C to 5 dpa.
2. The upper-shelf energy (USE) decreases dramatically from 6.1 J for the unirradiated material to 2.2 J for the irradiated one, which yields a ratio of USE irr/USE unirr = 0.36.
3. The slope of the impact energy in the transition regime decreases correspondingly.

The influence of final heat treatment on the impact behaviour of the unirradiated MANET-I steel as well as of the material following irradiation at 300°C to 5 dpa has likewise been investigated. The main final heat treatments studied till now are represented by:

a) material in the reference condition, heat treated for high toughness, 980°C/2h + 1075°C/0.5h + 750°C/2h,

KfK91IMF0306CW/D

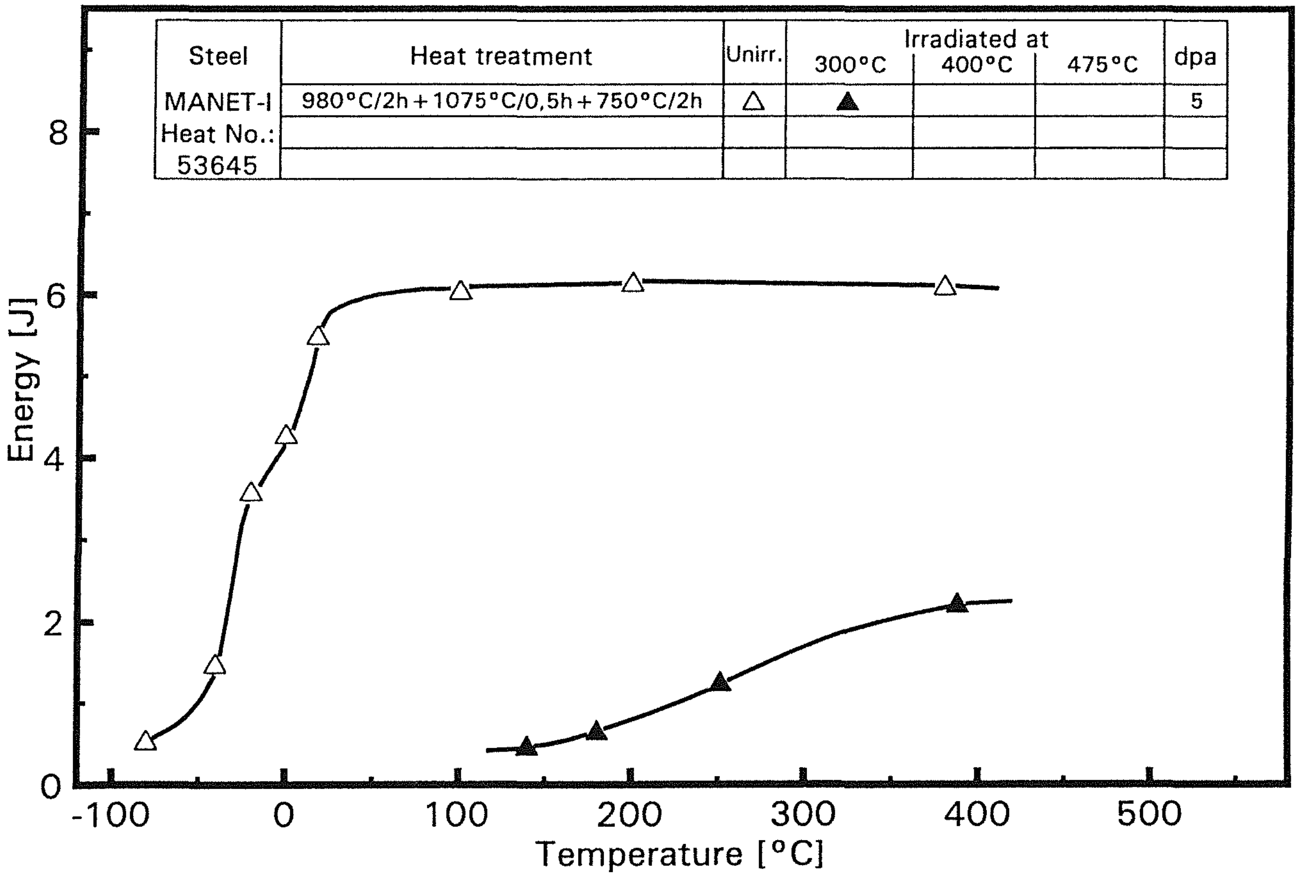

Fig. 1: Effect of irradiation on the impact properties of MANET-I steel

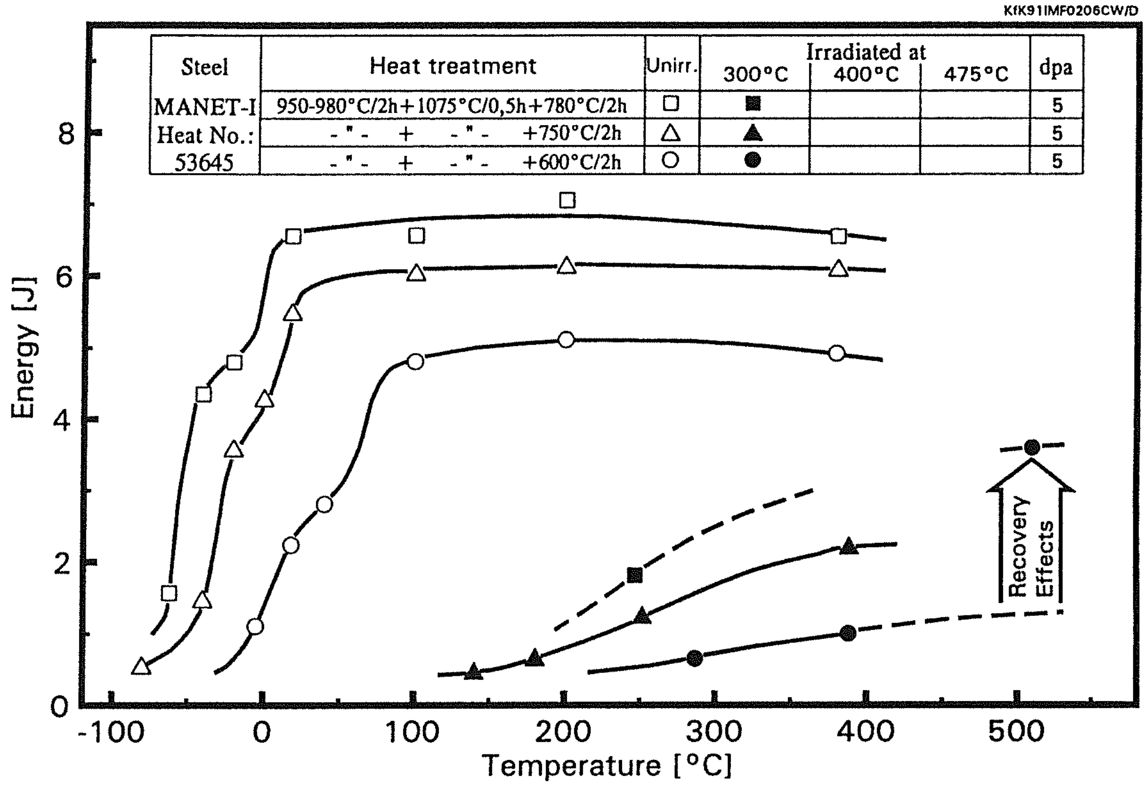

Fig. 2 : Effect of final heat treatment and neutron irradiation on the impact properties of MANET-I steel

b) material, heat treated for high creep strength, 950°C/2h + 1075°C/ 0.5h + 600°C/2h,

c) over-aged material, heat treated for maximum toughness, 950°C/2h + 1075°C/ 0.5h + 780°C/2h.

As illustrated in Fig. 2 the following behaviour emerges from the evolution of the experimental results:

1. The DBTT of the unirradiated material increases with decreasing final heat treatment temperature, e.g., from -45°C for the material heat treated for maximum toughness to 25°C for the material heat treated for high creep strength.

2. The DBTT of the material irradiated at 300°C to 5 dpa increases with decreasing temperature of final heat treatment from approximately 210°C for the material heat treated for maximum toughness, to approximately 310°C for the material heat treated for high creep strength.

3. The irradiation induced shift of the ductile-to-brittle transition temperature, DDBTT, is primarily a complex function of the irradiation conditions and much less dependent on the pre-irradiation final heat treatment.

References:

1. C.Wassilew, M. Rieth, B. Dafferner Verfahren zur Störgrößenkompensation bei instrumentierten Kerbschlagbiegeversuchen, KfK 4796, (Oktober 1990)

2. C. Wassilew et al.: unpublished reoprt of KfK

Staff:

B. Dafferner
A. Kräutter
H. Ries
O. Romer
C. Wassilew

MANET 5 Ion-Beam Irradiation Fatigue and Creep-Fatigue Tests

The Dual Beam Facility of KfK, where alpha-particles (< 104 MeV) and protons (< 40 MeV) are focussed onto a target, was developed as a research tool for materials within the European Fusion Technology Programme. This high energy Dual Beam Technique allows the simulation of fusion neutrons by the systematic variation of hydrogen, helium and damage production in thick metal and ceramic specimens as well as the simulation of Tokamak relevant thermal and mechanical loadings in proposed plasma-facing materials.

1. Development of in-beam-fatigue tests

The effect of irradiation on mechanical properties is studied in the vast majority by means of postirradiation experiments. This means that the irradiation induced microstructure is fully developed before the mechanical test is started. However, realistic fusion conditions with simultaneous irradiation and fatigue loading can lead to an inherently different material response. Therefore, we have focussed the experimental activities on the development of "in-situ" fatigue experiments.

Fully instrumented in-beam low cycle fatigue tests on macroscopic specimens as they are envisaged here are of special complexity, because they combine simultaneously the irradiation technology with the push-pull fatigue testing. Meanwhile the beam lines, the endurance machine, the vacuum chamber as well as various irradiation devices were assembled in the irradiation bunker. Strain controlled fatigue tests at room temperature in vacuum and air have shown that the hollow specimens with their square cross section intended for the in-beam fatigue experiments have fatigue lives very similar to those of massive specimens. The in-beam fatigue set-up is presently tested under various conditions.

2. Postirradiation low cycle fatigue experiments with hold times

In the next generation of fusion devices much longer plasma burn times are strived for. To investigate the effect of holding times in the tensile as well as in the compressive phase, and to emphasize thereby the effect of different He-dose/damage ratios on the low cycle fatigue behaviour, LCF specimens made of the martensitic European reference steel MANET I were irradiated at 450 °C with a fusion typical He-dose/damage ratio of about 10 appm He/dpa, and much higher ones up to 170 appm He/dpa in vacuum at a defect rate of $2x10^{-6}$ dpa/s. The irradiation temperature was controlled by the flow rate of a helium gas stream inside the tubular specimens. After irradiation the specimens were transferred to the Hot Cells and low cycle fatigue tested in air at test temperatures equal to the irradiation temperature. Hold times of 2 minutes were applied at peak tensile strain and peak compressive strain, respectively.

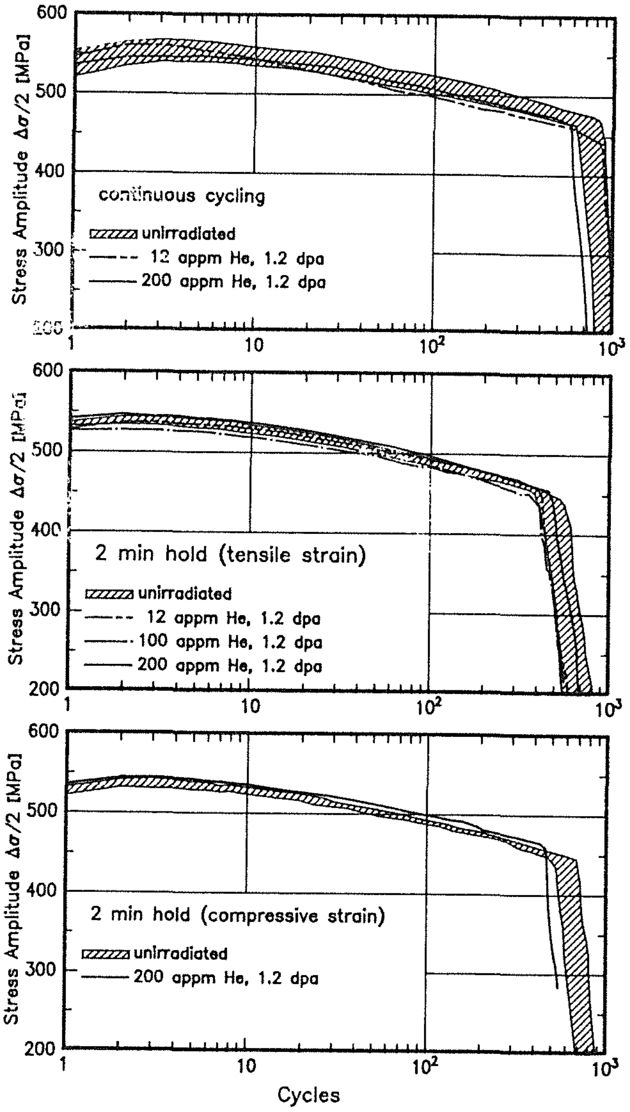

Fig. 1: Fatigue behaivour of the 12 % Cr-steel MANET I (DIN 1.4914). $T_{irr} = T_{test} = 450$ °C, $\Delta\varepsilon_t = 1.2$ %, $\dot{\varepsilon} = 5x10^{-4}$/s.

The results of these strain controlled LCF-experiments are given in Fig. 1. From a comparison of the scatterbands of unirradiated specimens follows, that hold times reduce both the stress amplitude $\Delta\sigma/2$ and the number of cycles to failure N_f at 450 °C. While the $\Delta\sigma/2$ relaxation at $N_f/2$ is only 4 %, hold times of 2 minutes in the compressive phase reduce fatigue life by 18 - 20 % and in the tensile phase by 35 - 40 %. The smaller lifetime reduction in the compressive phase can be explained by the fact, that compressive stresses do not contribute to crack propagation. During the hold times a stress relaxation of 70 - 80 MPa and a small increase of the plastic strains was observed both in compressive and tensile phase. Because plastic strains are closely connected with fatigue life, the observed lifetime reduction in fatigue tests with hold times can be explained at least qualitatively. Although the hold time contributes with 86 % to the fatigue test time, the observed lifetime reduction is small. Consequently, fatigue failure still dominates creep failure in these hold time experiments.

The effect of irradiation on fatigue life with and without hold times is small at 450 °C and nearly independent of He-dose/damage ratio. This was expected in that temperature regime, where a balance between helium bubble induced hardening dominating at temperatures below 400 °C and point defect induced softening prevailing above 500 °C was observed in earlier investigations. Fig. 1 shows, that even 200 appm helium, this is about 2.4 times the integral NET-first wall content, reduce fatigue life by less than 20 % in fatigue experiments with and without hold times. A quantitative analysis of various strengthening contributions in this martensitic 12 % Cr-steel have been performed, and the postirradiation effects as well as the cyclic softening behaviour is well understood.

The SEM-analysis of the fracture surfaces could not establish significant differences between irradiated and unirradiated specimens, even at helium contents of 200 appm. But also between continuously cycled specimens (Fig. 2 a) and specimens cycled with hold times (Fig. 2b) no differences could be observed. In all cases the cracks propagate perpendicular to the applied stress leaving typcial fatigue striations behind. Under all conditions, the rupture mode remained ductile and transcrystalline. Fig. 3 shows a TEM-micrograph of a helium implanted and fatigue tested specimen. During fatigue testing with and without hold times a distinct equiaxial subcell structure has been developed at all irradiation conditions investigated (a). The irradiation induced defects consisting in the vast majority of He-bubbles at 450 °C (b) are stable up to the number of cycles to failure N_f even in fatigue tests with hold times. The rigidity of these bubbles during fatigue testing and their low concentration at lath and cell boundaries may be the reason for the observation that intergranular fracture does not occur or in other words, that fatigue life is only marginally affected by helium implantation.

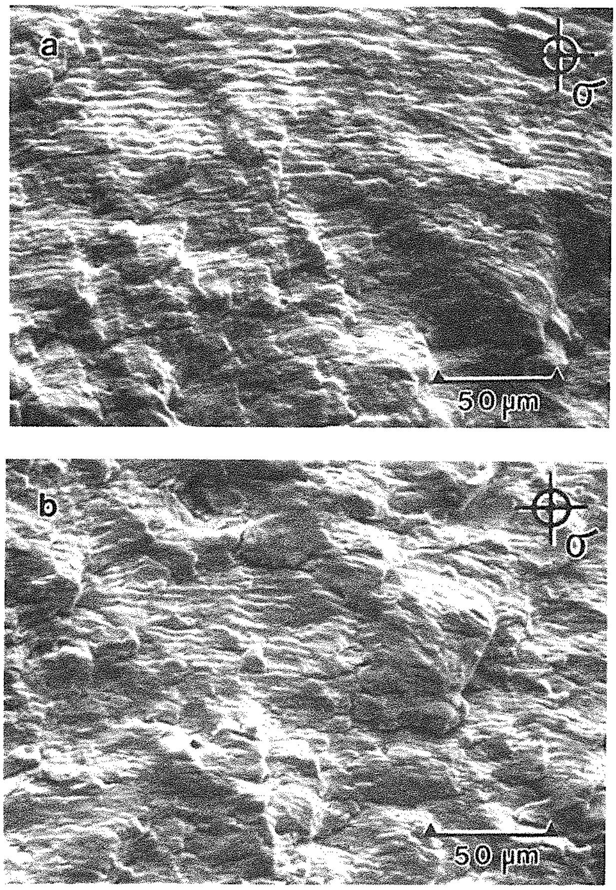

Fig. 2: Fracture surfaces of MANET I, fatigue tested with 2 min hold at peak tensile strains. a) unirradiated, b) irradiated (200 appm He, 1.2 dpa).

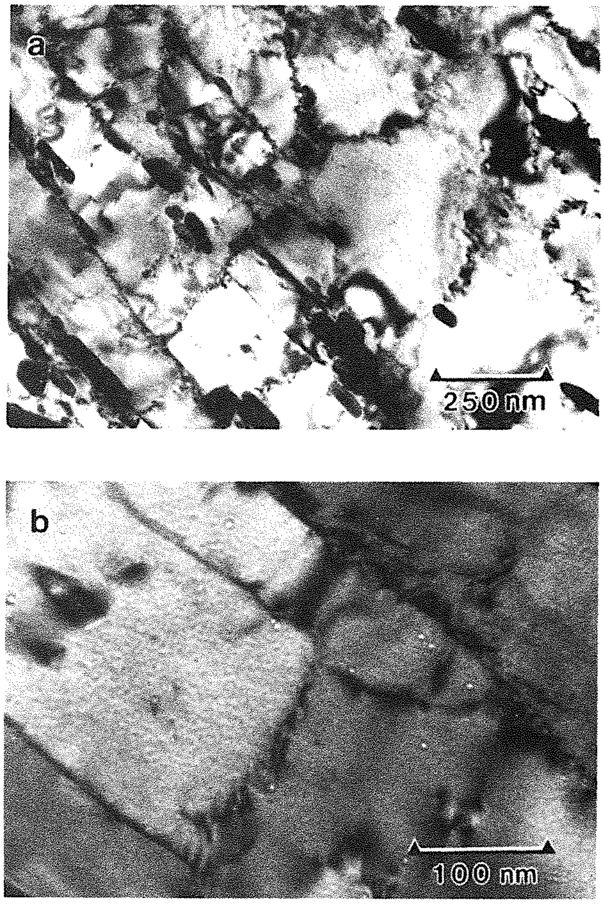

Fig. 3: TEM micrographs of MANET I irradiated (200 appm He, 1.2 dpa) and fatigue tested (2-min hold at peak tensile strain) at 450°C

References:

[1] A. Möslang, D. Preininger and K. Ehrlich; "The Effect of Helium and Damage on Strength of the Martensitic 12 % Cr-steel 1.4914"; All-Union Conference of the Effect of Irradiation on Materials of Fusion Reactors; Leningrad SU; 18-20 Sept. 1990.

[2] D. Preininger; Jahrestagung Kerntechnik 1991; ISSN 0729 9207; p. 589.

[3] R. Lindau und A. Möslang; Jahrestagung Kerntechnik 1991; ibid; p. 585.

[4] R.Lindau und A. Möslang; J. Nucl. Mater. 179-181 (1991) 753.

Staff:

S. Baumgärtner
G. Bürkle
R. Lindau
A. Möslang
D. Preininger
G. Przykutta

Test Blanket Development

Introduction:

Within the European Fusion Technology Program blanket development is divided in work for the NET/ITER basic machine and work for the test blankets. In agreement with the NET-Team and after establishing two European working groups KfK has concentrated its efforts on the development of test blankets for NET/ITER. By test blankets we understand blankets for the next step towards a commercial power station, so called DEMO relevant blankets. In the DEMO-reactor, the potential of a fusion machine to produce electricity shall be tested for the first time. Consequently the test blankets have to be designed for DEMO relevance in terms of breeding rate, temperatures and pressure. Structural materials, maintainability, reliability and safety have to satisfy the more stringent requirements of power production in comparison with driver or shielding blankets for the NET/ITER basic machine. The boundary conditions mentioned above cannot be satisfied full scale and at the same time in the test positions available in NET/ITER. Therefore the definition of test objects and the testing program is one of the main objectives of KfK besides the proof of DEMO relevance of the KfK blanket design alternatives.

The European Test Blanket Development Groups mentioned above deal with two development lines, one with solid breeder helium cooled, the other with liquid metal breeder and either liquid metal (selfcooled) or water cooled blankets. Both KfK developed designs, the selfcooled lithium-lead blanket and the helium cooled, breeder out of tube, canister blanket are accepted alternatives within the European test blanket development program - see BS-DE and BL-DE tasks. A part of the work defined by the partners - KfK, CEA, ENEA and JRC Ispra - consists of common work, relevant to all blanket designs, whereas the design work itself remains independent for the time being. It is foreseen to reduce the number of blanket alternatives to two in 1994/95, one solid breeder and one liquid metal breeder design, which will than be tested in NET/ITER.

The Solid Breeder Blanket Tasks (BS)

Solid breeder design, already mentioned above (DE-D-1), includes besides the design work proper, also small scale thermomechanical and fabricability tests. The KfK solid breeder material program has concentrated, in agreement with the European partners, on lithium orthosilicate. The program tasks include preparation, characterization, irradiation and postirradiation examination as well as measurement of the physical, chemical and mechanical properties. Of special interest are the in and out of pile tritium release studies, performed at KfK and within the common breeder development program in several European reactors. The KfK breeder program is described in tasks BR-D-1 through D-8. The main non nuclear testing facility to prove the feasibility of KfK's solid breeder design will be the helium loop HEBLO, in which elements as well as canister sections may be tested - see NN-D-1.

The Liquid Metal Blanket Tasks (BL)

Design activities (DE-D-1) concentrate on a solution featuring an inboard / outboard blanket without beryllium as a neutron multiplier. The liquid metal breeder blankets are so far the only blanket alternatives, including solid breeder blankets which allow a sufficiently high tritium breeding rate, not using beryllium.

Of great importance to the development of the selfcooled blanket is the knowhow and the data base of magneto-hydrodynamic behaviour of liquid metal flow aquired in theoretical and experimental studies of task MH-D-1. The test facility MEKKA and the cooperation with Argonne National Laboratory play a central role in MHD development.

In addition to design and MHD activities KfK studies the physico-chemical behaviour, task PC-D-1, especially corrosion of structural materials in the lithium lead eutectic (Pb-17Li) and the behaviour of impurities (Polonium) including methods of clean-up. Newly taken up in the development of electrically insulating coatings. Task EX-D-1 describes tritium removal and recovery by permeation and cold trapping. The sodium-potassium loop WAWIK and the Pb-17Li loop TRITEX are the main testbeds for the experimental studies.

The BL CO activities are dedicated to the development of crucial components like the electrically insulating flow channel inserts and ancillary loop components (steam generator, pumps).

BS DE-D 1 Solid Breeder Test Blanket Design

In the reporting period design work concentrated on a DEMO blanket based on the KfK canister blanket concept [1, 2].

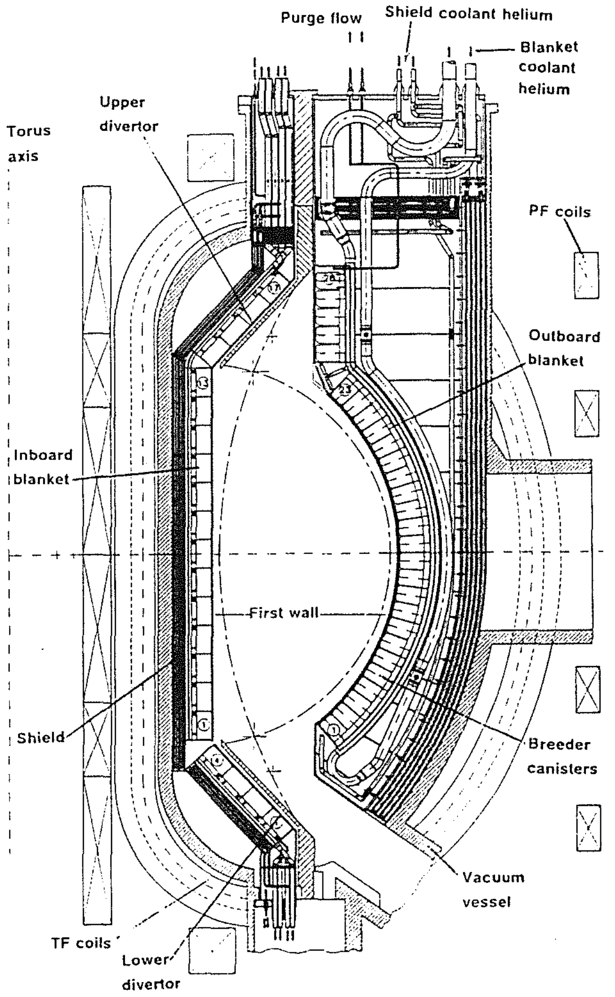

Fig. 1: DEMO-reactor with solid breeder canister blanket vertical cross section

Fig. 1 shows a vertical cross section of the torus with the proposed blanket. As in the case of the outboard blanket design for NET, the canisters are contained in a segment box, however, due to the greater space available in the radial direction, the blankets are thicker and a canister solution is now available for the inboard blanket as well. Blanket canisters are placed also behind the divertors. The coolant tubes for the lower divertor and canisters are coming from below. Due to the small place available at the neck in the upper region of the inboard boxes, the diameter of the coolant helium feeding tubes is relatively small (126 mm o.d.), thus the helium pressure has to be higher than in the outboard blanket (10 MPa against 8 MPa) to keep the pressure drops within reasonable limits. The vacuum vessel and the magnet are protected against an excessive neutron flux by helium cooled steel shields. At the inboard side the shields should contain about 10 % zirconium hydride to reduce the neutron fluence in the vacuum vessel below the allowable limit.

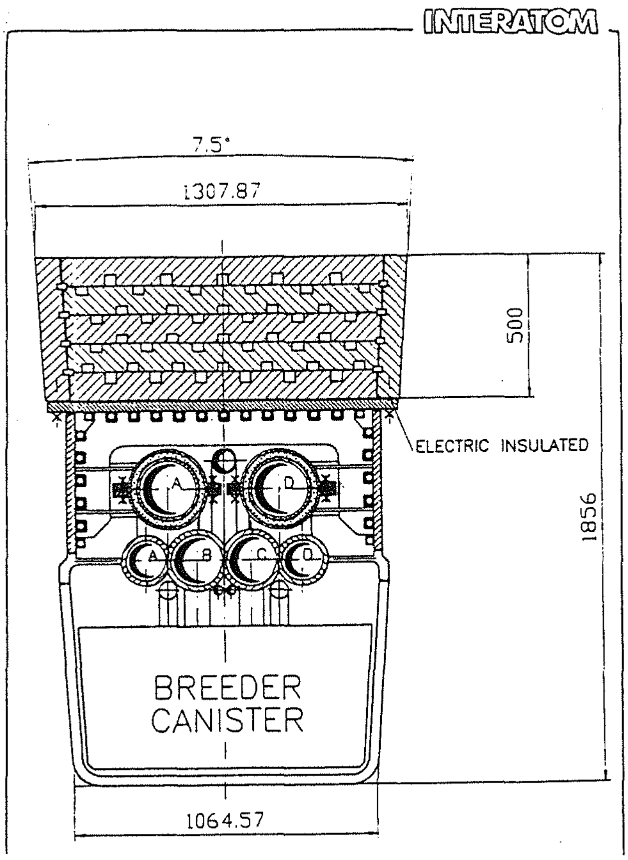

Fig. 2: DEMO outboard blanket segment horizontal cross section

Fig. 2 shows a radial toroidal cross section of a segment of the outboard blanket. It looks similar to the NET design, however, there are some significant differences mainly due to the choice of the structural material. Due to the higher neutron fluence in the DEMO-reactor, the martensitic steel Manet has been chosen rather than austenitic steel like for the NET blanket. This dictates the choice of the coolant helium temperature of 250 °C at the blanket inlet to keep the Manet at temperatures above the DBTT (Ductile-Brittle-Transition-Temperature) level. The reduced difference between outlet and inlet helium temperature, and the better thermal conductivity of Manet allow to have the inlet and outlet helium feeding tubes welded together (Fig. 2). Thus they make the back wall of the box, allowing a considerable simplification at the back of the box in respect of the NET solution. Blanket, coolant supply box, and movable shield form a unit.

Fig. 3 shows a radial-toroidal cross section of a segment of the inboard blanket. The canister is similar to the outboard canister, however the helium coolant coils lie in radial-toroidal planes rather than in radial-poloidal ones like in the outboard blanket.

The segment mainly consists of blanket box, piping and radial shield, all contained in the segment box. A horizontal shield is installed in the upper segment region to protect the TF-coils, the flange region and the piping from neutron radiation (Fig. 1).

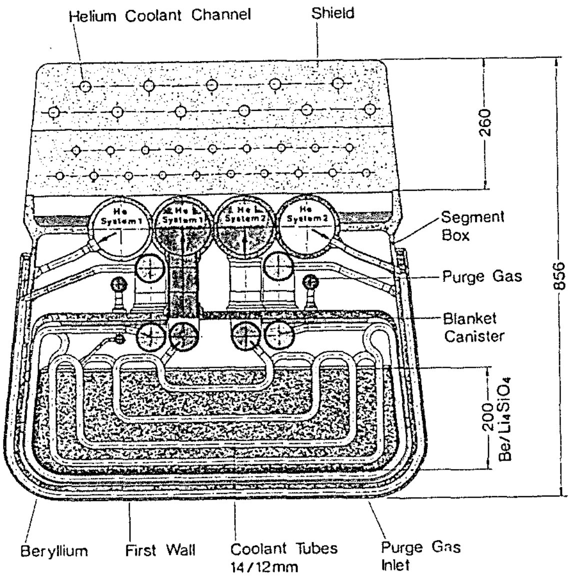

Fig. 3: DEMO inboard blanket segment horizontal cross section

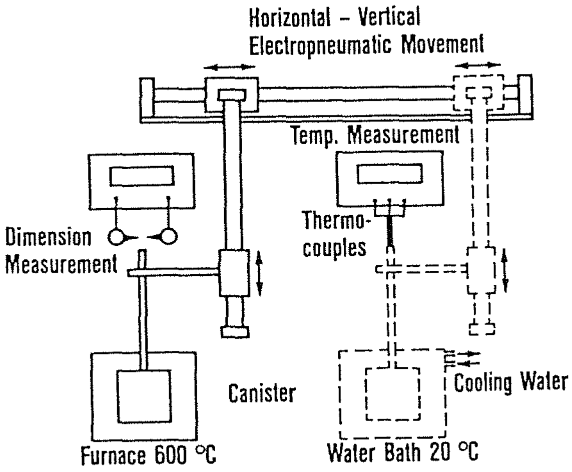

Fig. 4: Apparatus for thermal cycling tests

The radial shield consists of steel blocks with cooling channels which are welded together. The steel blocks should contain 10 ÷ 20 % zirconium hydride pellets to reduce the neutron fluence in the vacuum vessel and in the magnets below allowable limits.

Tests were carried out on the diffusion welding of different kinds of walls which have to be cooled (first wall, canister walls). The work is in progress no results can presently be reported.

New measurements of the effective thermal conductivity of pebble beds and the heat transfer coefficient at the walls of the bed container were performed with an experimental device described in a previous progress report [3]. The effective thermal conductivity data of a bed of Li_4SiO_4 pebbles with diameters in the range of 0.35 - 0.6 cm (DEMO reference) differed little from those of a bed with 0.5 cm diameter Li_4SiO_4 pebbles. So the same correlation can be used. The heat transfer coefficient of the walls increased however, from 0.45 to 0.62 W/cm^2K.

In order to test the thermomechanical behaviour of the Li_4SiO_4 pebbles thermal cycling tests were carried out which simulated the mechanical and thermal stresses that are imposed on the pebble bed in the blanket of NET or DEMO. The pebbles are tightly filled into a flat (6 mm) but very stiff container and the container is heated up to 600 °C (see Fig. 4). Then the container automatically is transferred to and dropped into a water bath of 20 °C.

Thereby the container (≈ 80 °C) is shrinked on to the still hot pebbles (500 °C), thus exerting strong compressive forces on the pebbles. The pebbles from the most recent fabrication [4, 5] behaved well under these tests which greatly exaggerate the real conditions.

References:

[1] M. Dalle Donne et al., "Pebble-bed canister: The Karlsruhe ceramic breeder blanket design for the Next European Torus", Fus. Techn. 14 1357 (1988).

[2] M. Dalle Donne et al., "The Karlsruhe Solid Breeder Blanket and the Test Module to be Irradiated in ITER / NET", Second ISFNT Karlsruhe 2 - 7 June 1991.

[3] Fusion Technology Programme, Semi-annual Report October 1985 - March 1986, KfK 4076 (1986).

[4] G. Schumacher et al., "Lithium-Orthosilicate Spherical Particles with High Density and Mechanical Stability", Proc. 16th Symp. on Fus. Techn. London 1990.

[5] G. Schumacher et al., "Improvement of the Mechanical Stability of Lithium-Orthosilicate Pebbles", Second ISFNT Karlsruhe 2 - 7 June 1991.

Staff:

L. Boccaccini
E. Bojarsky
M. Dalle Donne
H. Deckers
U. Fischer
M. Küchle
P. Norajitra
G. Reimann
H. Reiser
G. Schumacher

BS BR-D-1 Preparation of Ceramic Breeder Materials

The preparation of lithium containing monosilicates, especially Li_4SiO_4, and metazirconates, Li_2ZrO_3, are under development to be used as breeder materials within the European Fusion Program. The development was concentrated on the preparation of a variety of sintered specimen of Li_4SiO_4 with different grain-sizes and different amounts of lithium carbonate, Li_2CO_3, to obtain more informations of the tritium release behaviour under neutron irradiation.

Based on a detailed study concerning the grain-growth of Li_4SiO_4 during sintering, different samples of sintered pebbles were prepared for irradiation tests with small grain-sizes of 10 µm and large grains of about 100 µm. The specimen were irradiated at the KfK-cyclotron in closed capsules and at the SILOE-reactor under purged helium gas (CORELLI 1). As a result, the tritium release increases with decreasing grain-sizes in Li_4SiO_4 and with increasing irradiation temperature. At lower temperatures about 400 oC the influence of the grain-sizes was not significant.

Impurities of lithium carbonate, Li_2CO_3, showed a significant influence on the tritium release behaviour of Li_4SiO_4. Samples of cylindrical shaped pellets were prepared containing different amounts of Li_2CO_3 (pure Li_4SiO_4, 5, 10, 20 wt% Li2CO3, and pure Li_2CO_3) and irradiated at the KfK-cyclotron (ZYK 5). As a result of post-irradiation experiments, the tritium release decreases significantly with increasing carbonate content at lower temperatures and is shifted towards a temperature level of 700 °C.

Table 1: Materials for irradiation test and material property measurement

experiment material	shape of material		remarks
CORELLI 1 Li_4SiO_4	sintered pebbles 0,5 mm Ø	grain-size 10 µm, 100 µm	irradiation test at SILOE-reactor
ZYK 5 Li_4SiO_4	sintered pellets 8x8 mm	pure Li_4SiO_4 5 % Li_2CO_3 10 % Li_2CO_3 20 % Li_2CO_3 pure Li_2CO_3	irradiation test at KfK-cyclotron
INR Li_4SiO_4	sintered pebbles 0,5 mm Ø	1.5 kg	pebble-bed thermal cond.
HEBLO Li_4SiO_4	sintered pebbles 0,5 mm Ø	4.5 kg	canister concept mat. prop.
LONG-TIME TEST Li_4SiO_4	sintered pebbles 0,5 mm Ø molten pebbles 0,5 mm Ø		mat. prop. during long-time annealing
Li_2ZrO_3	sintered pellets 8x8 mm		
$LiAlO_2$	sintered pellets 8x8 mm		

A long-term annealing test has been started with a variety of specimen of Li_4SiO_4, Li_2ZrO_3 and $LiAlO_2$, as pointed-out in **Table 1**, to gain more informations on the long-time behavior of the breeder materials at elevated temperatures. The grain-size distribution and the mechanical strengths of the samples will be analyzed in a sequence of two weeks. A decrease of the mechanical strenghts is expected during the annealing time as a results of grain-growth in the different materials. To obtain similar experience under irradiation European long-time irradiation experiments are projected at the PHENIX-reactor and at HFR-Petten (EXOTIC).

A larger batch of 6 kg sintered pebbles of Li_4SiO_4 were fabricated to measure the thermal conductivity in a larger pebble-bed and to obtain more knowledge on the behaviour of the breeder materials of the Karlsruhe pebble-bed canister concept (HEBLO).

References:

D. Vollath, H. Wedemeyer:
Aluminium Doped Lithium Orthosilicate as Breeder Material, Advances in Ceramics 27 (1990) 3-12.

D. Vollath, H. Wedemeyer, H. Zimmermann, H. Werle:
Doped Lithium Orthosilicate: Preparation and Properties, J. Nucl. Mater. 174 (1990) 86-91.

H. Wedemeyer, E. Günther:
Fabrication of Powders and Sintered Spheres of Lithium Ceramics as Breeder Materials in Nuclear Fusion, The First European East-West Symp. on Materials and Processes, J. Matrials & Product Technology (in press).

H. Wedemeyer, H.-J. Ritzhaupt-Kleissl, E. Günther, H. Werle:
Fabrication of Grain-Size Controlled Lithium Orthosilicate, Proc.- 16th Symp. on Fusion Technology (SOFT 16), Sept. 1990, London, pp. 877-880.

W. Breitung, H. Elbel, H. Wedemeyer, H. Werle:
Tritium Realease from Low- and High-Density Lithium Meta- and Orthosilicate (Irradiation DELICE 2), Proc.- 16th Symp. on Fusion Technology (SOFT 16), Sept. 1990, London, 886-890.

R.-D. Penzhorn, H.R. Ihle, P. Schuster, H. Wedemeyer:
Thermochemical Comparison of Lithium Orthosilicate Pebbles Manufactured by two Different Procedures, Fusion Engineering and Design 12 (1990) 493-494.

Staff:

E. Günther
U. Hain
J. Heger
H. Wedemeyer

BS BR-D-2 Characterization of Ceramic Breeder Materials

This is a continuation of earlier characterization work on ceramic breeder materials. One of the main activities was the characterization of lithium ceramic samples for the ALICE 03 and the CORELLI 1 irradiation experiment. The samples were characterized with regard to phase analysis by x-ray diffraction, density by mercury intrusion porosimetry and helium pycnometry and microstructure by optical and scanning electron microscopy.

For the ALICE 03 experiment, molten and sintered pebbles of lithium orthosilicate and sintered pebbles of lithium metazirconate were characterized. Some amounts of a foreign phase (possibly SiO_2) were observed in the molten pebbles, whereas in the sintered lithium ceramic samples, lithium metasilicate and zirconia, respectively, could be detected, due to lithium losses during sintering. The densities of the molten samples are about 96 %TD and those of the sintered samples 86 % TD. Some cracks, which may be due to thermal stresses during cooling, and some hollow spheres could be observed in the molten material. Grain sizes of 20 and 30 µm for lithium silicate and zirconate, resp., were measured.

In order to examine the relation between tritium release and grain size, the CORELLI 1 experiment was performed using lithium orthosilicate pellets of two different grain sizes. In both samples small traces of lithium metasilicate were detected. Due to different sintering times of the samples, grain sizes of 80 and 10 µm and densities of about 90 and 85 %TD, resp., were obtained. With He-pycnometry no closed porosity was measured.

For the ZYK 5 experiment, samples with different amounts of lithium carbonate were characterized. The densities of the pure materials lithium orthosilicate and lithium carbonate were 84 and 94 %TD, respectively. For the mixed materials with 1, 10 and 20 wt% lithium carbonate, densities of about 90 %TD were measured. Only in the sample containing 1 wt% Li_2CO_3 traces of Li_2SiO_3 could be detected. Consequently, this sample has a closed porosity of about 8 %, due to a partial melting at 1024 oC.

The first samples of a long-term annealing test of lithium ceramic materials are currently being characterized, also with regard to the mechanical strength.

Staff:

R. Hanselmann
R. Knitter
W. Laub
Chr. Odemer

BS BR-D3 Irradiation Testing and Post Irradiation Examination

1. Irradiation Testing

The ELIMA 1 in-pile experiment of 24 specimen capsules containing lithium orthosilicate and lithium metasilicate breeding material irradiated in the fast flux of the KNK II reactor will be terminated after operational delays and an irradiation time of about 120 full power days.

ALICE 3 has been another irradiation experiment performed in the OSIRIS reactor in a collaborative effort with the French and Italian partners. The six KfK specimen capsules have meanwhile been transported to the KfK Hot Cells.

At IMF III an equipment was developed in cooperation with INR and HVT/HZ for measurement of the thermal conductivity at small pebble beds consisting of irradiated breeder ceramic spheres. After cold testing this equipment ill be installed in the Hot Cells.

Staff:

H.E. Häfner
K. Heckert
K. Philipp

2. Post Irradiation Examination

X-ray diffractometry is a most suited method for determination and assay, resp., of the lattice dimensions on crystalline substances. According to that method, the incoming X-ray waves are diffracted on the so-called lattice planes (the atoms in crystals can be combined to lattice planes) of the crystal lattice into discrete orientations in space. The lattice parameters can be calculated with high accuracy from the position of the direction of diffraction. With careful adjustment made, an accuracy of determination of the lattice constants of at least $1 \cdot 10^{-4}$ should be achieved which means that the change in lattice constants should be significantly detectable for values on the order of 1/10 000 of Ångström units and 1/100 picometer units, resp.

A new facility was conceived for these measurements, built with the Seifert company, and set up in the KfK Hot Cells in a shielded gas thight box.

The arrangement of the facility is event from Figures 1 and 2.

The measurement on radioactive specimens with characteristic radiation a shielding cylinder (tungsten alloy) has been provided which can be lowered onto the specimen by means of a hoisting device. Consequently, the radiation emitted by the specimen is absorbed directly at the point of origin. A monochromator attached to the detector side ensures in addition suppression of any kind of scattered radiation because only the diffracted monochromatic X-rays are directed towards the detector.

One of the most important prerequisite of lattice parameter determination with high precision lies in the proper adjustment of the 2θ-angle (tube) and the θ-angle (specimen). In doing so, it must be taken into account that the goniometric measurement is associated with a systematic error induced by dispersion. By differentiation of the Bragg equation the following expression is obtained for that error:

$$\frac{\Delta d}{c} \sim \frac{\Delta \alpha}{\alpha} = -\, cotg \theta \Delta \theta$$

where $\Delta\theta$... is the error in reading the angle values,

and $\Delta\alpha$... is the error of the lattice constant determined.

This means that the errors Δd and Δα, resp., decrease with the diffraction angle increasing. On the other hand, the reflections are less intense in the rear part due to the lower atomic density on lattice planes with the higher indices. Thus, a compromise is found in the range of measurement from 50 deg. to 70 deg.

Assuming an inaccuracy of the angle of 0.005 deg. in this range which is present in our diffractometer, the achievable precision in determination of the lattice constants is 0.005 %. For the lattice constant of the silicon standard of 5.46088 Å this corresponds, e.g., to a standard deviation of ± 0.00025 Å. As a evident from the table below of the measured and tabular values of Si-standards, this accuracy has been almost achieved by us. For the reasons stated above, the first lattice plane (111) has not been taken into account in calculating the mean value.

At present, the following parameters and influences, resp., on the lattice constant are tested on lithium silicate specimens in the cold condition (unirradiated):

a) pulverized (ground pellets),

b) solid (pellets),

c) baked out at 850°C,

d) not baked out.

It is the goal pursued in this series of measurements to be able to exclude the influence of the shape and temperature in later measurements to be made on irradiated specimens.

For these measurements the standard specimen shape was modified such that the pellet and the powder, resp., are held only by a narrow web. This keeps minimum the disturbing scattered radiation. The new shape is evident from Fig. 3.

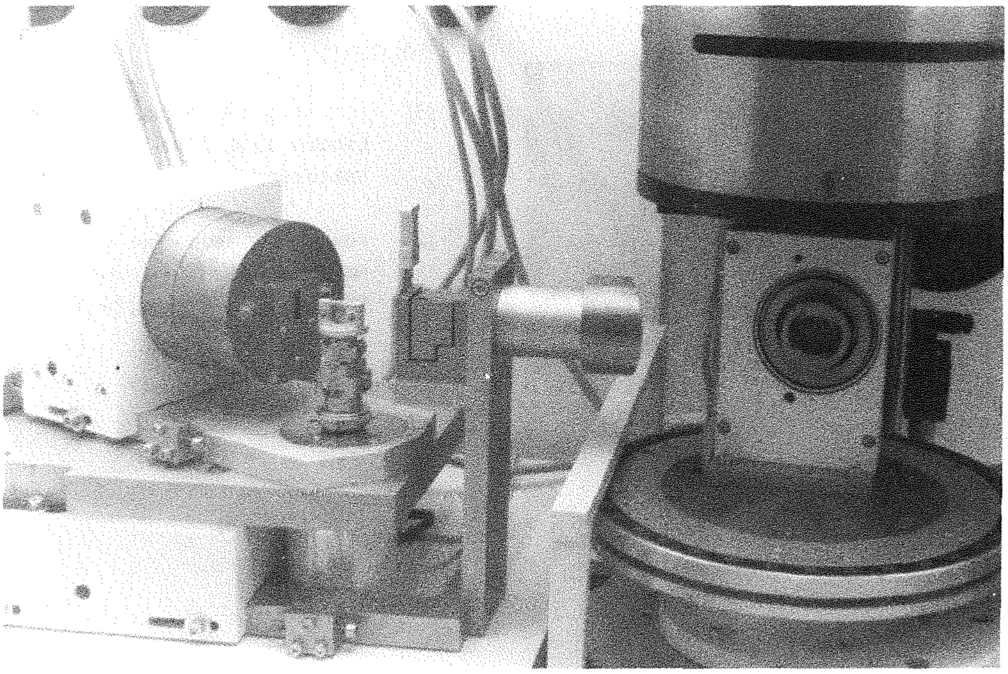

Fig. 1: X-ray diffractometry measuring station in the Hot Cells - view into the interior of the α-tight shielded box.

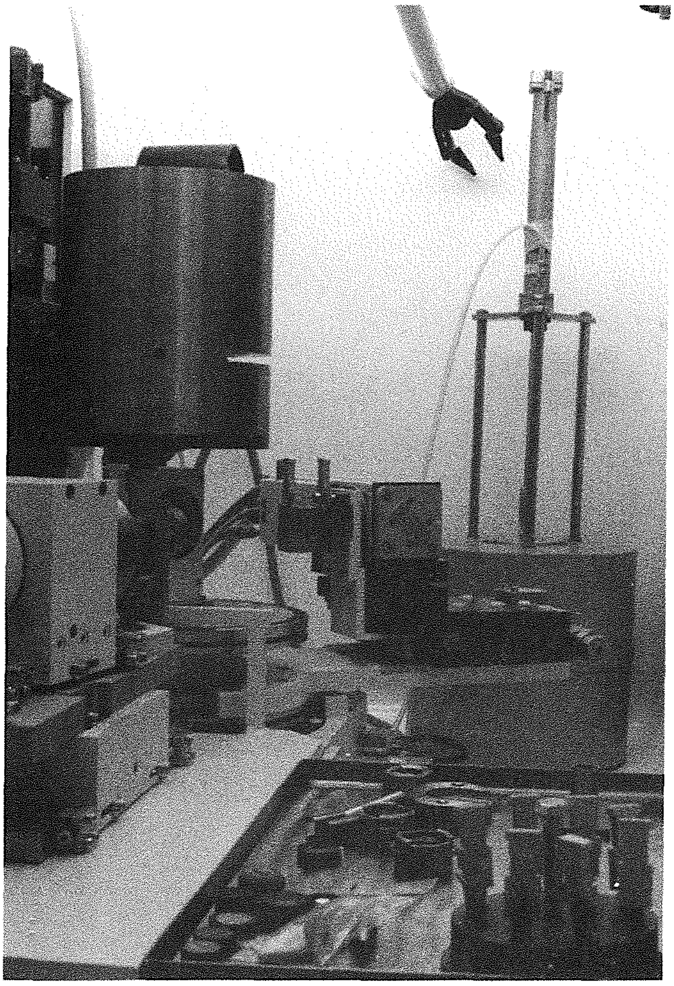

Fig. 2: x-ray diffractometry measuring station in the Hot Cells - view (from the side) into the interior of the α-tight shielded box.

Table 1: Tabular and measured d-values of the Si-standard

	Lattice Planes	ICPS[2] Tabular Data d = (Å)	Hot Cells Measurement d = Å
1.	111	3.1355	3.1330
2.	220	1.9201	1.9199
3.	311	1.6375	1.6374
4.	400	1.3577	1.3579
5.	331	1.2459	1.2459
6.	422	1.1086	1.1087
7.	511	1.0452	1.0452
8.	440	0.9600	0.9600
9.	531	0.9180	0.9180
		mean value (2÷9) a =5.4309 ±0.0002	mean value (2÷9) a =5.4310 ±0.0005

In Table 2 the results of measurement of highly compacted pelletized orthosilicate have been complied and compared with the tabular values [2].

The agreement of the measured values with the tabular values is good. It is further aimed to reproduce the d-values within accuracies of $\pm\ 2\cdot10^{-4}$ Å as achieved for the Si-standard.

A present, the facility does not operate without any troubles. Specimen rotation does not work perfectly and needs readjustment.

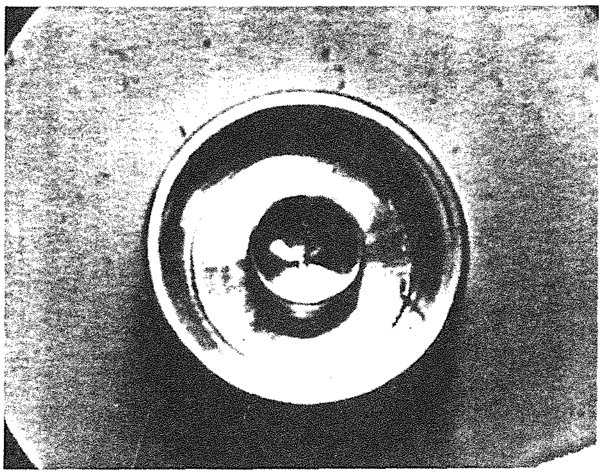

Fig. 3: Specimen shape for the diffractometric measurements on powder or pellets

Table 2: Measured and tabular values [2] of orthosilicate (Li_4SiO_4); highly compacted pellets

hkl	I/I_0	Tabular Values [2] (Å)	Measured Data First Measurement	Measured Data Second Measurement
100	30	5.29	5.27	5.27
001	20	5.15		
-110	100	4.00	4.00	4.000
011	80	3.93	3.93	3.924
-101	10	3.70		
101	45	3.68	3.67	3.671
-111	55	3.16	3.16	3.162
020	16	3.05	3.06	
-120	100	2.645	2.637	2.6401
021	25	2.623		
002	55	2.574	2.570	2.572
-121	30	2.352		
211	10	2.193		
-122	18	1.846	1.8464	
202	10	1.841	1.836	
300	18	1.782	1.787	1.786

Further steps of investigations carried on concern items a, b, c, d for a number of materials. Some of the scheduled measurements have been deferred due to lack of personnel.

References:

[1] H.P. Klug, L.E. Alexander, John Willey and Sons, London 1974: "The precision of determination of lattice constants", in X-ray diffraction procedures

[2] Powder Diffraction File, Card. No. 27-1402 and Card No. 20-637,Joint Committee on Powder Diffraction Standards, Swarthmore, PA (1979).

Staff:

R. Pejsa
W. Kohnert

BS BR-D 4 Tritium Release

In assessing the performance of ceramic breeders, tritium release is an important aspect. KfK concentrates on lithium orthosilicate and metazirconate. Purged inpile tests and out-of-pile annealing tests are performed.

The primary objective of the purged inpile test SIBELIUS, performed April to October 1990 in the SILOE reactor at Grenoble, was to assess the compatibility of ceramic (Li_2O, $LiAlO_2$, Li_4SiO_4, Li_2ZrO_3) /Be/ steel in a neutron environment [1]. PIE compatibility studies will start soon. In addition, the effect of ceramic / Be contact on tritium release was studied. Whereas for LiAlO2 and Li_2ZrO_3 no effect was detected, for Li_4SiO_4 tritium release at low temperatures (460 °C) was slower than in previous tests. It is not clear if this is due to a bad sample quality, irradiation effects or Be contact. Further studies are required.

The CORELLI purged inpile test, again performed in the SILOE at Grenoble, started June 91. Two types of orthosilicate pellets with different grain sizes were tested by KfK. In agreement with annealing results, tritium was observed to be released faster from the small than from the large grains in the first reactor cycle with He+0.1 vol% H_2 purge gas. But, whereas at 600 °C the ratio of residence times is about 10 (which corresponds to the ratio of grain sizes), at 400 °C it is less than two. Because the blanket inventory is essentially determined by the residence time at the minimal blanket temperature (≈ 400 °C), the blanket inventory is expected to decrease by only a factor two if the grain size is reduced from 80 to 7 µ.

In the second joint European medium term purged inpile test EXOTIC-6, performed at the HFR Petten, the currently best (reference) materials of the participating laboratories are tested. The main objectives are to compare the tritium release of the different materials and to study irradiation effects. Preliminary estimations of residence times from the first cycle with He+ 0.1 vol% H_2 [2] agree for the KfK pebbles (Li_4SiO_4 Schott 90/6 tempered, Li_2ZrO_3 Hitec) within about a factor two with TRIDEX results [3].

The TRIDEX series of purged inpile tests are performed in collaboration with KFA Jülich at the FRJ-2 reactor of KFA. Dependance of tritium release on purge gas chemistry has been studied for a variety of orthosilicate and metazirconate samples. Tritium release is remarkably improved by adding H2 to, or by reducing the O_2 partial pressure of the He purge gas (Fig. 1). In addition, reproducibility of tritium release for different charges of pebbles, produced from molten orthosilicate (Schott procedure) was demonstrated [3].

Annealing studies with low- and high-density meta- and orthosilicate of the closed capsule irradiation DELICE 2 have been finished. The main conclusions are [4]:

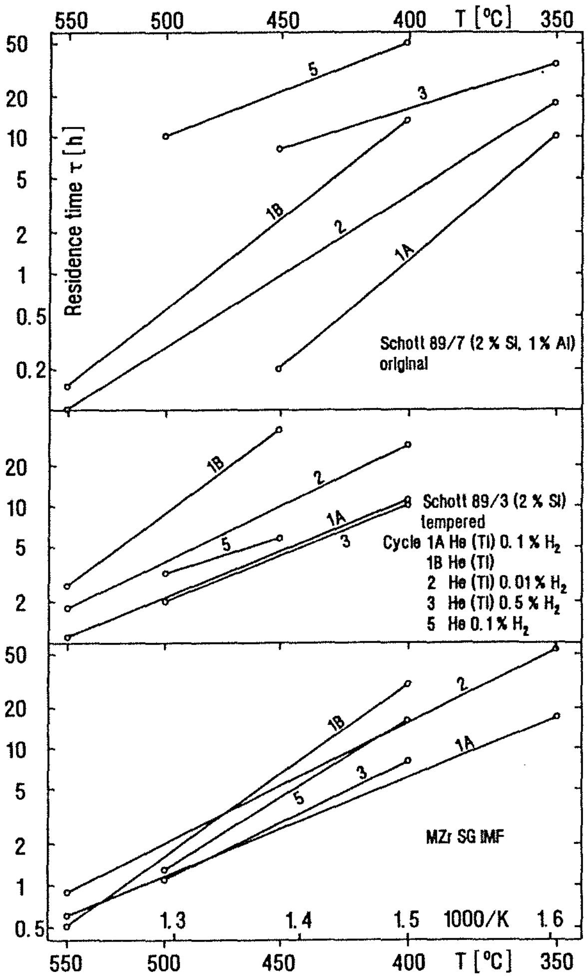

Fig. 1: Residence time as function of temperature for two types of orthosilicate Schott spheres and metazirconate sinter granulate (MZrSG) for different purge gases from TRIDEX tests (He(Ti)): residual O_2 of the high-purity He purge gas reduced by hot Ti)

- Tritium release from orthosilicate is considerably faster than from metasilicate
- Orthosilicate release depends only slightly on sample density and size, but is accelerated by H_2 and H_2O in the purge gas
- Release from orthosilicate is mainly determined by two grain surface processes involving lattice- and contamination (CO_2)-chemisorbed OT. Contamination-chemisorbed OT is strongly bonded and will therefore retard tritium release.

The last conclusion from DELICE 2 was confirmed by annealing studies with samples irradiated at the KfK cyclotron (irradiation Zy5 [5]). Both, tritium and CO_2 release from orthosilicate containing CO_2 impurities (from sample preparation and / or adsorption at air) during heating with 5 °C / min is characterized by a high temperature (≈ 700 °C) peak (Fig. 2).

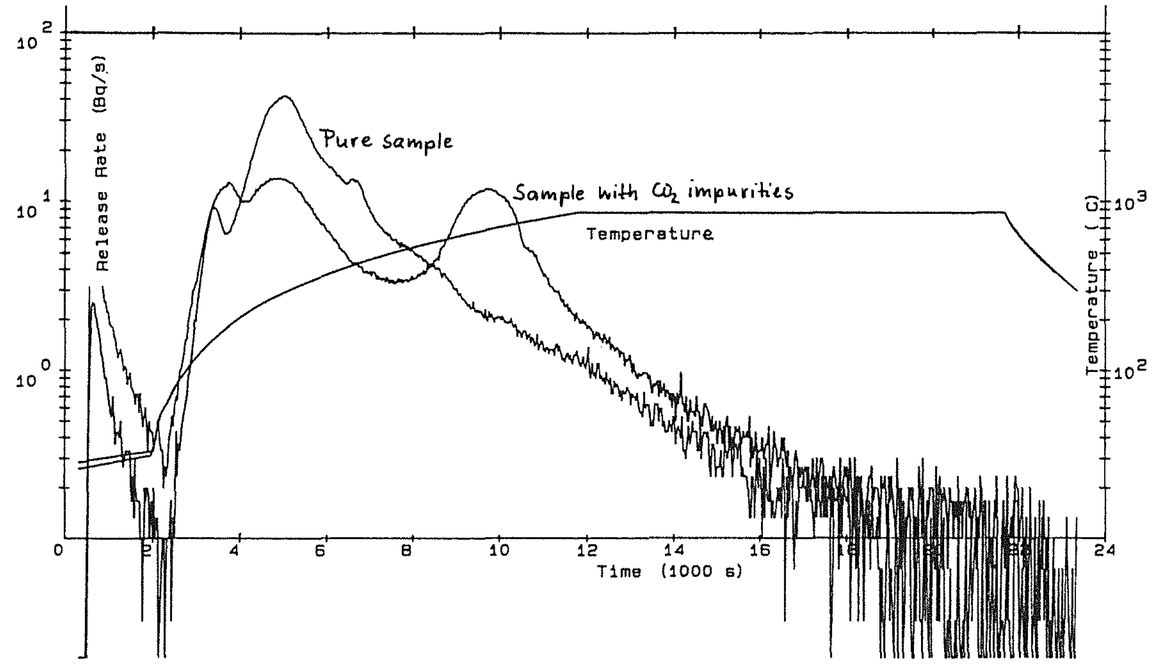

Fig. 2: Influence of CO_2 impurities on tritium release from orthosilicate (samples: DELICE 2, 90 % TD, ramp 5 °C / min, purge gas He+0.1 vol.% H_2)

Annealing studies of the joint European fast / thermal neutrons irradiation COMPLIMENT are nearly finished. Tritium release studies of ceramic, but especially also of Be samples from the purged inpile test SIBELIUS are in preparation.

References:

[1] M. Briec, "The SIBELIUS Experiment", CEN Grenoble, Note Technique DTP / SECC / 90 / 90, Dec. 1990

[2] R. Conrad et al., "Irradiation Progress Report No. 1, Cycle 91.05, EXOTIC-6", Technical Memorandum HFR / 91 / 3242, July 1991

[3] W. Krug et al., "Inpile Tritium Release from Ceramic Breeder Materials in TRIDEX Experiments 1 to 6", Second Int. Symp. on Fusion Nuclear Technology (ISFNT-2), Karlsruhe, June 1991

[4] W. Breitung et al., "Tritium Release from Low- and High-Density Lithium Meta- and Orthosilicate (Irradiation DELICE 2)", 16th SOFT, London, 1990 in: Fusion Technology 1990, Vol. 1, Eds. B.E. Keen, M. Huguet, R. Hemsworth (Elsevier, Amsterdam, 1991) p. 886

[5] W. Breitung, H. Werle and W. Krug, "Tritium Release from Lithium Orthosilicate and Metazirconate: Influence of Purge Gas Additives and Sample Impurities; Order of Release Reaction", Third Specialists' Workshop on Modeling Tritium Behaviour in Ceramic Fusion Blankets, Kernforschungszentrum Karlsruhe, June 10 - 11, 1991

Staff:

W. Breitung
T. Eberle
J. Lebkücher
M. Möschke
H. Werle

BS BR-D-5 Physical and Mechanical Properties

In the following thermophysical properties of Li_4SiO_4 are recommended. The thermophysical behaviour of Li_4SiO_4 has to be seen on the background of the Li_2O-SiO_2 phase diagram **(Fig. 1)** and with respect to the preparation process of the densified material. Temperature and time during densification play a dominant role for the quality and properties of the resulting product. Two kinds of materials were investigated:

I powder chemically precipitated, pressureless sintered for 6 hours at 1200 °C in air, density $\rho = 0.95\ \rho_{th}$

II Li_4SiO_4 spheres from the melt, isostatically hot pressed for 10 min at 1200 °C and annealed in air for 4 - 6 h at 800 °C, $\rho = 0.99\ \rho_{th}$

Characterization

The sintered product investigated by differential thermal analysis (DTA) shows always the eutectic peak of the Li_4SiO_4 - Li_2SiO_3 (Fig. 1) - eutecticum at 1022 °C (Fig. 2), indicating a dissociation of Li_4SiO_4 during sintering. This never occurred with hot pressed samples. Correspondingly the microstructural analysis shows two very different products (Fig. 3). Sintered samples in fact are composites made of two phases Li_2SiO_3 - Li_4SiO_4 (in our samples 13.0 vol.% Li_2SiO_3). The eutectic mainly composed of Li_2SiO_3 forms a matrix, which includes the grains of Li_4SiO_4. This was not observed in the hot pressed samples, but due to high grain size (~ 55 µm) and the lattice anisotropy of Li_4SiO_4 a widening of grain boundaries is always observed. From these results of characterization it is to be expected:

1. The sintered samples must have different thermal expansion coefficients α_{th} and thermal conductivity λ compared to the pure Li_4SiO_4 samples as shown in Fig. 3, below. Furthermore it must valid

$$\alpha_{th}\ (Li_4SiO_4) > \alpha_{th}\ (Li_4SiO_4\ \text{sintered}) > \alpha_{th}\ (Li_2SiO_3)$$

$$\lambda\ (Li_4SiO_4) < \lambda\ (Li_4SiO_4\ \text{sintered}) < \lambda\ (Li_2SiO_3)$$

2. The grain boundary widening of the pure Li_4SiO_4 may influence especially the thermal conductivity, if measurements are carried out in different atmospheres.

Measuring conditions

All samples were preheated in vacuum at 300 °C for 8 - 12 hours to avoid influences of moisture during storage of samples. Property values without hysteresis could be attained by performing the experiments in inert atmosphere (Ar and/or He). For the determination of the thermal conductivity of the pure Li_4SiO_4 a special procedure was applied. After preheating at 300 °C Ar or He was introduced into the equipment and the sample was held for 1 - 2 days under these conditions. After measurement, the gas was removed by pumping for 3 - 4 days at 300 °C. Then the gas was changed from Ar or He to He or Ar and the procedure as described repeated. Under these conditions we could not find an influence of the nature of the gas atmosphere on the thermal

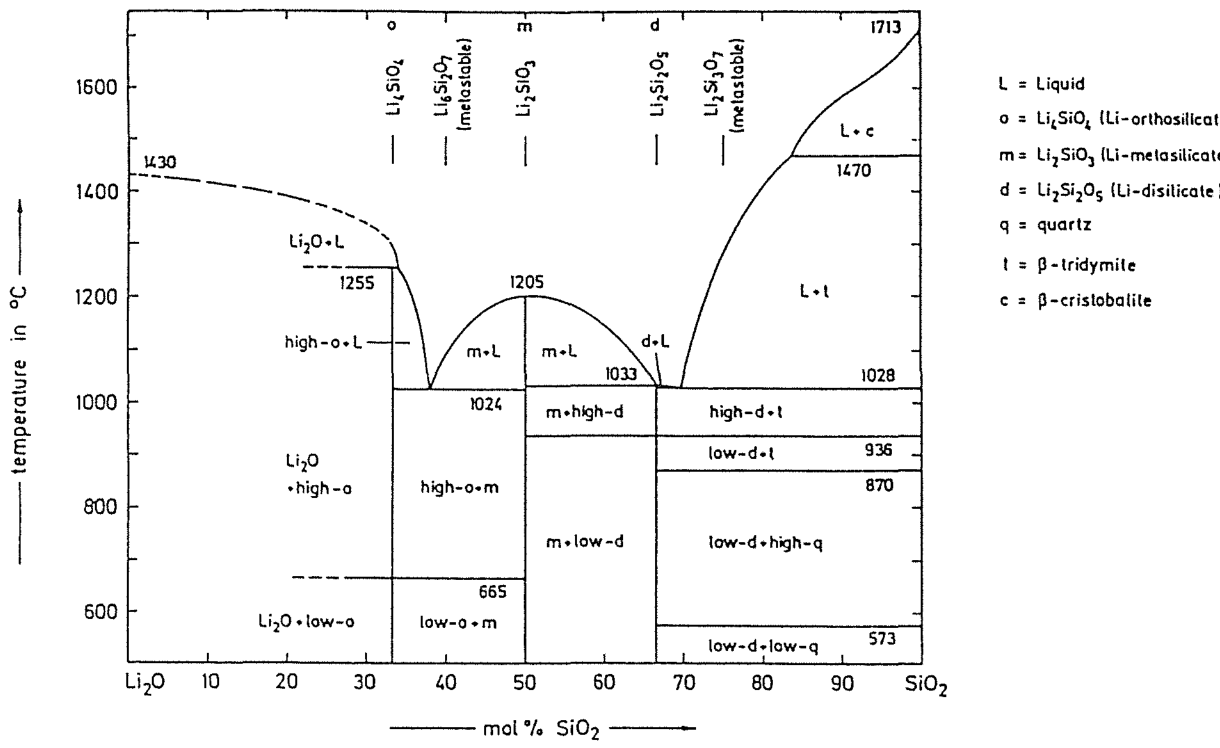

Fig. 1: Li_2O-SiO_2 phase diagram

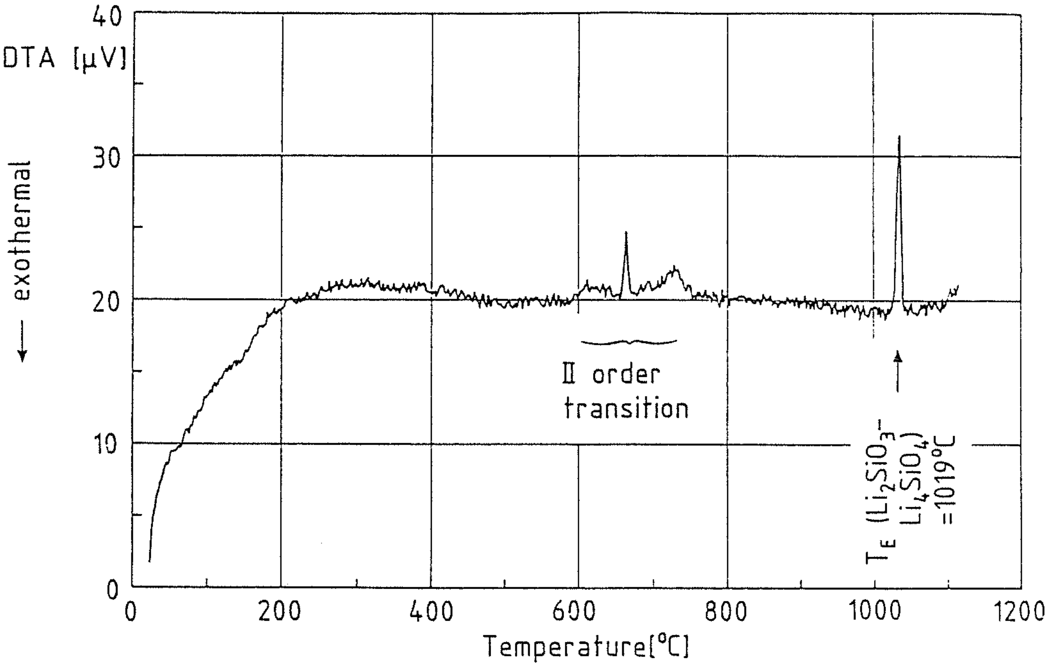

Fig. 2: DTA diagram of sintered Si_4SiO_4

conductivity of the pure Li_4SiO_4, except one sample, the result of which is not shown below.

Specific heat

Specific heat data were measured with a Differential Scanning Calorimeter (DSC2). The results are shown in Fig. 4 and can be expressed as follows [2]:

Li_4SiO_4: $300 < T < 900$ K, $c_p = 0.775 + 16.31 \cdot 10^{-4}\ T + 9000/T^2$, J/g·K

Li_2SiO_3: $300 < T < 1000$ K, $c_p = 1.504 + 2.803 \cdot 10^{-4}\ T - 44700/T^2$, J/g·K

The data should be correct within ± 2 %. They agree with experiments described in [3].

Thermal expansion

Data were evaluated in using differential dilatometry (Sapphire from NBS was the reference material) at isothermal conditions. Results are given in Fig. 5, showing clearly the difference in thermal expansion for sintered and pure Li_4SiO_4. The data for $\Delta l/l_0$ should be correct within ± 3 %.
Pure Li_4SiO_4: $\alpha_{th} = 1/l_0\ dl/dT = +\ 31.2 \cdot 10^{-5}\ K^{-1} \pm 5\ \%$

Thermal conductivity

Measurements were carried out with a laser flash equipment determining the thermal diffusivity

$$a = \frac{\lambda}{c_p \cdot \rho}$$

For conversion to conductivity the given specific heat data (Fig. 4) c_p and the density function according to the thermal expansion (**Fig. 5**) were used.

No porosity correction was performed for the pure Li_4SiO_4 (Fig. 6), while for the sintered Li_4SiO_4 the well known equation

$$\lambda_p = \lambda_0 (1 - P)^{3/2}$$

was applied, P = porosity, Index p, 0 refers to porous and dense material.

As was expected the sintered Li_4SiO_4 shows higher thermal conductivity than the pure material. To check for consistancy the equation

$$1 - c_{Li_4SiO_4} = \frac{\lambda_{Li_4SiO_4} - \lambda_{(Li_4SiO_4 + 13\ vol.\%\ Li_2SiO_3)}}{\lambda_{Li_4SiO_4} - \lambda_{Li_2SiO_3}}$$

$$\cdot \sqrt[3]{\frac{\lambda_{Li_2SiO_3}}{\lambda_{(Li_4SiO_4 + 13\ vol.\%\ Li_2SiO_3)}}}$$

valid for the thermal conductivity of composites with spherical inclusions [4] was applied to calculate the thermal conductivity of pure Li_4SiO_4 in using the data for Li_2SiO_3 and the sintered Li_4SiO_4. The agreement between measured and calculated data for the thermal conductivity is fairly good. The following value is recommended for pure Li_4SiO_4:

$300 < T < 800$ K, $\lambda = (0.014 \pm 0.002)$ W/cmK

References:

[1] F.C. Kracek, J. Phys. Chem. 34 (1930) 2641

[2] R. Brandt, B. Schulz, J. Nucl. Mater. 152 (1988) 178

[3] G.W. Hollenberg, D.E. Baker, Hanford, HEDL-SA-2674FP (1982)

[4] B. Schulz, KfK-Report No. 1988 (1974)

Staff:

G. Haase
B. Schulz

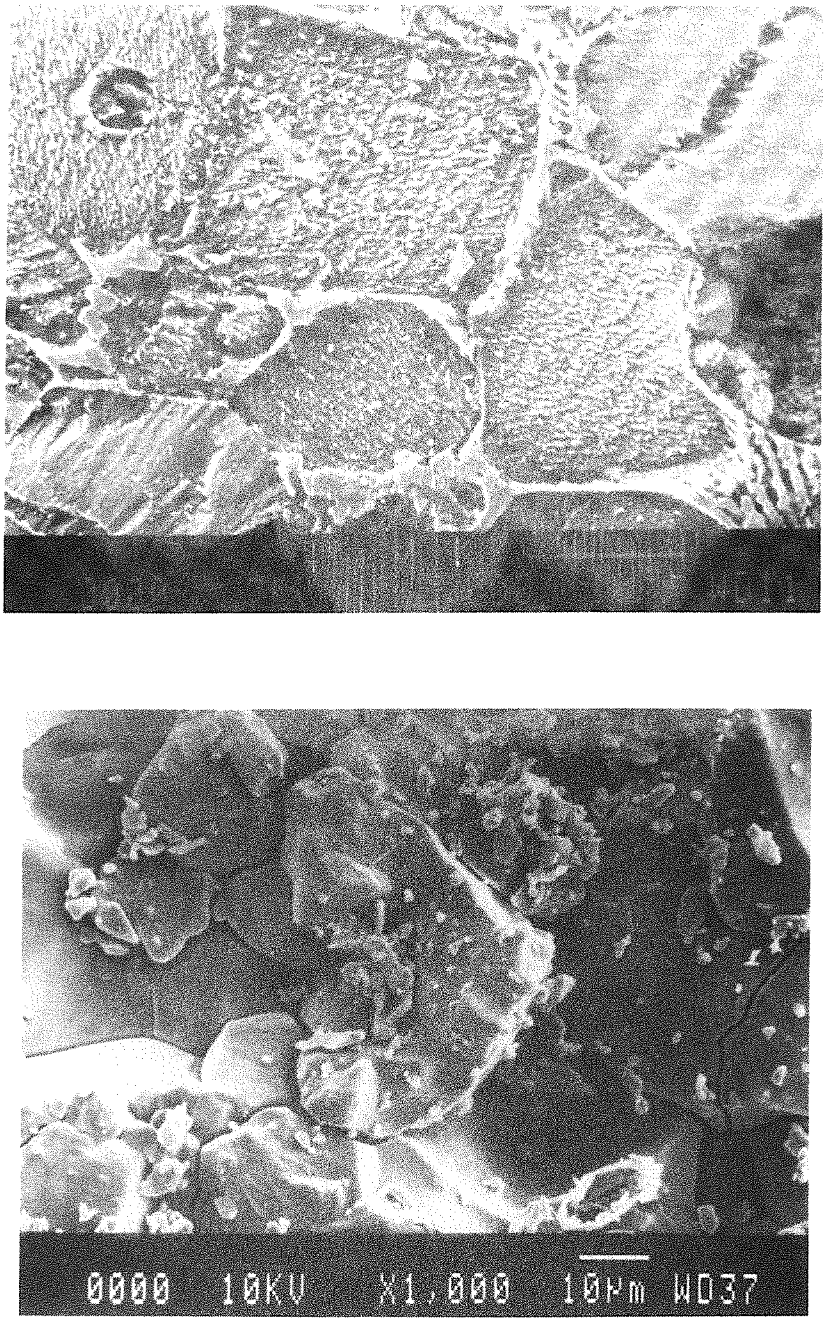

Fig. 3: Microstructure of sintered (above) and hotpressed Li_4SiO_4 (below)

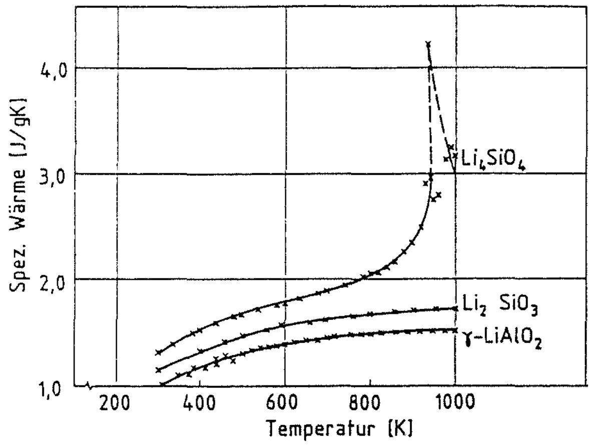

Fig. 4: Specific heat of ceramic breeder materials

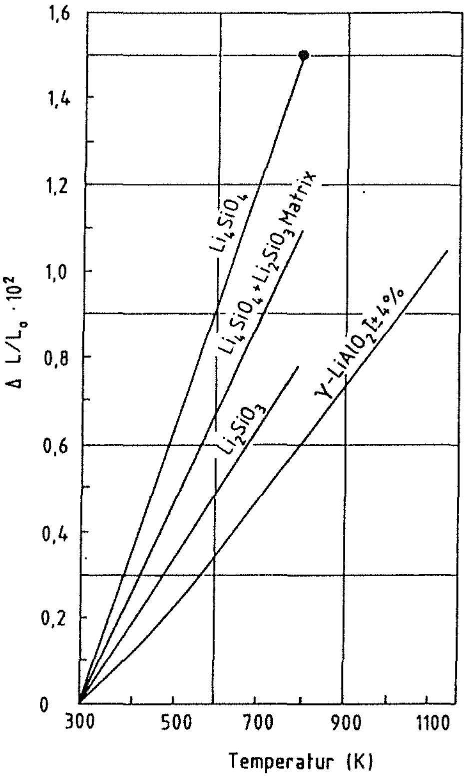

Fig. 5: Thermal expansion of ceramic breeder materials

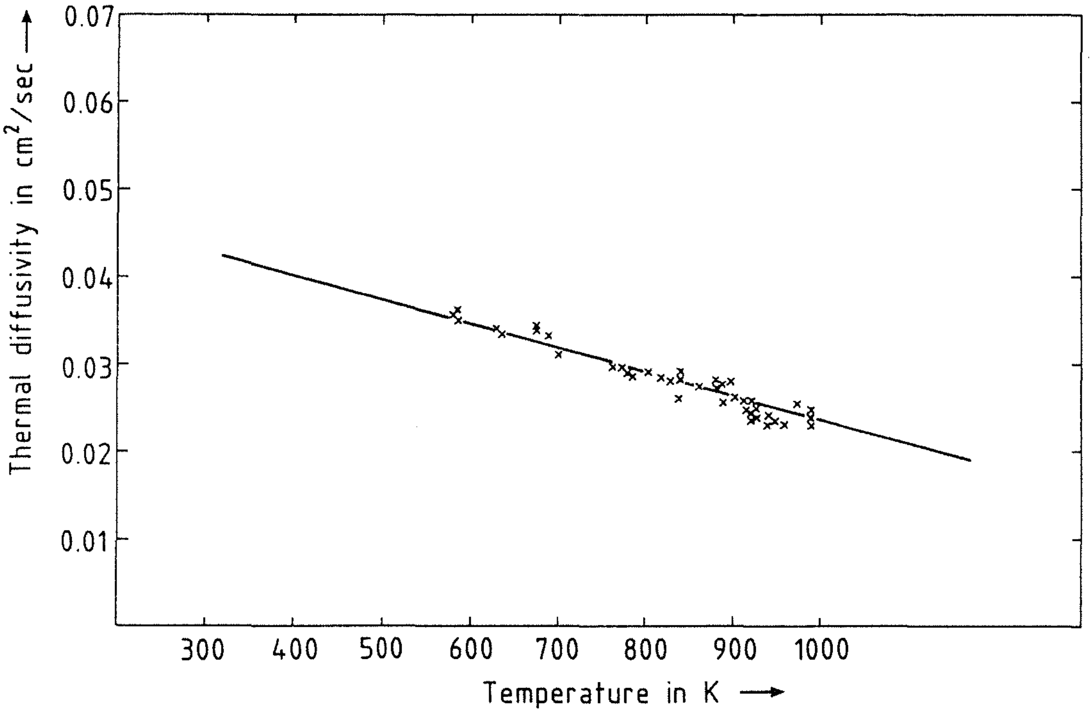

Fig. 6: Thermal diffusivity of pure Li_4SiO_4

BS BR-D-6 Compatibility

To investigate the chemical interactions of Li-silicates (Li_2SiO_3, Li_4SiO_4) with stainless steel AISI 316 at defined H_2O partial pressures, the reaction experiments in a flowing Ar atmosphere with a constant H_2O partial pressure of 10 Pa (100 vpm) and 100 Pa (1000 vpm) have been extended to higher and lower temperatures (900 °C, 600 °C). The annealing times varied between 24 and 1000 h. The compatibility behavior of Li_2O and Li_2ZrO_3 was studied in addition, in the full temperature range from 600 to 900 °C. A sheet of stainless steel was embedded in the Li-oxide compounds each, which were dried before at 900 °C for 2 hours.

The preliminary results for temperatures between 600 and 800 °C show that the extent of interactions between the Li-oxide compounds and stainless steel AISI 316 depends on the H_2O partial pressure. At 100 Pa the reaction rates are generally larger (about a factor of 5) than those at 10 Pa. Li_2O shows the best and Li_4SiO_4 the worst compatibility of the compounds examined. Li_2SiO_3 and Li_2ZrO_3 behave very similar and their reaction rates are between those for Li_2O and Li_4SiO_4. But at 900 °C Li_2O interacts strongest for 100 Pa H_2O. At this temperature no data are available up to now for 10 Pa H_2O.

The experiments and the evaluation work have not yet finished and therefore the temperature dependence of the reaction rates has still to be analyzed. In addition, the reaction behavior of the Li-oxide compounds with the martensitic-ferritic steel 1.4914 will be examined.

Staff:

J. Burbach
P. Hofmann
H. Metzger

BS BR-D-7 Constitution, Interaction with Water Vapour

The phase relations of the Li_2O-Al_2O_3 system were experimentally investigated in the range between Li_2O and $LiAlO_2$. Liquidus and solidus temperatures were measured by thermal analyses (DTA) and by observation of the sample melting with a two colour micro-pyrometer. The stability of the phases reported in the literature was confirmed, no additional phases were detected. The phase transformation, range of homogeneity and melting behaviour of Li_5AlO_4 was studied particularly with isothermal and transient temperature experiments and crystal structure investigations by X-ray diffraction. With the results obtained a phase diagram of the part Li_2O-$LiAlO_2$ of the Li_2O-Al_2O_3 system could be proposed (Fig. 1).

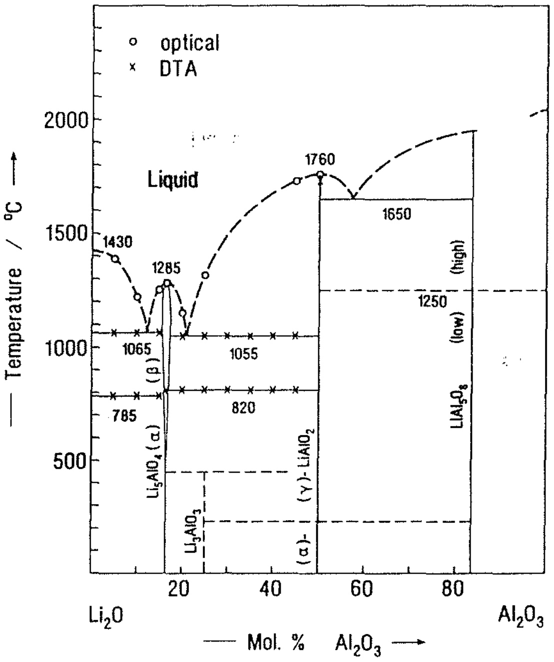

Fig. 1: Phase diagram of the Li_2O-Al_2O_3 system

Concerning the interaction of Li_4SiO_4 with water vapour some additional experiments were conducted. Samples of technical relevance were investigated by thermal gravimetry at temperatures between 100 and 600 °C and water vapour partial pressures between 4 and 105 Pa. The results obtained can be described by Langmuir adsorption isotherms. Minimum water vapour interaction was observed at 400 °C. Physisorption is the dominating mechanism at lower, chemisorption at higher temperatures.

Reference:

A. Skokan, Phase stability investigations in the ceramic breeder systems Li_2O-Al_2O_3 and Li_2O-ZrO_2. Fusion Technology 1990, Proc. of the 16th Symp. on Fusion Technology, 3-7 Sept. 1990, London, Vol. 1, pp. 772-776

Staff:

Ch. Adelhelm
D. Linder
V. Schauer
G. Schlickeiser
A. Skokan
H. Strömann

BS BR-D 8 Mass Spectrometric Free Evaporation Measurements on Lithium-orthosilicate Surfaces

The thermochemistry of ceramic lithium compounds can be investigated by Knudsen effusion mass spectrometry, a method that enables the identification and measurement of vapor constituents. From the partial pressure of the saturated vapor over condensed phases and from Gibbs free energy functions the enthalpy changes of the sublimation reactions are calculated.

The Reaction of Lithium Orthosilicate with Water Vapor: Formation of Lithium Hydroxide

The volatility of lithium bearing gas species constitutes one of the limitations with respect to the highest temperature at which a ceramic breeding material can be used. Formation of gaseous lithium hydroxide by reaction with water vapor, however, sets much lower limits to the highest temperature of use, if one plans to remove tritium from the bare surface of the ceramic with a sweep gas. So far, experimental data on this reaction exist in the literature only for lithium oxide. Therefore, we initiated a study on the reaction of lithium orthosilicate with water vapor to define the conditions under which lithium hydroxide is formed and to determine the thermochemical data of this reaction.

The equilibrium constant for the formation of lithium hydroxide by reaction of water vapor with ceramic lithium compounds is shown in Fig. 1; the activities of the solids are assumed to be unity. The results of log k (T) obtained with lithium oxide by Berkowitz et al. by mass spectrometry and by Tetenbaum and Johnson using a transpiration technique are in good agreement with each other and are about 4 orders of magnitude higher than those obtained in this work for the reaction with lithium orthosilicate

$$Li_4SiO_4\,(cr) + D_2O\,(g) = 2\,LiOD\,(g) + Li_2SiO_3\,(cr)$$

$$K = p^2\,(LiOD)/p(D_2O)$$

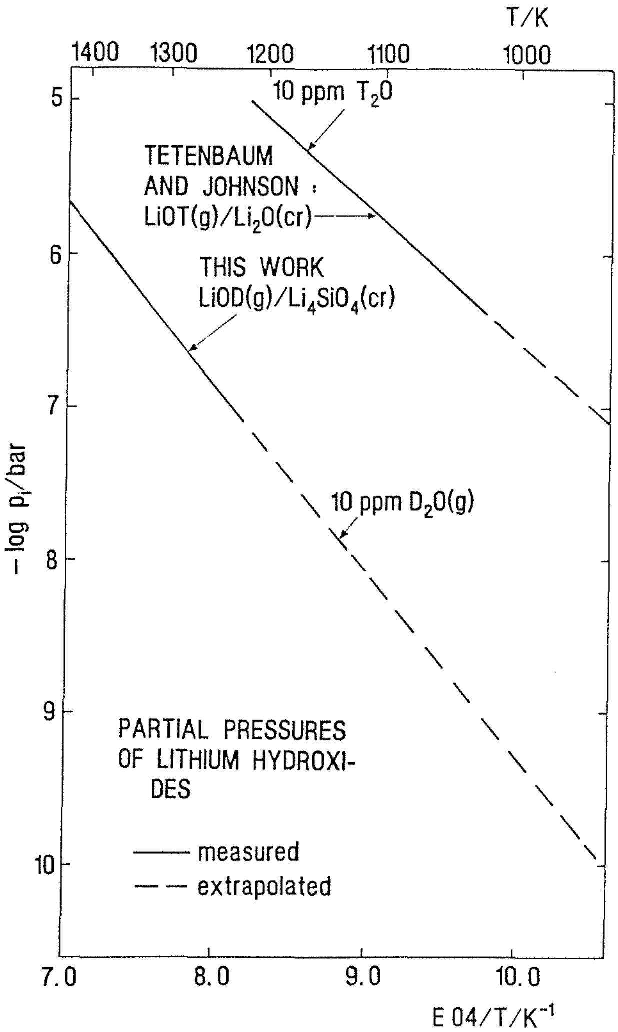

Fig. 1: Equilibrium constants ofthe reactionof water vapor with Li_4SiO_4 (cr) and with Li_2O (cr)

Table 1: Coefficients A and B for the temperature dependence of the equilibrium constant K according to

$$-\log K = -A/T + B$$

of the reaction between lithium orthosilicate and water vapor

Run	A	B	Temperature Range K
1	24 482	10.798	1221 - 1422
2	24 920	11.115	1222 - 1421
3	23 981	10.394	1219 - 1421
4	23 489	10.038	1188 - 1422
Av.	24 218±619	10.586±0.470	

Also it is seen that the slope of the log K (T) curve for the reaction with lithium orthosilicate is higher than that for the reaction with lithium oxide. Coefficients A and B for the temperature dependence of the equilibrium constant of the reaction between lithium orthosilicate and water vapor obtained from four runs are given in Table 1 Deuterium oxide was used in all experiments for reasons of background in the mass spectrometer. The D_2O pressures ranged from 0.5 to 1.5 Pa. Table 2 gives data of the equilibrium constant of one run in the temperature range from 1188 to 1422 K and the standard heats of reaction calculated from each data point. The mean value agrees very well with heat data averaged over four runs., e. g. ΔH°_{298} = (469 ± 10) kJ/mol. The temperature dependence of the partial pressure of LiOD obtained in this study is shown in Fig. 2 in comparison with the results of Tetenbaum and Johnson in a study of the reaction of lithium oxide with water vapor. The hydroxide pressure over lithium orthosilicate is roughly two orders of magnitude lower than that over lithium oxide at the same water vapor pressure; it also decreases more steeply with

Table 2: Equilibrium constant K and derived heat of reaction ΔH°_{298} obtained from one single run.

T/K	- log K/bar	ΔH°_{298} kJ/mol
1188	9.6264	463.14
1249	8.8244	468.65
1301	8.1344	471.76
1350	7.4124	471.54
1422	6.3634	469.11
	Av. =	468.84 ± 3.48

decreasing temperature. E. g. at 1 Pa D_2O pressure a LiOD pressure of 0.01 Pa over Li_4SiO_4 is reached at 1236 K, whereas the same hydroxide pressure over Li_2O is reached at 963 K. The heats of the lithium hydroxide forming reactions with lithium orthosilicate and with lithium oxide are compared in Table 3. They are found to be about 40 % higher for lithium orthosilicate than for lithium oxide.

Staff:

S. Huber
H. R. Ihle
R.-D. Penzhorn
P. Schuster

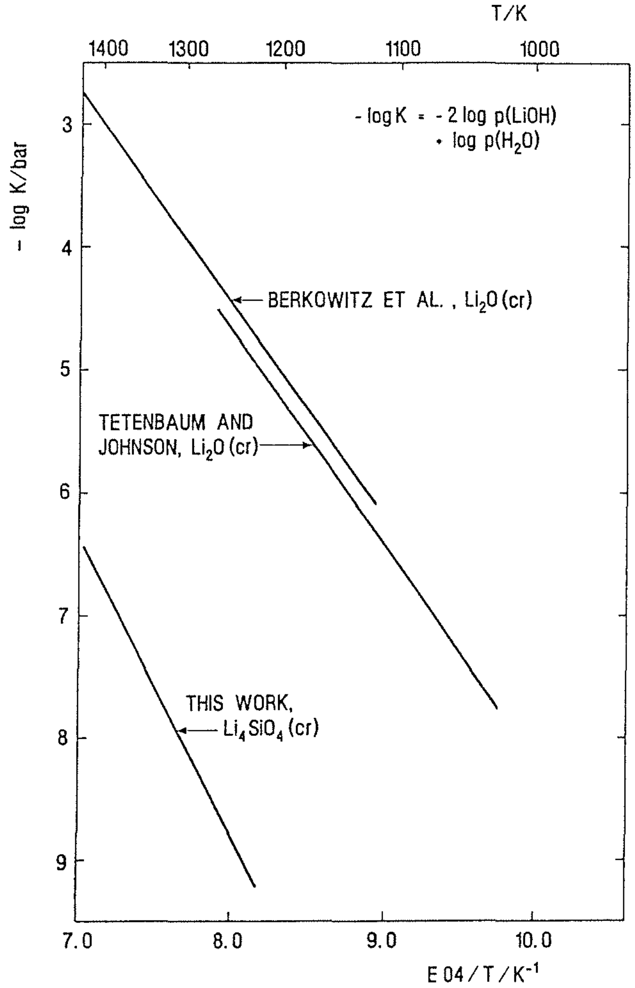

Fig. 2: Partial pressures of lithium hydroxides over Li_4SiO_4 and over Li_2O; sweep gas pressure 1 bar

Table 3: Comparison of heats of reaction leading to the formation of gaseous lithium hydroxides

a) Reaction: $Li_4SiO_4(cr) + D_2O(g) = 2\,LiOD(g) + Li_2SiO_3(cr)$

ΔH°_{298}	= (469 ± 10) kJ/mol	3rd law, this work
ΔH°_{1325}	= (464 ± 10) kJ/mol	2nd law, this work

b) Reaction: $Li_2O(cr) + H_2O(g) = 2\,LiOH(g)$

ΔH°_{298}	= (335 ± 8) kJ/mol	3rd law, Berkowitz et al.
ΔH°_{1300}	= (326 ± 13) kJ/mol	2nd law, Berkowitz et al.
ΔH°_{298}	= (344 ± 4) kJ/mol	3rd law, Tetenbaum and Johnson
ΔH°_{1150}	= (331 ± 13) kJ/mol	2nd law, Tetenbaum and Johnson

BS NN-D-1 Helium Blanket Test Loop

A Helium Blanket Test Loop (HEBLO) is being constructed for thermomechanical tests on gas cooled blanket components. This loop is to permit two types of experiments to be performed:

1) Thermal cycling tests involving elements which can be directly heated electrically. Typical examples include wall elements with brazed or welded cooling coils or channels. The thermal cycles can be generated in the test by variation of the heating power and/or the coolant flow through the coolant channels. This type of test is performed in the HEBLO primary circuit whose maximum helium flow rate is 100 m3/h at 80 bar operating pressure. The maximum heat removal capacity available is 115 kW.

2) Tests on components or - preferably - on original blanket assemblies, which cannot be directly heated electrically. The cyclic variation of the temperature in the test object and hence the thermal stresses must be generated by quick variations of the cooling gas temperature. A special Temperature Cycle Test Facility, connected with the primary circuit, is being built for these tests. It allows temperature cycles to be generated between 280°C and about 460°C at the maximum.

Meanwhile, all components of the loop system - except for the compressors with gas bearings - have been delivered and assembling of the pipework has started. The order has been placed for the measuring and control system. Work on the software and hardware for this system allowing control of test operation is in progress with the manufacturer.

It is expected that the commissioning tests will start still in 1991.

Staff:

E. Bojarsky
M. Dalle Donne
H. Deckers
H. Lehning
D. Piel
H. Reiser

BLDE-D-1 Liquid Metal Test Blanket Design

Subjects of this task are the design of self-cooled liquid metal blankets for the application in a DEMO-reactor, the development and the design of blanket test modules in NET/ITER, and, for both cases, the conceptual design of suitable external loops for heat- and tritium extraction.

Blanket Segments in DEMO

Based on the present definition of a fusion DEMO reactor which has been released by the Test Blanket Advisory Group (TAG) in March 1990 a concept of a self-cooled liquid metal blanket is under development at KfK. This concept uses the eutectic lead-lithium alloy Pb-17Li both as breeder material and as coolant. The reference concept is characterized by an integrated first wall with liquid metal flowing in toroidal direction. This direction is parallel to the main magnetic field and allows, therefore, velocities high enough for first wall cooling without excessive high magneto-hydro-dynamic (MHD) pressure drop.

A completely different approach is to combine helium-cooling of the first wall with self-cooling of the breeding zone of a Pb-17Li blanket. This method has been used in the design of an alternative blanket concept shown in Fig. 1. The concept is characterized by a stiff first wall box with rectangular cooling channels in toroidal direction. Connected to this box is a grid of steel plates forming large ducts for liquid metal cooling in poloidal direction. This is a novel design not yet analysed in details. The main advantages are a real double containment of the liquid metal, a more simple geometry and much less problems with liquid metal cooling. Most of the MHD-problems in self-cooled liquid metal blankets are caused by the surface heat flux to the first wall requiring relatively high liquid metal velocities. This is avoided here by using gas-cooling which results in much lower temperatures at the steel/liquid metal interface and decisively lower liquid metal velocities. First estimates indicate that this concept is feasible and that the breeding ratio will be roughly the same as for the reference design. The disadvantage is the need for a second coolant with separate ancillary systems. On the other hand, there is no auxiliary cooling system required for after heat removal since this is possible either with the helium cooling of the first wall or with the liquid metal cooling of the breeding zone.

Blanket Test Object Design for NET/ITER

NET/ITER offers the unique possibility to test simultaneously all aspects of DEMO blanket concepts in the real geometrical configuration, with the real magnetic field, and with an incident neutron flux having the real neutron spectrum and spatial distribution. The main differences to DEMO are the lower neutron wall load (1.0 MW/m^2 instead of 2.2 MW/m^2) and the shorter burn time.

There is a large number of issues involved in a blanket concept. The most critical ones for self-cooled liquid metal blankets are:

- MHD pressure drop and flow distribution
- electrical insulation of the flow channels either by flow channel inserts or by direct insulation
- potential chemical reactions between the liquid metals (Pb-17Li, NaK) and air, water, or concrete
- response of blanket segments to plasma disruptions.

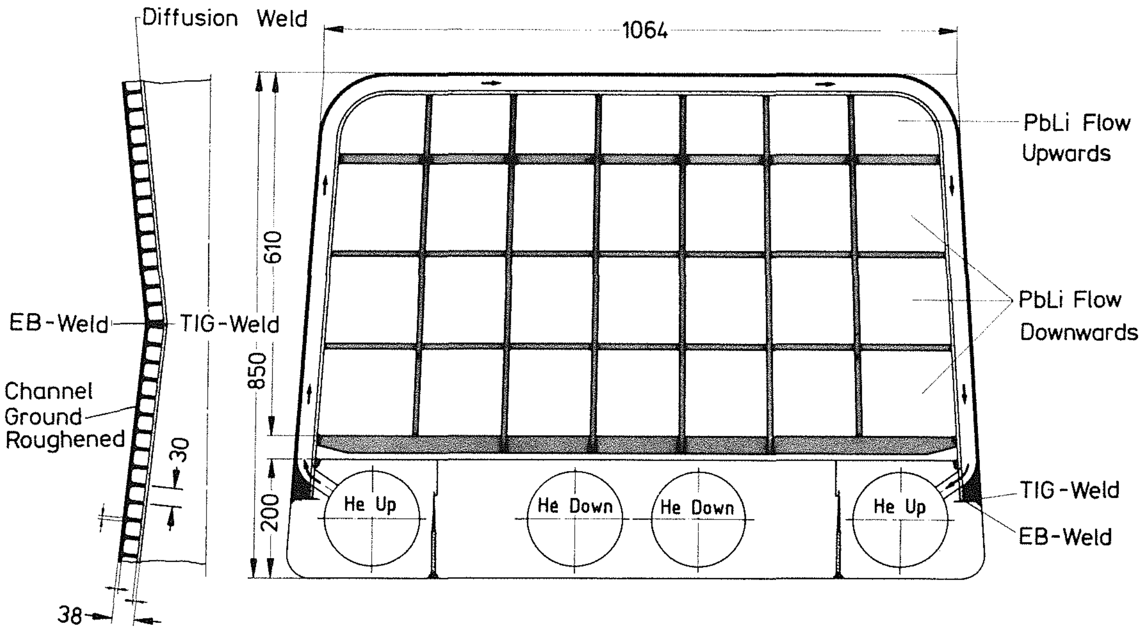

Fig. 1: Self-cooled liquid metal breeder blanket with heliumcooled first wall

All these issues either require tests in NET/ITER or have to be taken into account in designing test objects, ancillary loops and interfaces for the basic machine.

Different test objectives require dedicated test modules. The basic machine will be designed for a frequent replacement of test modules. For this purpose a number of blanket test ports are allocated at the equatorial midplane, each of them roughly 3 m high and 1 m wide. In order to cope with the very limited testing time, it is anticipated to divide a test port into up to four sub-ports for a number of tests. Figure 2 shows such a quarter-sized test module which is designed for exchanging it completely independent of the neighbouring sub-modules. The module shown in this figure is located behind a first wall provided by the basic machine. This is anticipated for all tests during the physics phase of NET/ITER operation and for the first part of the technolgy phase respectively in order to limit the risk to the machine caused by blanket tests. Exposure of the test modules to the plasma required for final tests of a blanket conept will be allowed only after extensive testing of the concept behind the first wall.

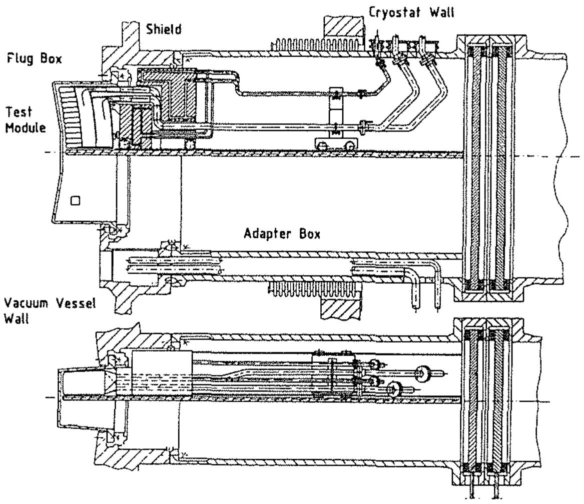

Fig. 2: Test module for the self-cooled Pb-17Li concept

External Loops for Heat- and Tritium-Extraction

The ancillary loop systems extract the heat and tritium from the blanket. For the NET/ITER test module one system (5 MW thermal power) consisting of a Pb-17Li loop, a NaK intermediate loop and a water cooling loop is proposed. For DEMO, concerning the last conceptual design, 80 independently working loop systems consisting of a Pb-17Li loop, a double walled heat exchanger with a tritium extraction system using NaK in the pipe gap and a water-steam loop each, are proposed. 32 loop systems (20 MW) are working for the inboard blankets and 48 loop systems (30 MW) for the outboard blankets. A detailed description of the system is given in [2, 3, 7, 8].

A tentative reliability study of the total reactor loop system concerning the steam generators, the Pb-17Li pumps and the valves, showed that the availability of the system is unacceptably low if all loops are working independently. The reason is the high number of basic construction elements like pipe length, number of welds, pumps, valves etc. By the concentration to bigger components resulting in a smaller amount of loops this problem cannot be improved essentially, because the total pipe length and the length of welds stays about unchanged.

Only by redundantly connecting the primary Pb-17Li loops in the manner that if one loop fails the adjacent loop can overtake its function the availability of the reactor can be increased to an acceptable amount. Only between two inboard blankets and between the 3 outboard blankets of one sector is for electric reasons a connection allowed.

References:

[1] U. Fischer: Die neutronenphysikalische Behandlung eines (d,t)-Fusionsreaktors nach dem Tokamakprinzip (NET), KfK-4790, Oct. (1990).

[2] M. Tillak et al., ITER Test Program, ITER Document Series, No. 24, International Atomic Energy Agency, Vienna 1990.

[3] S. Malang et al., Self-Cooled Blanket Concept Using Pb17-Li as Liquid Breeder and Coolant, Fusion Engng. Des. 14(1991), pp. 373-399.

[4] U. Fischer: Impact of Ports on the Breeding Performance of Liquid Metal and Solid Breeder Blankets in the DEMONET-configuration, contribution to 2nd Int. Symp. on Fusion Nuclear Technolgy, June 2-7, 1991, Karlsruhe, F.R. Germany.

[5] S. Malang, G.P. Casini, P. Leroy, R.F. Mattas, Yu. Strebkov; Crucial Issues on Liquid Metal Blanket Design, Proc. Second International Symposium on Fusion Nuclear Technology (ISFNT 2), Karlsruhe, June 2-7 (1991), to be published in Fusion Engng. Des.

[6] P. Norajitra, unpublished report of KfK

[7] S. Malang, J. Reimann, H. Sebening (comp.): Status Report. DEMO relevant Test Blankets for NET/ITER, Part 1: Self-cooled Liquid Metal Breeder Blanket. KfK 4907, September 1991, Volume 1: Summary.

[8] H. John, S. Malang, H. Sebening (comp.): Status Report. DEMO relevant Test Blankets for NET/ITER, Part 1: Self-cooled Liquid Metal Breeder Blanket. KfK 4908, September 1991, Volume 2: Detailed Version.

Staff:

E. Bojarsky
H. Deckers
U. Fischer
H. John
S. Malang
P. Norajitra
H. Reiser

BL MH-1 Liquid Metal MHD

A main issue in designing a self-cooled liquid metal blanket is the strong magnetic field which causes high pressure drop of the liquid metal flowing through the cooling channels and the degradation of the heat transport by the liquid metal due to changed velocity profiles and the reduced turbulence.

In order to get a better data base, to learn about the physical problems and to verify computer programs used for design calculations the experimental program MEKKA (Magnetohydrodynamik Experiment in Natrium-Kalium Karlsruhe) was started in 1985.

The MEKKA Facility

To conduct fusion relevant MHD-experiments magnets with high field strengths and large testing volumes and a liquid metal loop with high flow rate are necessary.

Therefore, the MEKKA facility has been built up being now completed and in operation. The main components of this facility are briefly outlined:

For experiments with restricted testing volumes two magnets are available which cover different items of the MHD-program:

A normal conducting dipole magnet with a field strength of 2 Tesla and a test volume of 0.17mx0.5mx1.5m is used for duct flows perpendicular to the magnetic field.

A superconducting Solenoid-Magnet with 3.5 Tesla field strength, a warm bore of 40 cm diameter, and a length of about 1 m is foreseen to investigate all kinds of 3-dimensional MHD-flow problems, especially the radial to toroidal bend. Fig. 1 shows this magnet with the installed radial-toroidal bend test section.

The eutectic sodium-potassium alloy $Na^{22}K^{78}$ is used as the liquid metal. The NaK loop (Fig. 2) is characterized by the following specific features.

A canned motor pump with a maximum pressure head of 0.9 MPa at a flow rate of 25 m³/h is used to circulate the liquid metal at temperatures below 250 °C. An additional electromagnetic pump is used during the high temperature wetting phase. The dissipated heat is removed by an oil-cooled double tube heat exchanger. The oxygen content in the NaK is controlled by an oil cooled cold trap. The flow rate is measured by a gyrostatic flowmeter with an accuracy of 0.5%. The pressure in the loop and the pressure differences in the test section are measured by high accuracy pressure transducers with different measurement ranges. The entire loop is installed in a rack which can be moved on rails along the axis of the magnet. This method allows for local pressure and velocity distribution measurements at different regions of the magnets by only traversing the loop with a hydraulic piston.

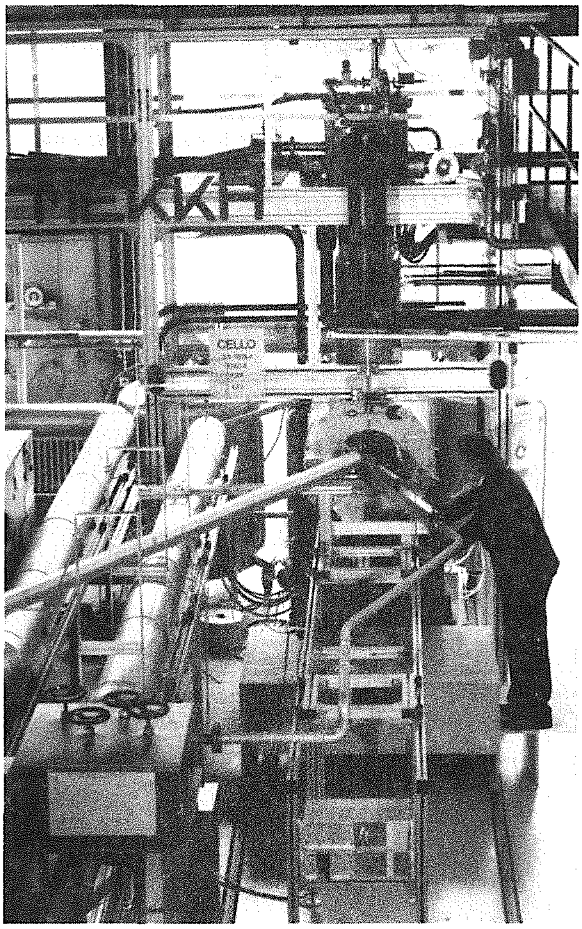

Fig. 1: The superconducting solenoid magnet with the installed TRT1 test section

MHD-experiments in radial to toroidal bends

The key problems of the reference design, based on the poloidal-toroidal flow concept are the pressure drop and the velocity distribution in the region of the poloidal-radial-toroidal bends. To investigate these effects and to verify the corresponding theoretical models single and multichannel experiments are conducted.

The joint ANL/KfK single channel toroidal-radial-toroidal bend experiment TRT1.

A first series of experiments with the single channel toroidal-radial-toroidal bend test section TRT1 was conducted jointly with the ANL. The test section was built at ANL, the experiments were conducted in the MEKKA test facility at KfK. Fig. 1 shows the test section installed in the superconducting Solenoid-Magnet. In the lower part of Fig. 3 a schematic view of the test section and the positions of the pressure taps are given. In the experiment potential distributions on the duct walls, pressure differences between different positions and potential differences within the liquid metal were measured using an automatic processing system. The experimental data were compared with the theoretical predictions based on the Core Flow Solution approach assuming inertialless and fully developed MHD-flow. Fig. 3

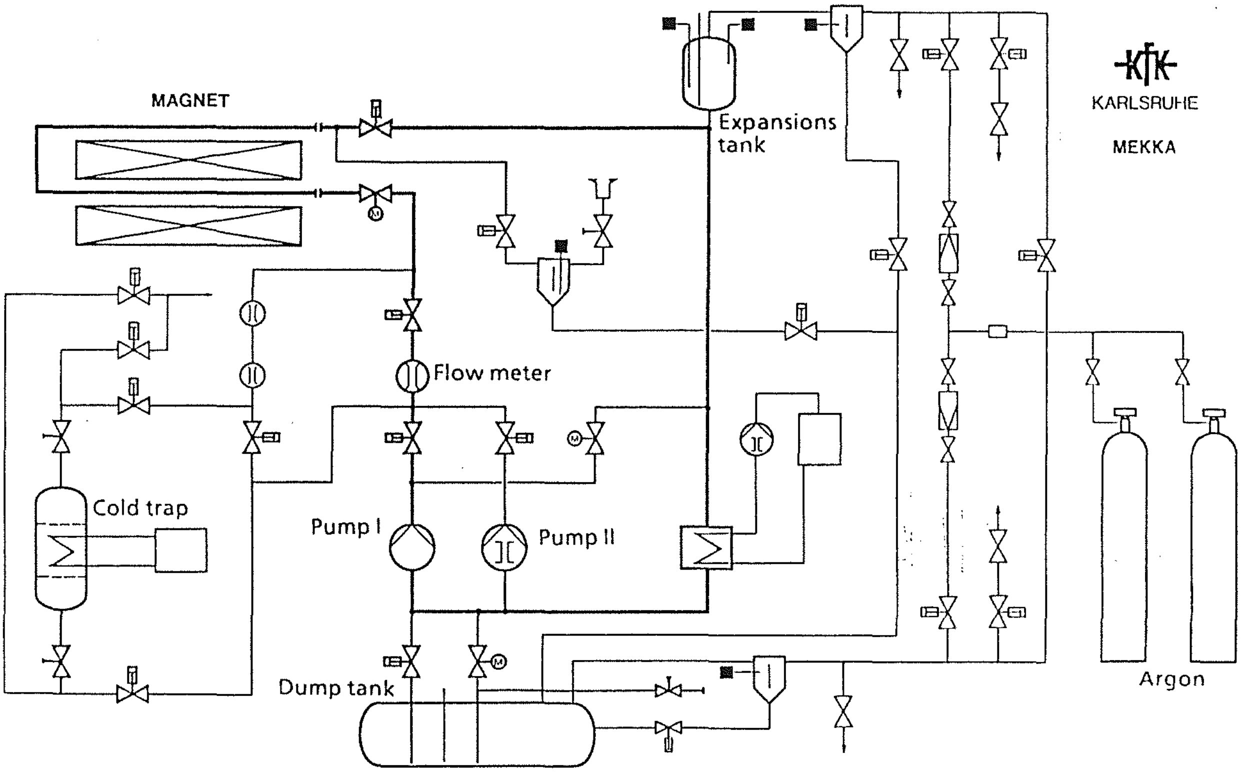

Fig. 2: The NaK1 sodium-potassium loop

(upper part) shows as an example the measured and predicted pressure differences along the outer wall. In the next series of experiments the parameter field will be completed.

The multichannel U-bend experiment

The largest uncertainty exists in respect to the interaction between the flow through parallel channels, especially if there are radial to toroidal bends. In electrically connected parallel ducts, currents are not restricted to the flow inside each channel, but, under certain conditions, so-called leakage currents can flow across the duct walls into the adjacent channels.The large current circuit through the parallel radial channels is closed by the toroidal channels and causes a large pressure drop and an unequal partitioning of the total flow rate into the parallel channels.

These effects will be investigated with multichannel U-bend experiments (Fig. 4) which will also be conducted in the superconducting Solenoid-Magnet. The constructions of the test sections is finished, the manufacturing will start in the near future. The installation of the test section in the loop is foreseen for middle of 1992.

The test sections have five parallel channels with a cross section of 26x26 mm. In one test section the channels are electrically connected, in the other, the channels are insulated in the region where the magnetic field is perpendicular to the flow direction.

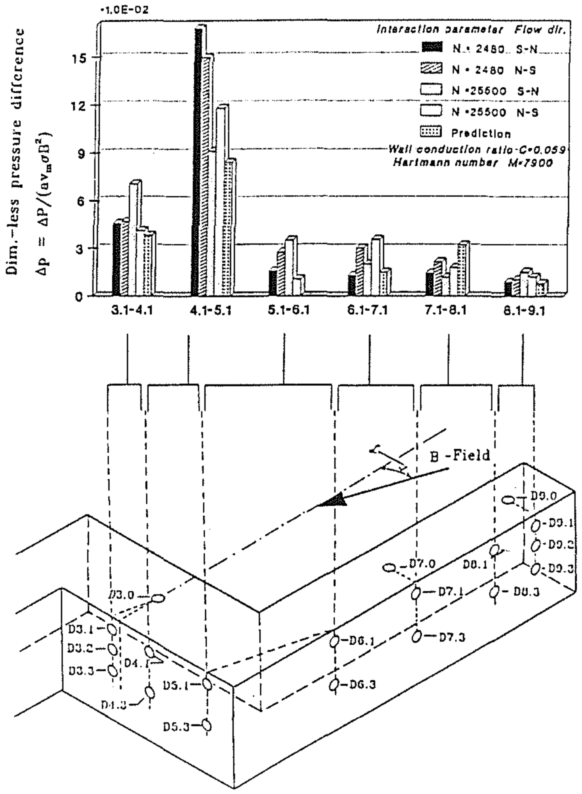

Fig. 3: Measured and predicted pressure differences at the TRT1 experiment

In parallel to this multichannel experiment in the MEKKA facility, preliminary tests were performed with a plexiglas

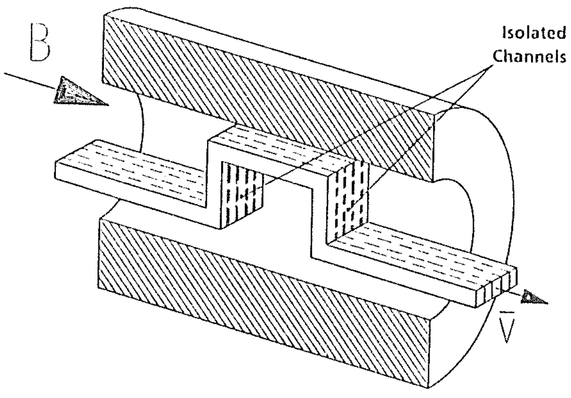

Fig. 4: U-bend test section with countercurrent poloidal flow

multichannel test section in the superconducting Solenoid magnet of the Latvian Academy of Sciences in Riga, Latvia. Quantitative experiments are planned for the end of this year.

Code development

Two kinds of codes are developed at KfK to describe MHD flow in ducts numerically: the "core flow solution" and the "full solution"

- The core flow solution developed by ANL and the Urbana University was adopted by KfK and was improved for more complex geometries. This method was used to calculate the MHD-flow in the meander shaped front channel of the reference liquid metal blanket concept. Fig. 5a shows the pressure drop along this meander channel, Fig. 5b the velocity distribution at the 3. bend.

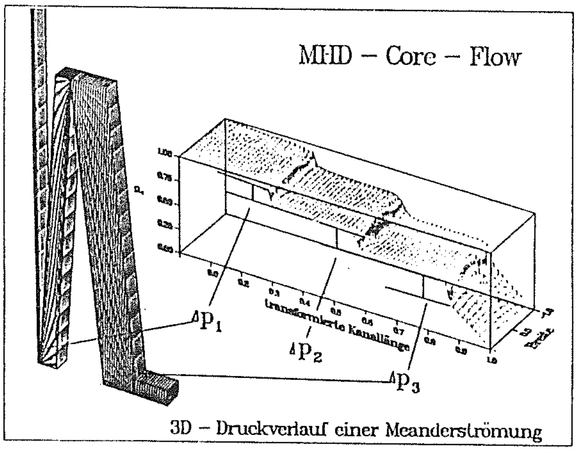

Fig. 5a: Pressure distribution for a meander flow

- The full solution developed at KfK is further developed and improved to calculate the complete flow behaviour in complex geometries, like a radial to toroidal bend. In a first step the binding together of the MHD flows of two separate straight channels was successful. In the next step, two or more sections of straight channels are connected under different angles.

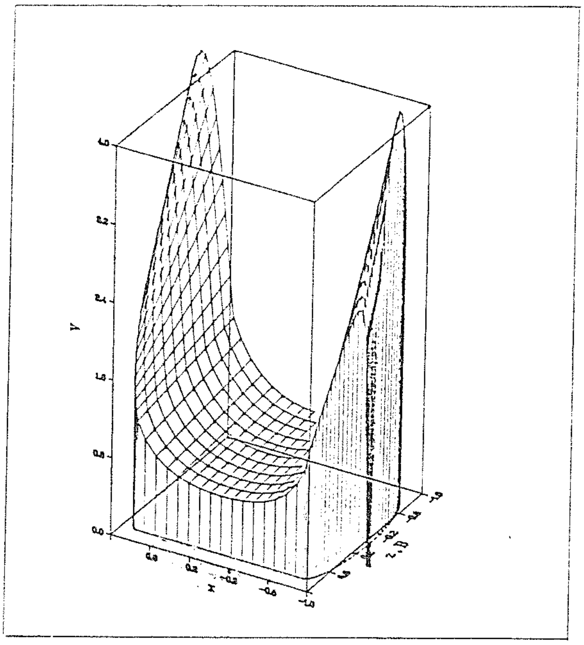

Fig. 5b: Velocity profile in the third meander bend

MHD feasibility of alternative blanket concepts

The feasibility of two alternative blanket concepts concerning the MHD problems was investigated.

- A quasi-two-dimensional geometry for a liquid-metal blanket duct combined with the poloidal-toroidal concept.

  This geometry has the potential of excluding both currents caused by three-dimensional effects and integral currents in the blanket module. The pressure drop can be assessed more easily than for the reference concept due to the two-dimensional flow. Additionally, this novel design opens the possibility of affecting the flow structure in a desired way.

- Considerations on a self-cooled liquid metal blanket with poloidal flow.

  Analytical tools were derived in order to calculate easily the heat transfer and the MHD-pressure drop for different magnetic field strengths and heat loads of the first wall. The results show that with the techniques and cooling channel concept discussed for the time being a poloidal flow is not possible for DEMO-conditions with lithium lead as coolant and breeding material, but possible for pure lithium due to its better thermodynamic properties.

  Improvements of the heat transfer by promotion of turbulence and the reduction of the MHD-pressure drop by insulating the walls of the cooling channels electrically or by reducing the length of the high heat loaded front channels or using a different cooling channel concept could make it possible to use a poloidal flow concept. But these proposals still need intense experimental and theoretical investigations.

Staff:

L. Barleon
L. Bühler
E. Höschele
H. Kreuzinger
L. Lenhart
K.J. Mack
I. Platnieks
J. Reimann
D. Schlindwein
R. Stieglitz
R. Vollmer

BL PC-D-1 Corrosion of Structural Materials in Flowing Pb-17Li

The KfK liquid metal breeder blanket uses Pb-17Li as coolant and 316L (NET) and MANET (DEMO) as structural materials. Became of the elevated temperatures (400°C) compatibility (corrosion) must be studied. Furthermore coated materials will be investigated, which are electrically insulating to reduce MHD pressure drop. Main experimental device to study corrosion is the PICOLO-loop.

The corrosion tests in the PICOLO loop at 550 and 500 °C were terminated [1,2]; they were extended to 450 °C. The test series at 450 °C has now reached an exposure time of > 3000 hours. Additional to MANET and Type 316 L(N) steel, two specimens of aluminized Type 316 L(N) steel provided by CEA (Fontenay-aux-Roses) are in the test series.

The impurities collected in the magnetic traps have been characterized by chemical analysis, electron- and Auger electron-microprobe analysis. The impurities in form of particles were distributed after the two runs by the same pattern: At the inlet and in the center the amount of the particles was found to be between 5 to 7 % and at the outlet below 0.01 % of the liquid alloy (Tab.1) [3].

Tab.1 : Main metallic impurities in Pb-17Li of the magnetic traps

(%)	inlet	center	outlet
Fe	4,2 - 5,0	3,3 - 4,2	< 0,001 - 0,007
Cr	0,3	0,1 - 0,2	< 0,002
Ni	0,01 - 0,02	0,01 - 0,04	< 0,001
Al	0,002 - 0,0038	0,004	< 0,002
Nb	0,008 - 0,011	0,001	< 0,003
V	0,005	0,002 - 0,005	< 0,002
Mn	0,006	0,005	< 0,002

The particles are mainly metallic, and their integral composition corresponds to the ferritic steel of the hot leg and the corrosion specimens exposed therein.

Two types of particles have been observed by micro-area-analysis: one with high iron content (77-97 %) and the other with high chromium content (50-85 %). Even within a particle the composition differs. Chromium is often enriched at the border of the particle. Following conclusions can be drawn from the analytical results. The particles are not eroded as solid grains from the tubes of the hot leg. The liquid alloy heated up to 550 °C dissolves iron and the other elements from the steel. During cooling down to 305 °C the dissolved elements precipitate as iron- and chromium- based particles. These are fixed by the magnetic trap and grow by preferential uptake of chromium and less iron. Although the liquid alloy leaving the trap has a high purity, additional magnetic particles were detected in the flow meter. A magnetic trap is not sufficient for purification purpose.

The coulometric titration of the oxygen content of Pb-17Li using one of the yttria doped zirconia oxygen meters revealed very low oxygen concentrations in the range of 10^{-6} µg/g. There is, however, some uncertainty due to the fact that the experimental set-up was not fitted to this coulometric titration. It is planned to repeat the titration using a changed experimental set-up [4,5].

Static corrosion tests of completely dried Al_2O_3 crucibles with Pb-17Li at 500 °C demonstrated the good compatibility of this material with the eutectic melt in agreement with earlier thermochemical considerations.

The plating of steel with aluminium by dipping into the molten metal can be applied to form hard, high-melting intermetallic phases on low Ni alloy. The Al layer was successfully transformed into the intermetallic by means of a thermal treatment. The formation of oxide layers on the iron aluminide layer was reached by an eloxation process.

The testing of enamel on steel in liquid Pb-17Li at 400 °C indicated a chemical reaction between this insulator and the liquid metal. The enamel was not optimized in respect of stability against chemically reducing environment as the Pb-17Li eutectic alloy.

References:

[1] H.U. Borgstedt, H.D. Röhrig, "Recent Results on Corrosion Behaviour of MANET Structural Steel in Flowing Pb-17Li Eutectic", J. Nucl. Mater. 179 - 181 (1991) 596-598

[2] H.U. Borgstedt, G. Frees, M. Grundmann, Z. Peric, "Corrosion and Mechanical Properties of the Martensitic Steel X18 CrMoVNb 12 1 in Flowing Pb-17Li", usion Engng. and Design 14 (1991) 329-334

[3] Ch. Adelhelm, E. Nold, G. Streib, S. Winkler: "Corrosion products of a Pb-17Li loop collected in a magnetic trap", presented at ISFNT 2, Karlsruhe, June 2-7, 1991

[4] Ch. Adelhelm, H.U. Borgstedt, "Löslichkeit und Bestimmung von Sauerstoff in der eutektischen Schmelze Pb-17Li", in: Nichtmetalle in Metallen '90", Ed.D. Hirschfeld, DGM Informationsgesellschaft, Oberursel 1990, p.17-22

[5] Ch. Adelhelm, H.U. Borgstedt, D. Linder, G. Streib, "Methods for the Determination of Lithium and Impurities in Pb-17Li", Fusion Engng. and Design 14 (1991) 235-239

Staff:

Ch. Adelhelm
H.U. Borgstedt
G. Frees
P. Judex
D. Linder
E. Nold
Z. Peric
G. Streib
S. Winkler

BL PC-D-2 Impurities and Clean-up of Molten Pb-17Li

Staff:

H. Feuerstein
J. Oschinski

As in any liquid metal system also in a molten Pb-17Li(LM) blanket impurities may cause safety and operational problems. The aim of this work is to characterize the different kinds of impurities, to study their transport behavior in the blanket, and to find methods for their removal from the liquid metal.

1. Behavior of Po-210

Po-210 is formed by activation of bismuth impurities:

Bi-209 (n,γ) Bi-210 (β-) Po-210

However even if Bi free LM is used, Po-210 will be formed during operation of the reactor because of the build-up of bismuth from lead.

Without on-line removing of bismuth to levels below 1 ppm, the specific Po-210 activity will be higher than 109 Bq/kg. Chemically however polonium will be present always only like tracers in the ppb range.

The element polonium has a high vapor pressure, high evaporation rates were expected. Experiments showed however that actually the evaporation is orders of magnitude smaller (Fig. 1). Probably, similar to the lithium in the eutectic, chemical compounds between polonium and lead are formed, reducing the coefficient of the chemical activity to 10^{-4} to 10^{-3}.

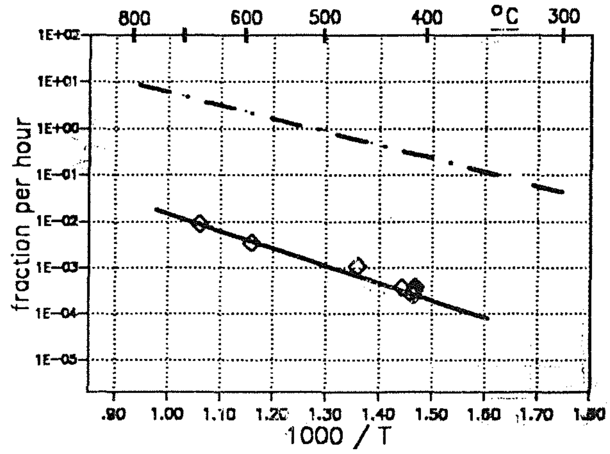

Fig. 1: Relative evaporation rates of Po-210 from molten Pb-17Li. Dashed line calculated using the Langmuir equation.

The experiments will continue to study the behavior of Po-210 in static thermal gradients and in a thermal convection loop.

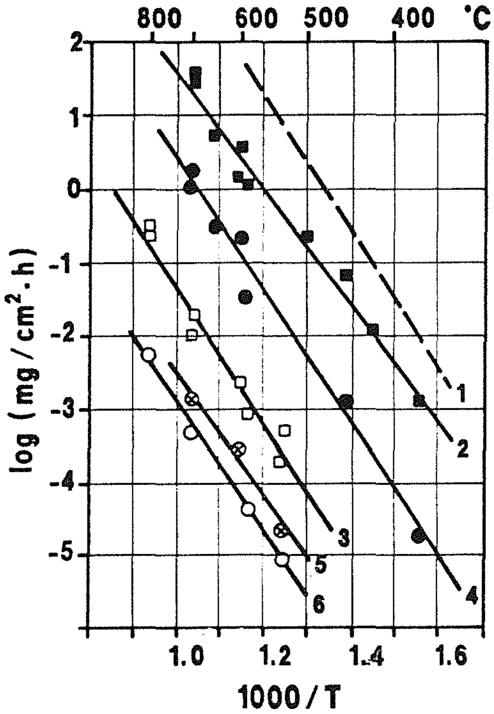

Fig: 2: Evaporation rates from molten Pb-17Li
1 : calculated for Pb;
2 : Pb, vacuum;
3 : Pb, He or Ar;
4 : Li, vacuum
5 : Li, Ar;
6 : Li, He

2. Pb-17Li loop TRITEX

TRITEX is a pumped ferritic steel loop. It was operated in run number IV during 3100 hours. During this run the temperature in the cold trap was kept between 250 and 260°C, while the temperature in the main loop was varied between 300 and 500°C. Currently samples are taken from the magnetic trap, the cold trap and from the metal in the drain tank. The investigations are under way.

The particle distribution and composition from austenitic thermal convection loops was studied in detail. The Ni concentration in the bulk LM was only 150 ppm. Nearly all of the Ni dissolved from the steel was deposited in form of particles. Very interesting is the formation of an intermetallic Ni-Mn compound, found in the coldest area of the loop. It might be possible to remove the radioactive isotope Mn-54 by a cold trap if sufficient Ni is available.

3. Formation of Aerosols

The evaporation rate of Pb and Li from the molten Pb-17Li was investigated between 300 and 800°C in vacuum and inert gas atmosphere. Fig. 2 shows the results. Evaporation rates are small and no aerosol problems will exist with normal blanket operation (1). Aerosol concentrations at the outlet of a vessel will be only in the range of 10^{-9} to 10^{-6} g/m^3.

References:

(1) H. Feuerstein et.al., paper 101 at ISFNT, Karlsruhe 1991

Staff:

H. Feuerstein
H Gräbner
S. Horn
G. Kieser
J. Oschinski

BL EX-D-1 Tritium Extraction by Permeation and Cold Trapping

The selected tritium removal technique for the self-cooled Pb-17Li blanket with an intermediate NaK loop consists of tritium permeation into the NaK and precipitation as tritide in a cold trap. For tritium recovery, the tritide is decomposed by heating up the cold trap and the tritium gas is pumped off.

Both the precipitation and release kinetics are investigated in the WAWIK-facility. In these experiments, hydrogen (protium) is used instead of tritium.

Hydrogen Precipitation Kinetics

Precipitation experiments were performed [1] with experimental cold traps (ECT) mainly consisting of a vertical pipe (inner diameter: 102 mm, height: 500 m) filled with up to 9 wire mesh packings (height of each: 50 mm) with a given specific surface A_{spec}. There is a cooling zone where the liquid metal is countercurrently cooled by air, followed by an isothermal zone without cooling.

In order to determine the mass transfer characteristics, two kinds of experiments were performed:

i) The cold trap outlet concentration c_o was measured as a function of time during hydrogen loading at constant operating parameters (mass flow rate $\dot{m}_{NaK}$, cold trap inlet concentraton c_i, inlet and outlet temperatures T_i and T_o). Of special interest is the difference between c_o and the saturation concentration $c_{o\ sat}$, determined with the cold trap outlet temperature T_o. From these measurements the global cold trap efficiency η can be determined.

ii) In some experiments the cold trap was operated at constant conditions for a long time period (20 to 40 hrs). After termination of these experiments the axial distribution of the deposited hydrogen in the cold trap was determined. From these measurements local mass transfer rates can be evaluated.

Figure 1 shows a characteristic example for the cold trap efficiency as a function of loading time. This experiment is compared with a Na experiment where a similar cold trap design was used, but with a considerably smaller specific surface $A_{spec} = 340$ m^2. In the present experiments the temperatures were chosen such to obtain equal inlet and outlet concentrations.

In the Na experiment, the efficiency increased from a value of about $\eta = 0.6$ after 0.5 hrs to a value of about η 0.8 after 20 hrs. Then, the efficiency becomes fairly constant. In the present experiment, efficiencies close to $\eta = 1$ are observed after a loading time of a few hours. During the first hours, the efficiency is also surprisingly high. Further experiments are required in order to prove if this different behaviour is only due to the different specific surface or if the precipitation mechanisms are different.

Other experiments with minimum cold trap outlet temperatures of 40 °C proved that the precipitation is still very efficient in this low concentration range. This result is essential for the tritium removal from the fusion reactor blanket.

Hydrogen Release Kinetics

Two types of experiments were performed [2]: hydrogen was recovered either from complete cold traps (CCT-Exps.) or from single wire mesh packings (SP-Exps.). In both cases, the liquid metal was drained from the packings. The evacuated vessels were heated uniformly to a given temperature. Then, a valve was opened and the hydrogen passed a vapour trap to prevent transport of metal vapour to the vacuum pump. The hy-

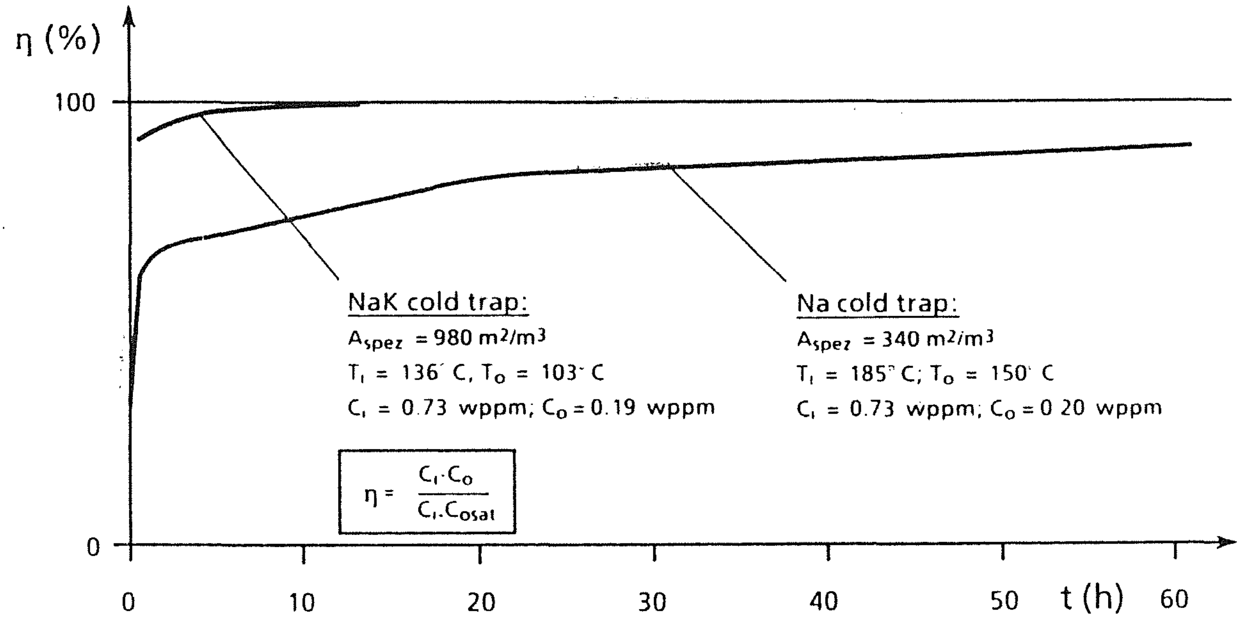

Fig. 1: Cold trap efficiency as a function of the hydrogen loading period

drogen was collected in a gasometer. In all experiments the liquid metal, produced by the decomposition of the hydride, could drain freely to the vessel base.

For the CCT-Exps., the cold trap stayed in the WAWIK loop. For the SP-Exps. the drained cold trap was transferred to a glove box and dismounted. Samples of hydride-loaded wires were taken for further visualization by optical and scanning microscopy and analyses of the chemical composition by the EDAX technique (Energy Dispersive Analysis X-ray).

The EDAX method proved that all crystals in the total cold trap consist of pure potassium hydride. The occurance of KH is suspected due to the higher chemical activity of potassium compared to sodium, however, this fact was not proven experimentally yet.

Figure 2 shows the release rate constants in a plot of logk against T^{-1}. For the SP-Exps. the arithmetic mean temperature of the thermocouples inside the mesh were used as the characteristic temperature. In the CCT-Exps. the differences between the various thermocouples were larger as indicated in the figure. No significant dependence of the inital hydride mass or the type of experiments is observed. The results were fitted by the following correlation

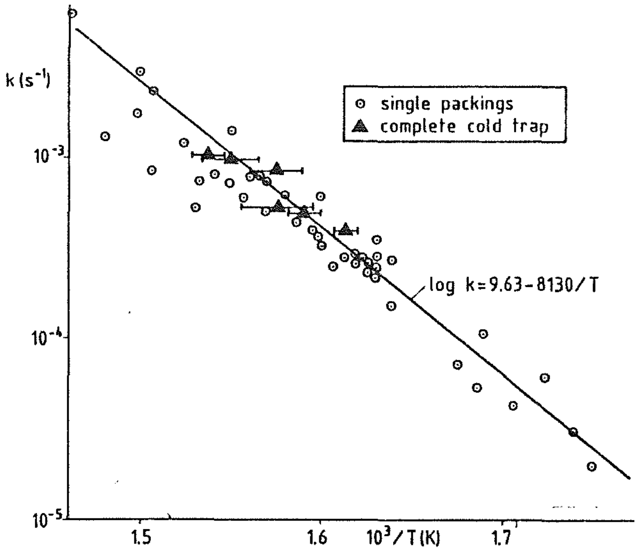

Fig. 2: Hydrogen release rate coefficients as a function of temperature

$\log k(s^{-1}) = 9.63 - 81.3 / T(K)$

These results are close to previous results [3] obtained with KfK crystals generated in a small thermal convection loop.

Applying these results for a fusion blanket cold trap, 99 % of the tritium would be released in about three hours for a release temperature of 400 °C. Two regeneration cycles per day could be feasible; the tritium inventory in the two cold traps (batch operation) would be about 0.5 tritium productions per day.

References:

[1] J. Reimann, R. Kirchner, M. Pfeff, and D. Rackel, "Tritium removal from NaK-cold traps: First results on hydride precipitation kinetics", Fourth Top. Meet. Tritium Techn., Albuquerque, USA, Sept. 29 - Oct. 4, (1991), to be published in Fusion Technology.

[2] J. Reimann, R. Kirchner, and D. Rackel, "Tritium removal from NaK-cold traps: Investigation of hydrogen release kinetics", ISFNT 2, Karlsruhe, Germany, June 2-7(1991), to be published in Fusion Engng. Des.

[3] J. Reimann, "Tritium inventory and recovery for a self-cooled Pb-Li blanket." Fusion Engineering and Design 14(1991) 413-425, North-Holland.

Staff:

R. Kirchner
M. Pfeff
D. Rackel
J. Reimann

BL EX-D-2 Tritium Extraction from Molten Pb-17Li with Solid Getters

Several methods were proposed for the extraction of tritium from a molten
Pb-17Li blanket. This work is concerned with the use of solid getters.

In the last annual report it could be described that tritium extraction from the molten eutectic by solid getters is possible.

The behavior of deuterium in austenitic thermal convection loops can now be described by models (1). In run IV of the facility TRITEX the transport behavior of deuterium could be confirmed for a ferritic pumped system. A new Test Section is now installed in TRITEX for final investigations of getter materials and for the use of tracer amounts of tritium.

References:

(1) H. Feuerstein et. al., Nucl.Engin.Des./Fusion 14 (1991) 261

Staff:

H. Feuerstein
H. Gräbner
S. Horn
G. Kieser
J. Oschinski

BL SA-D-1 Functional Analysis of a Liquid Metal Self-cooled Blanket

During the last year a report [1] was prepared on the functional analysis for the liquid metal self-cooled blanket proposed by KfK. Based on the description of the system at present stage a failure mode and effect analysis was performed and event trees have been set up.

The most important hazard potential to the environment is considered to arise from activity release to the containment.

For a first qualitative classification concerning only safety aspects the final events of the event trees are divided into four groups:

- Events with release of PbLi coolant into the vacuum vessel,
- Events with direct release of radioactive material into the containment,
- Events with loss of blanket cooling and additionally failure of plant shut down or detector of initiator,
- Events with failure of decay heat removal.

For each group starting points of accidents are given, necessary investigations on open questions are listed and possible design requirements in case of unacceptable consequences of an accident sequence are listed. The definition of possible design basis accidents is not possible at the present stage of design.

In preparation of future safety analyses some work could be done, e.g. the investigation of the chemical reaction characteristics of the coolants used in the system with air and/or steam generator failures on NaK-H2O reactions and finally the installation of computer codes for accident analysis.

References:

[1] Bogusch et. al.:
Functional Analysis for Blanket and Cooling System of a DEMO-Reactor based on the KfK-PbLi Self-cooled blanket.
KfK Contract 315/02966180/033

Staff:

R. Meyder

BL SA-D-2 Electromagnetic Forces

The existing code CARIDDI which computes the eddy currents and electromagnetic forces in toroidal structures has been improved. By introduction of the extended memory option the number of degrees of freedom which can be considered could be increased significantly. Thus modelling of complex, asymmetric structures with internal walls and electrically conducting fluids is possible. For such large problems also a reduction of the computing time could be achieved by optimization of the data processing.

Applications of CARIDDI to complex blanket models showed that some of the computed quantities revealed a slow but monotonic increase which is obviously not a correct description of the real behavior. Detailed investigations of the matrices used in CARIDDI showed that small inaccuracies of some matrix elements are the reason for this erroneous behavior. In the meantime a procedure has been developed which allows to correct the matrix elements such that the above problem does no longer occur.

It is state-of-the-art that the forces calculated by CARIDDI are used as input to carry out structural dynamics analyses. The feedback of the structural deformations on the electromagnetic behavior and thus on the resulting forces is neglected. Detailed investigations of this feedback revealed that the coupled treatment of the phenomena leads to differential equations of third order. Assessments showed that for most cases an approximation by differential equations of second order is possible. Then the feedback is represented by an additional damping matrix which can be calculated using the results of CARIDDI. A program for calculation of this damping matrix has been developed.

Application of the modified CARIDDI to a rather realistic blanket model is on the way. It is assumed that caused by the plasma disruption the plasma current decays linearly from 20 MA to zero within 20 ms while the magnetic field of the coils remains unchanged. The external and internal walls as well as the liquid metal coolant were described by more than 2000 degrees of freedom.

For the calculation of the dynamic blanket response the structure will be described by a finite element program. In a first step the feedback of the fluid motion on the forces acting at the structures is neglected. In a second step, however, this feed back (dynamic fluid structure interaction) will be considered. Finally also the feedback of the blanket movement on the electromagnetics will be approximated by introducing of the damping matrix.

Staff:

Th. Jordan
R. Krieg

BL CO-D-1 Flow Channel Inserts

Flow Channel Inserts (FCI) shall avoid electrical short circuits through the steel structure of a liquid metal cooled blanket. These short circuits - driven by an electrical potential induced in the flow - would effect unacceptable additional pressure drop. The FCI , a laminated element (steel-ceramic-steel), are fitted loosely into the coolant ducts of the blankets.

The development of FCI was carried out in collaboration with MBB. MBB should develop the fabrication methods, KfK the testing of the behaviour of the FCI. The objective of the development was not attained. Good mechanical bonding of the steel ceramic compound could not be achieved as required. Due to the different thermal expansion of stainless steel and ceramic, and due to the low mechanical strength of plasma sprayed ceramic the bonding failed or the ceramic layer cracked.

The work is continued in KfK. Stainless steel is replaced by martensitic steel, which has a low thermal expansion. For coating process plasma-spraying, chemical, vapour deposition, and melting of class-compounds will be investigated.

Staff:

V. Casal
M. Gegenheimer

BL CO-D-2 Liquid Metal Loop Components and Testing

For the DEMO ancillary loops straight tube double-wall steam generators (SG) with Pb-17Li around the outer pipes, water/steam in the inner pipes and NaK in the gaps between the pipes is planned. Concerning the safety for such a three fluid steam generator the possibility of a wastage of the inner structures in case of a water leakage into the NaK system can be a crucial point. This point has been investigated together with Interatom and the design of the SG has been so far improved that a wastage is uncredible. If NaK comes into contact with water/steam it will react under formation of hydroxides, oxides and hydrogen at a high temperature level. In case of a small leak and a sufficient free NaK volume a reaction flame can be formed causing wastage of the adjacent structures. In the gap region such a formation of a flame is not possible. The reaction products will drive out the NaK of the gap and a wastage may start first in the region of the NaK collection chambers. Fig. 1 shows the arrangement of wastage protection in the NaK collection chambers with 4 bores of 5 mm Ø for the exit of the NaK flow. This bores are arranged in an additonal gap in a wastage protection plate. The possibility of a wastage is eliminated by this measure, but in case of a rupture of the inner pipe the outlet of a higher water flow through the bores in the sleeves into the NaK collection chamber can result in pressure waves up to 90 bars. The NaK components must be designed to withstand such pressure waves.

Staff:

H. John
S. Malang

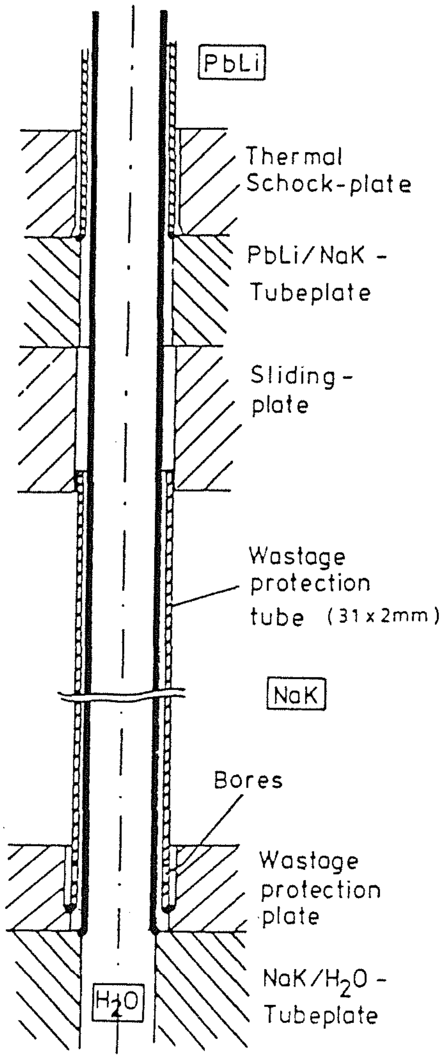

Fig. 1: Wastage Protection Tube

Development of ECRH Power Sources

Introduction:

The program aims at developing high-power millimeter-wave sources (gyrotrons) to supply current plasma experiments at the Max-Planck-Institut für Plasmaphysik (IPP Garching) and NET/ITER with electron cyclotron wave (ECW) systems for various applications. The frequency of 140 GHz corresponds to the second harmonic of the electron cyclotron resonance in the confining magnetic field of the stellarator Wendelstein W7-AS ($B = 2.5T$). In addition this frequency is a reference frequency for ECRH sources development for NET/ITER with the goal: 1 MW unit power in continuous wave (CW). ECRH development is the subject of cooperation between KfK Karlsruhe (power generation and millimeter-wave diagnostics), IPF University of Stuttgart (millimeter-wave transmission and detection) and IPP Garching (plasma experiments). Gyrotron design and prototype testing is the specific task of KfK, whereas fabrication of tube components and complete gyrotron tubes is done by industry. The experiments of IPP Garching on Wendelstein 7-AS present an intermediate goal for the development in terms of pulse length and output power requirements.

Long Pulse Operation of the TE03 Prototype Gyrotron

After a series of long pulse test measurements on the TE03 prototype tube with at least 500 pulses (pulse duration 100 ms) the oscillating region of the TE03 mode in the beam voltage/modulation voltage diagram was strongly restricted (see Fig. 1, middle part of the hatched area) compared to the original short pulse operation regime. Obtainable output power and efficiency were reduced from 300 kW and 36 % to 120 kW and 23 %, respectively. At the same time, the oscillation frequency of the cavity was up-shifted by about 0.5 GHz corresponding to a decrease of the resonator diameter due to irreversible deformation by cyclic fatigue as a consequence of the thermo-mechanical stress (max. power density on the cavity wall up to 10 kW/cm² at an output power of 200 kW). Nevertheless, the specific parameters for plasma experiments at IPP Garching, 100 kW and 0.1 s, could still be obtained reproducibly.

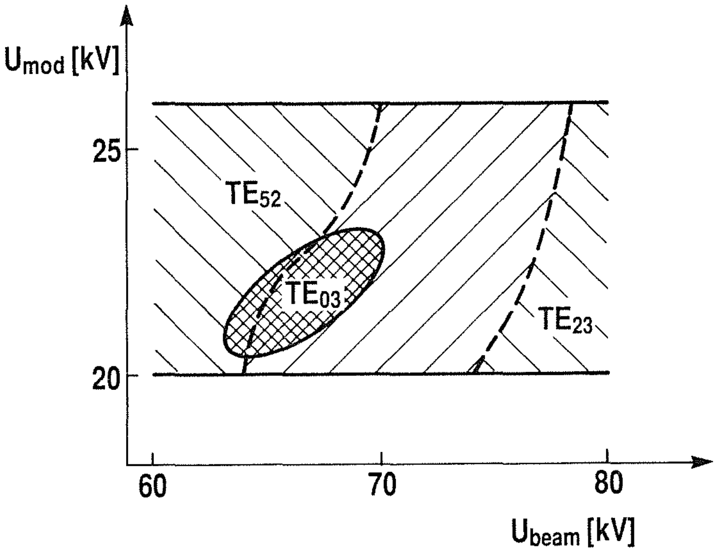

Fig. 1: Oscillation mode map of the TE03 mode before long pulse operation (hatched area) and after long pulse operation (cross hatched area).

The output mode purity was measured in collaboration with IPF University of Stuttgart with the help of a wavenumber spectrometer. Fig. 2 shows the measured mode spectrum. From this measurement we conclude that the contribution of the TE03 mode to the total output power ist at least 97 %.

The use of the gyrotron at IPP Garching for electron heat wave experiments requires the possibility of modulating the output power during a single pulse. By changing the modulation voltage by a few kV we were able to switch the output power on and off. Modulation frequencies up to 3 kHz have been achieved.

140 GHz ECRH Experiments on Wendelstein 7-AS

The 140 GHz TE03 prototype gyrotron has been installed at the Garching stellarator W7-AS and tested again. The maximum pulse duration could be increased to 0.5 s. A pulse length of 1 s and peak power of 100 kW were obtained in pulses with rectangular on/off modulation (duty factor of 50 %). Fig. 3 shows the modulated output power (200 Hz) of a 0.5 s pulse.

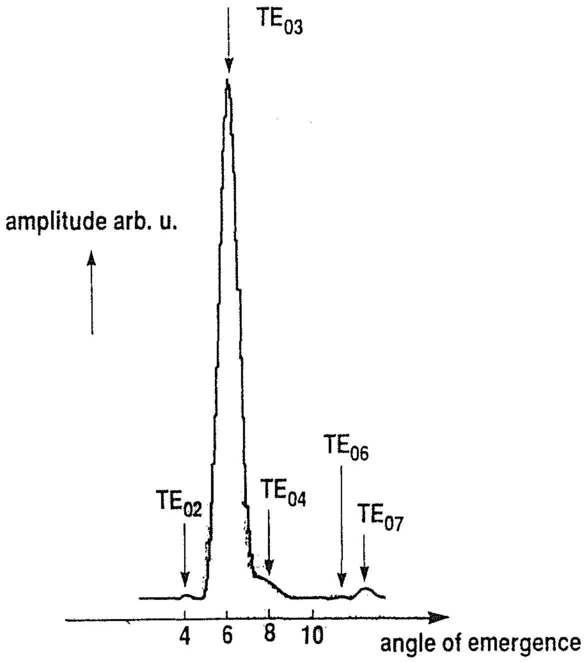

Fig. 2: Mode spectrum taken with a wavenumber spectrometer (I.D. = 63.5 mm). The angle is defined as zero in the direction of the load.

Using the KfK gyrotron the worldwide first 140 GHz ECRH experiments have been performed by the collaboration of IPP, IPF and KfK. The millimeter waves are transmitted from the gyrotron to the W7-AS torus over the distance of about 35 m by a quasi-optical mirror system. This transmission line was developed by the IPF Stuttgart and is designed for future 1 MW millimeter-wave power transmission. The most important aspect of 140 GHz ECRH is the extension of the accessible plasma density to twice the value of the existing 70 GHz W7-AS ECRH system, i.e. the cut-off electron density is $n_e = 1.2 \times 10^{20}$ m^{-3} at the resonant magnetic field of 2.5 T (second harmonic extraordinary mode). The high density operation offers indirect ion heating (Coulomb collisions) and the possibility to combine neutral beam injection heating (NBI) and ECRH. Several series of detailed ECRH and millimeter-wave plasma diagnostics experiments produced the following results:

(1) plasmas with electron temperature $T_e = 0.8$ keV and electron density of $n_e = 2 \times 10^{19}$ m^{-3} could be sustained alone by 65 kW, 140 GHz ECRH.

(2) 140 GHz ECRH is well localized in the plasma center for plasma densities up to the cutoff 1.2×10^{20} m^{-3}.

(3) Both the power deposition profile and the electron heat diffusivity can be derived from the measurement

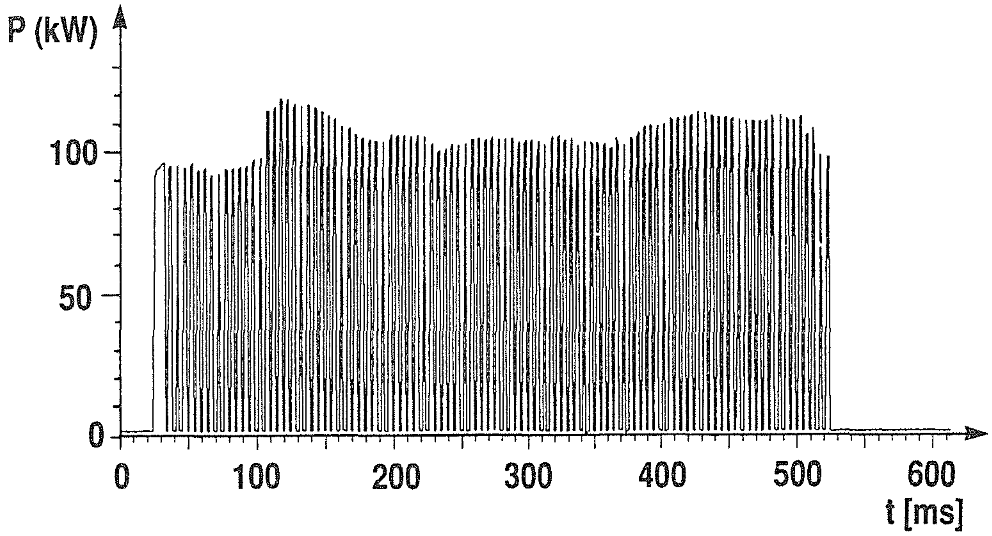

Fig. 3: Modulated output power of the TE0,3 mode, achieved by modulating the gun anode voltage.

of the phase shift and amplitude decay of an electron temperature modulation generated by a 100 % amplitude modulation of the incident microwave beam (heat pulse propagation analysis). This method was applied for the first time to a NBI-heated target plasma with a density well above the 70 GHz cut-off.

These encouraging results support the wish to have much more 140 GHz ECRH power available. To reach higher power at increased pulse length a higher order gyrotron resonator mode must be chosen in order to reduce the ohmic losses in the cavity.

High Power Gyrotron Development

KfK has designed, built and is testing a modular 140 GHz gyrotron which operates in the TE10,4 mode (asymmetric volume mode: AVM). The tube has a conventional axial output window and is installed in the present superconducting magnet (for TE03-mode gyrotrons). A schematic diagram of the 2 MW gun for this TE10,4 gyrotron is plotted in Fig. 4.

The magnetic compression ratio of 30 was chosen in order to keep the gun diameter below 100 mm. As a consequence, the maximum emitter current density is around 6 A/cm^2.

Theoretical and measured frequencies of the working mode and the competing modes of this AVM gyrotron are summarized in Table I.

The experimental frequencies agree very well with the calculated values. Very first measurements without ultimate parameter optimization gave output power up to 380 kW (with short pulse length of about 0.5 ms). The capabilities of this asymmetric volume mode approach in generating high power levels will be further studied. An external quasi-optical mode transducing antenna which converts the rotating TE10,4 mode to a free space Gaussian beam has been designed and constructed; it will be tested in the near future.

Table I: Calculated and experimental frequencies of the TE10,4 resonator

Mode	Calculated Frequency (GHz)	Observed Frequency (GHz)
$TE_{7,5}$	137.32	137.3
$TE_{10,4}$	**140.22**	**140.21**
$TE_{5,6}$	140.47	140.46
$TE_{3,7}$	142.48	142.40
$TE_{8,5}$	145.08	145.01

The next version of a 500kW AVM gyrotron at KfK will be installed in a new magnet (with larger inner bore hole) and will use a built in quasi-optical mode converter and a radial window (see Fig. 5) in order to separate the mm-wave output and the electron beam. It may then be possible to extend the pulse length up to 1 s.

Extension to higher output powers and CW operation will require a still higher order asymmetric volume mode. A preliminary study indicates that a TEm,p mode with m > 20 and p = 4-6 is promising.

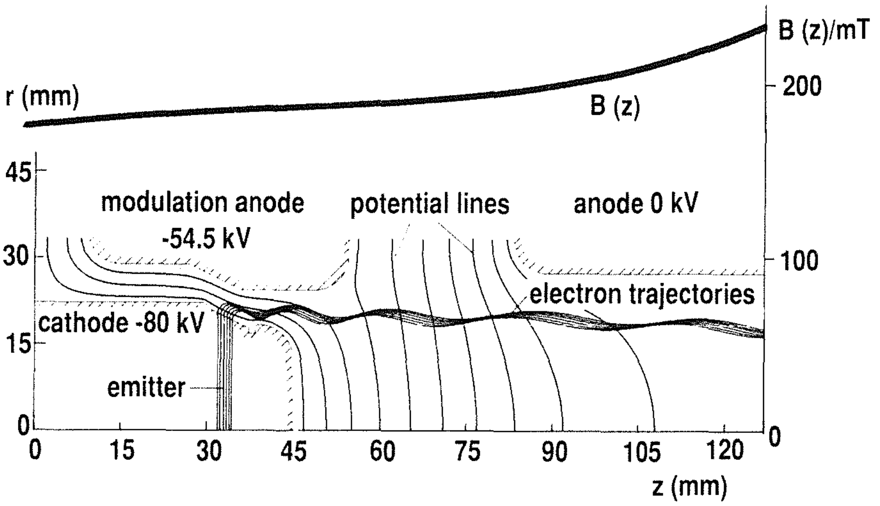

Fig.4: Schematic of the 2 MW electron gun for the TE10,4 gyrotron with electron beam trajectories, potential lines and axial magentic field B(z).

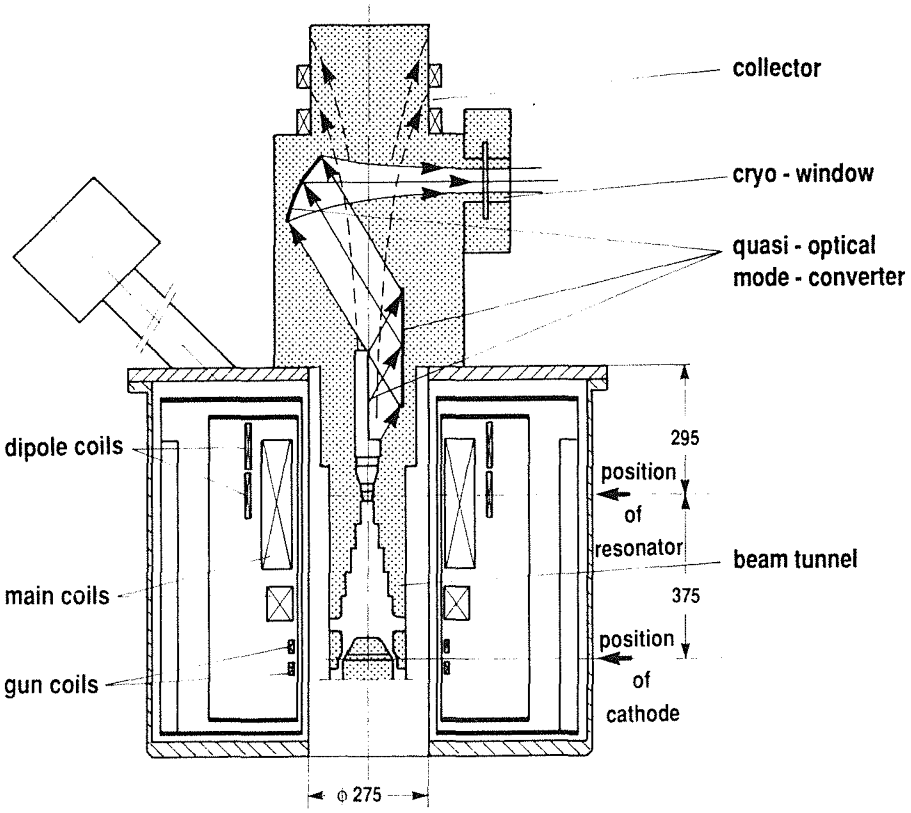

Fig 5: Schematic layout of an advanced AVM gyrotron with quasi-optical mode converter.

References:

[1] Gantenbein, G.; Dammertz, G.; Geist, T.; Hochschild, G.; Kuntze, M.; Liao, Z.; Nickel, H.-U.; Piosczyk, B.; Long Pulse Experience with the KfK 140 GHz Gyrotron. 16th Symp. on Fusion Technology, London, UK, 3-7 September 1990, Proc., Vol. 2, North-Holland, 1991, pp. 1161-1165.

[2] Borie, E.; Dammertz, G.; Dumbrajs, O.; Gantenbein, G.; Geist, T.; Hochschild, G.; Kuntze, M.; Liao, Z.; Möbius, A.; Nickel, H.-U.; Piosczyk, B.; Thumm, M.; Wenzelburger, H.; 140 GHz Gyrotron Development at KfK Karlsruhe. 15th Int. Conf. on Infrared and Millimeter Waves, Orlando, Fla., December 10-14, 1990. Conference Digest Bellingham: Int. Soc. of Optical Eng. 1990, pp. 493-495 (Proc. SPIE; 1514).

[3] Pioscyzk, B.; Compensation of the beam space charge and consequences for the design of a gyrotron. 15th Int. Conf. on Infrared and Millimeter Waves, Orlando, Fla., December,10-14, 1990. Conf. Digest Bellingham :

Int. Soc. for Optical Eng. 1990, pp. 499-501 (Proc. SPIE; 1514).

[4] Borie, E.; Gantenbein, G.; Self consistent theory for gyrotrons including effect of voltage depression. 15th Int. J. of Infrared and Millimeter Waves, Vol. 12, No. 2, 1991, pp 65-78

[5] Thumm, M.; Jacobs, A.; Pretterebner, J., Generation of rotating high-order TEm,n modes for cold-test measurements on high-power quasi-optical gyrotron output mode converters. 15th Int. Conf. on Infrared and Millimeter Waves, Orlando, Fla., December 10-14, 1990. Conf. Digest Bellingham: Int. Soc. for Optical Eng. 1990, pp. 204-06 (Proc. SPIE; 1514).

[6] Borie, E.; Dammertz, G.; Dumbrajs, O.; Gantenbein, G.; Geist, T.; Hochschild, G.; Möbius, A.; Nickel, H.U.; Piosczyk, B.; Wenzelburger, H.; Design of high power gyrotrons for KfK. 2nd Joint USSR-FRG Meeting on ECRH and Gyrotrons, Moskow, SU, June 18-23, 1990, Workshop Contributions. Gorky: Inst. of Applied Physics, Academy of Sciences of the USSR, 1990, pp. 63-73.

[7] Dammertz, G.; Nickel, H.U.; Gyrotron components. 2nd Joint USSR-FRG Meeting on ECRH and Gyrotrons, Moskow, SU, June 18-23, 1990, Workshop Contributions, Gorky: Inst. of Applied Physics, Academy of Sciences of the USSR, 1990, p.p. 51-62.

Staff:

W. Baumgärtner
E. Borie
H. Budig
G. Dammertz
O. Dumbrajs (TU Hamburg-Harburg)
U. Feißt
G. Gantenbein
T. Geist (UNI Karlsruhe)
P. Grundel
A. Hornung
M. Kuntze
R. Lehm
A. Möbius
N. Münch
H.-U. Nickel
B. Piosczyk
G. Redemann
M. Thumm
R. Vincon

High Power Windows

Window systems are needed both for hermetical sealings of the gyrotron towards the transmission system and for the fusion plasma supply system. These windows should be suited to accommodate 1 MW power at passage in permanent operation.

KfK is developing the concept of a single-disk window cooled at the edges [1]. Compared to the double-disk window with surface cooling this concept offers the advantage that no coolant is present in the zone of the high frequency beam. Consequently, cooling of the window edge can be done ad lib and in case of fracture of the window the coolant does not automatically enter the gyrotron or/and the transmission system. Moreover, the single-disk window design is probably simpler and more reliable (Fig. 6).

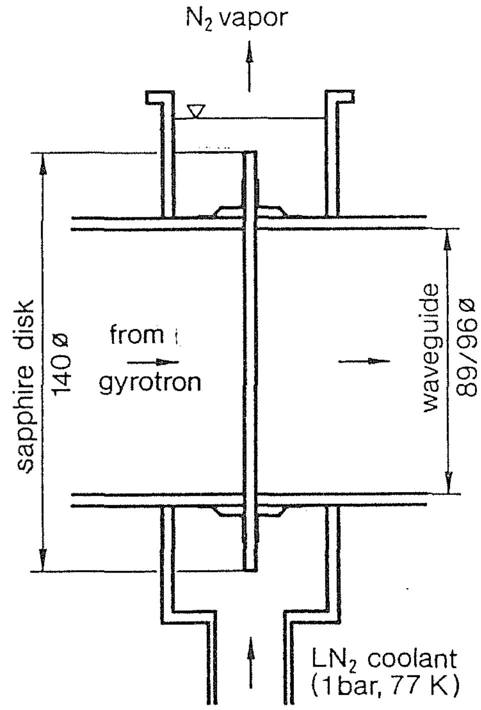

Fig. 6: Schematic of single disk window edge cooled by boiling liquid nitrogen

In order to attain the development target a window material is required with high thermal conductivity and low power absorption. The favorite material is sapphire. This Al_2O_3 monocrystal has the required avantageous properties at low temperatures. Eligible coolants might be liquid nitrogen and, in addition, helium at very low temperature.

During the period of reporting liquid nitrogen cooling was studied for the initial step. It is less expensive in engineering terms and more economical in operation. The impacts of various parameters and factors on the power limit have been demonstrated in a study and, in addition, the uncertainties still existing now have been indicated [2, 3]. It became particularly apparent that of all parameters investigated the influence of the absorption factor tan δ is strongest. On account of the presently still high uncertainties of the measured results a precise power limit cannot yet be given. Figure 7 shows the dependence of power at passage on the thickness of the disk and the coolant temperature for mean tan δ values as well as the maximum and minimum values of the error bar. According to that figure, a power at passage of 0.7 MW would be admissible for the optimum values of tan δ at 1.76 mm disk thickness and for open pool boiling in liquid nitrogen (Tc = 77.35 K). Values higher by 40% would be attainable upon pressure reduction to 0.4 bar (Tc = 70 K). For unfavorable tan δ values, lower temperatures must probably be chosen (helium cooling). The limiting factor is not the heat removal due to bubble boiling at the edge of the window but the radial heat removal in the disk proper (bottleneck effect).

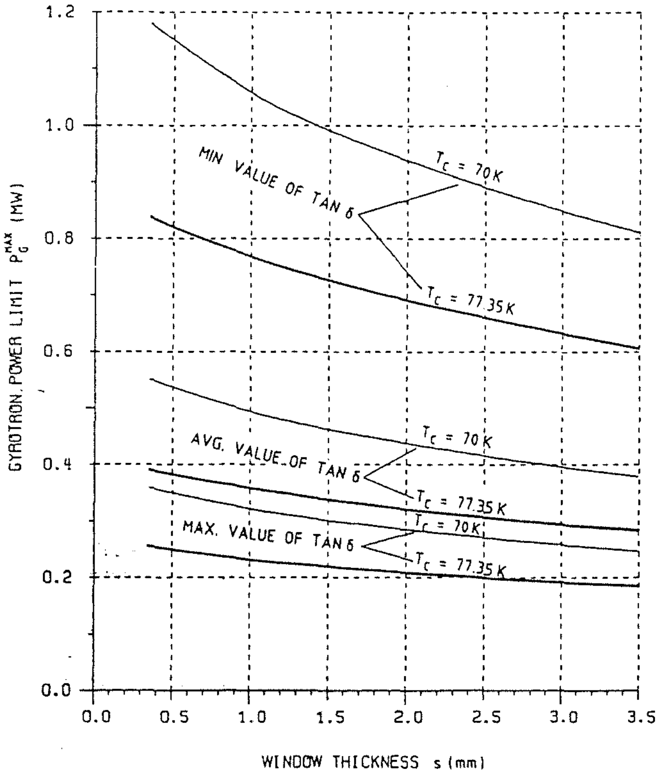

Fig. 7: Dependence of the power at passage on the thickness of the pane, the coolant temperature, and the loss tangent.

The selected window concept is presently being tested in an experimental setup.

References:

[1] H.E. Häfner, P. Norajitra, E. Bojarsky, H. Reiser: unpublished report of KfK

[2] P. Norajitra: Cryo-cooled High-power Window for High-frequency Plasma Heating, Thermodynamic Study of the Single-disk Concept with Liquid Nitrogen Edge Cooling, KfK-Bericht 4930

[3] R. Heidinger, A. Hofmann, H.-U. Nickel, P. Norajitra: The Impact of Neutron Irradiation to the Performance of Cryogenically Cooled Windows for Electron Cyclotron Resonance Heating, 2nd International Symposium on Fusion Nuclear Technology, Karlsruhe, June 2-7, 1991

Staff:

E. Bojarsky
H.E. Häfner
K. Heckert
A. Hofmann
H.-U. Nickel
P. Norajitra
N. Münch
K. Philipp
H. Reiser
R. Vouriot

Studies for NET

Introduction:

By granting study contracts to KfK, NET draws upon special expertise available in the laboratory. In contrast to the technology tasks which extend over a longer period of time and consist in most cases of experimental work, study contracts are agreed on short notice and are of limited duration. In the term span the KfK has spent approximate two manyears for this kind of arrangements. Subjects scatter widely according to the need arising from the design activity for NET/ITER.

Fatigue Characterization of Jacket Materials at 4K

In order to cover the uncertainties arising with manufacture related surface defects cryogenic mechanical investigations were carried out with the candidate stainless steel 316 LN type material to establish basic engineering data for the structural design of the superconductors jacket of the ohmic heating coil. To determine the jacket materials performance during the cyclic loading fatigue-life and fatigue crack growth rate measurements were performed with specimens bearing predefined surface flaws.

1. Specimens

The fatigue-life specimens were 100 mm long smooth cylindrical type with a reduced section of 20 mm length and 3.5 mm diameter. The centerly located flaw of these specimens was machined by electro discharge method (EDM) and it was possible to machine predefined semi-circular flaws in the range of ~ 0.2 mm depth. For the surface crack growth characterization specially machined 100 mm long specimens with rectangular cross section (4 mm thick and 10-7 mm width) were used. Similar semi-circular flaws as in the case of the fatigue-life specimens were located in the center of the width to initiate the crack by fatigue loading.

2. Test equipment

All these cyclic investigations were conducted in a helium flow cryostat equipped with a servohydraulic tensile machine of ± 25 kN capacity (MTS, Modell 810).

3. Test Procedure

The flawed specimens for the fatigue-life tests were loaded at $R = 0.1$ with a frequency of 30 Hz. During cycling the EDM-notch was directly observed with a built-in fiberscope (magnification 22x) to record the beginning of the crack emanation. Beside this a high resolution clamp-on extensometer mounted on the specimen was used to monitor the displacement situation on a 2 channel oscilloscope to determine the strain condition in the vicinity of the flaw region. The crack initiation and the further fatigue crack growth result in a steady displacement increase of this region at constant cyclic load. By displacement control it was possible to load the specimen at a constant stress condition with respect to the remaining non-fractured cross section. According to this technique constant stress vs. life of the material at different stress levels could be determined for the case when loading was started with an EDM-notch or with an already existing, predefined fatigue crack in the specimen.

The behavior of surface cracks under fatigue loading were investigated with the 4 mm thick rectangular specimens (see Fig. 1). An EDM-notch of ~ 0.2 mm depth served as a crack starter. The crack growth observation was performed directly with the fiberscope and the grid on the specimens surface. Several specimens were cycled at 295 K and at 12 K to see whether any difference of crack shape exists between these two temperatures. No significant difference was detected between these temperatures concerning the crack profile. The semi-circular crack shape was preserved at least until 3/4 of the specimen thickness B. This figure has been taken as a last position before fracturing the specimen. The semi-circular crack shape at different crack depths (below 3/4 thickness) could be double checked with two different techniques. First by load shedding technique (beach marks) and second by stopping the loading for the reason of marking, i.e. fatigue precracking at 295 K colors the crack surface by air oxidation dark, whereas at 12 K and at He-gas environment the crack surface remains clear (Fig. 1, see C, D, and E). The width (2b) was varied between 10 mm to 7 mm and did not show any effect on the crack shape and on the FCGR. The stress intensity factors K at c and a positions ($\Phi = 0°$ and $90°$, respectively) were computed by Raju & Newman equations (1), where K is a function of Φ, a, c, b, B and stress range $\Delta\sigma$ (see Fig. 1, G). The determination of da/dN vs. ΔK at 295 K and 12 K was performed unter constant load condition (K-increasing) after precracking at 295 K. The crack length was measured incrementally during the fatigue loading by monitoring the mirror polished surface via the built-in fiberscope with an accuracy better than 0.1 mm. The crack surface of the fractured specimens was inspected under high resolution stereo microscope concerning their circularity, the total propagated crack length, and the dark colored initial

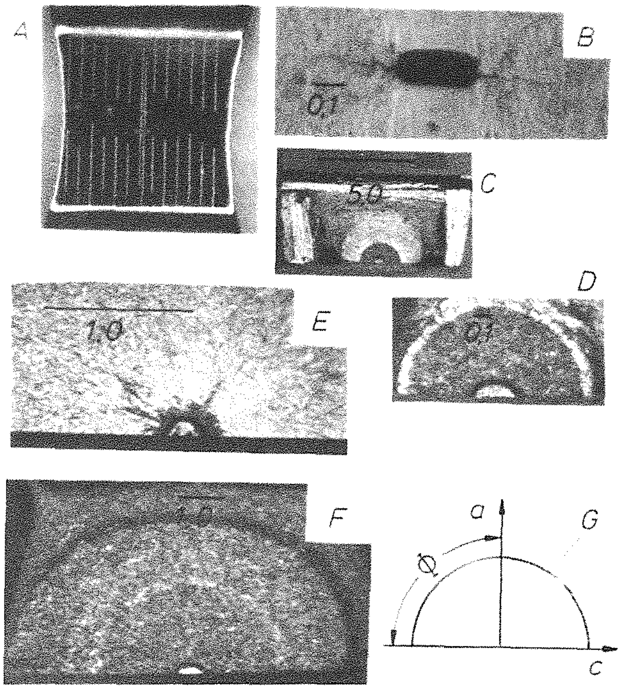

Fig. 1: Surface crack investigations. A) Specimen with the grid of 0.5 mm spacing. B) Crack penetration at the surface from the EDM-notch at 295 K. C) and D) 295 K (dark) and 12 K (light) semi-circular crack growth. E) 295 K semi-circular crack growth started from a non-circular EDM-notch. F) 295 K beach marks at different stages of crack growth. G) Surface crack growth designations according to Raju and Newman[1].

crack length, which differes clearly from the crack propagated regime at 12 K (see Fig. 1, C, D, and E).

4. Results and Discussion

Constant fatigue stress-life investigations with 316 LN flaw bearing base metals show considerably lower fatigue life performance as compared to non-flawed specimens. Figure 2 shows the determined stress vs. cycle plots of the flawed specimens in comparison with the previously recorded findings with 316 LN and Incoloy 908 base and welded metals, respectively.

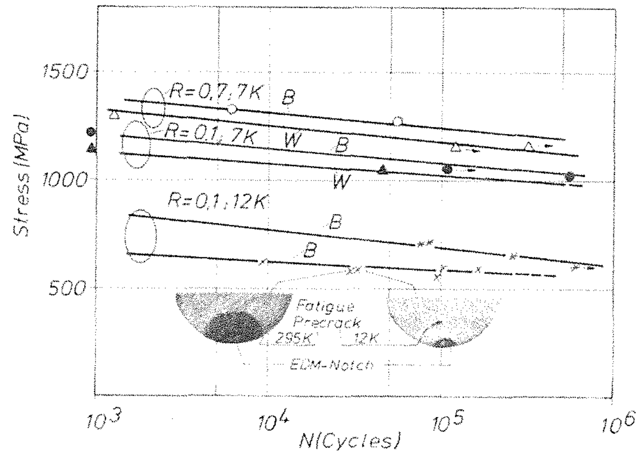

Fig. 2: 7 K fatigue-life results of smooth cylindrical specimens with 316 LN and Incoloy 908 base metals (B) and their flash butt weldments (W) at R = 0.1. (*) 12 K results of 316 LN base metal starting from a small EDM-notch at constant stress condition. (x) 12 K fatigue-life results of 316 LN base metal starting with a predefined fatigue crack. Fatigue crack initiation performed either at 295 K or at 12 K.

The fractured surface of the specimen (Fig. 2) indicates the constant stress condition due to the fine sectional separation. Starting with a EDM-flaw require a considerable amount of cycles to emanate the initial crack. In this context it is worth mentioning that SEM inspection of the EDM surfaces shows virtually small microcracks introduced by thermal shock process during the electro-discharge in the oil bath. This means that any other artificial flaw (e.g. scratches, etc.) will behave not so severe as the one with the EDM-flaws. Marking the penetrated crack either by beach marks at 12 K or heat tinting at 295 K and further constant stress fatigue loading at 12 K (with respect to the remaining cross section estimated after the test on the broken halves) show no differences between a crack opened at 295 K or at 12 K in this stress regime. A specimen failure with a started predefined crack (most severe case) shows approximately ~ 20% lower performance as compared to a severe artificial flaw (EDM-notch)

The FCGR of surface cracks for the 316 LN base metal (as received) yield between 10 to 35 MPa√m a linear relationship at R = 0.1 in the double logarithmic da/dN vs. ΔK diagram. The 12 K results of five specimens plotted in this diagram gives a scatterband for the crack propagation law in c-direction (see Fig. 1, G) Paris law constants of N = 4.19 and C between $3.21 \cdot 10^{-11}$ - $5.14 \cdot 10^{-11}$. For 295 K the obtained values for n and C are n = 3.16,C between $4.0 \cdot 10^{-9}$ - $4.9 \cdot 10^{-9}$ (C in mm/cycle). Regarding this fact the cryogenic environment seems to be not so harmful as compared to the 295 K case, contrary to the obtained findings with CT-specimens (embedded cracks[4]). To check the performed tests towards their consistency the cyclic life was predicted for all broken specimens concerning their initial crack a_0 and the final crack. Substituting the obtained growth law constants n and C in a system of equations as given by

$$N = \sum_{i=1}^{1=m} \Delta a / C \cdot \Delta K_i^n , \; \Delta K_i = f(\Delta\sigma, a, c, b, B, \Phi) \qquad (1)$$

$$and \; a = a_o + \sum_{i=1}^{1=m} \Delta a$$

a numerical computation could be carried out and it could be confirmed that for all specimens the predicted cycle numbers fit with the experimentally determined cycle numbers.

Staff:

A. Nyilas
H. P. Raber
J. Zhang

Test of Stress Induced Degradation of Subcomponents of the NET OH Conductor

This report describes the final measurements of "Cable in Conduit" (CIC) conductors at KfK Karlsruhe manufactured by the wind-and-react method and delivered by Asea Brown Boveri (ABB) and Europa Metalli-LMI (LMI).

Different subsize conductors were fabricated based either on triplet or braid type cable with the reduced scale of 1:21 to 1:7 and the corresponding number of 27 to 108 strands. For all samples "Modified Jelly Roll" processed ternary Nb_3Sn strands with Ø 0.78 to 0.96 mm were used delivered by Teledyne Wah Chang Albany (TWCA). The cables were inserted into a thin walled steel pipe and swaged down to the final diameter which corresponds to the desired void fraction for LHe cooling of $V_f \approx 40$ vol.%, and then heat treated up to 650°C according to the TWCA specification. Fig. 1 shows a CIC conductor fabricated by ABB consisting of a braided cable with 87 strands (Ø 0.93 mm) and a SS conduit with an OD = 14.2 mm and void fraction $V_f = 43\%$.

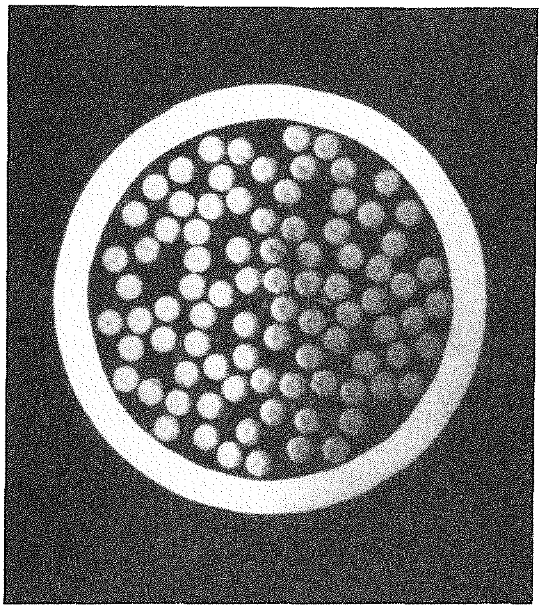

Fig. 1: CIC conductor consisting of braided cable with 87 strands (Ø 0.93mm) and steel conduit with OD = 14.2 mm, $V_f = 43\%$, fabricated by ABB.

The critical current, I_c, as a function of the magnetic field, B, without applied strain was measured, as shown in Fig. 2. (Sample identification: A or L: sample delivered by ABB or LMI, 27: number of strands). Due to the current limitation of the respective test rig, the strands A1U2-7L could be tested at 13 T, the subcables A81/A87 at 12.5 T, and the subcables L108 at 12-13 T only. The single strand I_c values are multiplied by 27 in order to compare this value with the subcables. Two identical samples from the twisted (A27S1/2L) and the braided subcables (A29S1/2L) were measured in the field range of 9 to 13 T. An almost perfect agreement is observed for the two samples of both conductors A27 and L108 while the I_c values of the A29 cables differ 6 - 8% from each other. Between the two types of subcables A27 and A29, however, the difference of I_c amounts to about 20%. Furthermore all subcables exhibit a degradation of about 50-60% at 13 T in comparison to the corresponding amount of basic strands. These effects can be explained on the basis of the different prestrain behaviour on I_c.

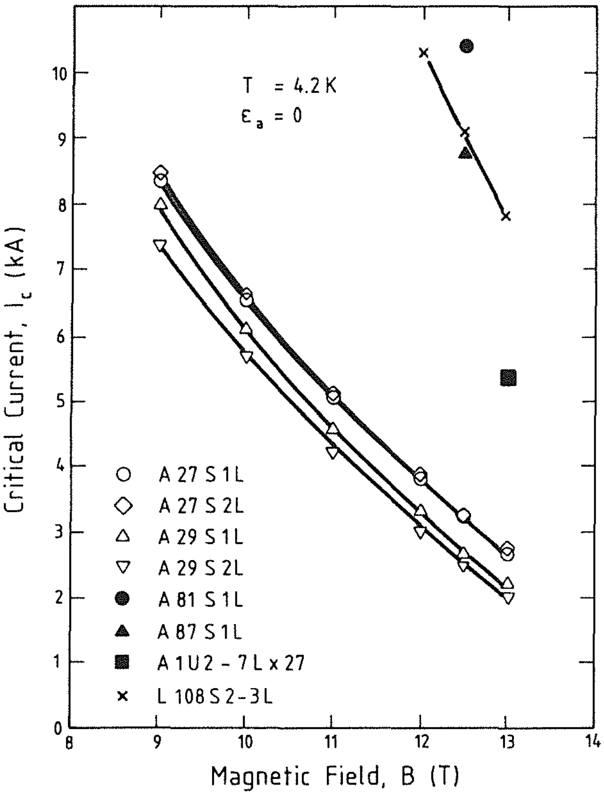

Fig. 2: Critical current as a function of magnetic field for strand (Ø 0.96 mm, A1), tripleted cable conductor A27, A81, L108 and braided cable conductor A29, A87.

The axial strain dependence on I_c at B = 13 T for the LMI sample (108 strands, Ø 0.78 mm) in loaded and unloaded states is shown in Fig. 3. Like the ABB conductors a drastic decrease of I_c can be observed, expressed by the ratio I_{co}/I_{cm}. For all tested CIC conductors I_{co}/I_{cm} ranges from 0.41 to 0.60, while the peak value of the critical current, I_{cm}, occurs at $\varepsilon_m \approx$ 0.7% for most samples. The enhanced degradation of I_c results from the higher prestrain onto the Nb_3Sn filaments, introduced mainly by the higher thermal contraction of the simultaneously heat treated (650°C) steel jacket in comparison to the Nb_3Sn.

Cycling strain up to 10^3 cycles, applied to the sample at T = 4,2 K in the strain range of 0.17 to 0.4% shows no effect on the I_c vs ε_a characteristic (Fig. 3), confirming earlier results under similar conditions.

The values of I_{cm} at B =12.5/13 T of the higher stage subcable (81, 87 and 108 strands) exceed the limit of 10 kA of the power supply for the sample current. Therefore I_c vs ε_a

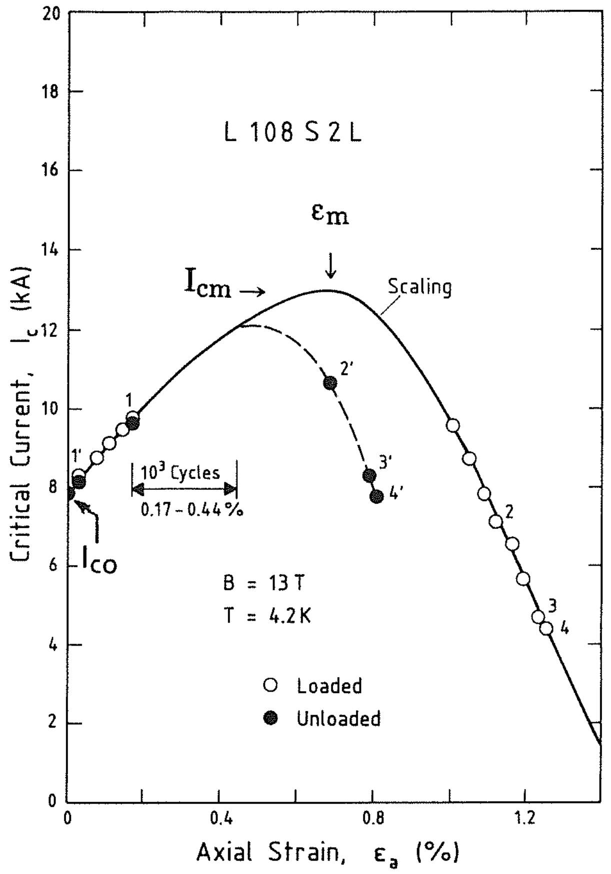

Fig. 3: Strain dependence of critical current of LMI conductor with 108 tripleted strands (Ø 0.78 cm). Open and full circles represent measurements and solid line scaled functions

measurements of these samples could be performed at low and high strain values only, leading to a "window" around ε_m of this curve, as shown in Fig. 3 by open and full circles. Using Ekin's scaling low on can fit this function with sufficient accuracy (solid line).

Both conductors showed the expected degradation of about 40% for sero strain as consequence of the prestress induced by the heat treatment. No other degradations were observed so that the conductors are applicable for fusion magnets by the assessment of present subcable investigations.

The work was concluded. The final report was transmitted to the NET team and accepted

Staff:

H. Kiesel
M. Klemm (till March 31, 91
W. Specking

Laser Beam Welding Technology Optimization for Long Longitudinal Welds of the NET Conductors

The application of laser beam welding technology was successfully demonstrated for the conductor of the Polo model coil. The gained experience was evaluated and summarized in a report.

One of the open points was the determination of the depth of the welding seam during the production of the conductor. For a conductor length required for a NET model coil pancake a control of the welding depth is indispensible.

In collaboration with a company experienced in ultra sonic measurements tests were performed to optimize the sensor position at the conductor surface. On test samples it was demonstrated that signals were obtained in relation to the welding depth (Fig. 1).

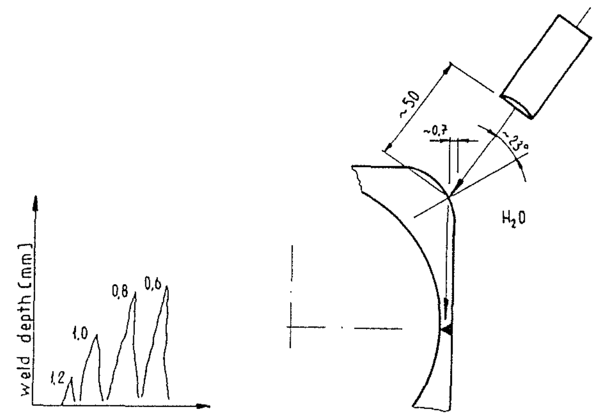

Fig. 1: Optimization of the angle and the distance of the ultra sonic head relative to the inspected weld seam of the Polo conductor and sensitivity check.

A test equipment suitable for making these measurements during the conductor fabrication was constructed (Fig. 2). The conductor is guided by rollers on both sides of a container. These rollers fix the ultra sonic sensor accurately relative to the conductor. The ultra sonic wave is coupled in the conductor by a water column supplied by running water which is then collected in the container. The ultra sonic sensor is adjustable in certain limits relative to the conductor surface. The system was tested with 6 m Polo conductor length prepared with different welding depths. Signals were obtained wnich were suitable to control the welding depth in future fabrication lines. Specially a reduction of the nominal welding depth of 0.2 mm resulted in a clear visible signal while for bigger deviations the sensitivity is decreasing.

This result allows the continuous control of the welding deth and adjustment of the welding parameters during the welding process.

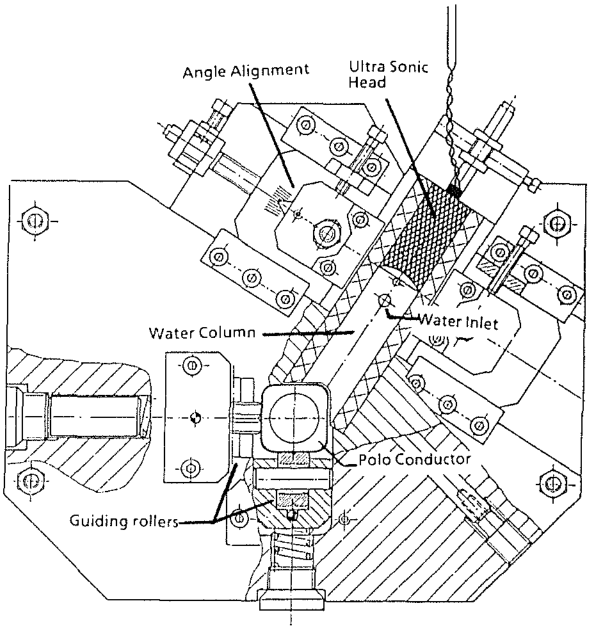

Fig. 2: Equipment for guiding the conductor relative to the ultra sonic head. The ultra sonic wave is coupled by a fluent water column in the conductor. The water is collected in the container.

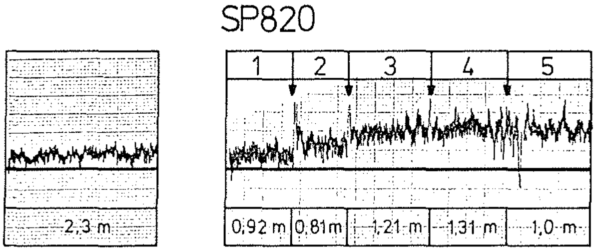

Fig. 3: Ultra sonic signal along a Polo conductor with different welding depths (1 = 1.53 mm nominal; 2 = 1.43 mm, 3 = 1.34 mm; 4 = 1.24 mm, 5 = 1.14 mm.

For later application in fusion conductor jackt fabrication continuous and discontinuous laser beam welding is assessed based on the obtained experience.

Staff:

S. Förster
A. Nyilas
U. Jeske
E. Ratjen
F.Feketitch
A. Ulbricht

Specification of Vacuum System Prototypes

The requirements for the turbomolecular pumps (TMP) have been discussed with the NET-team and most of them have been defined. The most critical requirement is maintaining the torus pressure at 1×10^{-3} mbar during the glow discharge mode with deuterium (total throughput 100 mbarl/s) and at 3×10^{-3} mbar with helium (total throughput 300 mbarl/s.) In the latest conceptual design draft (CDD) for TMP (NET-study contract No. 89-793) these values could not be achieved with the TMP unit size investigated.

In agreement with the NET-team a forepumping stage is required for the TMP. With this stage higher outlet pressures can be achieved at the TMP and the capacity of the forepumping station can be substantially reduced.

To achieve the required values during the glow discharge mode, as defined in the ITER CDD Fuel Cycle, the TMP rotor must be increased in length from 700 to 800 mm to be suitable for a double flow pump. The new values for the technical specification of the TMP have been estimated as follows:

- At an inlet pressure of 2.4×10^{-3} mbar the TMP shall provide a minimum helium throughput of 43 mbarl/s with a minimum outlet pressure of 3.0×10^{-1} mbar.

- At an inlet pressure of 7.1×10^{-4} mbar the TMP shall provide a minimum deuterium throughput of 1.43 mbarl/s with a minimum outlet pressure of 1.3×10^{-1} mbar.

After reviewing the 3rd draft of the Technical Specification for TMPs the NET-team decided to give up the ITER CDD requirements for the glow discharge mode and adopt again the former smaller TMP version. The 4th draft of the Technical Specification for TMPs has been completed.

Staff:

H. Illbruck
D. Perinic

Appendix I: Allocation of Tasks

Task No.	Title	KfK Departments
Plasma Facing Components		
PSM 3	Pre- and Post-Irradiation Low Cycle Fatigue of Reference 316 L Steel and Welds	IMF II
PSM 4	Pre- and Post-Irradiation Properties of Joinings	IMF II
PSM 8	Coatings and Surface Effects on 316 L	IMF II
PPM 0	Development and Characterization of Graphites and CFCs Including Neutron Irradiation Effects	IMF II
PPM 1	Development and Characterization, Neutron Irradiation Effects, Development of Coating Techniques for Doped C Composites	IMF I
PPM 4	Material Characterization and Irradiation Effects in Ceramic Insulators	IMF I, IMF II
PDT 1	Thermomechanical Tests of First Wall Mock-ups	IMF II, IATF
PDT 2	Tests of Divertor Samples and Mock-ups	IRE
Superconducting Magnets		
MCON	Manufacturing of Short Length of Full-Size 40 kA Conductor	ITP
MTOR	Design, Manufacturing and Test of an Outer Coil for TORE SUPRA	ITP
MTOS	Upgrade of the TOSKA Facility for Model Coil Testing	ITP, HIT
MBAC	Development of Conductor Cooling Technique at 1.8 K	ITP
MFAU 1	Safety Relevant Models for NET Magnets	IRE, ITP
MTC 1	Industrial Manufacturing of React-and-Wind Nb_3Sn Conductors and of TF Model Coils (December 1990 concluded)	ITP
Vacuum and Fuel Cycle		
TPV 1	Development of Solid Particle Separators for Plasma Exhaust	HIT
TPV 2	Optimization of the Cryogenic Vacuum Pumping of Helium	HIT
TEP 1	Cryosorption on Molecular Sieves or Alternative Cryosorbents	IRCH
TEP 2	Plasma Exhaust Processing Alternative Options	IRCH, IMF I
TCP 3	Atmospheric Processing	IRCH
Nuclear Engineering / Basic Blanket		
NSN 1	Neutronics Data Base for Shielding	INR

Remote Handling / Maintenance

RHS 1	Qualification of Standard Components	HIT
RHS 2	Material Tests for Remote Maintenance Equipment	HIT, IRE
RHS 3	Mock-up of In-Vessel Components and Test Facilities	HIT
RHT 1	Articulated Boom Transporter	HIT, IRE, IDT

Safety and Environment

SEP 2	Environmental Impact of Tritium and Activation Products	INR
SEA 3	Analysis of Reference Accident Sequences	IRE
SEA 5	Assistance in Preparation of the Safety Reports	IRE, ITP

Long Term Program for Materials Development

LAM 2.1	Low Activation Fusion Materials Development	IMF II
LAM 3	Development of Low Activation Martensitic Steels	IMF I, IMF II
LAM 5	Development of Low Activation Non-Ferrous Alloys	IMF II
MANET 1	Characterization and Optimization of MANET I and II Steels	IMF I, IMF II
MANET 3.2	Pre- and Post-Irradiation Fatigue Properties	IMF II
MANET 3.4	Pre- and Post-Irradiation Fracture Toughness	IMF II, HVT/HZ
MANET 5	Ion-Beam Irradiation Fatigue and Creep-Fatigue Tests	IMF I

Test Blanket Development

BS - Solid Breeder Test Blankets

BS DE-D-1	Solid Breeder Test Blanket Design	IMF III, INR
BS BR-D-1	Preparation of Ceramic Breeder Materials	IMF III
BS BR-D-2	Characterization of Ceramic Breeder Materials	IMF III
BS BR-D-3	Irradiation Testing and Post Irradiation Examination	IMF III, HVT/HZ
BS BR-D-4	Tritium Release	INR
BS BR-D-5	Physical and Mechanical Properties	IMF I
BS BR-D-6	Compatibility	IMF I
BS BR-D-7	Constitution, Interaction with Water Vapour	IMF I

BS BR-D-8	Mass Spectrometric Free Evaporation Measurements on Lithium-orthosilicate Surfaces	IRCH
BS NN-D-1	Helium Blanket Test Loop	IMF III, INR

BL - Liquid Metal Test Blankets

BL DE-D-1	Liquid Metal Test Blanket Design	IMF III, INR, IATF
BL MH-D-1	Liquid Metal MHD	IRB
BL PC-D-1	Corrosion of Structural Materials in Flowing Pb-17Li	IMF I, IMF III
BL PC-D-2	Impurities and Clean-up of Molten Pb-17Li	HIT
BL EX-D-1	Tritium Extraction by Permeation and Cold Trapping	IRB
BL EX-D-2	Tritium Extraction from Molten Pb-17Li with Solid Getters	HIT
BL SA-D-1	Functional Analysis of a Liquid Metal Self-cooled Blanket	IRE
BL SA-D-2	Electromagnetic Forces	IRE
BL CO-D-1	Flow Channel Inserts	IATF
BL CO-D-2	Liquid Metal Components and Testing	IATF

Development of ECRH Power Sources

ITP, IMF III

Appendix II: Table of NET Contracts

Theme	Contract No.	Working Period
Fatigue Characterization of Jacket Materials at 4 K	372/89-4/FU-D/NET	5/89 - 10/90
Test of Stress Induced Degradation of Subcomponents of the NET OH Conductor	392/89-8/FU-D/NET	10/89 - 3/91
Laser Beam Welding Technology Optimization for Long Longitudinal Welds of the NET Conductors	408/90-1/FU-D/NET	2/90 - 7/91
Specification of Vacuum System Prototypes	426/90-7/FU-D/NET	8/90 - 12/91

Appendix III: KfK Departments Contributing to the Fusion Project

Kernforschungszentrum Karlsruhe GmbH Telephone (07247) 82-1
Postfach 3640 Telex 17 724 716
D-7500 Karlsruhe 1 Telefax/Telecopies (0) 07247/825070
Federal Republic of Germany

KfK Department	KfK Institut/Abteilung	Director	Ext.
Institute for Data Processing in Technology	Institut für Datenverarbeitung in der Technik (IDT)	Prof. Dr. H. Trauboth	5700
Institute for Materials Research	Institut für Material- und Festkörperforschung (IMF)	I. Prof. Dr.K.-H. Zum Gahr II. Prof. Dr. D. Munz III. Prof. Dr.K. Kummerer	3897 4815 2518
Institute for Neutron Physics and Reactor Engineering	Institut für Neutronenphysik und Reaktortechnik (INR)	Prof. Dr. G. Keßler	2440
Institute for Applied Thermo- and Fluiddynamic	Institut für Angewandte Thermo- und Fluiddynamik (IATF)	Prof. Dr. U. Müller	3450
Institute for Radiochemistry	Institut für Radiochemie (IRCH)	Prof. Dr. H.J. Ache	3200
Institute for Reactor Development	Institut für Reaktorentwicklung (IRE)	Prof. Dr. D. Smidt	2550
Central Engineering Department	Hauptabteilung Ingenieurtechnik (HIT)	Dr. H. Rininsland	3000
Institute for Technical Physics	Institut für Technische Physik (ITP)	Prof. Dr. P. Komarek	3500
Central Experimental Engineering Department	Hauptabteilung Versuchstechnik (HVT)	Dr. Schubert	3114
- Hot Cells	- Heiße Zellen	DI. Enderlein	3650
- Tritum Laboratory Karlsruhe	- Tritiumlabor Karlsruhe	DP. Jourdan	2514
Remote Handling Laboratory	Handhabungstechnik-Labor	DI. Müller-Dietsche	2942
Central Safety Department	Hauptabteilung Sicherheit	DP. W. Koelzer	2660

Appendix IV: Fusion Project Management Staff

Head of the Research Unit	Dr. J. E. Vetter	ext. 5460
Secretariat:	Fr. I. Sickinger	ext. 5461
	Fr. I. Pleli	ext. 5466
	Fr. M. Zimmer	ext. 5466
Project Budgets, Administration, Documentation	BW G. Kast	ext. 5462
Studies, NET Contacts	Dr. J.E. Vetter	ext. 5460
Blanket Development and Test Facilities	DI H. Sebening	ext. 5464
Superconducting Magnets **Gyrotron Development**	DI H. Knuth	ext. 5468
Tritium Technology **Structural Materials**	Dr. H.D. Röhrig	ext. 5463
Safety and Environmental Impact, Remote Handling	DI A. Fiege	ext. 5465

Address: Kernforschungszentrum Karlsruhe GmbH
Nuclear Fusion Project Management

Post Office Box 3640, D-7500 Karlsruhe / Germany

Telephone No: 07247-82- Extensions ....

Telefax No: 07247 - 82 - 5467

Telex No: 17 724 716